Hole Spin Qubits in Ge/Si Core/Shell Nanowires

Inauguraldissertation

zur

Erlangung der Würde eines Doktors der Philosophie

vorgelegt der

Philosophisch-Naturwissenschaftlichen Fakultät

der Universität Basel

von

Florian Norbert Matthias Froning

aus Deutschland

2021

Genehmigt von der Philosophisch-Naturwissenschaftlichen Fakultät

auf Antrag von

Prof. Dr. D. M. Zumbühl

Prof. Dr. Georgios Katsaros

Prof. Dr. Menno Veldhorst

Basel, den 23.06.2020

Prof. Dr. Martin Spiess

Dekan

Abstract

Spins in semiconductor quantum dots are among the most promising candidates for the realization of a scalable quantum bit (qubit), the basic building block of a quantum computer. Quantum dots in the common semiconductors Si and Ge profit from the compatibility with industrial microelectronic technologies, a small footprint, and thermal stability. Moreover, the low amount of isotopes with nuclear spin is beneficial for the qubit coherence. The rich physics in the valence band of Ge gives rise to particular properties which make holes attractive for the implementation of hole spin qubits. In particular, the strong spin-orbit interaction, termed direct Rashba spin-orbit interaction, that arises in one-dimensional Ge/Si core/shell nanowires due to the admixture of heavy hole and light hole states is promising for very fast qubit gates and all-electrical qubit control. In order to implement a spin qubit, a large degree of control over quantum dots and the spins confined in it is essential. We demonstrate the formation of single, double and triple quantum dots in Ge/Si core/shell nanowires. In a single quantum dot, we observe indications for single hole occupation. Furthermore, the transport through a double quantum dot at an effective (1,1)-(0,2) charge transition is governed by Pauli spin blockade, which leads to current rectification. In presence of spin-orbit interaction, the blockade is lifted at finite magnetic field and leads to a leakage current. The study of the leakage current as a function of external magnetic field and double quantum dot detuning yields information about the dominant lifting mechanisms. Here, we observe pronounced orbital effects and a renormalization of the g-factor which arises in presence of strong spin-orbit interaction. A spectroscopic model accounts for all these effects and allows to extract a spin-orbit interaction length of $l_{\mathrm{SO}} \approx 65\,\mathrm{nm}$ in a Ge/Si core/shell nanowire quantum dot. Finally, spin-orbit interaction is used to drive electric dipole spin resonance of a hole spin qubit in a Ge/Si core/shell nanowire. We demonstrate coherent Rabi oscillations and two-axis single qubit control. Important qubit parameters such as the Rabi frequency and the g-factor can be tuned over a wide range by changing the gate voltages. This tunability arises from the electric field dependent spin-orbit interaction in Ge/Si core/shell nanowires. In an optimal configuration, the Rabi frequency increases to 435 MHz at a drive frequency of $f_{\mathrm{MW}} = 3.4\,\mathrm{GHz}$, thus almost entering the strong driving regime. The results shown here demonstrate the suitability of Ge/Si core/shell nanowires to implement a hole spin qubit which can be electrically switched between a control state, enabling fast qubit gates, and an idle state, prolonging qubit coherence.

Contents

1 Introduction

Around the turn of the year 2020, numerous outlooks on "technologies that will shape the next decade" have been published [Dur19; Mar20; Ban20]. Amongst others, one prominent contestant is quantum computation, which is expected to be further commercialized and to demonstrate its superiority over classical computation based on supercomputers. The exact benchmark, as well as the terminology, for so-called 'quantum supremacy' is controversial [Pre12; Har17; Cro19; Vil20], which is also apparent in the debate about the performance results of Google's latest quantum device named *Sycamore* [Aru19; Ped19]. Nevertheless, the increasing interest in quantum computation, and generally quantum technologies, is reflected in the growing amount of investments into such technologies [Gib19], thus making quantum technologies a key market for the future. Without any doubt, new quantum technologies will impact and change the world in many aspects [Hun20]. Yet, to build a full-scale universal quantum computer is difficult, but the most advanced quantum devices [McC19; IBM20; Aru19; Kel18] to date are reaching a capacity which allows these "noisy intermediate-scale quantum" (NISQ) devices to perform tasks beyond the capabilities of classical computers [Pre18]. These quantum devices use error-prone qubits, thus the term 'noisy', and the scalability to larger than 'intermediate' sized circuits, that is arrays of 50-100 qubits, is hard. Quantum error correction [Ter15; Fow12] can compensate for erroneous single qubits, although at the expense of an even larger number of qubits.

It becomes clear that a large number of high-quality qubits is necessary to build a fault-tolerant universal quantum computer. The quantum bit, or qubit, is the elemental information unit of a quantum computer, similar to the bit of a classical computer. Likewise the digital bit information '0' and '1', a qubit comprises a quantum two-level system with basis states $|0\rangle$ and $|1\rangle$. What is more, qubits exploit quantum mechanical effects such as superposition and entanglement for computation, which have no classical counterpart and therefore constitute the power of a quantum computer. In order to

observe such quantum effects, often extreme environmental conditions are necessary, such as temperatures near absolute zero, high vacuum and large magnetic fields. Not to mention, quantum effects can mostly be observed in systems with dimensions on the nanoscale only. These requirements demand specifically tailored systems for usage as qubits and also pose a challenge for the transition from small, single-qubit systems to large arrays.

There are a number of different physical implementations of qubits. The first quantum computer devices of the NISQ era are based on superconducting circuits [Kja20; Dev13; Oli13], which make use of Josephson tunnel junctions that form a resonant LC-circuit. The Josephson junction is a key ingredient for superconducting qubits, because it is a nonlinear inductor and therefore gives rise to an anharmonicity of the LC-oscillator. The two lowest energy levels of this quantum anharmonic oscillator form the basis states for qubit operation. Besides the non-equidistant energy levels, also dilution refrigerator temperatures are necessary to avoid undesired excitations into higher energy levels of the qubit. Another platform for qubits are ions which are confined in a radiofrequency trap [Hit13; Bru19]. The basis states of trapped ion qubits are electronic states of the ions, such as hyperfine states or Zeeman-split levels, which can be optically manipulated and read-out with lasers. Trapped ion qubits feature a good reproducibility, because the ions of one atom species are identical. The qubit coherence times are long, however, gate operation times are typically slow and the scalability and connectivity beyond linear arrays is challenging.

Another representative of optically addressable qubits are qubits in defects, where the most prominent example is the nitrogen-vacancy (NV) center in diamond [Gor13; Liu18]. These qubits can be operated at room temperature and exhibit very good coherence [Her19], but because they are embedded in a diamond host they are still susceptible to decoherence induced by fluctuations of the thermal and the nuclear bath. One challenge is the coupling of multiple NV centers in a large-scale system.

Direct coupling of neighbouring NV centers requires a high alignment precision when placing the defects. Long-range coupling in turn can be achieved by interfacing the NV center qubit with other solid-state systems, such as nanomechanical resonators, or by direct coupling via optical photons.

Finally, solid-state quantum computation can also be implemented with other semiconductor materials, where three main categories can be distinguished: qubits using the nuclear spin of donors in silicon [Kan98], topological qubits based on exotic particles such as Majorana fermions [Kit03], and spin qubits in quantum dots [Los98]. Quantum dots can be, for instance, electrostatically defined in a semiconductor host material such as GaAs or Si. The qubit information is then encoded in the charge or spin states of electrons confined in the quantum dot. Spin states are favored due to the weak coupling between the spin and the environment, which yields a better protection of the qubit state. There are multiple choices for the qubit basis states, for example the two spin states 'up' and 'down' of a single electron, also referred to as "Loss-DiVincenzo qubit" according to the original proposal [Los98], or the singlet-triplet configurations of two electrons [Van19]. Since spin qubits in semiconductor quantum dots are the main topic of this thesis, more advantages and challenges of such qubits will be discussed throughout the following sections.

Overall, many different qubit platforms have emerged, but regardless of the detailed realization, certain criteria, known as the DiVincenzo criteria, have to be met in order to build a quantum computer [DiV00b]. In particular, the criteria state that a qubit platform must *(1)* be scalable, *(2)* provide state initialization, *(3)* feature sufficiently long coherence times, *(4)* provide a universal set of gates, and *(5)* comprise a readout capability. Across the different qubit platforms, the criteria *(1)* scalability and *(3)* coherence are commonly the dominant challenges. First, since qubits exploit the quantum effect of superposition, coherence is an important figure of merit since it defines the timescale after which the qubit information is lost and thus it sets an upper limit for

the qubit gate time. It takes very little to either kick a system out of a coherent quantum state, since they are very fragile, or to relax to a different qubit state which leads to quantum leakage to the environment with irretrievable loss of quantum information if the qubit leaves its computational space [Cai19]. Especially in solid-state quantum computation approaches, such as spin qubits, where the qubit interacts strongly with the environment, careful optimization is needed to achieve adequate coherence times. Therefore, topological qubits hold promise for quantum computation because they are resilient to local perturbations [Lah17; Fie18]. Second, all qubit realizations face the challenge of scalability. For full-scale universal quantum computation, a large amount of qubits is necessary, not least because of the error rate of qubits which requires an even larger number of qubits for quantum error correction schemes such as the surface code [Fow12]. Moreover, all qubits of an array must be well characterized in terms of the qubit Hamiltonian, couplings to other states and qubits, as well as interactions with the environment [DiV00b]. Today, most qubit platforms are very proficient on the single and two qubit level, but the extension to large linear or two-dimensional arrays is difficult. Nevertheless, quantum computers in the NISQ era, although not yet as powerful as fault-tolerant quantum computers, are capable of solving hard problems [Pre18].

We now focus on spin qubits hosted in semiconductor quantum dots and their prospects in the NISQ era. Spin qubits have proven to be a powerful platform and since the initial spin qubit proposal [Los98], enormous leaps forward have been achieved. Quantum dots defined in GaAs two-dimensional structures have been the workhorse for many years. In this system milestone qubit experiments have been demonstrated such as single [Kop06; Now07] and two-qubit control [Pet05], but also useful techniques such as for qubit readout [Elz03; Lu03; Elz04] and decoupling [Fol09; Blu10; Nak20] have been established. Also Pauli spin blockade has been observed first in a GaAs system [Ono02] and has since then become an versatile tool in the field of spin qubits.

Furthermore, coupling charge and spin of a qubit to a resonator has been successfully implemented [Fre12; Sto17; Lan18], a milestone on the way to long-distance qubit-qubit coupling mediated by photons of a cavity. In conclusion, these seminal technological developments position spin qubits in semiconductor quantum dots well for future quantum computation devices.

Meanwhile, qubits in silicon structures [Zwa13] have evolved to a prime candidate for large-scale quantum computation with spin qubits [Cas18; Sch18]. This is due to the long coherence times compared to GaAs, high gate fidelities and compatibility with complementary metal-oxide-semiconductor (CMOS) technology. Therefore, silicon-based spin qubits address the two major challenges of quantum computation discussed before, coherence and scalability. Spin qubits in silicon [Mau12; Vel14; Mau16] feature good coherence times often limited by magnetic noise from nuclear spins of the host material or charge noise [Wu14]. In isotopically purified silicon [Ito14], however, this source of decoherence is eliminated. Accordingly, extremely long coherence times have been achieved with gate-defined qubits in silicon [Yon18; Hua19; Sig19; Tak20]. Moreover, the long coherence enabled single qubit gates with fidelities at or beyond the threshold for fault-tolerant quantum computation [Yon18; Fow12; Tak16; Vel14]. In fact, two-qubit gate fidelities are now becoming the bottleneck [Hua19]. In conclusion, a good basis for quantum computation is established with single-spin qubits in silicon [Fer20; Vel15; Zaj18; Wat18a].

Also the challenge of upscaling qubit arrays is addressed with silicon spin qubits. For large-scale quantum computation, qubits have to be arranged in arrays, providing a large number of well-characterized qubits, individual qubit control and interconnectivity between qubits at the same time. The CMOS compatibility of silicon-based qubits provide the potential for large and dense arrays of reproducible qubits [Vel17]. At the same time, the resemblance to state-of-the art microelectronic technology eases

the interfacing with classical control electronics for controlling and addressing individual qubits [Van17; Li18a]. Individual qubit readout in large arrays is enabled by recent advances in gate-reflectometry based readout [Wes19; Cri19; Urd19; Zhe19] and quantum non-demolition measurements [Yon20], which can boost the readout and initialization fidelity. The interconnectivity between qubits in such arrays is enabled by strong charge and spin coupling to photons in a superconducting cavity [Bur20; Mi17a; Mi18a; Sam18; Bor20], shuttling and swapping of qubits [Mil19; Fuj17; Mor18], or floating gates [Tri12]. Finally, the technological effort that is required for qubit operation, such as the cooling to temperatures near absolute zero, challenges the development of large-scale quantum devices. The operation of dilution refrigerators is technologically as well as economically demanding, and space is limited inside such setups. Increasing the qubit operation temperature by just about 1 K appears insignificant compared to the actual operation temperature near absolute zero, but has compelling implications on the technical effort that is needed for qubit operation. The available cooling power at 1 K is much larger than in the mK regime, hence heat, which is generated by the densely packed electronic structures, can be extracted effectively. Recently, experiments with silicon qubits have demonstrated the capability of operation at elevated temperatures around 1 K [Yan20; Pet20]. This advance is possible due to the good isolation of the qubit basis from other states. Silicon-based qubits thus provide powerful solutions to the two major challenges of coherence and scalability.

After years of dominance of silicon-based classical electronics, in recent years germanium has recurred [Pil11] as a promising transistor material boosting low-power and high-speed microelectronics [Gol14]. What is more, germanium has also emerged as a platform for quantum computing [Sca20]. The compatibility with silicon CMOS technology, the high material quality and the rich physics of holes in the valence band combine the elements for fast and all-electrically controllable hole spin qubits. Germanium-based qubits thus incorporate the above-mentioned assets of silicon qubits and add new

and refined features. It is the valence band states in germanium that stand out from the crowd of spin qubit implementations. Germanium has the highest hole mobility of all known semiconductors and a comparably small effective hole mass, thus easing the device fabrication. Moreover, the reduced contact hyperfine interaction of holes and the ability to isotopically purify the already to 92 % nuclear spin free material promises long spin lifetimes. But at the heart of hole spin qubits in low-dimensional germanium systems are the large g-factor and the strong spin-orbit interaction, which furthermore are both electrically tunable.

Three main platforms for hole spin qubits in germanium are identified: planar Ge/SiGe heterostructures, Ge hut wires and Ge/Si core/shell nanowires. These systems have a large common ground, but also feature distinct differences with advantageous implications for each system. For instance, the band structure of holes confined in quantum dots is significantly affected in presence of confinement and strain [Sca20]. In bulk germanium the valence band comprises the split-off band, as well as the heavy-hole (HH) and light-hole (LH) bands, which are degenerate at the Γ-point. Adding a confinement in one direction as in planar germanium heterostructures and in hut wires, the HH and the LH band split, with the heavy hole states being energetically preferred [Ter20]. In Ge hut wires, a slight admixture of the HH states with LH states is observed due to the additional confinement in a second direction [Wat16]. For Ge/Si core/shell nanowires, due to the pronounced one-dimensional geometry and the large band edge offset between the Ge core and the Si shell, a large admixture of HH and LH states is found. It is this strong admixture of different hole states, which gives rise to a special type of strong spin-orbit interaction, termed direct Rashba spin-orbit interaction (DRSOI) [Klo11; Klo18] due to its resemblance to standard Rashba spin-orbit interaction. In planar heterostructures and in hut wires, the DRSOI is less pronounced as it is suppressed by the HH-LH splitting. Nevertheless, already small HH-LH admixtures as well as other spin-orbit interaction terms can contribute to the spin-orbit interaction

of holes, and ultimately it is strong enough to allow for qubit operation in all of the three mentioned germanium systems.

Since spin-orbit interaction is intrinsic to hole spins in germanium, it allows for very efficient spin manipulation via electric dipole spin resonance. Indeed, hole spin qubits in germanium have caught up with silicon spin qubits exceptionally fast. To date, in germanium single-qubit [Wat18b; Hen20b] and two-qubit [Hen20a] operation has been demonstrated alongside with qubit readout [Vuk18] and coupling to superconducting resonators [Li18b; Wan19a; Xu20b]. Altogether, hole spin qubits in germanium have matured to a powerful platform for quantum computation [Sca20].

However, hole spin qubits in Ge/Si core/shell nanowires are less well-studied in comparison to planar heterostructures and hut wires, despite the profound properties that arise from the reduction of size and dimensionality in these nanowires. While also in planar and in hut wire nanostructures important features emerge which are not available in bulk material, the unique properties of Ge/Si core/shell nanowires are outstanding. For this reason, section 2 gives an overview over the most important aspects of nanowires, quantum dots in nanowires and in particular the properties of Ge/Si core/shell nanowires. In section 3, some general aspects of spin qubit operation are outlined. Furthermore, the prospects of hole spin qubits in Ge/Si core/shell nanowires are emphasized.

Section 4 covers the fabrication of devices for quantum dots in Ge/Si core/shell nanowires and section 5 outlines the basic setup that is used for experiments in this thesis. Generally, hole spin qubits in germanium are based on well-defined and controllable quantum dots which are formed electrostatically in the respective planar heterostructure [Hen18], hut wire [Xu20a] or core/shell nanowire [Bra16c; Hu07; Rod08], and which ideally hosts a single hole spin [Hen20b]. In section 6 of this thesis, we demonstrate the formation of single, double and triple quantum dots in Ge/Si core/shell nanowires. Owing to the significantly smaller quantum dot confinement

compared to previous experiments [Bra16c; Hu07; Rod08], we observe indications of single hole occupation in a quantum dot. The gate control over quantum dots and their tunnel couplings allow for further experiments towards hole spin qubits described in this thesis.

Since the strong and tunable spin-orbit interaction of hole spins in germanium is the foundation of fast and all-electrically driven spin qubits, it is of fundamental interest to study the spin-orbit interaction in Ge/Si core/shell nanowires. Previous experiments have concurrently found a strong spin-orbit interaction along with indications for electric field tunability, in good agreement with the theoretically expected DRSOI [Hao10; Hig14b; Bra16a; Wan17; Sun18; dVri18]. In section 7 we develop a model to describe the observed leakage current in a Pauli spin blockade configuration in presence of strong spin-orbit interaction and pronounced orbital effects. This allows us to determine the strength of spin-orbit interaction in a Ge/Si core/shell nanowire, which is indeed found to be very strong. Additionally, the model also accounts for the consequent renormalization of the g-factor in presence of such strong spin-orbit interaction.

Finally, in section 8 we establish an ultrafast and gate-tunable hole spin qubit in a Ge/Si core/shell nanowire quantum dot. Electric dipole spin resonance mediated by spin-orbit interaction allows for coherent hole spin control around two axis of the Bloch sphere. Furthermore, the Rabi frequency is highly tunable by small changes of the electric field generated by the confinement gates and can reach record high values for spin qubits, which are near the threshold to the strong driving regime.

Ultimately, the prospects of such tunable and fast hole spin qubits in Ge/Si core/shell nanowires are outlined in section 10. Future experiments will rely on improved devices, with advanced functionality, to further demonstrate the all-electrical control over the qubit. Finally, the strong spin-orbit interaction of holes holds promise for strong spin-photon coupling for long-distance qubit-qubit coupling, which will be investigated in hybrid semiconductor-superconductor samples, as discussed in sections 4.5 and 10.3.

In conclusion, the results presented in this thesis contribute to the development of a solid-state qubit with the capability to fulfill the five criteria for a large-scale quantum computer. While the currently most advanced NISQ devices are based on other qubit implementations, it becomes clear that spin qubits in semiconductor quantum dots have excellent prospects due to the small footprint, fast speed, thermal stability and compatibility with current semiconductor microelectronic technology. The NISQ era just emerged and indeed the next decade of the twenties will provide more insight into the potential of quantum computers. Undoubtedly, the technological achievements of this decade will pave the way for more powerful, large-scale quantum computers of the next generation ultimately pionieering the fault-tolerant quantum computing era [Pre18].

2 Nanowire Quantum Dots

Dimensionality and size of an object are two physical quantities that, when varied, impact comprehensively the properties of matter. For instance, the density of states of electrons in a solid state material depends strongly on the dimensionality. If the size of an object is reduced to a length scale comparable to the electron wavelength, quantum effects emerge from the confinement of electrons. In particular, for semiconductors, with their variable properties such as electron density and band gap, the control of dimensionality at the nanometer scale enables the study of basic chemical and physical effects. Semiconductor nanowires can be considered as true one-dimensional systems with their large aspect ratio up to 1000. The size of nanowires does not exceed the nanometer regime in cross-section, while the length of a nanowire can be as large as a few micrometers. Modern nanowire synthesis methods, such as chemical vapor deposition, allow the fabrication of semiconductor nanowires with endless variations of material composition, morphology, and size [Jia19]. This large extent of control enables the application of nanowires in various fields, such as in optics for lasers [Eat16] and single-photon source [Ara20; Män19], or in electronics [She19].

Nanowires in combination with low temperature, provide access to phenomena that are only observable when the electronic level spacing exceeds the thermal energy. One example is single-electron tunneling [Dev92; Kou97], which can be observed in zero-dimensional quantum dots [Kou98]. The cylindrical geometry of nanowires with the strong transverse confinement is an ideal basis for the zero-dimensional confinement of electrons and holes. Quantum dots can be formed in nanowires, for instance, by built-in barriers [The03] or external gates [dFra03; Fas05], which both provide confinement inside the one-dimensional nanowire in the remaining third dimension along the nanowire axis. The performance of quantum dots, for instance in terms of how they interact with the environment, depends to a large extent on the properties of the host material, which, in case of nanowires, can be widely controlled, making nanowire

quantum dots interesting objects to study [Sal10].

This section provides an overview of effects that arise from the interplay of the size of nanostructures and the dimensionality, as in one-dimensional nanowires and zero-dimensional quantum dots. Section 2.1 discusses applications of nanowires, which rely on the one-dimensional character and the nanosize, and outlines the potential of nanowire quantum dots, which are largely influenced by the nanowire properties. Then, section 2.2 motivates the usage of the semiconductors germanium and silicon in nanowire heterostructures for the implementation of a hole spin qubit. Finally, this section concludes with an overview of basic quantum dot properties (section 2.3), arising from both their size and dimensionality, including important spin physics such as Pauli spin blockade and its revocation.

2.1 From One- to Zero-Dimensional Systems: Quantum Dots in Nanowires

The natural relatives of nanowires in nature are metal whiskers. These hairlike, tiny filaments form on the surface of metals, and often cause failure of electronics due to electrical shorts, for instance when they grow from solder tin [Lei06]. Despite their importance for the design of electronics, the mechanism of whisker formation is not fully understood [Kar14]. However, the studies of silicon whisker growth lead to the development of the vapour-liquid-solid growth of semiconductor nanowires [Wag64], which still represents the most important process for nanowire synthesis. Since then, a variety of semiconductor nanowires have been synthesized from group III, IV and V elements, with specifically designed electronic and morphological properties that can not be found in the bulk materials or other geometries [Jia19].

The fields of application of nanowires are numerous [Zha16]. In medical applications nanowires have prospects for e.g. detection of neural activity, drug delivery

or imaging [Zha16, ch. 11]. For biological studies, nanowires allow the sensitive detection of molecules in field effect transistors, or enable intracellular electrical measurements [Zha16, ch. 10]. The precise control over the band gap of semiconductor nanowires is used in nanophotonics [Zha16, ch. 6], leading to nanoscale light sources [Ara20; Män19], photodetectors and lasers [Eat16]. Other applications of nanowires are novel types of scanning probe microscopy tips, for instance as ultrasensitive force sensors [Bra19].

Nanowires became a substantial area of research in nanoelectronics, too. Not only nanoscale electronic devices such as field effect transistors and diodes [Zha16, ch. 5], but also hybrid semiconductor-superconductor devices are possible with nanowires. When interfacing a semiconductor nanowire with a superconducting material, a superconducting phase is induced in the nanowire due to the proximity effect. This leads to the emergence of Majorana zero modes localized at the ends of the nanowire, which hold excellent promise for topological quantum computation [Sta13; Fro13]. Furthermore, such hybrid devices can be used as a Josephson junction [Zha16, ch. 7], which features a wide range of physical phenomena if the normal conducting part of the junction is reduced to a zero-dimensional quantum dot, interfacing the electron condensate on the superconductor with single electrons in the quantum dot [dFra10].

Nanowires are often referred to as one-dimensional systems, although it is strictly speaking incorrect since often more than one subband is occupied. Nevertheless, owing to the geometry and to distinguish nanowires from two-dimensional planar heterostructures, the adjective one-dimensional prevails for nanowires. Consequently, the constraint of nanowires along the principal axis can be seen as a reduction to a zero-dimensional quantum dot. In nanowires, such constraint can be achieved with different approaches [Sal10]. One possibility is the growth of built-in barriers in the nanowire, that is short segments of a different material alternating with the principal nanowire material [The03]. In a more simple approach, metal contacts to the semiconductor

nanowire form a tunneling barrier which forms a quantum dot with a size determined by the contact spacing [dFra03]. Similarly, a set of closely spaced gates can be patterned above or below the nanowire, which couple only capacitively to the nanowire and allow the formation of an electrostatically defined quantum dot [Fas05]. This last approach enables a high control over the size, position, coupling and occupation number of the quantum dot.

Quantum dots in nanowires are interesting objects to study in the context of the development of quantum computation architectures based on spin qubits [Los98; Klo13a; Fro13]. For quantum computation, a high degree of control over a single electron (or hole) in terms of its spin state and its coupling to the surrounding are required. Gate-defined nanowire quantum dots provide such control over the occupation number down to the single-particle level [Bjö04; Sho06; Zwa09]. Furthermore, the coupling between nanowire quantum dots can be precisely controlled, allowing to smoothly merge two quantum dots into a single quantum dot [Bra16c]. The precise control over single charges in quantum dots enables the observation of spin physics as well, resulting in the observation of Pauli spin blockade [Pfu07; Pri13], which is explained in detail in section 2.3.3.

The goal of implementing a spin qubit requires control over the spin state (see also section 3.2). For spin control, electric dipole spin resonance mediated by spin-orbit interaction can be employed. Here, nanowire quantum dots benefit from either the intrinsic properties of the nanowire host material such as in InAs or InSb, or from the control over nanowire heterostructures, which allow to tailor nanowires with strong spin-orbit interaction such as Ge/Si core/shell nanowires (see section 2.2). For example, the presence and strength of spin-orbit interaction for electrons confined to quantum dots in an InAs nanowire has been characterized [Fas07], which led to the demonstration of single spin control [Nad12; Pri13; vdBer13]. Also, the coupling of a

nanowire quantum dot to a resonator has been demonstrated, paving the way for long-range qubit-qubit interactions [Pet12]. One obstacle of nanowire based spin qubits is the uncontrolled and vertical position on the growth chip of traditional VLS-grown nanowires, which makes the scalability to nanowire-based qubit arrays challenging. However, the progress in site-controlled nanowire growth [McI20] approaches this challenge, considering all kinds of growth processes such as VLS growth, template-assisted growth or Stranski-Krastanow growth, and promising results are obtained [Gao20].

In conclusion, nanowires are a one-dimensional platform for the study of a wide range of phenomena. Moreover, nanowires also pass on properties to quantum dots and spins therein, which prove useful for the implementation of spin qubits. Many spin qubit experiments employed InAs or InSb nanowires, due to the strong intrinsic spin-orbit interaction which enables efficient all-electrical spin manipulation. An alternative material system is represented by Ge/Si core/shell nanowires, made of group IV elements and featuring a number of characteristics that will be discussed next.

2.2 Ge/Si Core/Shell Nanowires

Nanowires comprising a radial heterostructure of Ge and Si synergize properties arising from the usage of Ge and Si and their stacking to a one-dimensional nanostructure. Key properties are the formation of a hole gas in the Ge core and the emergence of a strong spin-orbit interaction, which exists only due to the one-dimensionality of the nanowire. Ge/Si core/shell nanowires are one example of how a precise control over nanowire morphology and composition enable the tailoring of properties that are inherited to spins confined in quantum dots. As a result, hole spins in Ge/Si core/shell nanowires hold promise for fast and tunable hole spin qubits, as will be discussed in section 3.1.

This section starts with a general motivation for the usage of the group IV elements Ge and Si (section 2.2.1). The impact on the band structure arising from epitaxial

stacking of Ge and Si are discussed in section 2.2.2. Finally, the emergence of spin-orbit interaction in Ge/Si core/shell nanowires, as outlined in sections 2.2.3 and 2.2.4, motivates the investigation of this system as a platform for all-electrical tunable hole spin qubits.

2.2.1 Germanium and Silicon Nanowires

The day before Christmas eve in 1947 is known as the birthday of the transistor, when Bardeen, Brattain and Shockley demonstrated the first point-contact transistor based on a block of germanium. The conquest of semiconductor transistors started. Many more types of transistors have been developed, and eventually they became the fundament of modern electronics with an eventful history [Rio04]. Germanium was long thought to be the best transistor material due to its high carrier mobility and the first transistor based on silicon was demonstrated only in 1954. Soon after, the discovery of silicon surface passivation and the invention of the MOSFET (Metal Oxide Semiconductor Field Effect Transistor) promoted silicon as the standard semiconductor material for industrial products. Amongst others, the stable native oxide and the easier production, made silicon superior over germanium for many applications. But history is not black and white, so also SiGe alloys and heterostructures have proven their applicability [Mey94; Sch97]. Finally, germanium experiences a revival as a material enabling high-mobility and fast transistors [Pil11].

In nanoelectronics, silicon and germanium are materials of interest due to the vast experience gained in patterning them at the nanoscale, and their compatibility with semiconductor industry processes. Furthermore, the high abundance of isotopes with zero nuclear spin in both materials promises reduced hyperfine interaction which is advantageous for electron spin coherence. Naturally, Ge contains about 92 % and Si about 95 % isotopes with zero nuclear spin. Moreover, both materials can be isotopically purified to further reduce the amount of isotopes with nuclear spins.

The physics of electrons in Si nanoelectronics is largely influenced by the presence of valleys in the conduction band [Zwa13; Sal14]. While these valleys are degenerate in bulk Si, the degeneracy is lifted in nanostructures due to strain, confinement and electric fields, leading to hybridization of orbital and valley degree of freedom, which needs to be considered in quantum devices [Mi17b; Mi18b]. The large effective mass of electrons and holes in Si imposes restrictions on the size of quantum dots, which require to be smaller compared to other materials such as GaAs in order to observe quantum effects. In this regard, Ge is an interesting alternative because of the larger Bohr radius compared to that of Si [Pei11]. Moreover, similar to classical electronics, the usage of Ge is also motivated by the higher charge carrier mobility [Pil11].

For nanoelectronic devices such as nanowire-based field-effect transistors [Cui03; Wan03; Dua08; Zha16], the charge carrier mobility is an important quantity, as it determines characteristics such as the transistor switching speed. Especially with regard to the application in transistors, Si and Ge nanowires are extensively studied due to available control over nanowire properties, such as size and doping, which adjusts the electrical and optical properties [Jia19]. However, doping has a detrimental effect on the charge carrier mobility due to scattering at doping impurities, and further leads to low-frequency charge noise [Zwa13]. Furthermore, surface effects are more important in nanowires due to the large surface-to-volume ratio. While the sensitivity to surfaces can be exploited for instance for nanowire-based sensors, the electrical performance of nanowires is often affected by scattering at surface trap states. Therefore, additional measures of surface passivation need to be taken in order to passivate and clean the nanowire surface [Cui03].

In conclusion, the application of Si and Ge nanowires in nanoelectronics benefits from material properties like the low amount of nuclear spins and from the size control and designable electrical properties [Jia19]. On the downside, single-component Si and Ge nanowires might exhibit a reduced charge carrier mobility due to scattering at dopant

and surface impurities. Furthermore, achieving electrical contact to the nanowire with metal leads might involve additional processing, such as annealing, in order to reduce the Schottky barrier that normally forms at the semiconductor-metal interface. As an alternative, compound SiGe nanowires offer a wider range of possiblities to modulate electrical and optical properties by enabling variation of the material composition of SiGe alloy nanowires and the growth of axial and radial heterostructures [Ama14; Wen19]. Finally, Ge/Si core/shell nanowires hold promise to address some constraints discussed in the above, such as scattering at surface defects, by confining the transport channel in the core away from the surface, and at dopant impurities, due to the redundancy of intentional doping. Also ohmic contacts to the transport channel are possible, therefore easing electrical contacting. Amongst others, these properties will be discussed in the next section.

2.2.2 One-Dimensional, Radial Ge/Si Heterostructure

For a long time, Ge and Si have been considered for band structure engineering and a variety of Si and Ge based high-mobility heterojunctions were investigated [Sch97; Sam19]. Si and Ge heterostructures are of great interest because of the unique combination of similarities and differences. Both Si and Ge are group-IV elements, crystallize in the diamond lattice structure and they are completely miscible, thus any $Si_{1-x}Ge_x$ alloy with $0 \leq x \leq 1$ can be obtained. With increasing Ge content, the strain in the SiGe alloy increases due to the bulk lattice constant mismatch of about 4 % between pure Si and Ge. An important different between Si and Ge is the band gap, which is 1.14 eV for silicon and 0.67 eV for germanium at room temperature, which leads to a discontinuity of roughly 500 meV at the Si/Ge interface [vdWal86]. In SiGe heterostructures, the type of band offset (type-I or type-II) as well as the band gap depend on both the strain and the heterostructure stack composition. By engineering these

parameters, various kinds of heterostructures for a multitude of applications, such as for gateable quantum devices [Sam19; Sca20], can be obtained.

Here, in particular the Si/Ge isotype heterojunction is of importance [And60; vOpd69], that is a heterojunction comprised of two different materials with the same type of doping on both sides, in contrast to an anisotype heterojunction such as a *pn*-heterojunction. Consider the band structure of a Si/Ge interface in Figure 2.1 **a** before the materials are brought into contact. Indicated in Figure 2.1 **a** are the work function Φ, defined as the energy required to remove an electron from the Fermi level, and the electron affinity χ, defined as the energy difference between the conduction band edge and the vacuum level. In a heterojunction, the differences in Φ, χ and band gap energy lead to band discontinuities at the interface. When bringing the two materials into contact, charges diffuse from one material to the other, yielding the equilibrium band structure shown in Figure 2.1 **b**. In the equilibrium, the Fermi level aligns across the junction, leading to a bending of the conduction and the valence bend edges and hence generating spikes and notches at the interface. Note that the band alignment in an isotype heterojunction resembles the Schottky barrier formed at the metal-semiconductor interface, where the metal is now replaced by a narrow band gap semiconductor.

At the abrupt Si/Ge interface, localized surface states inside the band gap are formed, similar to the Si/SiO_2 interface [Cro76; Sta56; Kin56]. In a *n*-*n* (*p*-*p*) isotype heterojunction these acceptor (donor) like states trap electrons (holes) and lead to an inversion layer on both sides of the interface. These interface effects are of great importance for Si/Ge heterojunctions because the negatively charged interface states yield a rectifying behaviour of the junction [Pei12] and the inversion layers can lead to parasitic conduction channels in heterojunction devices. It is important to note, that the number of interface states and therefore the rectifying behaviour depends on the abruptness of the Si/Ge interface [Cro76; Bri93]. The barrier height of a heterojunction with a gradual variation from Si to Ge is decreased and the electrical behaviour of the junction

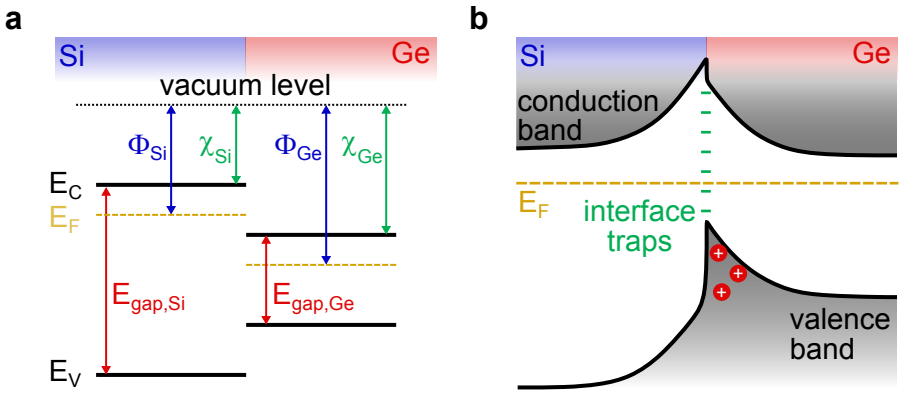

FIGURE 2.1 | **Band structure of a Ge/Si heterojunction. a** | Schematic band diagram of Si and Ge prior to contacting the heterojunction. Indicated are the band gap E_{gap}, the work function Φ and the electron affinity χ of both materials. **b** | Band structure of a Si/Ge isotype heterojunction. The formation of acceptor-like interface states yields an inversion layer in Ge. Adapted from [Pei12].

becomes ohmic.

To summarize the general case of a SiGe heterojunction, the resulting band structure and electrical properties depend strongly on the strain and the alloy composition. Taking the Si/Ge interface to the nanoscale and to a geometry with reduced dimensionality, as it is the case in a Ge/Si core/shell nanowire, the band alignment is additionally influenced by the quantum confinement. The effect of quantum confinement on the band gap of Si and Ge are different and thus influences the character of band offset [Yan08].

In a Ge/Si core/shell nanowire [Lau02], the radial stacking of silicon on germanium leads to a type-II band alignment with a potential well in the valence band inside the Ge core as depicted schematically in Figure 2.2 **a**. Similarly to the case of a planar heterojunction, negatively charged surface states form at the atomically sharp Si/Ge interface. Therefore, holes are injected inside the Ge core and accumulate in the potential well. The formation of a one-dimensional hole gas in Ge/Si core/shell nanowires has been experimentally confirmed with optical [Zha10; Li11; Fuk15; Zha18] and electrical measurements [Lau02; Lu05; Xia06].

As shown in Figure 2.2 **b** and **c**, the valence band states of a Ge/Si core/shell nanowire

are confined inside the Ge core, and spatially separated from the conduction band states in the Si shell [Ndu08; Yan08; Liu10]. The separation of hole states from the surface results in a very high charge carrier mobility with transport properties close to the ballistic regime, even at room temperature [Lu05; Lia07]. Importantly, the hole state confinement, and consequently the mobility, is very sensitive to the type-II band offset and therefore relies on an atomically sharp interface. With increasing Ge content in the shell, as a consequence of intentional alloying or interdiffusion, both the band offset and the hole mobility decrease [Nah12]. Lastly, the quantum confinement to the Ge core and thus the charge distribution also depends on the crystal direction along the main axis of the nanowire [Yan08; Ndu08]. This is in good agreement with the observed higher mobility of holes in nanowires along the [110] direction, as opposed to nanowires along the [111] direction [Con17].

In summary, the formation of a hole gas confined in the core of a Ge/Si core/shell nanowire is driven by the type-II band offset of the radial Si/Ge heterojunction. In analogy to two-dimensional planar heterojunctions, the band offset depends on the abruptness of the interface and the strain, but additionally on the quantum confinement in the one-dimensional nanostructure. At the core/shell interface, negatively charged interface states lead to the injection of holes into the potential well in the Ge core. Intriguingly, the hole gas forms independent of intentional doping. As a consequence the charge carrier mobility is very high due to reduced dopant and surface scattering [Ngu14; Con17]. In turn, the properties of the hole gas can be engineered with intentional doping of the shell [Ama11]. Ultimately, SiGe nanowires of any kind present a particularly interesting platform for nanoelectronics [Ama11; Web17].

Finally, it is remarked that strain comprehensively affects Ge/Si core/shell nanowires. The 4 % mismatch of the lattice constants of bulk Si (5.431 Å) and Ge (5.657 Å) leads to strain in epitactic composite layers, hence the Si shell exerts compressive strain on the Ge core as indicated schematically in Figure 2.2 **a**. Strain affects the band offset

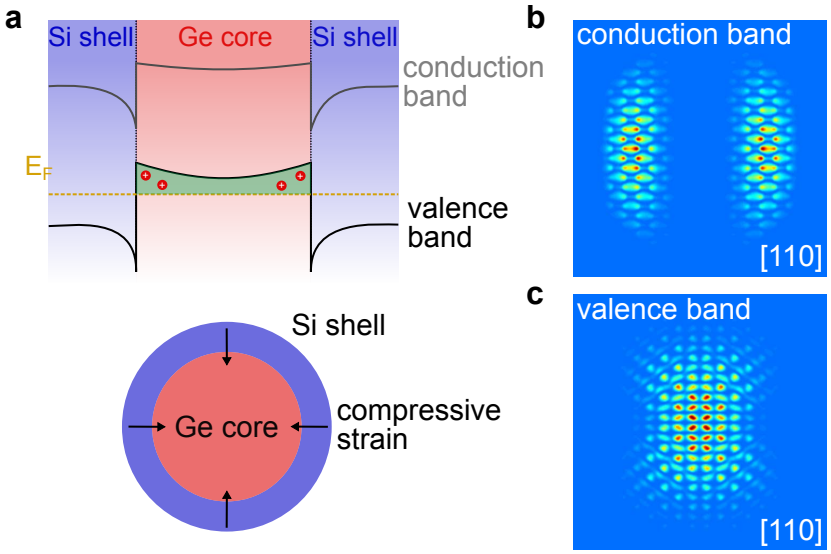

FIGURE 2.2 | **Band structure, strain and charge distribution in Ge/Si core/shell nanowires.** **a** | (Top) Schematic band structure alignment of a Ge/Si core/shell nanowire. The combination of band offset and interface states leads to the accumulation of a hole gas inside the Ge core. The schematic is adapted from [Lau02; Zha10]. (Bottom) Compressive strain is exerted on the Ge core by the Si shell due to the bulk lattice constant mismatch of about 4 %. **b, c** | The charge distribution in the conduction band (**b**) and in the valence band (**c**) of a [110] Ge/Si core/shell nanowire. Due to the type-II band offset electron and hole states are spatially separated, with the conduction (valence) band states being localized in the Si shell (Ge core). These simulations of 62 Ge and 200 Si atoms are adapted from [Yan08].

in Ge/Si core/shell nanowires and plays a crucial role [Lau02; Gol08a; Gol09; Day13]. Furthermore, it also affects important properties of hole states in Ge/Si core/shell nanowires, such as the effective mass [Klo11; Klo14]. In conclusion, the strain profile is overall an important parameter for the electronic properties of Ge/Si core/shell nanowires and the strain profile, engineered for instance by the Si shell thickness, becomes a powerful tuning parameter.

In stark contrast to two dimensional structures [Sam19; Ter20; Wat16], the confinement to one dimension in Ge/Si core/shell nanowires gives rise to a pronounced heavy hole-light hole mixing of the valence band states [Cso09; Klo11]. This mixing gives rise to a unique type of spin-orbit interaction, which only exists for holes in one-dimensional systems, and is described in detail in section 2.2.4. As a consequence, the Ge/Si

core/shell nanowire system exhibits an anisotropic g-factor, which is moreover highly tunable by electric fields. All these properties promise Ge/Si core/shell nanowires not only as a possible host of hole spin qubits for quantum computating [Klo13a], but also stimulate research of Majorana fermions [Mai14; Sca20] and general properties of holes in one dimensional systems.

2.2.3 Spin-Orbit Interaction

Spin-orbit interaction is the coupling of the orbital and the spin degree of freedom of a particle. In atomic physics, it is known as the coupling of an electron's spin $\vec{S} = 1/2$ and its orbital angular momentum $\vec{L}$ in the central potential of the atomic core, the Coulomb potential. An electron moving in the corresponding electric field experiences a magnetic field, which couples to the magnetic moment of the spin. Similarly, in solid state materials electric fields arising from the crystal structure lead to spin-orbit coupling. These electric fields typically arise from inversion asymmetries and two main terms of spin-orbit interaction are distinguished by the type of asymmetry. First, there is the Dresselhaus term (DSOI), which arises from bulk inversion asymmetry. The lack of an inversion center inside the unit cell stems from the zincblende crystal structure of coumpound materials such as GaAs, where the arrangement of lattice atoms leads to an asymmetry. In other materials, such as Ge, which crystallizes in the inversion symmetric diamond crystal structure, DSOI is absent. Secondly, there is the Rashba term (RSOI), which arises from structural asymmetry, for instance the asymmetric confinement potential in the z direction of a two-dimensional electron gas in GaAs. Both types of spin-orbit interaction can be distinguished by the spin σ and momentum p components which they couple. Dresselhaus spin-orbit interaction provides a coupling of type (in two dimensions) $\sim -p_\mathrm{x}\sigma_\mathrm{x} + p_\mathrm{y}\sigma_\mathrm{y} + \mathcal{O}(|p|^3)$, while Rashba spin-orbit interaction $\sim -p_\mathrm{y}\sigma_\mathrm{x} + p_\mathrm{x}\sigma_\mathrm{y}$ couples different spin and momentum components. Generally, the presence of spin-orbit interaction in solid state materials inspires a vast range of possible applications [Man15].

Figure 2.3 schematically depicts the most important bands around the Γ point (at $k = 0$) of a direct band gap semiconductor. The electron states in the conduction band are composed of s-like Bloch wave functions with orbital momentum $|\vec{L}| = 0$, thus in the simple picture no spin-orbit interaction would be expected. However, a finite coupling of the conduction to the valence band mixes the states and leads to

spin-orbit interaction for electrons via a higher order process. Because this coupling involves excitations across the band gap, the spin-orbit interaction is stronger (weaker) for materials with small (large) band gap.

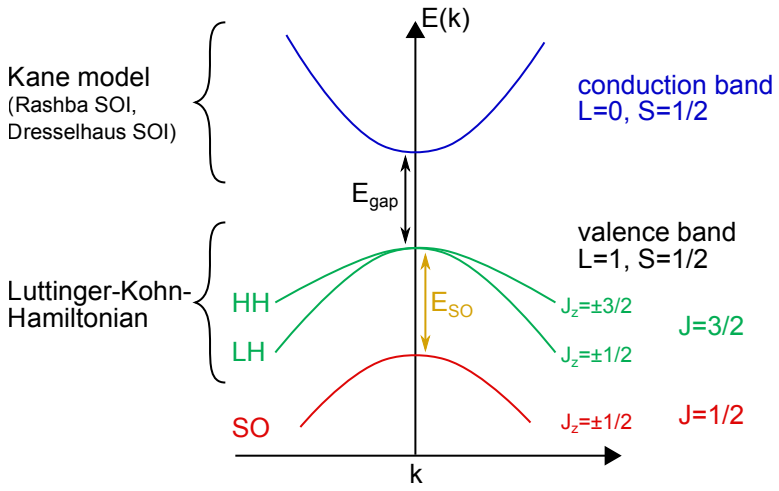

FIGURE 2.3 | **Semiconductor band structure in presence of spin-orbit interaction.** The simple model band structure of a semiconductor with direct band gap comprises around the Γ point ($k = 0$) the conduction band and the valence band. The latter consists of the doubly degenerate heavy hole (HH), light hole (LH) and spin-orbit split-off (SO) band. The split-off band is separated from the first two bands due to spin-orbit interaction by an energy E_{SO}. The conduction band can be described by a Kane model and exhibits spin-orbit interaction of Rashba type in third order approximation. The HH and LH valence bands are described by the Luttinger-Kohn-Hamiltonian.

In contrast to the conduction band, the valence band comprises multiple bands due to the p-type Bloch wave function of holes in the valence band, with $|\vec{L}| = 1$. Three doubly degenerate bands emerge, two of them with total angular momentum $J = L + S = 3/2$ and one band with $J = 1/2$. The latter band is split off in energy by the spin-orbit energy E_{SO} and thus is called the spin-orbit split-off (SO) band. The other two bands with $J = 3/2$ form the heavy hole (HH) and the light hole (LH) band. This denotation stems from the different effective hole masses, which is given by the inverse of the curvature of the bands.

It is this rich physics in the valence band which make holes interesting objects to study, especially with respect to the implementation of spin qubits [Zwa13; Sca20; Lil18;

Ono17]. In particular in one-dimensional systems such as Ge/Si core/shell nanowires, the hole spectrum contains features that prove to be useful for all-electrical control of spin qubits [Klo13a]. These features are a new type of spin-orbit interaction, termed Direct Rashba spin-orbit interaction (DRSOI), and an electric field tunable hole g-factor. The next section 2.2.4 outlines the most important points of the theoretical concepts of these properties.

2.2.4 Direct Rashba Spin-Orbit Interaction

The valence band states in semiconductor nanowires are well described by the Luttinger-Kohn-Hamiltonian, a subspace of the full Kane Hamiltonian which describes the eight most important bands (shown in Figure 2.3) in a multiband, envelope function approximation (Kane model) [Win03]. This Hamiltonian is modified by a cylindrical confinement potential due to the transverse confinement of the nanowire. The nanowire geometry leads to an admixture of heavy hole and light hole states, and as a result the energy spectrum of the nanowire is comprised of two degenerate subbands. Due to the confinement, the spin quantum number J_z along the nanowire axis z is not a good quantum number anymore and the lowest subbands are thus described by the effective quantum number $F_z = L_z + J_z = \pm 1/2$. One of these bands forms the ground state $|g_\pm\rangle$, and the other band is the excited state $|e_\pm\rangle$ The two bands $|g_\pm\rangle$ and $|e_\pm\rangle$ are energetically separated by an energy Δ. The degeneracy, denoted by the subscript $\pm$, is a consequence of the admixture of light hole states with different components of the heavy hole $|\pm 3/2\rangle$ states. The size of the splitting Δ is determined by the transverse confinement and the compressive strain on the Ge core as discussed in section 2.2.2 (Figure 2.2 **a**). Note, that static strain is an important parameter in Ge/Si core/shell nanowires because the curvature of the lowest-energy subbands depends sensitively on the strain, and can be anything between electron-like and hole-like [Klo11].

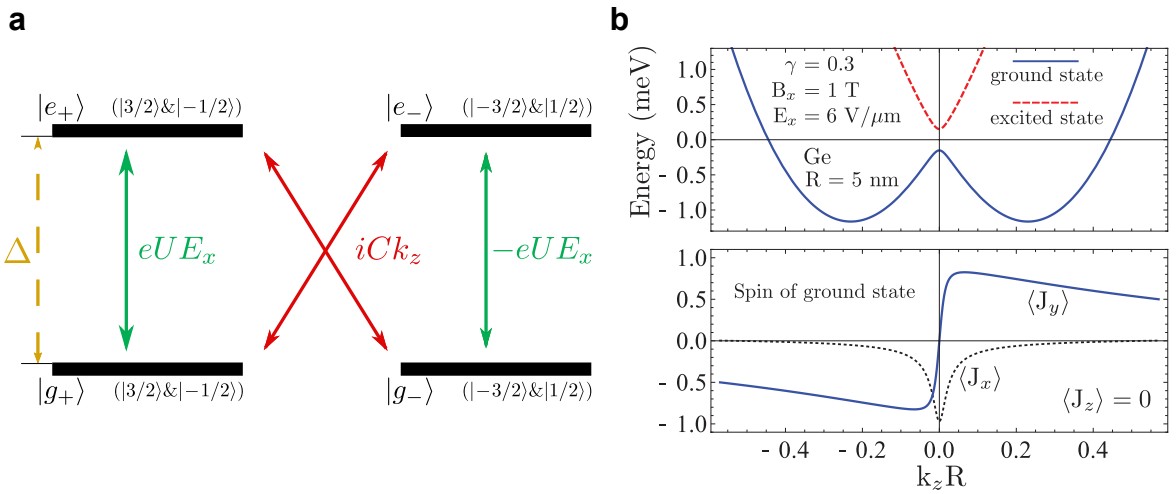

FIGURE 2.4 | **Direct Rashba spin-orbit interaction. a** | The confinement to one dimension leads to new eigenstates $|g_\pm\rangle$ and $|e_\pm\rangle$ which are an admixture of heavy hole and light hole states. The ground and excited states are split by an energy Δ. In presence of an external electric field E_x, (cross) couplings with coupling constants U and C arise as indicated by the green and red arrows. Schematic adapted from [Klo18]. **b** | Dispersion relation of the lowest energy bands in Ge/Si core/shell nanowires in presence of a magnetic field perpendicular to the nanowire axis. At $k_\mathrm{z} = 0$ a gap of 0.3 meV opens and the presence of direct Rashba spin-orbit interaction leads to two shifted parabolas (top). At the bottom, the spin of the ground state in all three directions is plotted, demonstrating the helical hole states, with the characteristic correlation between the spin state and the wave vector. [Klo11]

An external electric field perpendicular to the nanowire axis couples directly to the charge of the holes via a dipolar coupling, and gives rise to different couplings in the energy subspace of $(|g_\pm\rangle, |e_\pm\rangle)$. First, the electric field couples the ground and the excited states of the same spin type as indicated in Figure 2.4 **a** by the green vertical arrows. Moreover, due to the heavy hole-light hole mixing, cross-coupling terms emerge which couple states with different spin components (red arrows in Figure 2.4 **a**). The combination of these couplings gives rise to direct Rashba spin-orbit interaction (DRSOI) [Klo18], where the term direct stems from the direct dipolar coupling of the electric field to the spin. Therefore, the strength of DRSOI is widely tunable by the electric field and can exceed the strength of standard Rashba spin-orbit interaction (RSOI) by far [Klo11]. This is because DRSOI is a first-order effect and suppressed by the energy splitting Δ of the subbands, which is smaller than the band gap energy

E_{gap} that in turn suppresses RSOI. Overall, the nature of DRSOI resembles the case of RSOI and leads to a dispersion relation with two shifted parabolas in k-space, as seen in Figure 2.4 **b**. A helical ground state emerges where particles with opposite momentum have the opposite spin, too. These properties make Ge/Si core/shell nanowires also interesting as a platform for the physics of Majorana fermions [Mai14].

Experiments in Ge/Si core/shell nanowires indeed indicate the presence of a very strong spin-orbit interaction. A measure for the strength is the spin-orbit interaction lengths, defined as the distance that an electron (or hole) has to travel for a π rotation of the spin due to spin-orbit interaction. Regularly, spin-orbit interaction lengths on the order of 20 nm are extracted from quantum dot experiments in Ge/Si core/shell nanowires [Hao10; Hig14b; Wan17]. The implications of the presence of direct Rashba spin-orbit interaction for hole spin qubits are discussed in more detail in section 3.1.

2.3 Quantum Dots

Many fundamental physical effects are based on interactions of particles like electrons, protons and neutrons in their most natural host, an atom. Due to their small size, however, it is technically very challenging to experimentally study interactions on a single atom basis. Quantum dots (QD) are zero dimensional (D) structures which reproduce many characteristics of atoms on a length scale which is easier to access and therefore QDs allow to experimentally study effects fundamental in physics [Kou98]. QDs come in very different shape and size: from nanocrystals, containing only 1000-10'000 atoms, to micro- and nanostructured, complexly stacked semiconductors. While nanocrystals, due to their geometry, already provide an elemental confinement to a 0D-like object, in other QD implementations based on 2D-electron gases or 1D-nanowires, the electrostatic confinement can be provided by metal gate electrodes. This motivates the term 'gate-defined QD', owing to the fact that voltages on these nearby gates

generate static electric fields which serve as boundaries of a quantum well which is so small that it can be considered a 0D object.

The 0D confinement of electrons or holes leads to characteristics which resemble the behaviour of single electrons bound to an atom in the electrostatic potential of the nucleus. Therefore, QDs are also referred to as 'artificial atoms', as they show effects such as shell-filling and spin interactions well-known from atoms. In order to investigate the properties of electrons in QDs, optical or electronic experiments are usually performed. For the latter, the electronic transport through QDs is governed by classical, finite size effects as well as non-classical quantum effects.

QDs can not only confine electrons but also holes. While some QD realizations are specifically optimized for one type of charge carriers, others are ambipolar structures that can host electrons and holes in the same device [Bet14; Kuh18]. Regardless of the charge polarity, many effects work in the same way, yet there are fundamental differences between an electron QD and a hole QD. This becomes obvious when discussing qubit properties in section 3 where the various advantages and disadvantages of each system become prominent.

This section provides a brief overview over the most important phenomena of electrical transport through QDs [Kou01; vdWie02a; Han07]. The concepts discussed here are very general and not bound to a specific QD implementation. Whenever not explicitly stated otherwise, the same holds true for both electrons and holes. More specific examples will be based on QDs in Ge/Si core/shell nanowires. Section 2.3.1 is about single quantum dots, and section 2.3.2 extends the discussion to systems of multiple, coupled QDs. An important part of spin physics in QDs is based on the Pauli exclusion principle, leading to Pauli spin blockade which is discussed in section 2.3.3. Mechanisms that lift this blockade are discussed in section 2.3.4.

2.3.1 Coulomb Blockade and Coulomb Diamonds

Despite being observed in a 'quantum' object, an essential part of electronic transport is a classical effect: Coulomb blockade. This is a finite-size effect, which is observable due to the strong spatial confinement of electrons in QDs. Consider treating QDs as electrically chargeable islands, as shown schematically in Figure 2.5 **a**. The QD is tunnel-coupled to the source and drain lead, and capacitively to a plunger gate. The small size of a QD leads to a strong reduction of the capacitance of the island which scales in the simple approximation of a conducting sphere as $C = 4\pi\varepsilon_0 R$, with the vacuum permittivity ε_0 and the radius R of the sphere. The charging energy $E_\mathrm{C} = {}^{e^2}/_{C}$, with the elementary charge e and capacitance C, is defined as the energy needed to add one more electron to the QD, and becomes larger with decreasing R as $E_\mathrm{C} \propto {}^{1}/_{R}$. With a typical capacitance of only a few aF, E_C can readily achieve values of several meV. Hence, for QDs and at temperatures T below a few K, it can become energetically unaffordable to add another electron to the QD due to the reciprocal Coulomb repulsion of electrons. This effect is called Coulomb blockade. In electrical transport measurements, the effect of Coulomb blockade manifests itself as a blocked current through the quantum dot. The situation is illustrated in Figure 2.5 **b**: The chemical potential μ_N to add the Nth electron to the QD lies outside of the bias window defined by the chemical potentials μ_S and μ_D of the leads. This Coulomb blockade is only observed for low enough temperatures as otherwise the thermal energy $E_\mathrm{therm} = k_\mathrm{B}T$, with the Boltzmann constant k_B, would provide enough energy to overcome Coulomb blockade.

In practice, the capacitance of a gate-defined QD is the sum of the capacitances to source, drain and all gates i: $C_\mathrm{tot} = C_\mathrm{source} + C_\mathrm{drain} + \Sigma_\mathrm{i} C_\mathrm{gate,i}$. Then, in the framework of the constant interaction model, the total energy $U(N)$ of a QD with N electrons, can be calculated and becomes a function of the voltages on the gates [Kou01]. This, in turn, allows to electrically control the electrochemical potential $\mu(N) = U(N) - U(N-1)$

of the dot. In a transport experiment, where the electrochemical potentials of source, drain and QD are swept, this leads to Coulomb diamonds as shown in Figure 2.5 **c**. The particular diamond form (grey areas in Figure 2.5 **c**) arises due to the lack of electrical transport through the QD when it is in Coulomb blockade. This is the case, whenever $\mu(N)$ lies outside of the bias window defined by the electrochemical potentials of source and drain. Outside of these diamond shaped regions, a finite current through the QD is measured. Depending on the voltage bias V_{SD}, one or multiple channels for electrical transport are available and therefore the current increases stepwise with the number of channels. In Figure 2.5 **c** this is illustrated by the different shades of blue. The height of the Coulomb diamonds corresponds to the charging energy, as at the top of the diamond just enough energy can be provided by the potential difference between source and drain to lift Coulomb blockade.

A special case occurs if the plunger gate voltage is swept so high, that the capacitance of the QD island becomes so small, that even the addition of a single electron to the QD is energetically not possible. The QD is completely uncharged and thus called an empty QD, with N=0 electrons. In transport, a signature of this configuration is a half Coulomb diamond, which does not close anymore, as shown in Figure 2.5 **c**. Determining the regime of an empty QD purely in transport can be difficult, because often also the tunnel barriers between the QD and the leads increase due to the cross-capacitive coupling of the plunger gate. Therefore, other indications, such as even-odd spin-filling or excited state signatures need to be considered as well.

So far, only the contribution from classical Coulomb repulsion between electrons with quantized charge on a finite-sized island has been considered. However, the quantum confinement of electrons in a QD also leads to the quantization of the orbital states. The orbital energy E_{orb} and the charging energy E_{C} sum up to the addition energy of the QD. Since the orbital eigenstates of electrons in a QD are subject to the Pauli exclusion principle, the variation of the orbital energy with the number of electrons on

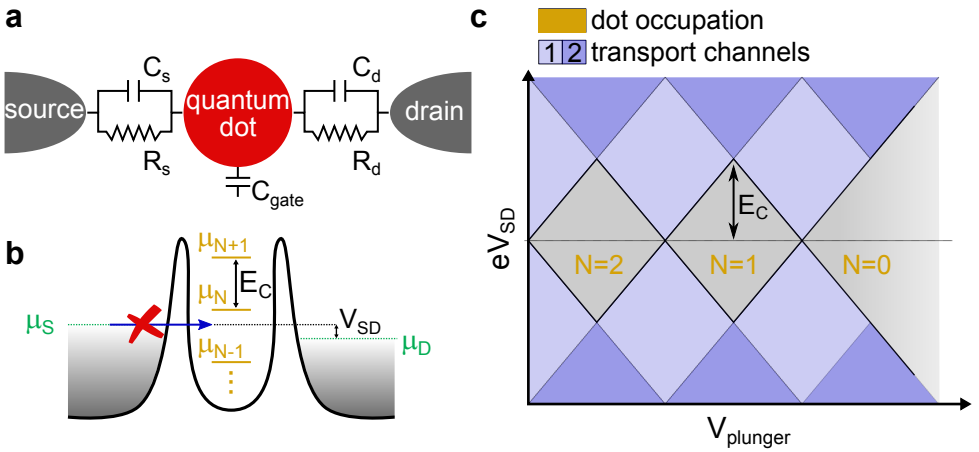

FIGURE 2.5 | **Single quantum dot. a** | Schematic illustration of a quantum dot as an island with finite capacitance which is tunnel coupled to a source and drain lead and capacitively coupled to a plunger gate. **b** | Coulomb blockade occurs if the electrochemical potential for the addition of another electron to the quantum dot is not within the bias window, defined as the difference between the chemical potentials of source μ_s and drain μ_d. In absence of, for instance, thermal excitations, the current through the QD is energetically blocked. **c** | Coulomb diamonds emerge as a function of bias voltage V_{SD} and gate voltage $V_{plunger}$ and are regions of blocked transport through the QD (grey areas) with constant occupation number N. Outside of Coulomb blockaded areas, the current through the QD increases stepwise, depending on the number of available transport channels (light and dark blue areas). A typical transport signature of an empty QD is the last Coulomb diamond which does not close anymore.

the QD leads to the emergence of a shell structure similar to that of atoms, therefore justifying the term artificial atom. Those quantum mechanical contributions can be observed as a variation of the height of Coulomb diamonds, which is then given by the addition energy, which is the sum of charging energy and orbital energy.

2.3.2 Multiple Quantum Dots

One single QD can be considered a unit cell for larger arrays of tunnel-coupled QDs. Both serial and parallel pairing is possible, with series of two and three QDs being the most common structures. A double quantum dot (DQD) system is similarly modelled by a network of the capacitive and resistive couplings of each QD to its gate, as well as to source and drain as shown in Figure 2.5 **a**. Furthermore, there is an additional

capacitive coupling C_M between the two QDs. This interdot tunnel coupling governs the behaviour of the DQD: in the case of a very strong interdot tunnel coupling, the DQD behaves similar to a huge single QD. On the other extreme, for a very weak tunnel coupling, the system behaves like two independent single QDs.

The most interesting regime is for intermediate interdot tunnel couplings, where electronic transport through the DQD is only possible at specific triple points where both electrochemical potentials of the left and the right QD are aligned with each other and with the chemical potential of source and drain. This yields the charge stability diagram shown in Figure 2.6 **a**, which depicts the occupation number N of each QD as a function of the left and the right gate voltage. Due to the mutual coupling C_M between the two QDs, the regions of constant occupation number become hexagonal, which results in a honeycomb pattern. In the linear transport regime with $V_{SD} \approx 0$, transport through the DQD is only possible at the triple points. At finite bias voltage, however, these discrete points expand into bias triangles with the boundaries being defined by the alignment of two electrochemical potentials. At sufficiently large bias voltage $eV_{SD} > E_{orb}$, higher orbital states than the ground state can contribute to transport as well, which appears as discrete lines in the bias triangle.

A doubly occupied DQD is a particularly interesting configuration, because the quantum dot states and transitions are governed by spin selection rules. Since electrons are fermions, the total wavefunction, which is the product of the orbital and the spin part, must be antisymmetric. In the case of two electrons, they can hence either form an spin singlet, if the orbital wavefunction is symmetric, or a spin triplet, if the orbital wavefunction is antisymmetric. These singlet-triplet states are useful for the implementation of a singlet-triplet qubit as well as for qubit readout via Pauli spin blockade, which will be discussed in section 2.3.3.

The energy spectrum of a DQD system with two electrons at the (1,1)-(0,2) charge transition is shown in Figure 2.6 **b**. The detuning ε describes the symmetry of the

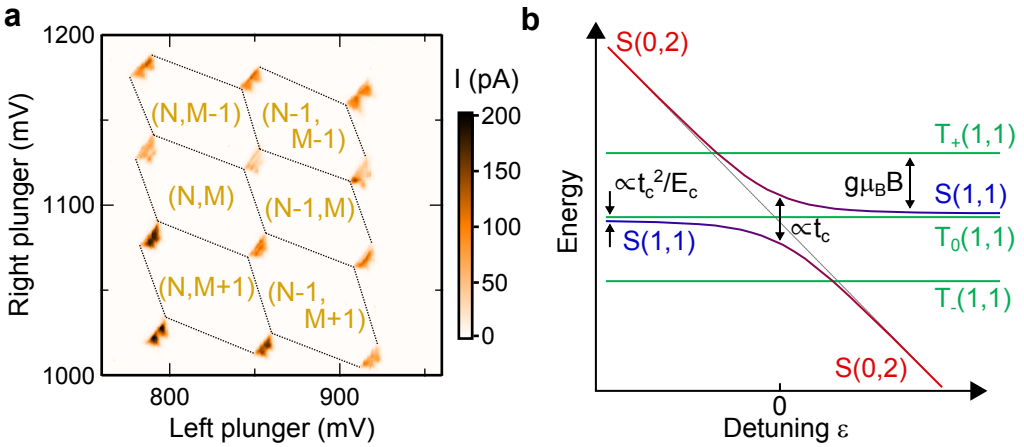

FIGURE 2.6 | **Double quantum dot. a** | The stability diagram of a double quantum dot system forms a honeycomb pattern (indicated by the black dotted lines). The triple points, where the chemical potentials of both quantum dots are aligned, extend to bias triangles at finite voltage bias. The charge occupation of the DQD is denoted by (N, M), where N (M) is the number of charges in the left (right) quantum dot. **b** | The energy spectrum as it arises from the possible spin and charge configurations for a double quantum dot occupied by two electrons. The singlet states $S(0, 2)$ and $S(1, 1)$ anticross due to the finite interdot tunnel coupling t_c. The triplet states are splitt by the Zeeman energy $g\mu_B B$, with the electron g-factor, the Bohr magneton μ_B and the magnetic field B. See also [Han07].

DQD confinement potential. At $\varepsilon = 0$, both QD potential wells are symmetric, while for $\varepsilon > 0$ the double potential well is is asymmetric and it is energetically more favorable for both electrons to reside in the right QD. Therefore, at very large detuning, the $(0, 2)$ state becomes the ground state of the system.

Five different states, reflecting the possible charge and spin configurations of the two electrons, are relevant in the energy spectrum of Figure 2.6 **b**. First, the two QDs are considered as independent, with a negligible interdot tunnel coupling t_c. In a spin singlet configuration, both electrons can either reside on the same QD in the $S(0, 2)$ states, or distribute over both QDs in the $S(1, 1)$ state. If the two electrons form a spin triplet, they can only reside in the same quantum dot if one electron occupies a higher orbital state. Hence, the triplet $(0, 2)$ states are split off by the single QD orbital level splitting. The $T(0, 2)$ states are not depicted in Figure 2.6 **b**, since in typical experiments at small detuning ε these states are energetically not available. In the

range of detuning shown in Figure 2.6 **b**, the two electrons must therefore occupy one of the three triplet states, which are ($T_{\uparrow\uparrow}$, $T_{\downarrow\downarrow}$, T_0). At zero magnetic field, these states are energetically degenerate but split up in finite magnetic field due to the Zeeman effect, which results in an energy difference of $g\mu_B B$.

Now, consider a finite, spin-conserving tunnel coupling t_c between the two QDs. At zero detuning the $S(0,2)$ and $S(1,1)$ are energetically degenerated, thus leads to an avoided crossing around $\varepsilon = 0$ which is proportional to the interdot tunneling rate. Note that the $T(1,1)$ states do not couple to the $S(0,2)$ in absence of spin-mixing mechanisms. for $\varepsilon < 0$, that is for a very symmetric DQD, the $T_0(1,1)$ state is energetically separated from the $S(1,1)$ by the singlet-triplet splitting $J \propto \frac{t_c^2}{E_C}$. This energy splitting is strongly detuning dependent as close to the avoided crossing at $\varepsilon = 0$ the singlet-singlet hybridization contributes significantly to J. Nevertheless, J can be described as an exchange energy and is thus referred to as effective exchange coupling.

Note that in the discussion of Figure 2.6 **b** any spin-mixing mechanisms are neglected. The picture changes for instance in presence of spin-orbit interaction, which yields transitions between $T_{\uparrow\uparrow,\downarrow\downarrow}(1,1)$ and $S(0,2)$ states. This mechanism becomes important when discussing the lifting of Pauli spin blockade in sections 2.3.4 and 7.

Adding another QD to the DQD yields a triple quantum dot (TQD). The stability diagram of a triple quantum dot (TQD) is similar to the honeycomb pattern of a DQD system. Due to the additional third QD, points of enhanced conductance appear in the stability diagram on a line with a third slope which is different from the other two slopes. Each slope corresponds to charging events on one of the three QDs. The geometric shape of regions of constant charge occupation of the TQD becomes more complex since more possibilities for the arrangement of the charges on the three QDs exist.

The interest in systems of multiple, tunnel coupled QDs is motivated by the importance of such structures as hosts for spin qubits for quantum computation. A single QD is the

most simple host for a spin-$\frac{1}{2}$ qubit according to the Loss-DiVincenzo proposal [Los98]. Here the qubit is encoded in the two basis states $|\uparrow\rangle$ and $|\downarrow\rangle$ of a single electron spin in a single QD. Alternatively, the qubit information can be encoded in two spins hosted in a DQD. The singlet and triplet configurations, as shown in the energy spectrum in Figure 2.6 **b**, form the basis states for a singlet-triplet qubit [Pet05]. A TQD can host other types of qubits such as the exchange-only qubit or the resonant exchange qubit [Rus17]. Independent of the qubit choice, the sequential addition of QDs is an aspect of research on scalable architectures for qubit arrays. Qubit arrays with nine qubits have been realized [Zaj16], made possible by the high control over the QD fabrication. Furthermore, not only linear arrays of qubits are of interest, but also other layouts such as a rectangular arrangement of four QDs have been investigated experimentally [Muk18].

2.3.3 Pauli Spin Blockade

Generally, electron and hole states in quantum dots are governed by the Pauli exclusion principle, which prohibits for two fermions to occupy the same quantum state. Thus, if they occupy a symmetric orbital state, they must form an antisymmetric spin state, and vice versa. In case of a doubly occupied DQD this restricts the possibilities to arrange the two electrons in the two QDs, as discussed in the previous section (see also Figure 2.6). In the (1,1) charge state, with one electron in each QD, both particles can occupy the orbital ground state without restrictions imposed by the spin alignment. However, if both electrons need to reside on the same dot, that is in a (2,0) or (0,2) charge configuration, both electrons can occupy the orbital ground state only if they form a spin singlet. Otherwise, for a spin triplet arrangement, the next higher orbital state needs to be involved in order to form one of the triplet $T(2,0)$ or $T(0,2)$ states.

In the electronic transport through the DQD system, these restrictions for the electron arrangement lead to current rectification at the (1,1)-(0,2) and the (1,1)-(2,0) charge

transition. This effect is called Pauli spin blockade (PSB), because the transport is blocked due to the Pauli exclusion principle. In forward bias direction $V_{SD} > 0$, if the system is prepared in the (1,1) charge state in a spin triplet configuration, the electron in the left QD can not tunnel into the right QD, therefore the system remains stuck in this configuration and the transport through the DQD is blocked. This situation is schematically depicted in Figure 2.7 **a**. The current through the DQD is an average over many electrons that are loaded from the source lead onto the DQD. Since both spin directions are equally probable to load, the DQD will eventually get stuck in a triplet configuration. The average time the DQD spends in this configuration until the blockade is lifted (see also the discussion of lifting mechanisms in section 2.3.4) is much longer than it spends in the unblocked singlet configuration. Therefore the current through the DQD at the (1,1)-(0,2) charge transition is reduced.

The blockade persists for detunings ε up to when the single dot singlet-triplet splitting is matched. Then, as illustrated on the right in Figure 2.7 **a**, the transition into the triplet state T(0,2) is energetically allowed and the blockade is circumvented. This transition appears as a line parallel to the baseline of the triangle but at finite DQD detuning.

In the reverse bias direction $V_{SD} < 0$, when transitioning from the (0,2) to the (1,1) charge configuration, it is always possible to load the correct spin from the lead reservoir in order to form a spin singlet $S(0,2)$. As depicted in Figure 2.7 **b**, the subsequent transfer of one electron into the left QD is always possible and hence no suppression of current is observed in this bias direction.

Figures 2.7 **c** shows the bias triangles at the corresponding (1,1)-(0,2) charge transition. At zero magnetic field, the current through the DQD is suppressed due to PSB, which appears as a reduced current on the baseline of the bias triangle. At finite magnetic field, the current on the baseline of the bias triangles increases, indicating that the spin blockade is lifted. Figure 2.7 **b** shows linecuts through the bias triangles in figures 2.7 **c**

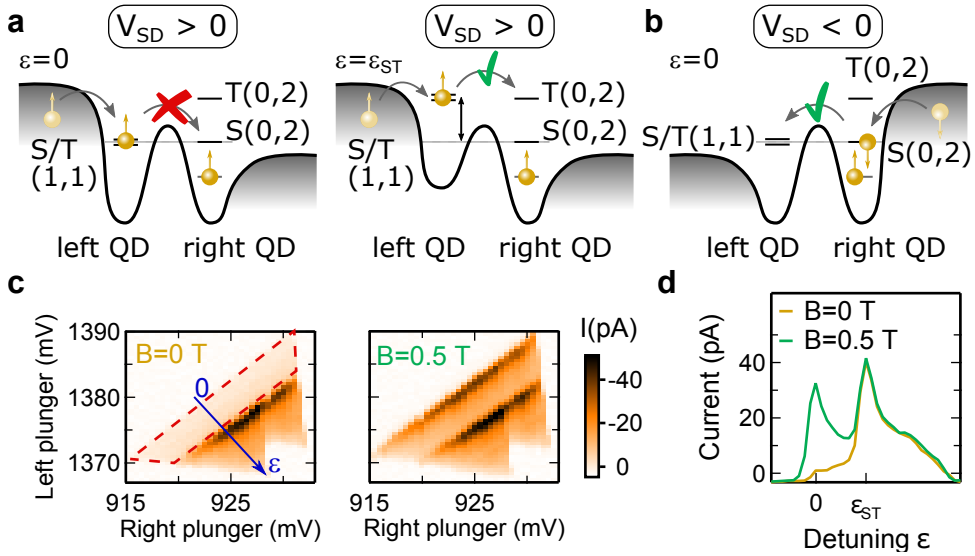

FIGURE 2.7 | **Pauli spin blockade.** **a** | In forward bias direction $V_{SD} > 0$, the transport through the DQD is blocked once a triplet state is occupied (left box). At larger detuning, exceeding the single QD singlet-triplet splitting ε_{ST} as indicated by the arrow, the triplet state $T(0,2)$ becomes energetically available and the blockade is lifted (right box). Note that at zero magnetic field $B = 0\,\mathrm{T}$ the triplet states are degenerate. **b** | In reverse bias direction $V_{SD} < 0$ transport is possible, since energetically it is always possible to separate the spins into a (1,1) charge configuration. Note that the mechanism of PSB works for both electrons and holes in the same manner. **c** | Bias triangles at $B = 0\,\mathrm{T}$ and $B = 0.5\,\mathrm{T}$ in presence of Pauli spin blockade. At zero magnetic field, the current inside the area encircled by the red dashed line is reduced. **d** | Linecuts along the detuning axis ε in the bias triangles in **c**. The absence of the first peak in the trace at $B = 0\,\mathrm{T}$, which appears at finite magnetic field (green trace), indicates Pauli spin blockade.

along the detuning axis, to illustrate the enhancement of current through the DQD. Such lifting of PSB at finite magnetic field can occur by spin-orbit interaction, which mixes different spin states. The effect of spin-orbit interaction and other mechanisms on spin blockade is discussed in the next section 2.3.4.

2.3.4 Lifting Mechanisms of Pauli Spin Blockade

Pauli spin blockade can be lifted by any process which leads to a spin flip of one of the electrons, which converts the (1,1) state from a triplet configuration into the non-blocked singlet configuration. On the one hand, this can be an intentional spin

rotation as discussed in section 3.2.2, which opens also the door for coherent spin manipulation, the basis for qubit operation. On the other hand, PSB can also be lifted by hyperfine interaction, spin-flip cotunneling, a g-factor difference between the two QDs, and by spin-orbit interaction. These inherent mechanisms will be discussed briefly in the following section.

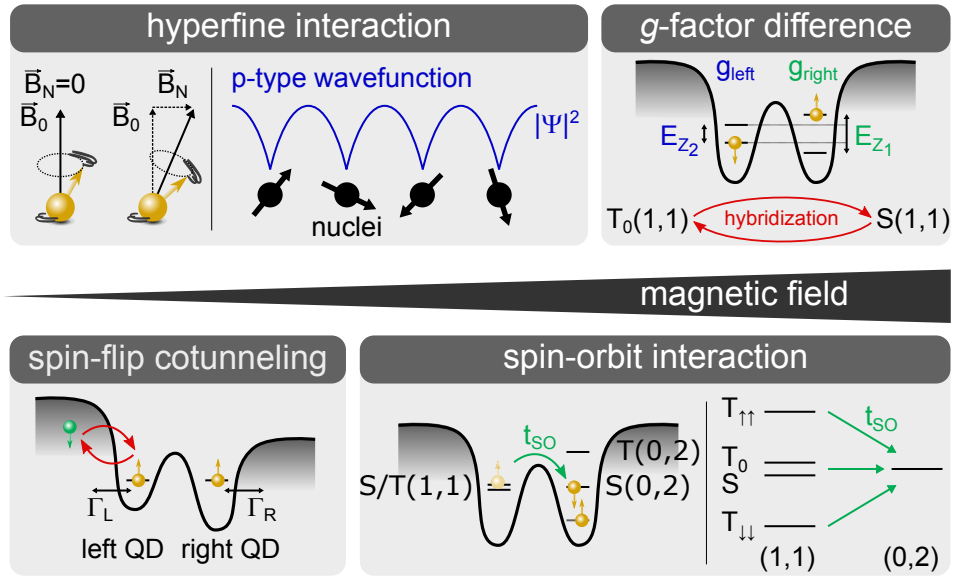

FIGURE 2.8 | **Lifting mechanisms of Pauli spin blockade.** Illustration of four mechanism that lift Pauli spin blockade and lead to a finite leakage current. *Hyperfine interaction* (top left) is due to the Overhauser $\vec{B}_\mathrm{N}$ field generated by the nuclei. For holes, due to the p-type Bloch wavefunction Ψ, contact hyperfine interaction is reduced because of the minimal overlap of $|\Psi|^2$ at the positions of the nuclei. A *difference in g-factor* between the left and the right quantum dot (top right) leads to different Zeeman splittings E_Z and hybridizes the $T_0(1,1)$ and $S(1,1)$ states. *Spin-flip cotunneling* (bottom left) exchanges the blocked spin state with an unblocked spin state from the reservoir in the lead in a co-tunneling process via a virtual intermediate state. *Spin-orbit interaction* (bottom right) introduces a non spin conserving interdot tunneling t_SO. Hyperfine interaction and spin-flip cotunneling are most efficient near zero magnetic field. Blockade lifting due to g-factor differences and spin-orbit interaction dominate at large magnetic field.

Hyperfine Interaction The QD environment consist of typically around 10^5 nuclei which can carry a nuclear spin I. These nuclear spins generate an effective magnetic field, also referred to as the Overhauser field $\vec{B}_\mathrm{nuclei} = \sum_k^N A_k \vec{I}_k$. Here, N is the

number of nuclei, A_k are the hyperfine coupling constants and $\vec{I}_k$ the nuclear spin momenta. Hyperfine interaction is the coupling of an electron or hole spin to $\vec{B}_{\text{nuclei}}$ and represents a source of decoherence but can also lead to spin flips. Generally, nuclear spin fluctuations are random and, in case of a DQD, lead to uncorrelated Overhauser fields for the left and right QD and also to slight variations of the spin precession frequency. This results in a mixing of triplet and singlet states, for instance it allows for the $T_0(1,1) = \frac{1}{\sqrt{2}}(|\uparrow\downarrow\rangle + |\downarrow\uparrow\rangle)$ state to evolve into the singlet state $S(1,1) = \frac{1}{\sqrt{2}}(|\uparrow\downarrow\rangle - |\downarrow\uparrow\rangle)$. Furthermore, direct electron-nuclear spin flip-flops may be permitted under special conditions, such as zero magnetic field. These effects provide a mechanism to lift PSB and generate a finite leakage current.

Hyperfine interaction is omnipresent in materials with isotopes containing net nuclear spins and can then only be impeded if random fluctuations are hampered, that is if the nuclear field is fully polarized. The Overhauser field $\vec{B}_{\text{nuclei}}$ is then maximal and static. This case occurs either at very low temperatures, where the Zeeman energy of the nuclear spin states exceeds the thermal energy, or at very strong magnetic fields. Both cases are extreme experimental conditions hence hyperfine interactions in a typical spin-blockade experiment leads to a leakage current peaking at zero magnetic field and dying out at higher magnetic fields.

For electrons with a *s*-type wavefunction, the dominant coupling term to nuclei is the isotropic 'Fermi contact hyperfine interaction'. The coupling strength in this case depends on the amount of nuclear spins overlapping with the electron envelope function. Without further measures to mitigate the effects of hyperfine interaction the electron spin coherence time is limited to a few nanoseconds only [Klo13a]. For holes, in turn, due to their *p*-type wavefunction, the isotropic contact hyperfine interaction is absent due to the lack of overlap with the nuclear spin sites [Pre16]. Anisotropic hyperfine interaction now becomes the dominant mechanism, but it is typically one order of magnitude weaker than the isotropic hyperfine interaction. For pure heavy holes, the

hyperfine interaction takes on an Ising form $\sum_k^N A_k^{\text{holes}} I_k^z s_z$, in contrast to the Heisenberg type of interaction for electrons, and therefore depends only on the z-component of the nuclear spins [Klo13a]. This implies, that in a transverse magnetic field, heavy hole spin dephasing due to hyperfine interaction is strongly suppressed. However, heavy hole-light hole mixing (see also discussion in section 2.2.4) gives rise to additional hyperfine coupling terms. Those are about one to two orders of magnitude weaker, though, and therefore hole spin dephasing due to hyperfine interaction is efficiently suppressed. Furthermore, in materials with a low amount of nuclear spins such as silicon and germanium, hyperfine interaction can be considered a negligible effect. For particularly sensitive applications, both materials can be isotopically purified to further reduce these numbers.

Spin-Flip Cotunneling The exchange of spins with Fermi reservoirs in nearby leads provides another mechanism to lift spin blockade [Coi11; Bie15]. Through an inelastic cotunneling process, the spin state of the QD can be changed by interchanging the spin in the QD with a spin of opposite sign from the reservoir in a co-tunneling process involving a virtual intermediate state. Here, the total energy in the system remains constant since the energy change of the QD state is compensated for by the lead with its continuous energy distribution. In a typical spin blockade measurement in a DQD, spin-flip cotunneling results in a finite leakage current independent of the DQD detuning. The peak fades out with increasing magnetic field as excitation processes out of the then triplet ground states become suppressed and the system remains in the blocked triplet state. In the low temperature limit, if the interdot tunnel coupling is larger than the thermal energy, also a shallow dip in leakage current can be observed near zero magnetic field.

Difference in g-factor Local variations of the Landé g-factor can give rise to a Δg between the two QDs. Such a difference can occur due to variations of the electric

field, the confinement potential, and the occupation number. In this case, Δg leads to an admixture of the singlet $S(1,1)$ and the triplet $T_0(1,1)$ state of the DQD system and hence can also generate a finite leakage current in a spin blockade configuration.

Spin-Orbit Interaction The coupling between the spin and the orbital momentum also provides a mechanism to lift spin blockade, because it enables nonspin-conserving interdot tunneling [Dan09]. Considering the energy spectrum of a doubly occupied DQD in Figure 2.6 **b**, the spin-conserving interdot tunnel coupling t_c results in the hybridization of the $S(1,1)$ and the $S(0,2)$ states, which yields an avoided crossing at the intersection of the two states. In contrast, transitions from the $T_{\uparrow\uparrow,\downarrow\downarrow}(1,1)$ states into the $S(0,2)$ are not allowed because it requires a spin-flip of one of the electrons. However, in presence of spin-orbit interaction the $T(1,1)$ and the $S(0,2)$ states hybridize, giving rise to a nonspin-conserving tunnel coupling t_{SO}. Consequently, as shown in Figure 2.8, these transitions are allowed hence lifting spin blockade and resulting in a finite leakage current. The leakage current due to spin-orbit interaction has a pronounced magnetic field dependence. The leakage current of predominantly spin-orbit interaction induced lifting of PSB exhibits a dip at zero magnetic field and increases with increasing magnetic field. In a simple picture, in absence of an external magnetic field, the spins are aligned along the internal effective spin-orbit field B_{eff}. With a finite external magnetic field applied, the spins start to precess around that magnetic field, which enables spin-flip tunneling [Wan16]. However, if the Zeeman splitting remains smaller than the avoided crossing of the singlet states, the interdot tunneling is energetically suppressed. Therefore, the width of the gap of leakage current around zero magnetic field depends on both the spin-conserving tunneling rate and the spin-orbit interaction strength.

All mechanisms discussed above have a characteristic dependency on the external magnetic field and the tunnel couplings. This allows to distinguish different spin mixing

mechanism in an experiment [Pfu07; Nad10b; Bra16b; Zar17; Wan16; Wan18a], for instance by measuring the magnetic field dependent leakage current for different interdot tunnel couplings.

Hyperfine interaction and spin-flip cotunneling are most effective near zero magnetic field. These processes thus lead to a peak of leakage current which decays when the magnetic field exceeds the mean value of the nuclear magnetic field or the Zeeman energy becomes larger than the thermal energy, respectively.

Leakage currents due to Δg or spin-orbit interaction, however, exhibit a dip near zero magnetic field and intensify with increasing magnetic field.

Section 7 provides an in-depth study of the leakage current and its sources in a Ge/Si core/shell nanowire DQD. There, we study the evolution of leakage current in magnetic fields up to 8 T. A model, including orbital effects and a magnetic field dependent g-factor ultimately allows to extract the spin-orbit interaction length for holes in this system.

3 Qubit Operation

The quest to build a quantum computer is motivated by the ample applications that become possible when exploiting quantum properties and employing them for information processing. The basic building block of a quantum computer is the quantum bit, or qubit, which contains the quantum information, similar to a bit in classical computation. Different implementations of this smallest information unit have been proposed and realized, each with distinct prospects as well as challenges [Lad10; Eck13] when considering basic requirements for the physical implementation of quantum computation [DiV00b; Dev13].

Amongst the most encouraging candidates for qubits are semiconductor quantum dot qubits [Eri13]. Interest in this category of qubits is fueled by their prospects for scaled-up architectures and their integration with classical electronics, due to the large overlap with today's semiconductor electronics [Vel17]. Quantum dots, as described in section 2.3, serve as the host for semiconductor qubits and are at the heart of research. The spin physics, such as the exchange interaction, of electrons (or holes) trapped inside such quantum dots are the basis for spin-qubit operation and a variety of implementations based on combinations of one to four electrons in one to three quantum dots exist [Rus17; Rus18].

The operation of qubits requires both reliable control and readout of the qubit state. In the case of semiconductor based quantum dots these can both be conveniently achieved by using the gates which define the quantum dot [Eri13; Han07]. The requirements to allow for qubit control depend strongly on the kind of qubit implementation, and may or may not include intrinsic material properties, on-chip micro- and nanostructures and external control electronics.

The focus of this work is on quantum dots in Ge/Si core/shell nanowires as a platform for the implementation of hole spin qubits. Spin qubits in semiconductors in

general, and especially in nanowires, have good prospects for a quantum computing architecture [Klo13a; Fro13]. In particular Ge/Si core/shell nanowires, due to the special properties arising from the one-dimensional geometry and the material composition (see section 2.2), hold promise for very fast, all-electrically controllable spin qubits with enhanced coherence. Section 3.1 discusses these unique possibilities. In the following sections, the key concepts of qubit operation are outlined. The actual computing operation relies on the control of single spins, which is described in section 3.2. More general, the necessary and available single qubit gates are discussed in section 3.3. After performing a number of operations on the qubit, the high fidelity readout of the qubit state is of great importance, yet not in the scope of this thesis. Regardless, section 3.4 outlines the most important concepts of qubit readout. Finally, as the utility of a qubit is inseparable connected to its stability in terms of how long the spin information is preserved, section 3.5 describes ways to characterize qubit relaxation and coherence.

3.1 Hole Spin Qubits in Ge/Si Core/Shell Nanowires

Semiconductor spin qubits in nanowires gain particular interest due to variability of material design, as discussed in section 2.1, which allows for a high control over nanowire properties. In comparison, nanowires host among the fastest single spin qubits [vdBer13; Wat18b], made possible by the strong spin-orbit interaction found in materials such as InSb, InAs and Ge [Fas07; Nad10b; Nad12]. Additionally, the large Landé g-factor in nanowires and its tunability with electric fields are useful for qubit operation in low magnetic fields [Bjö05; Nil09; Sch11b; Pri13]. Important milestones have been achieved with spin qubits in nanowires: coherent single spin control [Nad10a; vdBer13], single shot readout [Vuk18] and coupling to a resonator for long-distance qubit-qubit interaction [Pet12]. However, qubit coherence is an omnipresent challenge for spin qubits, regardless of the type of qubit realization, and often requires mitigating measures such as spin echo or dynamical decoupling [Kop08; Nad10a].

Hole spin qubits [Mau16; Wat18b; Hen20b] have become an attractive alternative due to their reduced contact hyperfine interaction [Hei07; Pre16]. Also implementation of hole spin qubits in Ge/Si core/shell nanowires, which is additionally a predominantly nuclear spin free host material, promises to be advantageous for qubit coherence. Previous studies have found coherence times of 180 µs for hole spins in this platform [Hig14c].

Moreover, hole spin qubits in Ge/Si core/shell nanowires are attractive due to the strong and tunable spin-orbit interaction that arises in this one-dimensional system (see section 2.2.4). The presence and electric field sensitivity of the spin-orbit interaction in Ge/Si core/shell nanowire implies important features for the operation of such a hole spin qubit. The first, and largely unexplored, implication is the effect of electric field magnitude and direction on relaxation [Mai13] and coherence [Klo13b; Wan19b] of hole spins. Next, the strength of spin-orbit interaction promises in theory spin-flip rates exceeding 1 GHz [Klo13b]. In practice, Rabi frequencies above 100 MHz are expected, comparable to other hole spin systems [Wat18b; Hen20b]. The third implication is

the g-factor anisotropy and its electric field tunability that arises from direct Rashba spin-orbit interaction [Mai13; Bra16a]. An electric field tunable g-factor allows for individual addressability of spin qubits in an array, for instance when coupled to a resonator. Lastly, the strong spin-orbit interaction also suggests a strong spin-photon coupling between a hole spin qubit and a resonator [Klo13b].

Altogether, hole spin qubits in Ge/Si core/shell nanowires have prospects as a platform for a quantum computing architecture with all-electrical control. Not only the qubit manipulation itself can be achieved by purely electrical means via electric dipole spin resonance mediated by spin-orbit interaction. Also the coupling strength of the qubit to environmental noise and to resonators can be adjusted in-situ. Based on the strong electric field dependence of the strength of direct Rashba spin-orbit interaction, a qubit with two settings, control and idle, can be envisioned. Figure 3.1 **a** illustrates this basic operation scheme. For controlling the qubit, the strength of spin-orbit interaction is electrically tuned to allow for fast qubit operations. Otherwise, the qubit can be switched to an idle configuration, with reduced spin-orbit interaction, hence isolating the spin from its environment, which prolongs qubit coherence. Figure 3.1 **b** shows the dependence of direct Rashba spin-orbit interaction on the electric field [Klo13b; Klo18] and indicates possible points of qubit operation in the "Idle" (green arrow) and "EDSR" (red arrow) control state. Note that already a relatively small electric field of a few $\mathrm{V\,m^{-1}}$ yields the desired effects. At the third point, the qubit energy is tuned into resonance with a microwave cavity (blue arrow), enabled by the electrically tunable g-factor shown in Figure 3.1 **c**. At this point, the qubit-qubit coupling strength, mediated by superconducting microwave resonators, can be switched on electrically. At the idle and control operation points, away from the cavity resonance, the qubit is decoupled from other qubits for single qubit operations or idling. Because every qubit can be individually controlled with local gate voltages, individual pairs of qubits can be tuned in and out of resonance with the cavity mode. Note that the exact choice of the

operation points "Idle", "EDSR" and "Cavity" can be optimized and varies depending on the dominant processes for decoherence and relaxation, as well as the actual device configuration in terms of electric field profile and resonator realization.

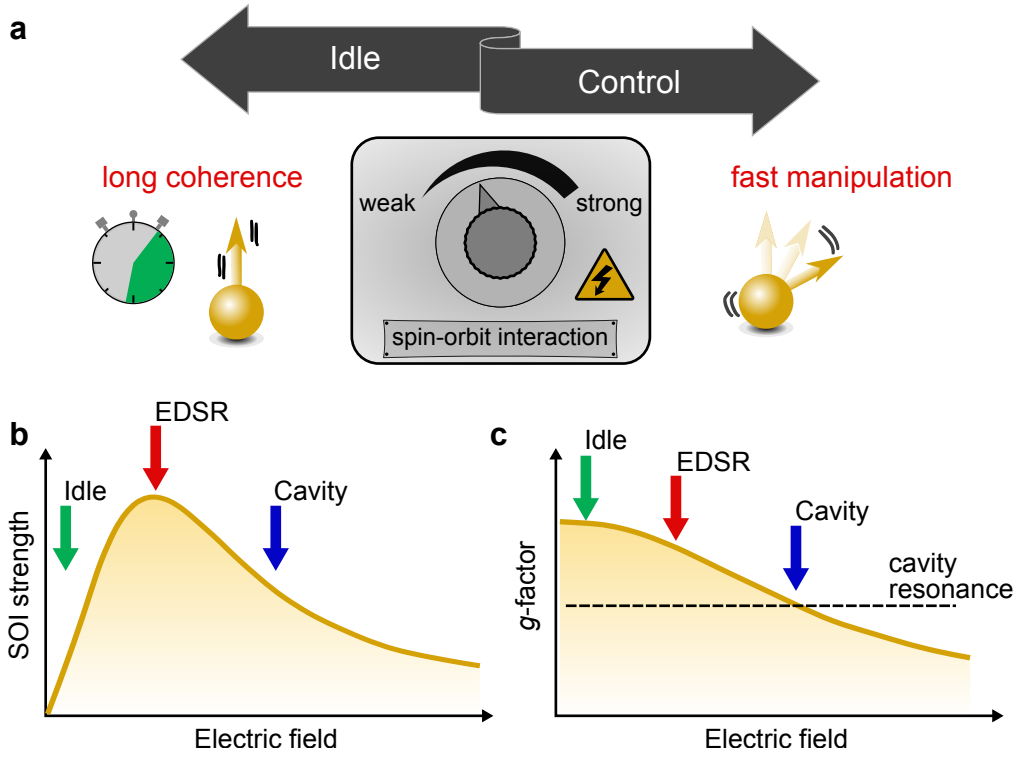

FIGURE 3.1 | **Electrical control of hole spin qubits in Ge/Si core/shell nanowires.** **a** | The tunability of spin-orbit interaction with electric fields allows to switch the hole spin qubit between a configuration with weak and strong spin-orbit interaction. In the idle state with weak spin-orbit interaction, the qubit is more isolated from the environment which prolongs coherence. The control state allows for fast spin manipulations of the hole spin qubit. **b** | Spin-orbit interaction strength as a function of the electric field. Possible configurations for the qubit states "Idle", "EDSR" and "Cavity" are indicated. **c** | The electric field tunable g-factor allows to adjust the qubit energy at the different points of operation. At the point "Cavity", the qubit and the microwave cavity are on resonance, therefore enabling long-range qubit-qubit interactions mediated by the microwave photons. At the points "EDSR" and "Idle" the qubit energy is detuned from the cavity thus disabling qubit-qubit interactions. Note that in general spin-orbit interaction strength and g-factor are not independently tunable and that the exact position of the three operation points can vary in actual devices. Subfigures **b** and **c** are adapted from [Klo13b].

Finally, Ge/Si core/shell nanowires not only hold promise for hole spin qubits, but also for topological quantum computation [Fie18; Lah17]. Here, particles with non-Abelian

statistics such as Majorana zero modes (MZMs) are used, which are topologically protected from decoherence. In nanowires with spin-orbit interaction and coupled to a superconductor, MZMs emerge at both ends of the nanowire when tuned into a regime of topological superconductivity, and appear in transport as a zero bias peak [Sta13; Paw19]. The four necessary ingredients for the emergence of MZMs in nanowires are one-dimensionality, strong spin-orbit interaction, superconductivity and an external magnetic field. Ge/Si core/shell nanowires meet these requirements in a particular manner. These nanowires represent a strongly confined system, which exhibits transport characteristics close to the single transverse mode regime and are therefore almost truly one-dimensional. Moreover, the strong direct Rashba spin-orbit interaction is an ideal prerequisite. Furthermore, it is possible to selectively exchange the Ge core with Al, thus enabling atomically sharp semiconductor-superconductor interfaces, which could potentially prove useful for experiments regarding MZMs [Rid20; Sis19; Luo20]. In conclusion, Ge/Si core/shell nanowires optimally meet the requirements for the emergence of MZMs and are therefore intensely studied [Mai14; dVri18].

3.2 Single Spin Control

At the heart of spin qubit operation is the controlled manipulation of the spin state of electrons or holes in a quantum dot. The basis states always form a quantum mechanical two-level system, and the transitions therein, as described in section 3.2.1, are the basis for qubit operations. Due to the small magnetic moment of an electron spin, directly addressing the spin state is difficult due to the weak interaction with the environment. Furthermore, the generation of local high-frequency magnetic fields, which are necessary for driving spin rotations, is demanding. Therefore, various techniques were developed in order to allow for single spin control, of which electric dipole spin resonance mediated by spin-orbit interaction is most important in the scope of this thesis and discussed in section 3.2.2.

3.2.1 Dynamics of a Two Level System

The basic concept of a qubit is to encode information in a two level system, which can be composed of, for instance, charge or spin states of electrons in quantum dots. A charge qubit for instance, uses the charge configuration of an electron in a DQD. The electron can reside in either the left or the right quantum dot, but since these two states are energetically equal, an avoided level crossing is formed in presence of an interdot tunnel coupling. The two charge states then hybridize and form the basis states of the two-level quantum level. Charge qubits suffer from the short coherence of the charge states due to the sensitivity to charge noise and the tunnel coupling to the reservoirs and are therefore, without additional measures such as the operation at sweet spots, limited in its utility [Pet10].

Meanwhile, it is beneficial to exploit the spin states of electrons and holes which are better protected from decoherence due to the weak interaction of spins with their environment. This establishes the field of spin qubits. Naturally, the two spin states of a spin-$\frac{1}{2}$ electron form a two level system, but other basis states such as the spin singlet and triplet states also form a suitable two-level system.

Regardless of the exact type of qubit, all of them can be conceptionally described as a two level system with the two levels $|0\rangle$ and $|1\rangle$ which form the computational basis of the qubit. The qubit state $|\Psi\rangle$ can be represented on a Bloch sphere as depicted in Figure 3.2 **a**. The vertical axis of the Bloch sphere, extending from the south pole to the north pole, represents the quantization axis. The north and south pole constitute the (pure) basis states $|0\rangle$ and $|1\rangle$, and every other point on the sphere corresponds to a superposition state of the form $|\Psi\rangle = \alpha\,|0\rangle + \beta\,|1\rangle$, where α and β are the amplitude coefficients and fulfill the normalization condition $|\alpha|^2 + |\beta|^2 = 1$.

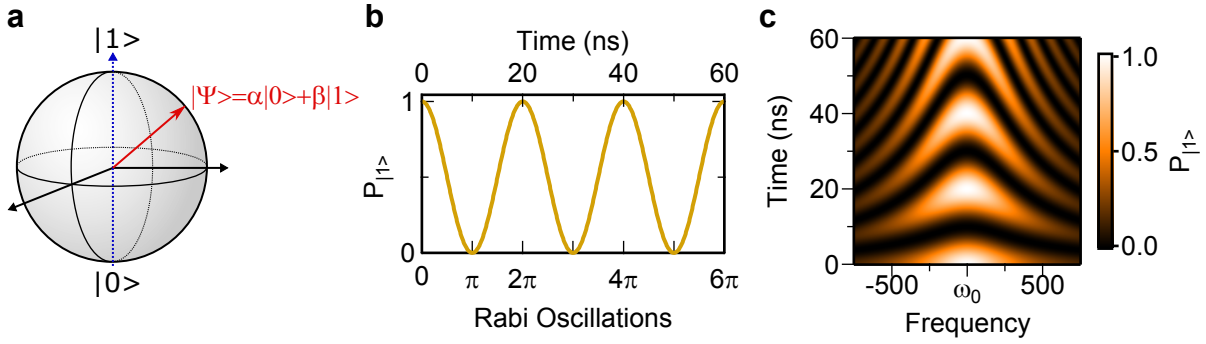

FIGURE 3.2 | **Rabi oscillations of a two level system.** **a** | Bloch sphere representation of the qubit state $|\Psi\rangle$ which is a superposition $|\Psi\rangle = \alpha\,|0\rangle + \beta\,|1\rangle$ of the basis states $|0\rangle$, $|1\rangle$ with coefficients α and β that fulfill the normalization condition $|\alpha|^2 + |\beta|^2 = 1$. **b** | Time evolution of the probability to find the qubit in state $|1\rangle$, as described by equation (3.1) with $\Delta\omega_0 = 0$. The probability oscillates between 1 and 0 with the Rabi frequency Ω_R. **c** | Probability to find the qubit in state $|1\rangle$ as a function of time and drive frequency. On resonance, Rabi oscillations as in **b** occur. If the drive frequency is detuned, the amplitude of the coherent oscillations decreases, while the frequency increases. The dynamics are covered by equation (3.1).

The Bloch sphere representation visualizes the qubit state and snapshots of its time evolution. The most important qubit dynamics are the Larmor precession and Rabi oscillations. A static magnetic field defines the quantization axis of the qubit (blue dashed vertical line in Figure 3.2 **a**) along which the two basis states $|0\rangle$ and $|1\rangle$ of the qubit are aligned. Any other qubit state, which is not aligned with the quantization axis, precesses around this axis. This behaviour is called Larmor precession. The frequency of precession is given by the energy difference between the states $|0\rangle$ and $|1\rangle$, which in case of a spin-$\frac{1}{2}$ is equal to the Zeeman splitting.

Rabi oscillations are coherent, periodic transitions between the two basis states, as seen in Figure 3.2 **b**, induced by a driving field which is perpendicular to the quantization axis. If the qubit is excited with the driving field on resonance with the Larmor frequency, the qubit oscillates back and forth between the two basis states $|0\rangle$ and $|1\rangle$ with the Rabi frequency Ω_R. The dynamics are well described by the Rabi formula

$$P_{|1\rangle}(t) = \frac{\Omega_R^2}{\Omega_R^2 + (\Delta\omega_0)^2} \sin^2\left(\sqrt{\Omega_R^2 + (\Delta\omega_0)^2} \cdot \frac{t}{2}\right), \tag{3.1}$$

which describes the probability P to find the qubit in state $|1\rangle$ after the time t, with the drive frequency being detuned by $\Delta\omega_0$ from the Larmor frequency. On resonance, the probability to find the qubit in state $|1\rangle$ oscillates between 0 and 1 as shown in Figure 3.2 **b**. When the drive frequency is detuned from the qubit resonance frequency $\Delta\omega_0 \neq 0$, the qubit oscillates faster between $|0\rangle$ and $|1\rangle$, but also with decreasing probability to find the qubit in a basis state. This yields the pattern shown in Figure 3.2 **c**.

A quantum two level system can be formed in many ways, whereas for a spin qubit the most prominent systems are the spin-$\frac{1}{2}$ and the singlet-triplet states. Transitions in such systems involve the rotation of a single electron spin, therefore requiring techniques to manipulate the state of a single spin for technical applications. These techniques will be discussed next.

3.2.2 Single Spin Manipulation by Electric Dipole Spin Resonance

From the discussion in the previous section it becomes clear, that it is essential for qubit operations to change the qubit's state through controllable manipulation of single spins. A single spin, however, is only weakly interacting with the environment due to its small magnetic moment. This makes the spin state a more attractive candidate for encoding the qubit information, when compared to charge states which are less stable. Yet it imposes technological challenges for the spin manipulation. Subsequently, various techniques for single spin control have been developed as illustrated in Figure 3.3 and discussed briefly in this section. Other literature [Han07; Han08; Wan18a] is referenced for more details and placement into a broader context. The focus of this section is then on single spin manipulation by electric dipole spin interaction (EDSR).

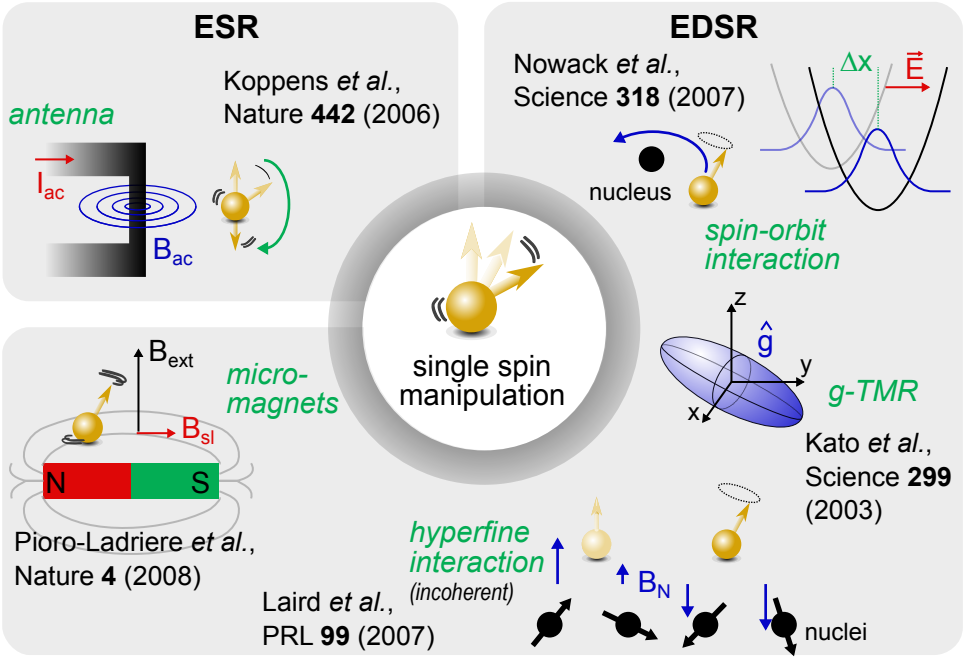

FIGURE 3.3 | **Mechanisms of single spin control.** Illustration of different mechanisms that allow for single spin control. In electron spin resonance, the magnetic moment of the spin couples to an oscillating magnetic field generated by a nearby coil. Electric dipole spin resonance can be mediated by micromagnets, flucuations of the nuclear magnetic field, g-tensor modulation, and spin-orbit interaction. The references are the first time demonstration of these experimental techniques.

The most intuitive approach for single spin manipulation is electron spin resonance (ESR) [Kop06; Pla12; Vel14], which is based on the magnetic coupling of the electron's spin to a magnetic field. Here, an oscillating magnetic field is applied perpendicular to a static magnetic field B_0 leading to spin precession. Resonant spin rotations between the spin-up and the spin-down state occur if the frequency of the oscillating magnetic field f_{ac} matches the spin's Zeeman splitting induced by the static magnetic field, $f_{\mathrm{ac}} = g\mu_{\mathrm{B}}B_0/h$, with the electron spin g-factor, the Bohr magneton μ_{B}, and Planck's constant h. The ac magnetic field is generated in this case by driving a current through a coplanar stripline [Deh13]. Particular challenges of this technique are the generation of magnetic fields with high enough frequency to match the resonance condition, the prevention of photon assisted tunneling due to accompanying electric fields, and the application at low temperature due to heating effects .

Due to these challenges of ESR, other approaches aim at eliminating the need of high-frequency magnetic fields and, instead, manipulating the spin with electric fields only. The utilization of high-frequency electric fields has the advantage of being easier to generate, apply and localize on the nanoscale than magnetic fields. However, in contrast to magnetic fields, electric fields do not couple directly to the spin and therefore a mediating mechanism is required to provide the coupling of the spin to the electric dipole of the ac electric field. There are multiple approaches to accomplish for such a coupling and thus to allow for electric dipole spin resonance. They are illustrated in Figure 3.3 as well.

The first approach is to use an inhomogeneous magnetic field which is locally generated by micromagnets made of a ferromagnetic material [Tok06; Pio08]. The stray magnetic field of the micromagnets forms a slanting magnetic field around the equilibrium position of the electron spin, as depicted in Figure 3.3. By periodically displacing the electron with an ac electric field along this magnetic field gradient, the spin experiences an effective oscillating magnetic field that subsequently drives spin rotations.

This spin manipulation approach requires the microfabrication of magnetic structures in close proximity to the qubit. Therefore, in order to reduce the device complexity, mechanisms which provide a coupling that is intrinsic to the qubit device, have better prospects in terms of scalability. One example is hyperfine interaction mediated EDSR, where the inhomogeneous nuclear magnetic field, due to random fluctuations of the Overhauser field, drives spin rotations [Lai07]. However, coherent spin rotation is not possible due to the randomness of the Overhauser field fluctuations. More controllable, however, are g-tensor modulation resonance (g-TMR) and spin-orbit interaction mediated electric dipole spin resonance.

In semiconductor systems, the g-factor is typically anisotropic and depends on electric fields [Win03; Sal01; Jia01]. The mechanism of g-TMR is based on variations of the g-tensor induced by gate voltage changes, which yields a time-dependent spin precession vector. The high-frequency modulation of direction and magnitude of the spin precession vector leads to resonant electron spin rotations [Kat03; Cri18]. The g-factor variation can be achieved by engineering a spatially varying g-factor in the heterostructure, or by exploiting the natural g-factor tunability with electric fields, as it arises from the presence of spin-orbit coupling.

Spin-orbit interaction offers another way for single spin manipulation via EDSR by purely electrical means, without the need of other elements. In this case, an ac electric field $\vec{E}(t)$ periodically displaces the charge's wavefunction, and the resulting modulation of the orbit induces spin rotations via the spin-orbit coupling [Gol06]. Figure 3.4 **a** illustrates this spin manipulation scheme. Because the necessary high-frequency voltage generating the ac electric field can be applied to a nearby gate electrode, such as the ones that define the quantum dot, this approach demands the least complexity of the qubit device.

The working principle is that an oscillating electric field $\vec{E}(t) = \vec{E}_0 \cos(\omega t)$, with frequency ω, periodically displaces the wave function due to the dipole interaction

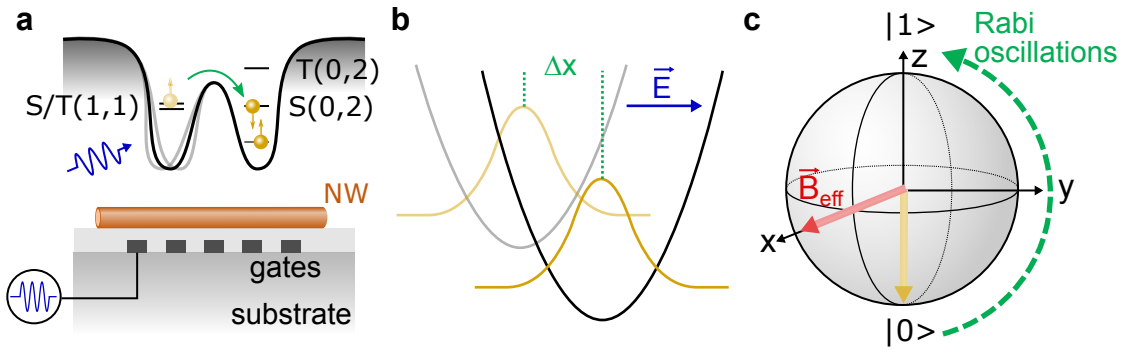

FIGURE 3.4 | **Electric dipole spin resonance mediated by spin-orbit interaction.** **a** | A double quantum dot potential is formed inside the nanowire with electrostatic gates. By applying a high-frequency signal to one of the gates, the quantum dot is periodically displaced. **b** | Illustration of the confined electron wave function in the quantum dot potential well. The modulation with a high frequency electric field $\vec{E}(t)$ leads to a displacement $\Delta x = \frac{e\vec{E}(t)l_{\mathrm{dot}}^2}{E_{\mathrm{orb}}}$ of the wave function. Adapted from [Now07]. **c** | Bloch sphere representation of electric dipole spin resonance. In presence of spin-orbit interaction, the periodic displacement of the wave function generates an effective magnetic field B_{eff} which can drive Rabi oscillations.

by $\Delta x = \frac{e\vec{E}(t)l_{\mathrm{dot}}^2}{E_{\mathrm{orb}}}$, with the elementary charge e, the dot length l_{dot} and the orbital level splitting E_{orb}. This situation is schematically depicted in Figure 3.4 **b**. In presence of spin-orbit interaction, this is translated into an effective magnetic field $\vec{B}_{\mathrm{eff}}$. The effective magnetic field is proportional and perpendicular to the externally applied, static magnetic field B_{ext}, and can be written as

$$B_{\mathrm{eff}} = 2B_{\mathrm{ext}}\frac{\Delta x}{l_{\mathrm{SO}}} = 2B_{\mathrm{ext}}\frac{l_{\mathrm{dot}}}{l_{\mathrm{SO}}}\frac{e\vec{E}(t)l_{\mathrm{dot}}}{E_{\mathrm{orb}}}, \tag{3.2}$$

with the spin-orbit interaction length l_{SO}. As a consequence, spin rotations can be driven through the oscillating B_{eff}, by applying the time varying electric field $E(t)$. In the Bloch-sphere picture shown in Figure 3.4 **c**, the induced Rabi oscillations around the direction of B_{eff} are illustrated. The magnitude of B_{eff} defines the speed of Rabi oscillations according to $\Omega_{\mathrm{R}} = \frac{g\mu_{\mathrm{B}}B_{\mathrm{eff}}}{2h}$, which therefore scales with the spin-orbit interaction strength.

Spin-orbit interaction mediated EDSR for electrons has been demonstrated in various material systems, including GaAs [Now07], InAs [Nad10a; Sch11b], and InSb [Nad12; vdBer13]. For holes, EDSR has been demonstrated in InSb nanowires [Pri13], Si [Mau16] and in Ge [Wat18b; Hen20a]. In Ge/Si core/shell nanowires, despite the strong spin-orbit interaction that was found, no EDSR has been demonstrated yet. Similarly to other hole systems, Rabi frequencies above 100 MHz can be expected, resulting from the strength of spin-orbit interaction.

3.3 Single Qubit Gates

To allow for arbitrary operations in quantum computing, both single qubit gates and two-qubit entangling gates are required. Control over the qubit state on the Bloch sphere is essential, therefore single spin control as described in section 3.2, which leads to Rabi oscillations, is the basis for single qubit gates. One example for a single qubit gate is the *NOT* gate, also called X-gate. It is a rotation of the spin from the north pole of the Bloch sphere to the south pole. Similarly, rotations by π around the y and the z axis can be defined and are called correspondingly Y- and Z-gate.

In a spin-$\frac{1}{2}$ qubit driven by EDSR, the execution of a X-gate corresponds to the application of microwave burst with a length τ_{X}, that corresponds to exactly half of a Rabi cycle, and a frequency that matches the Larmor precession frequency of the qubit, given by the Zeeman splitting. This rotates the spin from the initial state $|0\rangle$ to state $|1\rangle$, which corresponds to a rotation by π around the x axis.

Correspondingly, a Y-gate is defined as a spin rotation by π around the y-axis, where in this case the only difference to a X-gate is a 90° phase shift of the microwave burst. This requires precise control over the phase of the high-frequency signal, as can be achieved by IQ-modulation. Note that executing a X- or a Y- gate on a $|0\rangle$ qubit state has the same outcome, resulting in state $|1\rangle$. However, a combination of arbitrary fractions of X- and Y-gates allows to prepare any qubit state on the Bloch sphere.

Although combinations of X- and Y-gates are already enough for arbitrary single qubit state preparation, the realization of a Z-gate is also possible. It can be realized by changing the qubit Zeeman splitting for the duration of the Z-gate τ_{Z}, which changes the Larmor precession frequency and therefore corresponds to a rotation around the z-axis. This change of the qubit energy can be accomplished, for instance, by a change of the g-factor which determines the splitting between the $|0\rangle$ and $|1\rangle$ state. It becomes clear, that material systems with an electrically tunable g-factor, such as it is found in Ge/Si core/shell nanowires, provide all electrical control of qubit gates around any axis.

3.4 Qubit Readout

Besides the control over single spins, for spin qubit operation it is also crucial to determine the spin state with high fidelity, and in a single-shot technique. A qubit measurement is a projective measurement on to the quantization axis and, in the ideal case, returns probability p for state $|0\rangle$ and $1-p$ for state $|1\rangle$. The spin information is read out by mapping it to a charge state, which is subsequently detected [Fie93; Eri13]. The information transfer, or spin-to-charge conversion, can be achieved by energy selective tunneling [Elz04], spin dependent tunneling [Han05], or Pauli spin blockade [Ban03; Pet05].

In energy selective tunneling one measures if the electron on the quantum dot occupied the spin ground or the spin excited state [Elz04]. To do so, the Zeeman split quantum dot levels are aligned around the chemical potential of the reservoir, such that the electron can only exit the quantum dot if it occupies the spin excited state. After the electron tunneled out, the now empty quantum dot is filled again by another electron tunneling from the reservoir into the ground state. These tunneling events are detected with a charge sensor. The presence or absence of these tunneling events indicates the spin state of the electron. The energy selective readout requires a sufficiently large

Zeeman splitting to separate the two spin states such that thermal excitations are negligible. At typical Zeeman splittings of a few hundred µeV, this requires temperature of 1 K or below. Larger Zeeman splittings improve the readout by increasing the level separation, but also lead to faster spin relaxation.

Similarly, the spin information can be mapped onto the charge state with spin-dependent tunneling [Han05]. This enables for example to differentiate if two electrons on one quantum dot form a spin singlet or a triplet. Here, the tunnel couplings to the reservoir differ due to different orbital wave functions, giving access to the spin information through the timing of the detected tunneling events. Similar to the energy selective readout, also the tunnel rate selective readout is temperature sensitive due to the thermal smearing of the reservoir.

Spin-qubit readout via Pauli spin blockade [Pet05] allows to discriminate between singlet and triplet states of two electrons, based on the spin dependent interdot transition due to the Pauli exclusion principle. The crucial parameters for this technique to work are the control over the exact charge occupation of the DQD, the orbital level splitting, determined by the confinement of the QD, and the electron temperature. Typically, the orbital level splitting is on the order of a few meV, hence efficiently inhibiting lifting of the blockade by thermal excitations at typical experiment temperatures. Moreover, PSB is even suitable for qubit operation at elevated temperatures [Ono19; Pet20; Yan20].

All the aforementioned spin-to-charge conversions require the readout of the charge state, for which an on-chip electrometer [Han07], such as a quantum point contact or a single electron transistor, or gate recflectometry [Col13; Cri19; Wes19] can be employed. For spin-to-charge conversion based on Pauli spin blockade, also a readout in transport is possible. Here, the advantage is that it does not require additional on-chip structures or high-frequency electronics, yet it is incompatible with single-shot readout.

For qubits based on lateral quantum dots in two-dimensional heterostructures, commonly a sensor quantum dot is fabricated in close proximity to the quantum dot. In nanowires, however, this approach is less straightforward, yet it has been demonstrated for instance with Ge/Si core/shell nanowires [Hu07]. The charge readout via charge sensing requires a large enough bandwidth in order to resolve tunneling events as they occur during energy selective readout at the speed of the dot-to-lead tunneling rate. To increase the readout speed of the charge sensor, it is probed with a tank circuit attached to it, which is sensitive to the capacitance change of the quantum dot dependent on its charge state [Sch98; Lu03]. Changes of the quantum dot capacitance result in a damping of the resonant tank circuit. Similar, this reflectometry technique can also be applied directly by attaching the tank circuit to one of the gates that is capacitively coupled to a double quantum dot [Col13]. Tunneling inside the quantum dot system changes the quantum capacitance and leads to a dispersive shifts of the tank circuit's resonance frequency, which in turn leads to a phase shift and amplitude change of a reflected high-frequency signal. Recently, dispersive gate readout has reached the single shot readout regime [Pak18; Wes19; Urd19]. In particular for nanowires, where charge detection with an electrometer is challenging, this approach is straightforward, since it makes use of already present confinement gates and therefore reduces device complexity [Jun12; Hig14c; Vuk17; dJon19; Sab19].

3.5 Qubit Coherence and Relaxation

The lifetime of the qubit state sets an upper limit for the number of executable quantum gates, since after that time the information of the qubit is lost. Three timescales are important [Klo13a]: the spin relaxation time T_1, the spin coherence time T_2 and the dephasing time T_2^* of an ensemble measurement. The three timescales are related depending on the dominant relaxation or decoherence mechanisms, but usually it holds $T_2^* < T_2 \ll T_1$. For spin qubits, the dominant relaxation mechanism are interaction

with the lattice in combination with spin-orbit interaction, and the dominant decoherence channels result from spin-orbit and hyperfine interaction. Hyperfine interaction, however, is reduced for holes (see also section 2.3.4) and in materials with predominantly nuclear spin free isotopes, such as Ge and Si (see also section 2.2.1). Relaxation times are usually in the millisecond range [Hu12], and therefore less limiting for spin qubit operation.

The relaxation time T_1 can be measured with a pulsing scheme as depicted in Figure 3.5. Here, the qubit is pulsed into the excited state with a π_x pulse, following the initialization of the qubit in the ground state. Now, the probability of the excited state occupation as a function of the waiting time τ_{wait} after the π_x pulse decreases exponentially with the time constant T_1. From the decay curves, the relaxation time T_1 can be extracted.

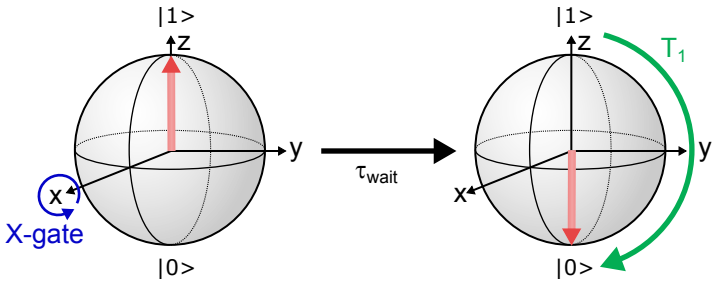

FIGURE 3.5 | **Qubit relaxation.** Pulse scheme for a measurement of the spin relaxation time T_1. After the initialization in the qubit ground state $|0\rangle$, a π_x rotation around the x axis drives the qubit into the excited state $|1\rangle$. After a waiting time τ_{wait}, the probability of the excited state $P_{|1\rangle}$ is measured. The probability decays exponentially with time constant T_1 due to relaxation into the ground state.

Qubit operation is typically limited by the coherence time. This limitation leads to, for instance, a decreasing amplitude of Rabi oscillations. In this case, however, the system is constantly excited by the microwave drive, thus the decay is not only given by the intrinsic decoherence, but can also be influenced by instrumental noise or pulse imperfections. For instance, frequency jitter or deviations from a step-function like onset of the microwave burst can lead to spurious spin rotations, which manifest as decay of the Rabi oscillation amplitude. Therefore, in a driven system, the intrinsic sources of decoherence can not be disentangled from decoherence induced by the environment.

A more meaningful determination of the qubit coherence is achieved by relying on the free evolution of the spin state, in absence of any external drive, in a Ramsey interferometry experiment. Figure 3.5 **a** depicts schematically the basic principle. The

qubit state, which was prepared in the ground state, is pulsed into the equatorial plane of the Bloch sphere with a $^{X}/_{2}$ gate, where it freely evolves for a time τ_{wait}. Afterwards, the qubit state is projected back onto the z axis with another $^{X}/_{2}$ pulse and the outcome is measured. Mainly two variations of this technique are used [Mau16; Nad10a]: First, the frequency detuning Δf of the $^{X}/_{2}$ pulses from the qubit resonance can be varied. This results in oscillations of the return probability as a function of the waiting time τ_{wait} with a frequency of Δf. An example pattern that results is shown in Figure 3.5 **b**. The amplitude of the oscillations decays on the timescale given by T_2, in this case 50 ns. Figure 3.5 **c** shows a linecut along the blue dashed line, depicting the oscillations with frequency Δf =50 MHz. The envelope function, given by the decoherence is shown in green. For long waiting times, the superposition of states $|0\rangle$ and $|1\rangle$ is completely decohered and the measurement outcome of any qubit state approaches the statistical value of 50 % for both basis states $|0\rangle$ and $|1\rangle$. For even longer waiting times, approaching the spin relaxation time T_1, the measurement outcome $P_{|1\rangle} \rightarrow 0$, since the qubit decays into the ground state $|0\rangle$. In the second variation, the phase ϕ of the second, resonant, $(^{X}/_{2})_{\phi}$ pulse can be shifted relatively to the first resonant $^{X}/_{2}$ pulse, which changes the rotation axis of the second pulse. Now, the probability oscillates as a function of the phase ϕ. In both cases, the amplitude of the oscillations decreases as a function of the waiting time τ_{wait} due to decoherence. Therefore, the decoherence time T_2^* can be determined from the envelope function of the oscillations, as shown by the green dashed line in Figure 3.5 **c**.

To extend the coherence of a qubit, a Hahn echo technique can be employed [Hah50; Kop08; Nad10a]. Here, the qubit state, prepared in one of the basis states, is first pulsed into the equatorial plane of the Bloch sphere with a $^{X}/_{2}$ pulse, as illustrated in Figure 3.7 **a**. The spin state then freely evolves for a time τ_{wait}, resulting in dephasing (see Figure 3.7 **b**). At this point, a refocusing X pulse is applied, which rotates the qubit state by π around the x axis, depicted in Figure 3.7 **c**. The state evolves again, but due

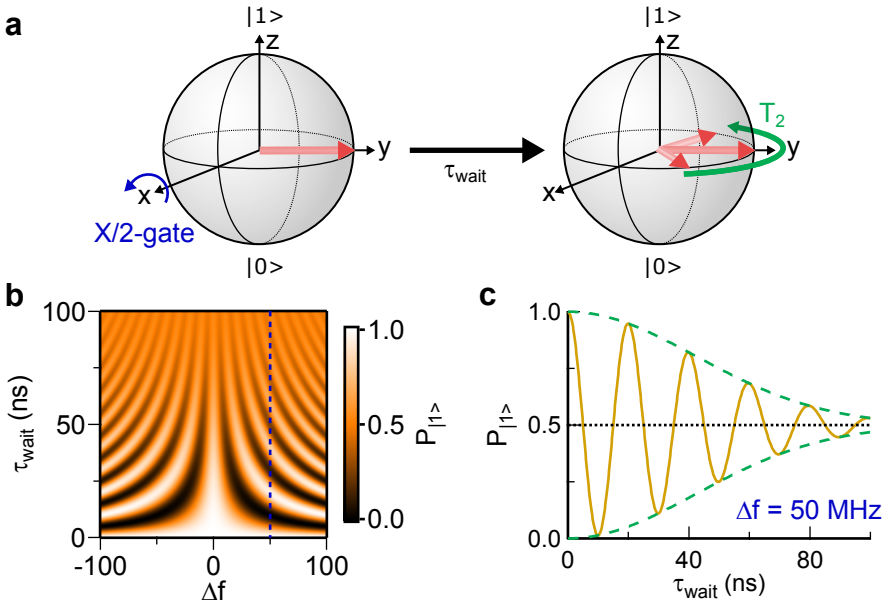

FIGURE 3.6 | **Ramsey interferometry.** **a** | Pulse scheme for a measurement of the spin coherence time T_2. The qubit is pulsed with a $^X/_2$ into the equatorial plane of the Bloch sphere, where it starts to decohere during the waiting time τ_{wait}. Afterwards, the qubit state is measured by applying a second $^X/_2$ pulse, which projects the spin state onto the z-axis. **b** | Probability to find the qubit in state $|1\rangle$ as a function of waiting time τ_{wait} and frequency detuning, with $T_2 = 50\,\text{ns}$. **c** | Linecut in **b** at a frequency detuning of $\Delta f = 50\,\text{MHz}$. Oscillations of $P_{|1\rangle}$ with frequency Δf are observed, as well as the decay of the amplitude due to the decoherence. The envelope function (green dashed curve) is given by the coherence time T_2^*.

to the π-rotation the dephasing now refocuses the spin state. Finally, in Figure 3.7 **d** and after a time τ_{wait}, a spin echo occurs with the dephasing being undone. The qubit state is projected onto the z axis with another $^X/_2$-pulse and the outcome is measured as function of the waiting time τ_{wait}. Again, an exponential decay of the return probability to the initial state is observed, but the decay time is given by the Hahn echo coherence time T_2^{Hahn}, which can be much longer than the inhomogenous dephasing time T_2^*. This is because the refocusing X-pulse reverses the dephasing which is caused by noise that is static on the time scale of the Hahn echo pulsing scheme. Therefore, the Hahn echo technique is very efficient for mitigating dephasing due to low frequency noise, that is for noise with dynamics slower than the qubit dynamics.

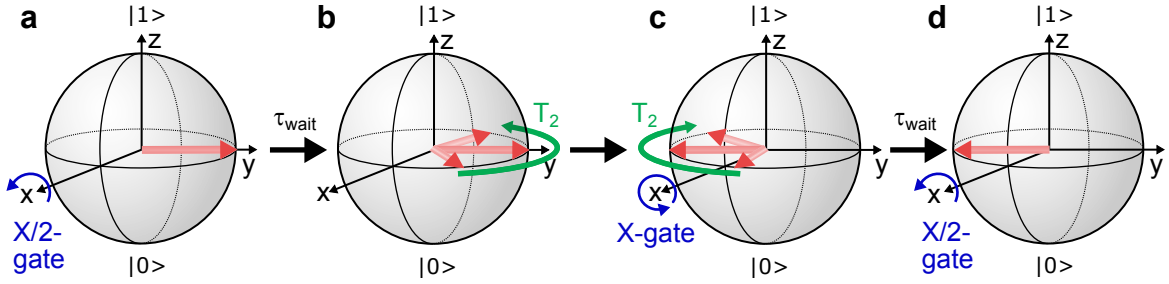

FIGURE 3.7 | **Hahn echo pulsing sequence. a** | After initializing the qubit in the ground state, a $^{X}/_{2}$-pulse is applied, aligning the qubit state in the equatorial plane of the Bloch sphere. **b** | During the free evolution for a time τ_{wait} the qubit state dephases. **c** | An X-pulse rotates the spin state by π and reverses the evolution of the spin state. Therefore, the spin state dephases in the opposite direction and refocuses. **d** | After the time τ_{wait} a spin echo occurs because the spin state is fully refocused. The readout is then accomplished with another $\frac{X}{2}$-pulse, which projects the spin state onto the z-axis.

The Hahn echo technique can be extended to a pulsing scheme with multiple X pulses in between the two $^{X}/_{2}$ pulses [Car54; Mei58], which leads to a dynamical decoupling of the spin, thus maintaining the coherent state longer. Depending on the noise source, these echo techniques allow to increase the qubit coherence by orders of magnitude, and furthermore enable frequency spectroscopy of the dominant noise sources [Pet05; Nad10a; Blu11; Mau16; Yon18].

Other approaches to prolong the coherence are the operation of the qubit at sweet spots [Hen20a; Wan19b], but it is self-evident that the qubit operation can be simplified if the qubit features long, inherent coherence times. Therefore, this motivates the investigation of more robust types of qubits [Rus17] as well as different material systems.

4 Fabrication of Quantum Dot Devices with Ge/Si Core/Shell Nanowires

Particular challenges arise when structuring semiconductors and metals at the nano- and microscale, but without any doubt, the technological capabilities of nanofabrication in modern cleanrooms have tremendously advanced over the past decades [Ste12b]. A variety of techniques have been developed which allow fabrication of nanostructures, such as nanowires, with diverse properties in terms of size, morphology and composition [Zha16]. The techniques can be distinguished in two categories: top down and bottom-up processes. Top-down processes pattern the micro- or nanostructure from bulk materials by means of lithography and etching. Bottom-up processes build up nanostructures from small building blocks, such as precursor gases, with the prime example of nanowires. Despite the advanced fabrication technologies, the demands of control over any device parameter are ever pushing the nanofabrication to its limits. Here too, the fabrication of quantum dot samples, as shown in this thesis, requires profound control over chemical as well as physical processes.

This section provides an overview of the most relevant fabrication processes used for the work presented in this thesis. To begin with, section 4.1 describes the growth of Ge/Si core/shell nanowires of high quality in terms of properties like crystal defect density and charge carrier mobility. Next, section 4.2 describes the main steps of the fabrication of devices that can host a user-defined number of quantum dots or qubits in a Ge/Si nanowire. The particular challenge at this juncture is described in section 4.3, which is the fabrication of a narrowly spaced array of gates in order to provide electrostatic confinement of holes. Another important component of the devices is the dielectric material used for electrical insulation. While the devices described in this thesis use Al_2O_3 as gate dielectric, other insulating materials, as described in section 4.4, promise interesting implications on the device performance. Despite not being discussed in the

main part of this thesis, section 4.5 briefly reviews the fabrication of hybrid quantum dot-resonator devices, where a Ge/Si nanowire will be coupled to a superconducting resonator.

4.1 Growth of Ge/Si Core/Shell Nanowires

This section reviews the most important steps of the synthesis of Ge/Si core/shell nanowires. More details regarding the nanowire growth can be found elsewhere [Con17]. The nanowires that were used in this thesis have been grown by Ang Li and Erik Bakkers at the Eindhoven University of Technology[1,2].

The Ge/Si core/shell nanowires are grown in a three step vapour-liquid-solid (VLS) growth process within a metal-organic vapor phase epitaxy (MOVPE) system [Con17]. The growth of nanowires from a vapor phase is a well established process for obtaining nanowires with high control over their morphology and electronic properties. An Au nanocluster with a diameter of about 10 nm catalyzes the growth process and the volatile precursors GeH_4 and Si_2H_6 provide the material for the nanowire crystallization.

To begin with, the Au droplets are dispersed on top of a $\langle 111 \rangle$ Ge substrate and subsequently heated close to the eutectic temperature inside the MOVPE reactor. Then, in the first step, a Ge nanowire is grown at 320 °C by admitting the gaseous precursor GeH_4 into the growth chamber. The growth process starts with the precursor condensating on the surface of the Au nanocrystal and subsequently decomposing into its constituents [Wu01]. The incorporation of Ge dilutes the Au droplet, the two materials form an alloy, and the droplet grows in size and liquifies. Due to the increasing Ge content, the alloy composition moves away from the Au-Ge eutectic point, and at

[1]Department of Applied Physics, Eindhoven University of Technology, P.O. Box 513, 5600 MB Eindhoven, The Netherlands

[2]QuTech and Kavli Institute of Nanoscience, Delft University of Technology, 2600 GA Delft, The Netherlands

a point of critical supersaturation the nucleation of a Ge nanocrystal begins. With further supply of Ge precursor, which keeps dissolving in the droplet and maintains the alloy composition, more Ge precipitates at the liquid-solid interface of the droplet and the axial growth continues layer by layer. In the VLS process, the nanowire diameter (typically around 20 nm) is controlled by the size of the Au droplet at growth conditions, which is larger than that of the pristine Au nanocrystal due to the presence of Ge in the eutectic. The length of the nanowire is controlled by the duration of this growth step and can reach typically a few µm. To avoid radial growth of the nanowire, which would lead to tapered nanowires, HCl is admixed to the precursor gas during the Ge nanowire growth. The addition of HCl has two effects: firstly, it prevents the diffusion of Au into the nanowire and, secondly, forms a different compound with the precursor of the form of $GeCl_x$ which can only be decomposed inside the Au droplet but not on the sidewalls. Therefore, uncatalyzed, radial nanowire growth is suppressed [Pot11; Con17].

In the next step, the precursor Si_2H_6 is admitted into the chamber in order to grow an axial Si separation segment, which pushes away the Au catalyst droplet from the as-grown Ge nanowire [Con17]. This extra segment further prevents diffusion of Au atoms into the Ge core, which is pronounced at temperatures as high as needed for Si shell growth [Day11]. Therefore, Ge nanowires with a Si separation segment grown at low temperature incorporate less Au impurity in the final Ge/Si nanowire, because the Si segment acts an energetic barrier for the Au diffusion.

In the third and last step of the process, the Si shell is grown by admitting the precursor Si_2H_6 into the chamber at 690 °C. At this temperature, which is much higher than during the previous steps, the decomposition of Si_2H_6 takes place non-selectively at all surfaces, leading to the growth of a conformal Si shell. The adjustment of temperature and Si_2H_6 partial pressure dictates the quality of the Si shell [Gol08a; Gol09].

Generally, the growth parameters such as temperature, partial pressures and chemical

species employed influence the morphology and crystallinity of the resulting nanowires, which in turn determine their electronic properties. For instance, the hole mobility of Ge/Si core/shell nanowires correlates with the crystal orientation, and is known to be maximum along the [110] direction [Con17]. Furthermore, the nanowire orientation typically depends on the radius [Gol09; Sch05], with the [110] orientation being preferred for Ge nanowire radii below 10 nm. The radius of the nanowire in turn is influenced by the size of the Au catalyst. Therefore, such complex interdependencies need to be taken into account in order to control the relevant nanowire characteristics and finally electronic properties.

4.2 Fabrication of Quantum Dot Samples

This section describes the fabrication of a typical sample that can host quantum dots in a Ge/Si core/shell nanowire. These devices are the basis for all experiments shown in this thesis. Most steps involve standard e-beam lithography processes with poly-methyl methacrylate (PMMA) as resist [Ste12b]. Particular challenges in the fabrication process are the production of clean heterostructures, to mitigate electrical noise, and good electrostatic confinement, aiming for the confinement of only a single hole. Process details to each step are listed in the appendix. Figure 4.1 shows a scanning electron micrograph of a finished quantum dot sample. In the follwing, the main steps of the fabrication process for such a device are described.

The fabrication starts with an off-the-shelf Si wafer. Different types of wafers were used, which are either intrinsic or heavily p^{++} doped silicon. The doped wafers comprise a 290 nm thick layer of thermal oxide SiO_x on top. The intrinsic silicon wafers are used with just the thin layer of native oxide. First, a marker grid with 200 nm edge length is patterned with UV lithography and subsequently metallized. Next, another set of markers for smaller structures and parts of the gate fan-out are patterned by electron beam lithography. These smaller markers are necessary for the fabrication of the finger

gates, which is described in detail in the next section 4.3. In a last electron beam lithography step, the bond pads and other metallic on-chip connections are patterned. On top of the finger gate structure and serving as a dielectric and insulating layer, roughly 20 nm of aluminum oxide Al_2O_3 are grown by atomic layer deposition. More details about the material choice and properties of the dielectric layer are discussed in section 4.4.

The next and last part of the fabrication is the placing and contacting of a Ge/Si core/shell nanowire. For this purpose, a single nanowire is picked up from the growth chip with a micromanipulator and placed deterministically across the set of finger gates [Flö11]. As nanowires with different crystal orientations grow all on the same chip, it is practical to distinguish them by the direction in which they grow, and only choose the thinnest wires. This is in order to increase the probability of transfering a nanowire with high mobility and good electrical properties, as discussed in section 4.1. After the transfer, the nanowire is contacted in another electron beam lithography step. Before metallization with a thin layer of Ti and a thick layer of Pd, the native oxide of the nanowire is removed in a short etch with hydrofluoric acid (HF). In this last step, special attention is paid to the adhesion of the resist to the surface of the chip, since the etch in diluted HF and the accompanying rinse in water can easily harm the mask and, in the worst case, destroy it. Therefore, an adhesion promoter and a more resilient PMMA/MMA resist are used for this lithography step. The adhesion promoter reacts with the substrate surface and forms a stable, hydrophobic layer, which improves the adhesion of the resist and prevents underetching, too [All20e]. Finally, the lift-off is performed in a bath of warm acetone.

Some samples feature an additional set of gates on top of and perpendicular to the finger gates, as seen in Figure 4.1. These side gates can be used to apply an additional electric field without changing the confinement potential of the quantum dot. However, in the main part of this thesis they were not used and left grounded. Section 10.1 of

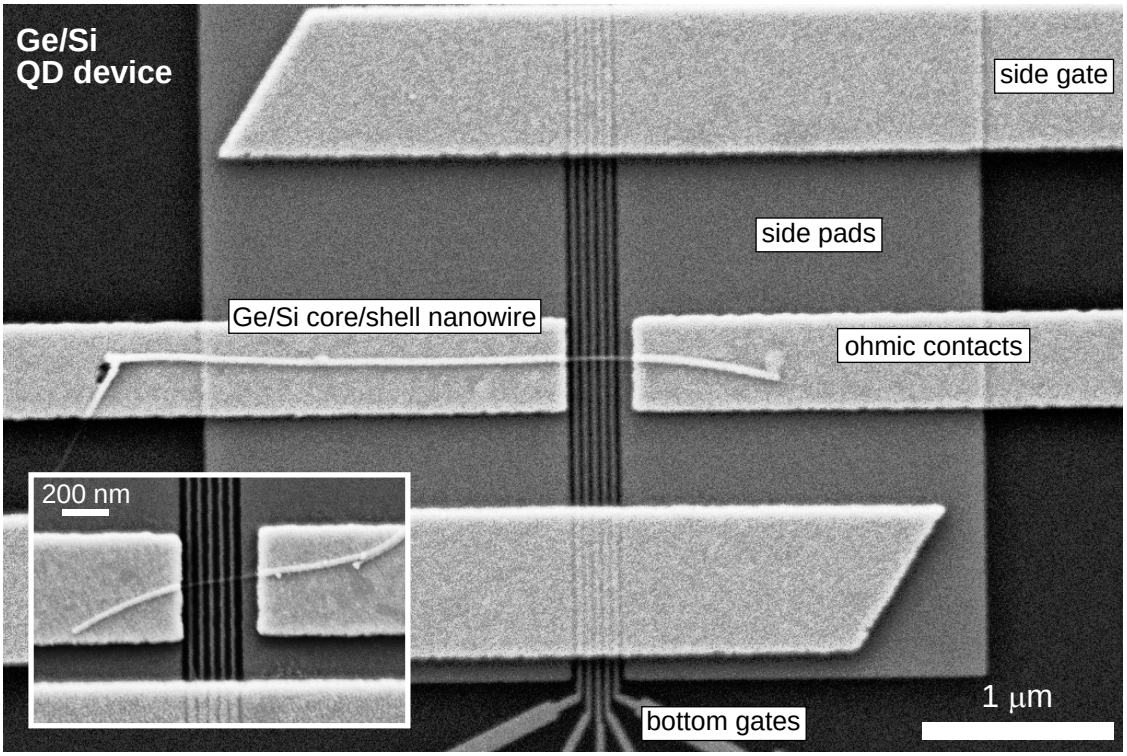

FIGURE 4.1 | **Ge/Si core/shell nanowire quantum dot device.** Scanning electron micrograph of a finished quantum dot sample. The five finger gates (vertical lines) are fabricated as described in section 4.3. The nanowire (center) is placed across the finger gates with a micromanipulator. Ohmic contacts to the nanowire are defined on either side by electron beam lithography. Additional side gates (horizontal topmost and bottommost structures) are fabricated for further experiments not described here. The inset focuses on the part of the nanowire above the finger gates of a different device.

the outlook discusses potential applications of these gates in future experiments.

4.3 Finger Gates with Narrow Pitch

This section describes the process which was developed in order to fabricate a set of narrowly spaced finger gates which electrostatically confine quantum dots in Ge/Si core/shell nanowires. The predominant challenge is to decrease the distance between adjacent gates in order to provide a good enough confinement for single holes in the nanowire. The following paragraphs outline the most important aspects of the process, which enables the fabrication of gates with 50 nm pitch (defined as the center to center distance of neighbouring lines) with a standard 30 kV electron beam patterning system from Raith. The final result can be seen in Figure 4.2 and technical details of the process can be found in the appendix.

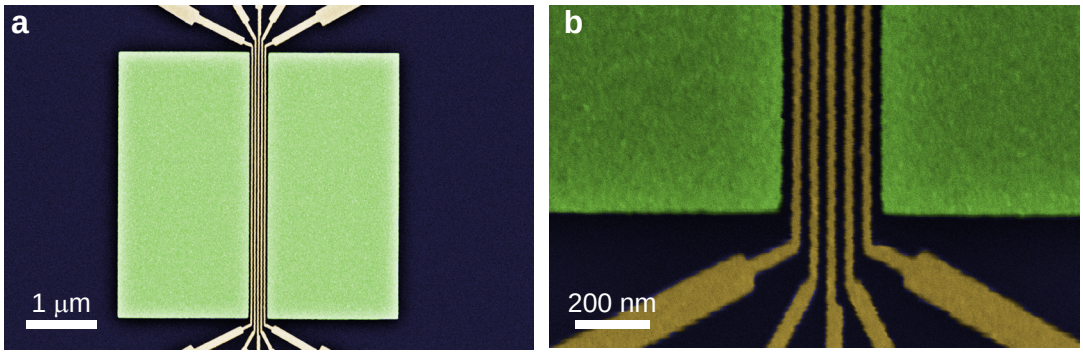

FIGURE 4.2 | **Finger gates with narrow pitch.** Colorized scanning electron micrographs of an array of five finger gates with additional side pads to support the nanowire on the sides. The gate pitch in this case is 50 nm and the side pads are 50 nm away from the outermost gates.

Resist For the fabrication of finger gates, a thin, single layer of standard PMMA with a molecular weight of 950 kDa is used. The final thickness of the resist layer should be roughly 45 nm to 50 nm after baking. This ensures that the exposed resist volume remains small, as the beam broadening due to forward scattered electrons becomes more pronounced after interacting with a thick resist layer (compare the line profile in Figure 4.3 **a**). Furthermore, the thin resist reduces the risk of collapse of the patterned

PMMA, which more likely for a high aspect ratio. Lastly, the resist layer thickness is an important parameter to consider in the process due to the proximity effect caused by backscattered electrons. These get scattered at large angles inside the substrate, and lead to resist exposure far from the point of incidence of the electron beam. Figure 4.3 **a** depicts traces of backscattered electrons at two different electron beam energies, based on Monte-Carlo simulations [Kys75], illustrating the resist exposure in the proximity of the patterned areas. Backscattering of electrons becomes more relevant for denser structures and is especially pronounced for the high acceleration voltages used here, as explained next.

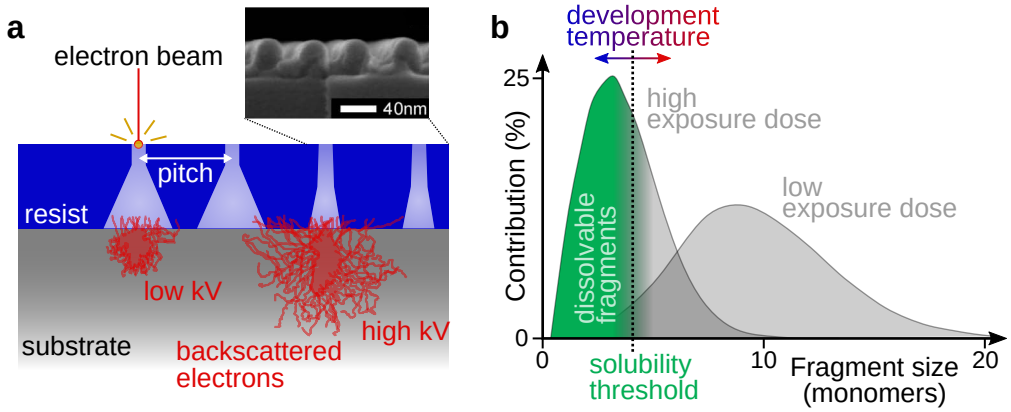

FIGURE 4.3 | **Electron beam lithography of finger gates. a** | Schematic of electron beam lithography of narrowly spaced lines in a cross sectional view. The light blue areas illustrate the area inside the resist (dark blue) that is exposed by the incident electron beam. In red are depicted simulated trajectories of backscattered electrons. The inset shows the resist profile of a 50 nm pitch grating [Ste10]. The schematics are based on simulations of the beam profile and electron trajectories in [Kys75; Ste10]. **b** | Effect of temperature on the dissolution of PMMA fragments during resist development. The solubility of PMMA in the developer decreases exponentially with fragment size and temperature. The probability distribution of PMMA fragment size depends on the exposure dose, with a narrower distribution centered at smaller average fragment size at higher exposure dose. Schematic is based on calculations in [Akt06].

Electron Beam Exposure For electron beam patterning of the gate structure, the acceleration voltage is set to the highest available value of 30 kV in order to reduce the undercut. Such undercuts stem from beam broadening due to deflection of forward

scattered electrons, and are more pronounced for low acceleration voltages. Figure 4.3 **a** schematically depicts the effect of the acceleration voltage on the spatial profile of the exposed areas (light blue) inside the resist (dark blue) for two different acceleration voltages. At low electron beam acceleration voltage, the beam broadens more due to forward scattering of primary electrons, and the broad beam profile results in a larger undercut. For higher acceleration voltages, the beam profile is much narrower with a smaller undercut. While the absence of an undercut inhibits a proper lift-off, a too large undercut, as it arises from low electron beam energies and thick resist layers, would ultimately lead to a collapse of the mask of structures as dense as required here [Ste10]. The choice of high acceleration voltage requires a high exposure dose of typically around 3000 pC/cm due to the low sensitivity of PMMA at large electron energies. The increased dose ensures that enough electrons are interacting with the PMMA and scissor the molecule chains into short enough fragments to be dissolved in the subsequent development step. As a positive side effect, the distribution of fragment size narrows down and is centered at lower average fragment size for increasing exposure dose [Akt06]. Figure 4.3 **b** shows the probability distribution as a function of the PMMA fragment size for two different exposure doses. At lower dose, the molecule fragments are typically longer and the size distribution is broader. At higher exposure dose, the PMMA fragments are more uniform and shorter.

Development After patterning, the resist is developed at a temperature of −15 °C, which is a sweet spot in terms of achievable resolution with PMMA resist [Cor07] and is understood as a point of optimal interplay between exposure dose and PMMA solubility. The effect of the electron beam is to break apart the long PMMA molecules into smaller, better soluble fragments. The resist solubility in the developer is a diffusion based process and thus is exponentially suppressed with decreasing temperature and increasing molecule length. At room temperature, typically PMMA fragments

shorter than ten monomers are dissolved during resist development [Akt06]. Therefore, at low development temperatures, partially exposed resist with longer molecule fragments does not dissolve, but "freeze" [Moh10]. Since partially exposed resist mostly occurs at the edges of trenches and far away from the incident point of the electron beam, that is at the outer edges of the beam profile inside the resist, the development at low temperature increases the resolution [Cor07] and the pattern quality [Hu04]. Figure 4.3 **b** schematically depicts the interdependence of development temperature and exposure dose. A lower development temperature moves the limit of maximum solvable fragment size to smaller values, therefore requiring a larger exposure dose in order to dissolve a substantial amount of PMMA fragments during the development. In turn, the increased exposure dose leads to a narrower probability distribution of fragment sizes, as discussed above. The alignment of the solubility threshold, indicated by the vertical dashed line in Figure 4.3 **b**, and the probability distribution of PMMA fragment size is the objective of process optimization. At temperatures above the optimum, too much of the resist is developed. Temperatures below the optimum, in turn, require such a high exposure dose, that PMMA cross-linking dominates over molecule scissoring, hence making the lithography process impossible. In conclusion, the sweet spot at $-15\,°C$ for PMMA development is the optimum between PMMA solubility and cross-linking. Finally, the addition of methyl ethyl ketone to the developer helps to increase the dissolution rate and to remove PMMA residues [Ber92].

Metallization In the last step, the mask is metallized following a short reactive ion etch cleaning in an O_2 plasma, which improves the cleanliness and quality of the trenches. Figure 4.4 demonstrates the line broadening after of a short etch of a few seconds as indicated. This step therefore needs careful optimization with the exposure dose and development temperature. Afterwards, a Ti/Pd metal stack with a total thickness of 15 nm is evaporated onto the mask in an electron beam evaporator. Finally, the mask lift-off is performed in a warm acetone bath.

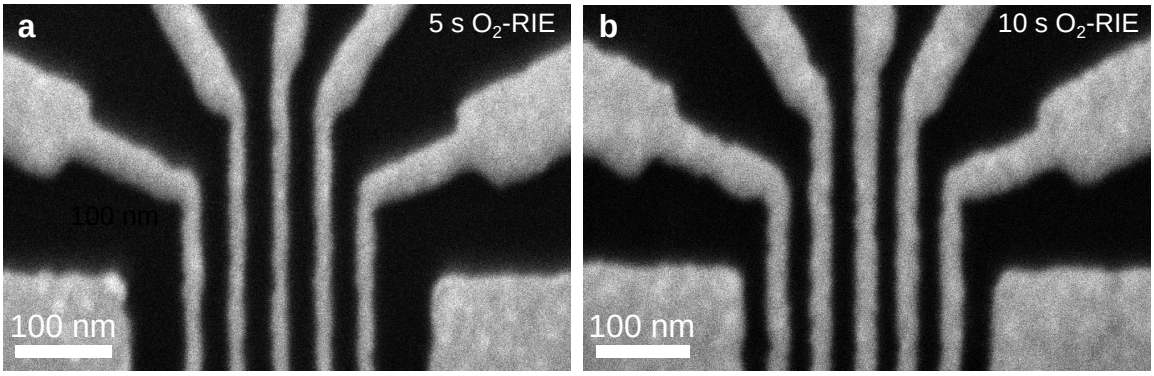

FIGURE 4.4 | **Line broadening due to reactive ion etching.** Scanning electron micrographs of finger gates, including a short reactive ion etch in an O_2 plasma after resist development. The etch cleans the trenches from resist residuals and leads to a line broadening, depending sensitively on etch duration. In both cases shown here, the exposure dose and development temperature were the same, but the mask was etched for **a** | 5 s in and **b** | 10 s prior to metallization.

The process described above is capable to yield parallel, metallized lines with a pitch of 50 nm as shown in Figure 4.2. The gates are accompanied by side pads, highlighted in green in Figure 4.2, which help to prevent bending of the nanowire next to the finger gates. Note that these additional, large areas in close vicinity to the finger gates require precise adjustment of the exposure dose due to the pronounced proximity effect.

4.4 Material Choices for the Gate Dielectric

Quantum states are very fragile and susceptible to any disturbances from the environment. Not only the host material, in this case the Ge/Si nanowire, but the entire device comprising layers of semiconductors, metals and oxides can be a source of undesired effects such as gate leakage or charge noise. In this section, different choices of the substrate and the gate dielectric are reviewed. More details, measurements and considerations regarding the implementation in the existing fabrication process of Ge/Si nanowire samples can be found in [Mül19].

All the devices that were used for measurements in this thesis use a roughly 20 nm thick layer of Al_2O_3 as a dielectric layer between the finger gates and the nanowire. It

is grown by atomic layer deposition (ALD), which is a technique routinely used to grow very thin films with numerous applications in micro- and nanofabrication. The basic working principle is the formation of one atomic layer per cycle by having first two precursors each uniformly covering the surface and then chemically reacting with each other to form one layer of the desired film material. The precursors are sequentially admitted into a vacuum chamber, which is heated to the process temperature of typically a few hundred °C. This relatively low temperature, compared to other chemical vapour deposition techniques, is one of the main advantages of ALD [Ste12b]. Other advantages are the growth uniformity even on complex topologies, and the self-limitation, yielding precise control over the film thickness [Les02].

The use of ALD grown Al_2O_3 is very straightforward, is commonly used especially for silicon based structures due to its passivation effect [Din10], and has the additional advantage of being easy to process, as it is etched very well by hydrofluoric acid. However, interface effects at boundaries of Si, SiO_2 and Al_2O_3 are pronounced and complex [Spr18]. For instance, a negatively fixed charge layer is formed at the SiO_2/Al_2O_3 interface, which on the one hand can be exploited for depletion mode quantum dot devices [Ami18], but at the same time can lead to unintentional remote doping of the nanowire and can act as a source of charge noise. In a system with strong spin-orbit interaction such as Ge/Si nanowires, this acts as a source of decoherence, too. In conclusion, the impact of ALD grown Al_2O_3 on the performance of Ge/Si quantum dot devices remains unclear [Mül19], as well as possible qualitative improvements through annealing or ozone cleaning of the oxide [Spr18].

An alternative candidate to Al_2O_3 is hafnium oxide HfO_2, a high-k dielectric which is also considered as a replacement of SiO_2 in semiconductor industries [Wil01; Rib05]. Just as Al_2O_3, it can be deposited by an ALD growth process in very high quality, and due to the larger dielectric constant the thickness could be reduced while maintaining the same capacitive coupling of the gate. So far, the performance of Ge/Si devices

using HfO_2 in comparison to devices using Al_2O_3 remains unclear due to the lack of experiments regarding improved or deteriorated properties [Mül19]. Finally, HfO_2 can also be combined with Al_2O_3 in a more complex stack of oxides, which inhibits the formation of the fixed charge layer [Sim15; Buc05].

A very different approach is the usage of few-layer hexagonal boron nitride (hBN) flakes as a dielectric. Its valuable properties are well recognized in graphene research [Dea10] and, despite adding complexity to the fabrication process, it has been successfully integrated into quantum dot devices [Wan19a]. Typically, hBN is exfoliated from a crystal. Single flakes with variable thickness, ranging from one monolayer and to several nanometers, are then transferred onto the substrate [Nov04; Dea10; Mül19]. Figure 4.5 shows two microscope images of a Ge/Si nanowire device, fabricated as described in section 4.2 but with an hBN flake as insulating layer between the finger gates and the nanowire. First measurements of quantum dots formed in such a device, however, were limited by gate leakage [Mül19].

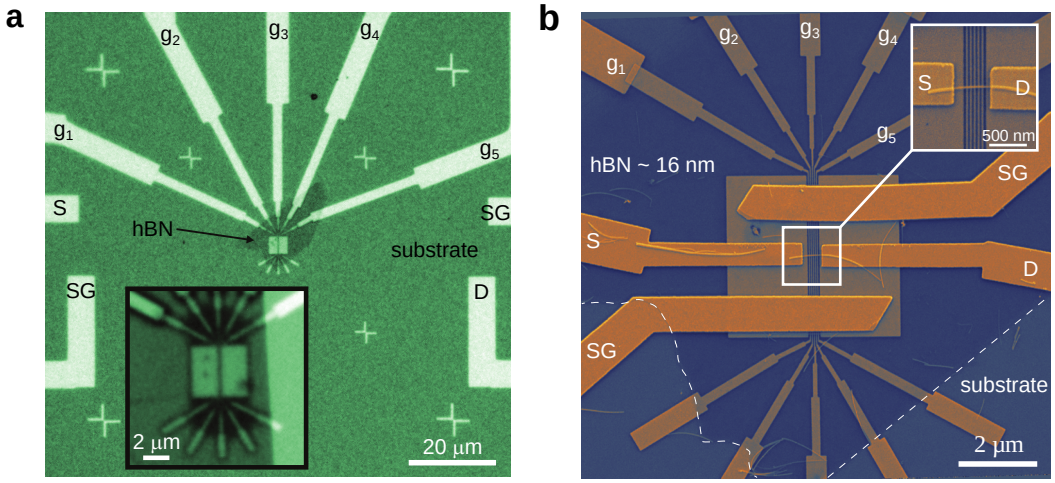

FIGURE 4.5 | **Ge/Si nanowire device using hBN as dielectric. a** | Optical microscope image of the device after transfer of the hBN flake onto to the finger gate structure. **b** | Scanning electron micrograph of the finished quantum dot device. After the flake transfer, a Ge/Si nanowire is transferred onto the gate structure and contacted as described in section 4.2. The outline of the flake is emphasized by the white, dashed line. Images adapted from [Mül19].

4.5 Hybrid Systems: Superconducting Resonators with Integrated Nanowire Quantum Dot

A key milestone in the development of a functioning quantum computer architecture is the implementation of long range interactions between distant qubits. One candidate for mediating the interaction is the photon electric field of a superconducting microwave resonator [Klo13a]. Figure 4.6 **a** shows an optical microscope image of an array of SQUIDs (superconducting quantum interference device), which forms a resonator with a resonance frequency in the GHz regime [Mas12; Cas07; Sto17]. At the bottom part, a Ge/Si quantum dot is placed and coupled via one of the plunger gates to the resonator. The inset shows a scanning electron micrograph of the quantum dot structure, which is fabricated according to the description in section 4.2. The SQUID resonator is fabricated in the group of Andreas Wallraff[3] at ETH Zürich.

Figure 4.6 **b** shows a different type of device which consists of a transmission line resonator made from a thin, superconducting NbTiN film [Kro19]. The resonator is fabricated in the group of Christian Schönenberger[4].

The fabrication of such hybrid devices is still ongoing and no measurements have been performed so far. More details regarding the importance and prospects of such devices are discussed in section 10.3.

[3]Department of Physics, ETH Zurich, CH-8093 Zurich, Switzerland
[4]Department of Physics, University of Basel, Klingelbergstrasse 82, 4056 Basel, Switzerland

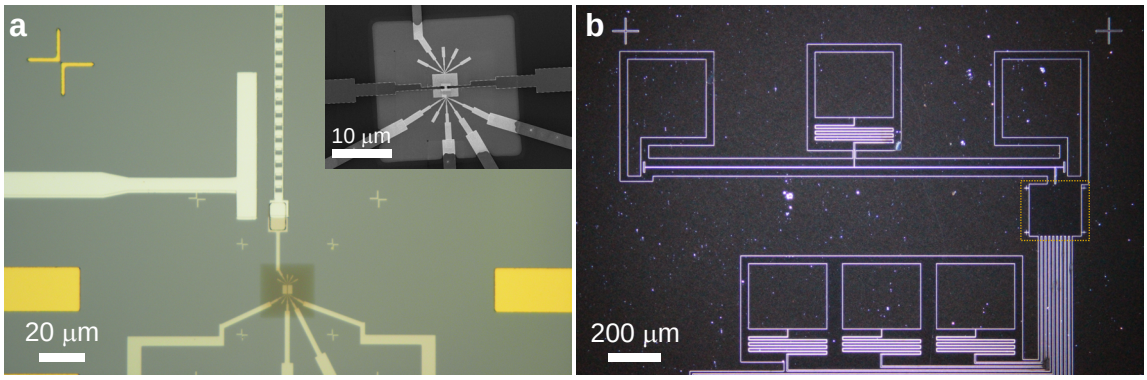

FIGURE 4.6 | **Fabrication of hybrid resonator-qubit devices. a** | Optical microscope image of a SQUID resonator with integrated Ge/Si nanowire quantum dot device. The inset shows a scanning electron micrograph of the quantum dot area. Image by courtesy of Pasquale Scarlino. **b** | Dark field, optical microscope image of a NbTiN resonator. The empty area at the center right (encircled by the dotted rectangle) is where the quantum dot structure will be fabricated, similar to the inset of **a**. Image by courtesy of Jann Ungerer.

5 Qubit Measurement Setup

This section briefly describes the setup that was used in this thesis for the operation of a hole spin qubit in a Ge/Si core/shell nanowire. The transport measurements presented in sections 6 and 7, were performed in a variable temperature insert (VTI) with a base temperature of 1.4 K. For the experiments performed in the VTI, only low-frequency wiring for direct current (DC) measurements were used. However, a key requirement for qubit operation is the application of radio-frequency signals, in order to realize the various qubit operations discussed in section 3. Such a setup and its main parts are outlined in the next section. This setup is used for the measurements discussed in section 8.

5.1 A Dilution Refrigerator with High-Frequency Electronics

The setup is based on a dry dilution refrigerator from Bluefors Oy [Blu20]. In comparison to wet systems, which require cooling with liquid helium, dry systems offer the advantage of more experimental space and lower maintenance. Furthermore, the system is equipped with a 8-4-1 T vector magnet and a bottom-loading insert which allows for fast sample exchange.

Figure 5.1 schematically shows the various electronic components that are relevant for the measurements discussed in section 8. From room temperature control electronics, which are discussed in the next section, a number of coaxial lines and DC lines are running through the various temperature stages and are finally thermalized to mixing chamber temperature. In total, eight semi-rigid coaxial lines made of silver-plated cupronickel are mounted in the setup. Out of those, three are used for qubit operation, and the remaining ones are available for other purposes such as gate-reflectometry. The coax lines are thermalized at the temperature stages of the dilution refrigerator with attenuators as indicated in Figure 5.1. Thermocoaxes with a total resistance of 150 Ω

at room temperature were used as DC lines because of their enhanced thermalization performance while also serving as an efficient low-pass filter. The DC lines connect the break-out-box via a Pi-filter with 300 pF with the wiring inside the refrigerator. At the mixing chamber the lines are filtered and further thermalized by microwave filters [Sch14; Bas20a] with a capacitance to ground of 7 nF.

Below the mixing chamber, the exchangeable sample probe (puck) inside a bottom-loading exchange mechanism is attached. The puck comprises a printed circuit board (PCB) containing the sample, as well as a filter PCB which filters the DC lines with two surface mounted components (SMC) *RC*-filters in series. From the filter board, a ribbon cable is connecting the DC lines to the sample PCB where, after another low-pass filter, the lines connect to the sample via bond wires. Inside the puck, flexible coax lines are used to connect the RF lines from the mixing chamber-puck interface to the sample PCB. There, the coax lines are combined with three of the DC lines, and can thus be used as fast gates on the sample.

Note that the setup is also equipped with a gate reflectometry setup, but since it was not used in this thesis it is omitted in Figure 5.1. Details and characterization of the complete setup, including the gate reflectometry, can be found in reference [Cam19].

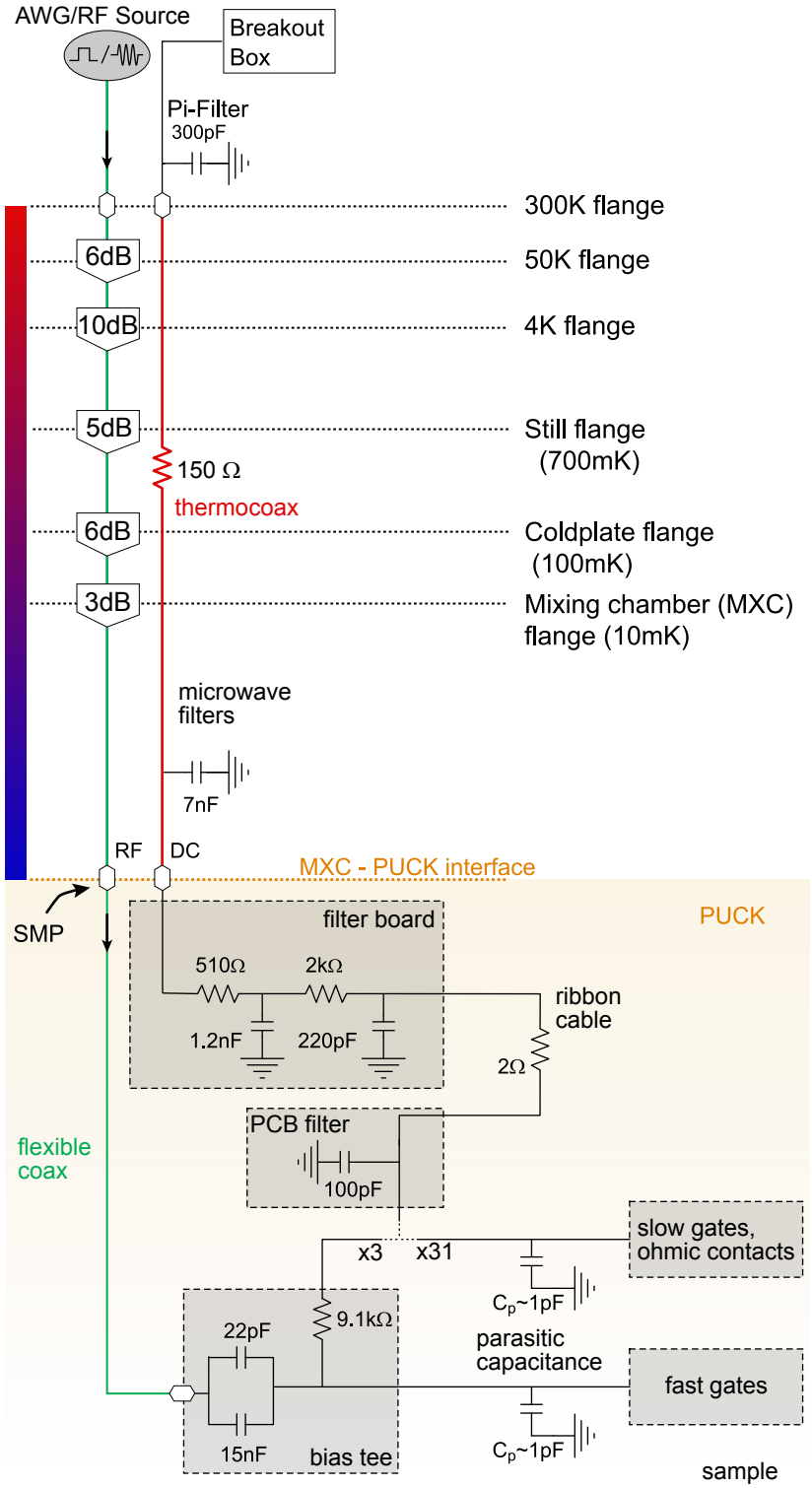

FIGURE 5.1 | **Wiring schematic of the setup.** The electric setup inside a dry dilution refrigerator features three coax lines (green) and 34 DC lines (red). Inside the puck, the DC lines are routed via a filter board to the main PCB which contains the sample and combines both the DC and the RF part of the setup. Three DC lines are combined via bias tees with the RF lines, thus enabling fast gates on the sample. The other 31 DC lines are available for DC biasing or gating the sample. Adapted from [Cam19].

5.2 Electronics for Qubit Control

This section discusses the room temperature electronics that is used in order to control the qubit. For qubit operation, three main types of voltages are necessary: quasi-static DC voltages, square pulses and microwave bursts. Quasi-static DC voltages control the confinement and the bias voltage on the quantum dots. Square pulses are applied to the plunger gates of the quantum dots in order to pulse to different positions in the charge stability diagram. Finally, controlled microwave burst drive spin rotations via electric dipole spin resonance. The difficulty of a qubit setup is due to the need of precisely timed, nanosecond microwave burst. In particular, for very fast qubits, clean microwave burst with burst times $< 10\,\text{ns}$ are necessary, since for instance a Rabi frequency of 100 MHz results in a $\frac{\pi}{2}$-gate pulse length of only 5 ns. In the framework of this thesis, two different setups were used, which differ in the way the microwave bursts are generated and controlled. The two setups are schematically illustrated in Figure 5.2. In both cases, the DC voltages are provided by an eight-channel digital-analog-converter (DAC) with low noise and high resolution from BasPI [Bas20b]. The voltages are then routed via the DC wires to the sample on the PCB as described in section 5.1. Transport through the nanowire is measured with a BasPI low-noise high-stability (LNHS) I/V converter attached to the drain lead of the nanowire sample. The measurement signal is measured with a Signal Recovery Lock-in model 7265, which modulates the RF signal generator output at the lock-in frequency. By demodulating the measurement signal from the sample, the lock-in measures the difference in current through the nanowire when the RF signal is applied and blanked. The square voltage pulses are generated by an arbitrary waveform generator (AWG). Two different models of AWGs were employed: a two-channel Tektronix AWG7122C in Figure 5.2 **a** and an eight-channel Tektronix AWG5208 in the setup of Figure 5.2 **b**.

The main difference between the two setups shown in Figure 5.2 is the manner of chopping the RF signal generated by the Keysight model E8257D (model E8267D)

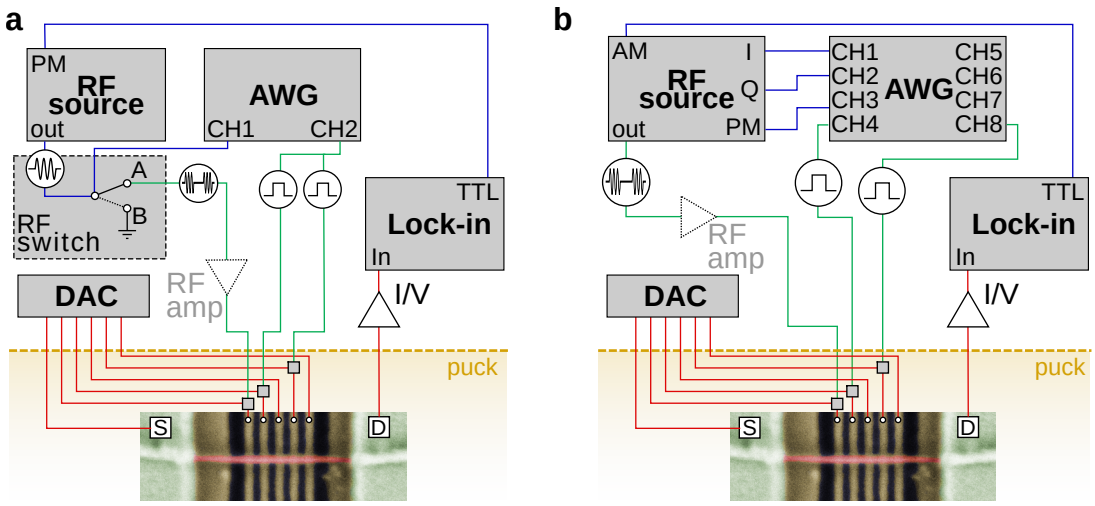

FIGURE 5.2 | **Room temperature circuitry.** The room temperature circuitry for qubit control comprises a DC part and a RF part. DC voltages are generated with a low-noise high-resolution DAC and the transport through the double quantum dot is measured with a low-noise high-stability I/V converter and a lock-in. The RF part consists of an AWG for square voltage pulse generation and a RF signal generator. The two setups differ in the way the microwave burst are generated. **a** | In this setup, a RF-switch is triggered by the AWG and chops the continuous wave RF signal from the source. **b** | Here, a vector signal generator is used, which allows for IQ modulation of the RF signal. Another output channel of an eight-channel AWG is used to control the the pulse modulation input. Note that in both setups **a** and **b** an optional RF amplifier can be inserted into the circuit, yielding an additional gain of microwave power of 45 dB. Furthermore, in the measurements shown in this thesis, one of the tree coaxial lines was not functional.

signal generator in figure 5.2 **a** (in figure 5.2 **b**). In Figure 5.2 **a**, the second output channel of the AWG controls a RF switch (ZASWA-2-50DRA+ from MiniCircuits), which chops the continuous wave RF signal into microwave bursts of desired length. Note, that here the reference signal from the lock-in gates the pulse modulation (PM) input of the signal generator and the AWG triggers the RF switch. Conversely, the roles of the AWG trigger and the lock-in reference signal can be swapped, too.

In the setup shown in Figure 5.2 **b**, the use of a vector signal generator allows for control over the phase of the microwave signal via IQ modulation. In this case, three AWG output channels control the I, Q and PM inputs of the signal generator, which generates the microwave bursts. The lock-in reference signal, which modulates the RF

output, is connected to the amplitude modulation (AM) input of the signal generator.

In both setups of Figure 5.2, optionally a RF amplifier can be inserted into the circuitry. This amplifies the available microwave power with a gain of 45 dB, which becomes necessary in case of a technically limited low level of output power of the signal generator. In particular, in combination with high attenuation inside the refrigerator, which is used for good thermalization, this additional gain in microwave power proves useful.

6 Single, double, and triple quantum dots in Ge/Si nanowires

F. N. M. Froning, M. K. Rehmann, D. M. Zumbühl, F. R. Braakman

Department of Physics, University of Basel, Klingelbergstrasse 82, 4056 Basel, Switzerland

J. Ridderbos, M. Brauns, F. A. Zwanenburg

NanoElectronics Group, MESA+ Institute for Nanotechnology, University of Twente, P.O. Box 217,7500 AE Enschede, The Netherlands

A. Li, E. P. A. M. Bakkers

Department of Applied Physics, Eindhoven University of Technology, P.O. Box 513, 5600 MB Eindhoven, The Netherlands

QuTech and Kavli Institute of Nanoscience, Delft University of Technology, 2600 GA Delft, The Netherlands

Abstract

We report highly tunable control of holes in Ge/Si core/shell nanowires. We demonstrate the ability to create single quantum dots of various sizes, with low hole occupation numbers and clearly observable excited states. For the smallest dot size we observe indications of single-hole occupation. Moreover, we create double and triple tunnel-coupled quantum dot arrays. In the double quantum dot configuration we observe Pauli spin blockade (PSB). These results open the way to perform hole spin qubit experiments in these devices.

This chapter is published [Fro18] in *Appl. Phys. Lett.* **113**, 073102 (2018).

6.1 Introduction

Single hole spins confined in quantum dots (QDs) in Ge/Si core/shell nanowires (NWs) combine several advantageous properties which makes them potentially very powerful quantum bits [Los98; Klo13b]. The natural abundance of non-zero nuclear spins in both silicon and germanium is relatively small and can be further reduced to a negligible amount by isotopic purification. Furthermore, hole spins have no contact hyperfine interaction due to their p-type wavefunction. These properties make hole spin qubits in silicon and germanium resilient against dephasing via interaction with nuclear spins.

A particularly promising feature of hole spins in Ge/Si core/shell NWs is the nature of spin-orbit interaction (SOI) in this system. Confinement to one dimension gives rise to an effective SOI in the valence band, which is predicted to be both strong and tunable [Klo11; Klo18], enabling fast all-electrical spin manipulation. An external electric field can be used to set the strength of this SOI. This promises the capability of electrical gating of the SOI, allowing to switch to a large SOI for high interaction strengths and fast quantum operations, or to turn off SOI for increased qubit coherence. Furthermore, this SOI results in a Landé g-factor that is locally tunable by external electric as well as magnetic fields [Mai13; Bra16a]. Local control over the g-factor makes it possible to selectively address individual spin qubits and allows for selective coupling to microwave cavities [Klo13b].

The confinement of single holes in QDs is an important step towards implementation of the basic ingredients of experimental quantum computation using hole spin qubits. [Los98]. Single QDs form the fundamental building blocks, and it is therefore imperative to be able to reliably form and characterize them [Bra16c]. Moreover, a high level of control over the exact position and shape of individual QDs is required to accurately tune level splittings [Klo11], spin relaxation times [Han07; Cam18], and tunnel coupling strengths.

In addition to single QDs, tunnel-coupled double QDs are of particular interest, since these are platforms for spin-to-charge conversion schemes facilitating spin read-out and coupling of spins to microwave cavities [Sam18; Mi18a; Lan18]. Spin states of double and triple QDs can be used as qubit encodings which are insensitive to fluctuations of a uniform magnetic field or of magnetic field gradients [Tay05; Tay13]. Moreover, quantum operations on these qubits may be performed using different mechanisms than for single spin qubits, for instance only relying on the Heisenberg exchange interaction [DiV00a; Med13]. Finally, double as well as triple QDs feature charge states with an increased dipole moment, potentially leading to enhanced coupling strengths of spin qubits to microwave cavities [Lan18].

In this Letter, we demonstrate a large amount of control over the formation of single, double and triple QDs in Ge/Si NWs, all with a low hole occupation number. Using five bottom gate electrodes, we tune the size and position of single QDs defined in the NW. Furthermore, we form tunnel-coupled double and triple QDs. In the double QD configuration, we observe Pauli spin blockade [Ono02; Han07] (PSB).

6.2 Device and Setup

We use a Ge/Si NW [Con17] with an estimated Ge core radius of 10 nm and Si shell thickness of 2.5 nm (see Fig. 6.1). Five Ti/Pd bottom gate electrodes are lithographically defined on a p++-doped Si substrate covered with 290 nm thermal oxide. The bottom gates have a thickness of ∼15 nm, a width of 20 nm, and are equally spaced with a pitch of 50 nm. On either side of these gates, a plateau gate (green in Fig. 1b) is defined, which serves to prevent bending of the NW. The bottom gates are subsequently covered by a layer of Al_2O_3 of thickness 20 nm through atomic layer deposition at 225 °C. In a next step, the NW is placed deterministically on top of the bottom gates using a micromanipulator setup. Electrical contact to the NW is made through two

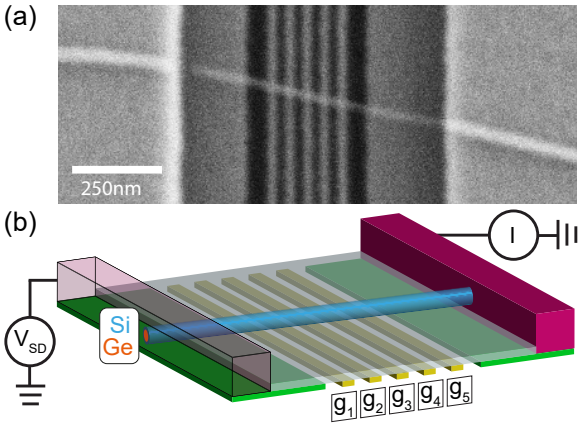

FIGURE 6.1 | (a). Scanning electron micrograph of a device similar to the one used in this work. (b) Schematic overview of device and measurement setup. The NW is shown in blue, with the core in orange, bottom gates are in yellow and green, and contacts in purple.

Ti/Pd (∼0.5/60 nm) contact pads, which are lithographically defined and metallized after a brief HF dip to strip the NWs native oxide.

Due to the type-II staggered band alignment of silicon and germanium, a hole gas accumulates in the core [Lu05]. By applying positive voltages to the gate electrodes, the hole density can be depleted locally, resulting in the formation of QDs. We perform transport measurements by applying a dc source-drain bias V_{SD} over the NW and measuring the differential conductance using standard lock-in techniques with a small ac excitation in the range of 20-100 μV applied to the source contact. All measurements were performed at a temperature of 1.4 K, without application of an external magnetic field, and with the doped part of the substrate grounded.

Figure 6.2a gives an overview of the different configurations of biased gates and dot sizes that were studied. QDs can be formed using two, three, four or five neighboring gates. For each dot size, the outer two gates (red in Fig. 6.2a) form tunnel barriers between the QD and the source and drain reservoirs. The voltage on individual or multiple middle gates (green in Fig. 6.2a) are used to tune the electrochemical potential of the QD. Unused gates (white in Fig. 6.2a) are grounded. In Figure 6.2b and c, measured charge stability diagrams (Coulomb diamonds) are shown for the case of a single QD

formed by two and three neighboring gates, respectively (see Fig. 6.2a, top panels). Similar measurements were made for larger QDs formed by four and five gates. In case of the QD defined by two adjacent gates, we find that sweeping the voltage on these gates has a large effect on the tunnel barriers defining the dot. As a result, only a few charge transitions can be observed for this configuration. For the other dot sizes, the tunnel barriers are much less affected by the voltage on one of the middle gates, and we observe a large number of regular Coulomb diamonds.

Table I summarizes parameters extracted from the Coulomb diamond measurements. In Figure 6.3 values of the hole addition energy E_{add} are plotted, which were extracted from the height of the Coulomb diamonds. We find that E_{add} is largest for the smallest dot and decreases for increasing dot size, in agreement with the expectation that both charging energy and orbital level splittings decrease with dot size.

The conductance measurements feature additional resonances at higher values of V_{SD}. We extract energies for these resonances by averaging the difference of the first resonance and the ground state transition, in windows similar to the one drawn in Figure 6.2c. Here we convert the difference in V_{SD} to energy using lever arms determined from the slopes of each Coulomb diamond. The third column of Table I lists typical energies E_{orb} found in this way for the different dot sizes. Consistent with the level splitting of orbital hole states [Kou01; Esc10], E_{orb} depends strongly on the longitudinal dot size, with smaller dots featuring higher values of E_{orb}. Note that incomplete knowledge of the exact confinement potential and the hole effective mass makes it difficult to compare our measurements to a theoretical model of orbital level splitting.

Furthermore, we estimate the lowest measurable hole occupation number N_{est} for the different dot sizes by comparing the used gate voltages with pinch-off voltages obtained at high V_{SD}. For dots formed by 3 to 5 neighboring gates, we find relatively low occupation numbers ranging from 15 to 38 (see Table I). This method is not reliable for QDs defined by only two gates, since both gates directly define the tunnel barriers of

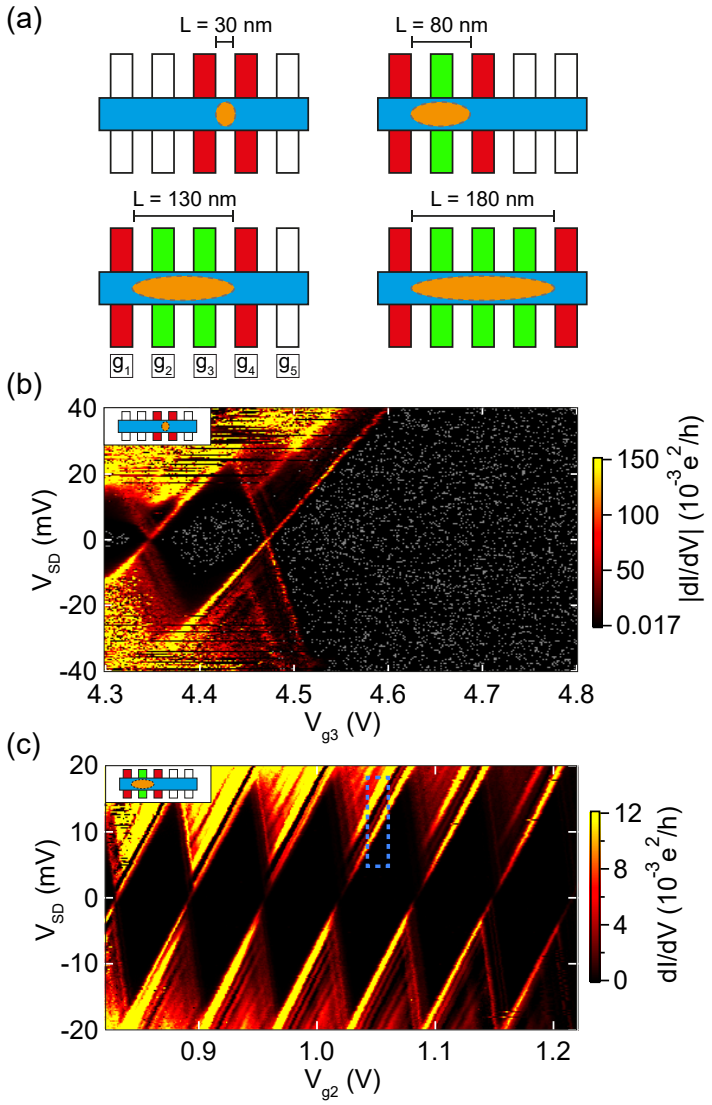

FIGURE 6.2 | (a). Schematic picture of the gate configurations used to form QDs (orange) of different lengths using 2, 3, 4 and 5 gates, respectively. (b) Lock-in signal dI/dV versus V_{SD} and V_{g3} of QD formed by two gates. To enhance contrast, values below the colorscale were given a grey color. Here $V_{g4} = 1700\,\text{mV}$. (c) Lock-in signal dI/dV versus V_{SD} and V_{g2} of QD formed by three gates. Here $V_{g1} = 2000\,\text{mV}$ and $V_{g3} = 4000\,\text{mV}$. Blue dashed rectangle shows an example of an averaging window used to extract excited state energies. Insets in (b) and (c) schematically show used gate configurations.

# gates	E_{add} (meV)	E_{orb} (meV)	L (nm)	N_{est}
2	26	12.8	30	1, see main text
3	17	4.8	80	15
4	13	2.1	130	35
5	10	1.3	180	38

TABLE 6.1 | Typical extracted single dot parameters: addition energies E_{add}, excited state energies E_{orb}, lithographically defined distances L between gates creating QD tunnel barriers, and estimated hole numbers N_{est}.

the dot. However, several indications suggest that single-hole occupation is reached in this case. First of all, the last Coulomb diamond edge visible in Figure 6.2b increases linearly up to at least $|V_{SD}| = 40\,\text{mV}$. Furthermore, even at high V_{SD}, no features involving tunneling of multiple holes are observed for the last visible Coulomb diamond (which would appear as lines intersecting the diamond edges on the high gate voltage side). We do find multiple resonances in the last diamond for low V_{SD}, which could arise from tunneling involving excited states. However, the splitting of these lines is lower than that found for the larger dots. Therefore, it is unlikely that these resonances correspond to excited orbital states in a small QD. Furthermore, we observe (not shown) that the splitting of the resonances strongly depends on gate voltages applied to g_2 and g_5 (flanking the barriers of the dot), again making it implausible that they correspond to excited orbital states [Möt10]. A likely explanation is that these lines arise from modulation of the reservoir density of states [Bjö04; Esc10; Möt10]. Finally, the energy of the first excited state in the second Coulomb diamond in Figure 6.2b (around $V_{g3} = 4.35\,\text{V}$) appears to be significantly reduced with respect to that found in the last diamond, consistent with an exchange energy appearing for two-hole states. More conclusive evidence of single hole occupation could be obtained by using a charge sensor [Hu07].

Finally, we observed in multiple devices that QDs formed by three or more gates tend to split up when biasing the center gates too positively. This impedes reaching single-hole occupation for the larger dot sizes. Moreover, conductance becomes too low to

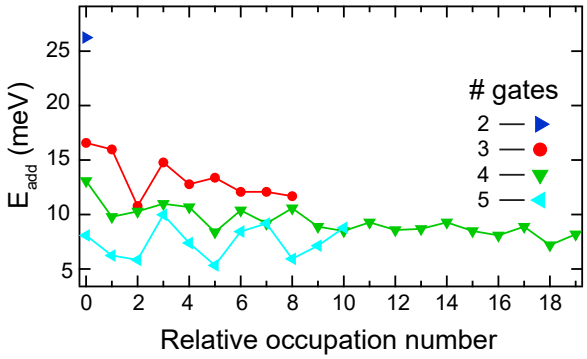

FIGURE 6.3 | Extracted values of E_{add} for various QD lengths as a function of relative occupation number.

measure when increasing the gate voltages, again potentially preventing the observation of single-hole occupation regimes. In the device studied here, this seems to be not the case for the dot made by two gates. The conductance exceeds $0.1\,e^2/h$ on the last diamond in Figure 6.2b, thus adding more evidence for the single-hole regime.

6.3 Formation of Double Quantum Dot

Next, we demonstrate controllable formation of double QDs. As shown in the charge stability diagrams in Figure 6.4a, a single QD formed by five gates can be continuously split up into a double tunnel-coupled QD, by increasing the voltage on gate g_3. Here, the voltage on gates g_2 and g_4 are swept and the current through the NW is measured for each point. The leftmost charge stability diagram shows single-dot behavior, in which diagonal lines are Coulomb peaks corresponding to sequential addition of single holes to the dot. The middle panel shows a charge stability diagram of a double QD featuring high coupling between the dots, as evidenced by the bending of the charging lines. The right panel shows conductance only when the electrochemical potentials of the two dots are aligned, in the form of bias triangles [vdWie02a]. The absence of conductance along the charging lines indicates that significant cotunneling with the lead reservoirs can be avoided. These measurements indicate that we have a large

amount of control over the capacitive coupling and tunnel-coupling between the two QDs.

Pauli spin blockade is a basic ingredient of many spin qubit experiments, in which interdot transitions are blocked for spin triplet but not for singlet states [Ono02; Han07]. As such, it forms a means of reading out spin qubit states. When measuring the conductance through a double QD, the blockade may be observed for one sign of V_{SD}, but not for the other. In this work, the relevant spin states are those of Kramers doublets formed by mixed heavy hole and light hole states [Klo11].

We observe signatures of PSB at several interdot transitions when measuring bias triangles for positive and negative V_{SD}, in the form of a region of reduced conductance inside the bias triangles for one sign of V_{SD}. Figure 6.4(b) focuses on one such an interdot transition where the current inside the region indicated by the dashed green line is suppressed by roughly a factor 10 for positive V_{SD}. The size of the blockaded region is determined by the singlet-triplet splitting ϵ_{ST} in the single dots (see white arrow in Fig. 6.4b, right panel). We find ε_{ST} to be 1 meV, which compares well with other measurements [Bra16b; Zar17]. Moreover, we observe a leakage current that depends on the detuning of the electrochemical potentials in the two dots and on the magnitude of an applied magnetic field. In particular, we find a small leakage current at low detuning that is consistent with an effective T(1,1) to S(0,2) transition, and a larger current at higher detuning consistent with a T(1,1) to T(0,2) transition. Various processes may lift PSB, including spin-flip cotunneling, spin-flip reservoir exchange [Bie15], hyperfine interaction, and SOI [Li15; Bra16b; Zar17]. The resulting leakage current thus forms a probe to detect the strength of these processes, but a detailed study of this goes beyond the scope of the present work.

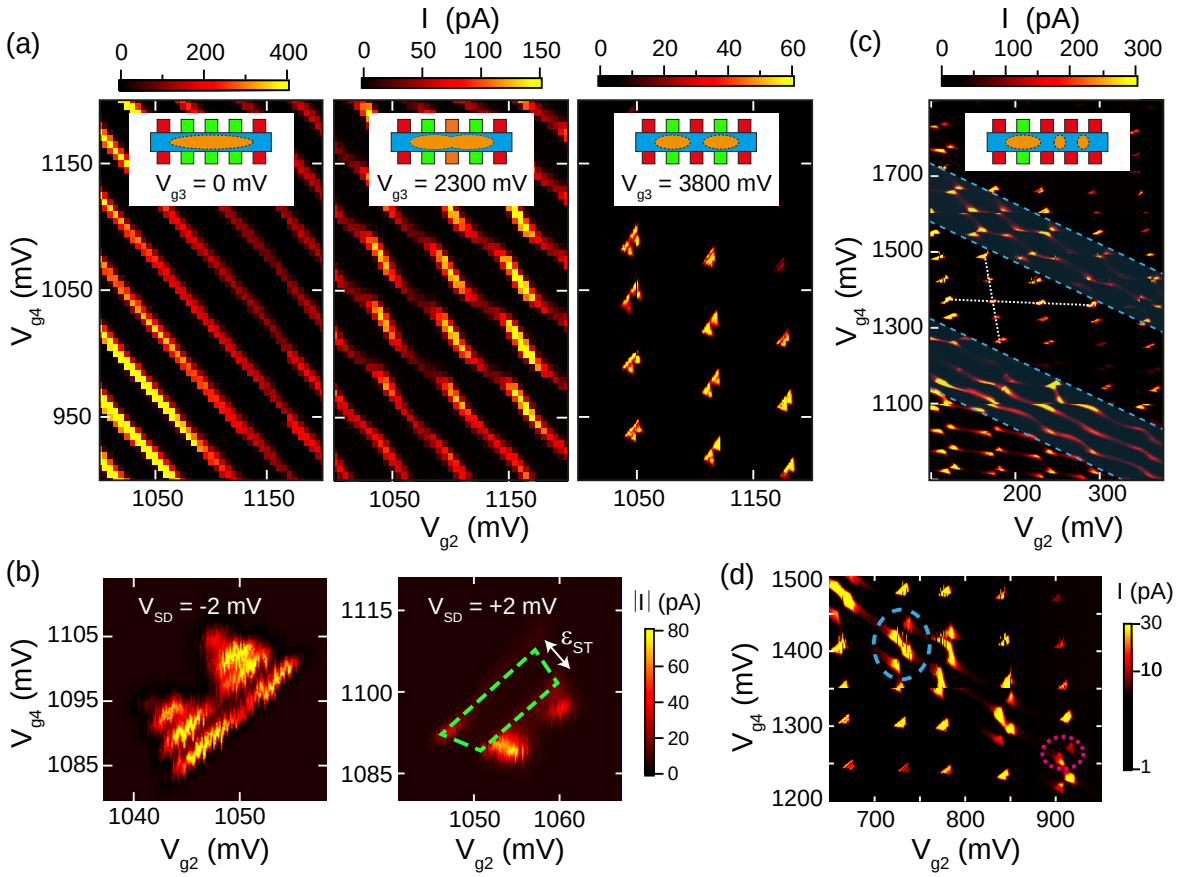

FIGURE 6.4 | (a) Charge stability diagrams for different values of the voltage on g_3, showing a transition from a single QD to a double QD, at $V_{SD} = 2$ mV. Insets schematically show QD configurations. (b) Zoom-in of a pair of bias triangles, at $V_{g3} = 3800\,\text{mV}$. Plotted is the dc current for positive and negative V_{SD}. The strong reduction in the area enclosed by the dashed green line indicates the presence of Pauli spin blockade. (c) Charge stability diagram with highlighted (shaded blue regions) triple QD features. White dotted lines indicate the slope of charge transitions of the outer two dots. (d) Charge stability diagram of triple QD. Dashed blue and dotted pink circles highlight triple dot resonances. In (c) and (d), $V_{g1} = 2000\,\text{mV}$, $V_{g3} = 3800\,\text{mV}$, and $V_{g5} = 2800\,\text{mV}$.

6.4 Formation of Triple Quantum Dot

We find that the double QD can be further subdivided into a triple QD, by increasing the voltage on g_4. In this case, the triple dot is likely composed of two small QDs between gate pairs g_3-g_4 and g_4-g_5, as well as a larger QD between g_1-g_3. In the charge stability diagram shown in Figure 6.4c, triple dot features appear as lines with enhanced conductance with an intermediate slope (see dashed blue lines). Figure 6.4d shows a zoomed-in region of the triple QD charge stability diagram. Similar to bias triangles in a double QD, conductance is enhanced when the electrochemical potential of the center dot is aligned with that of one of the outer dots (dotted pink circle in Fig. 4d), or when the electrochemical potentials of all three dots are aligned (dashed blue circle in Fig. 6.4d) [Sch07; Gra10]. The fact that we also observe conductance at points corresponding to DQD bias triangles suggests that there is cotunneling involving the center dot present in the measurements, resulting in conductance even when only the electrochemical potentials of two out of three dots are aligned.

6.5 Conclusion

The demonstration of tunable single, double, and triple QDs opens the way to perform spin qubit experiments with few holes in these devices. Reaching the single-hole regime is particularly important, as it makes single and two-qubit operations much more straightforward. Overall, we observe very good repeatability of the measurements, with gate voltage changes of 1 V leading to no observable shifts in charge stability diagrams. These results enable several follow-up experiments. In particular, the strength and electric field dependence of the SOI could be determined from magnetic field dependence of leakage current in a double QD in the PSB regime [Li15; Zar17; Bra16b]. Moreover, we expect that a slightly different gate design than used here will enable reaching single-hole occupation in a controllable way.

6.6 Acknowledgements

We thank C. Kloeffel, D. Loss, and M. Rančić for helpful discussions. We acknowledge the support of the Swiss National Science Foundation (Ambizione Grant No. PZOOP2161284/1) and Project Grant No. 157213), the Swiss Nanoscience Institute, the European Microkelvin Platform EMP, the NCCR Quantum Science and Technology (QSIT), and the Netherlands Organization for Scientific Research (NWO).

7 Strong spin-orbit interaction and g-factor renormalization of hole spins in Ge/Si nanowire quantum dots

F. N. M. Froning, M. J. Rančić, B. Hetényi, S. Bosco, M. K. Rehmann, D. Loss, D. M. Zumbühl, F. R. Braakman

Department of Physics, University of Basel, 4056 Basel, Switzerland

A. Li, E. P. A. M. Bakkers

Department of Applied Physics, Eindhoven University of Technology, 5600 MB Eindhoven, The Netherlands
QuTech and Kavli Institute of Nanoscience, Delft University of Technology, 2600 GA Delft, The Netherlands

F. A. Zwanenburg

NanoElectronics Group, MESA+ Institute for Nanotechnology, University of Twente, P.O. Box 217,7500 AE Enschede, The Netherlands

Abstract

The spin-orbit interaction lies at the heart of quantum computation with spin qubits, research on topologically non-trivial states, and various applications in spintronics. Hole spins in Ge/Si core/shell nanowires experience a spin-orbit interaction that has been predicted to be both strong and electrically tunable, making them a particularly promising platform for research in these fields. We experimentally determine the strength of spin-orbit interaction of hole spins confined to a double quantum dot in a Ge/Si nanowire by measuring spin-mixing transitions inside a regime of spin-blockaded transport. We find a remarkably short spin-orbit length of ∼65 nm, comparable to the quantum dot length and the interdot distance. We additionally observe a large orbital effect of the applied magnetic field on the hole states, resulting in a large magnetic field dependence of the spin-mixing transition energies. Strikingly, together with these orbital effects, the strong spin-orbit interaction causes a significant enhancement of the g-factor with magnetic field. The large spin-orbit interaction strength demonstrated is consistent with the predicted direct Rashba spin-orbit interaction in this material system and is expected to enable ultrafast Rabi oscillations of spin qubits and efficient qubit-qubit interactions, as well as provide a platform suitable for studying Majorana zero modes.

This chapter is published [Fro21a] in *Physical Review Research* **3**, 013081 (2021).

7.1 Introduction

The spins of single electrons or holes can be coupled to orbital degrees of freedom through the spin-orbit interaction. In a solid-state environment, this interaction arises from the motion of electrons or holes in electric fields associated with the host lattice atoms, structural or bulk inversion fields, or externally applied electric fields, and its strength can range from a typically small perturbation in the conduction band to a significant effect in the valence band [Win03]. Spin-orbit interaction is particularly useful for fundamental applications in spintronics and quantum information processing with spin qubits [Los98; Han07; Sca20], as it can be employed to realize fast manipulation of spin states purely through electrical means [Gol06; Now07]. For example, Rabi oscillations with frequencies of $\sim$100 MHz have been obtained for electron spins confined in group III-IV semiconductor nanowires, where the spin-orbit interaction was used to mediate a coupling of the spins to an electrical driving field [Nad10a; vdBer13]. Furthermore, spin-orbit interaction provides a promising path towards implementing entangling operations between distant spin qubits, by mediating the coupling of spins to electromagnetic cavity modes [Klo13c; Bur20] or floating gate architectures [Tri12]. An important advantage of using spin-orbit interaction for these purposes is that it requires no additional on-chip components such as micromagnets.

Furthermore, the emergence of Majorana zero modes in semiconductor nanowires relies on the presence of a strong spin-orbit interaction [Lut10; Ore10; Ali10; Kli12]. The strength of the spin-orbit interaction sets the range of Zeeman energies in which a topologically non-trivial phase exists together with a sufficiently large superconducting gap, making a strong spin-orbit interaction essential for experimental studies [Mai14].

Hole spins in semiconductor nanostructures can experience a spin-orbit interaction many times stronger than for electron spins [Win03; Bul05; Bul07]. In particular, a strong and electrically tunable direct Rashba spin-orbit interaction arises for holes confined in one-dimensional Ge- or Si-based nanostructures [Klo11; Klo18]. The direct

Rashba spin-orbit interaction results from direct dipolar coupling of holes to an external electric field, in combination with mixing of heavy and light hole states due to confinement to one dimension. This interaction is estimated to be 10-100 times stronger than the conventional Rashba-type spin-orbit interaction for electrons or holes.

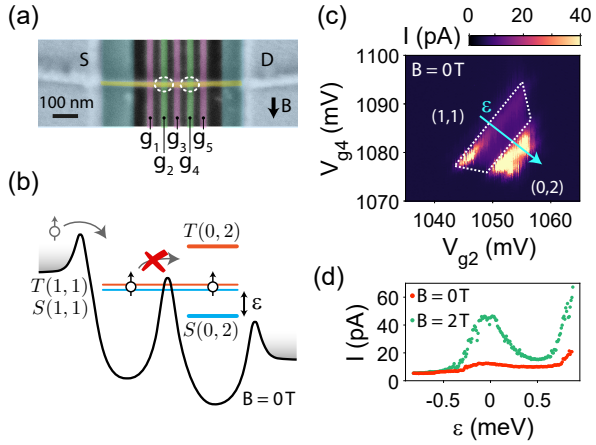

FIGURE 7.1 | Device and Pauli spin blockade. (a) False-colour scanning elecron micrograph of the device, used for all the measurements of this work. The finger gates $g_{1\text{-}5}$ (red: barrier gates, green: plunger gates) are biased with positive voltages $V_{g1\text{-}5}$ in order to create a double quantum dot in the Ge/Si core/shell nanowire (yellow). The source (S) and drain (D) contacts are defined on either side of the nanowire. Dashed ellipses indicate the approximate locations of the two quantum dots. (b) Schematic illustration of Pauli spin blockade, with zero magnetic field. When the double dot is occupied by holes in a triplet $(1,1)$ state, the current is blocked until mixing with a singlet state takes place. The double dot detuning is indicated by ε. (c) Bias triangles taken at $V_{SD} = 2\,\text{mV}$ showing signatures of Pauli spin blockade, through a suppression of current, in the area delineated by the dashed white lines. The blue arrow indicates the direction of the detuning axis. (d) Current as a function of detuning, swept along the arrow in (c), without (red) and with (green) applied magnetic field.

Such a strong spin-orbit interaction would enable pushing spin qubit Rabi frequencies into the GHz regime [Klo13c], an order of magnitude higher than recently demonstrated with hole spin qubits [Wat18b; Hen20a; Hen20b], and state-of-the-art electron-based spin qubits [vdBer13; Yon14; Yon18]. Moreover, a large electrical tunability of spin-orbit interaction strength promises exquisite control over qubit coherence and manipulation speeds, providing a gate-controlled *ON/OFF* switch of the coupling to electrical

environmental degrees of freedom, which could be used to, on the one hand, maximize the coupling to microwave drive fields and, on the other hand, minimize the coupling to charge noise. Such controllable coupling would make it possible to combine ultrafast qubit operations with long coherence times. Furthermore, such electrical tunability can be used to control the localization length of Majorana zero-modes confined to each end of a nanowire [Mai14], creating the possibility of electrically performing topologically non-protected operations on Majorana zero-modes.

Due to the tunable nature of the spin-orbit interaction, the magnitude of the g-factor of hole spins in Ge/Si nanowires can be modulated over a large range using applied electric fields [Mai13; Bra16a]. This feature enables local control over the Zeeman energy and allows to tune the energy of a qubit relative to a spin resonance driving field, or to a microwave cavity mode, making it possible to selectively address individual qubits in a multi-qubit device. Furthermore, in addition to strong and tunable spin-orbit interaction, hole spins in Ge/Si nanowires combine several other features that make them amenable for implementation of high-quality qubits. Hyperfine-induced decoherence is expected to be strongly suppressed, since holes have a p-type Bloch function, which has zero overlap with lattice nuclear spins [Fis08]. Furthermore, both Ge and Si have a low natural abundance of isotopes with non-zero nuclear spins (^{29}Si $< 5\%$, ^{29}Ge $< 8\%$), which can be made vanishingly small through isotopic purification. Finally, in contrast to electrons, holes in Ge and Si do not experience valley degeneracy, which for electron spins in Si-based devices can have a detrimental effect on qubit relaxation times [Yan13].

Here, we investigate the spin-orbit interaction of hole spins confined in a double quantum dot defined electrostatically in a Ge/Si core/shell nanowire [Fro18; Bra16c]. We use mixing of singlet and triplet spin states detected through lifting of Pauli spin blockade [Ono02; Kop05; Nad10b; Bra16b; Zar17] to perform spectroscopy on the effectively

doubly occupied double dot. Notably, we also find a large orbital effect of the magnetic field. We have developed a spectroscopic model, which fully takes into account these orbital effects, allowing to independently determine the Landé g-factor, the interdot tunnel coupling strength, and the strength of the spin-orbit interaction in this device. We find a particularly strong spin-orbit interaction, with a spin-orbit length of the same order as the dot size. Such a regime of strong spin-orbit interaction is expected to exhibit effects [Tri08; Dmy18] typically not observed in experiments with quantum dots. Specifically, it causes a renormalization of the g-factor, which we find here to lead to a Zeeman energy that is a non-linear function of the applied magnetic field.

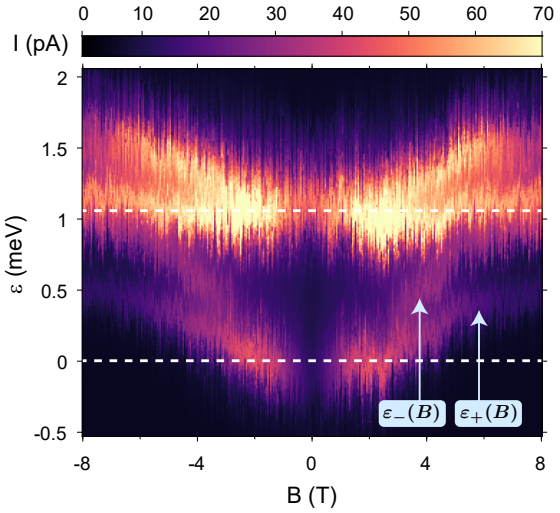

FIGURE 7.2 | Measured leakage current as a function of magnetic field for detunings covering the entire bias triangle, as shown by the arrow in Fig. 7.1(c). The dashed white lines delineate the spin-blockaded region also shown in Fig. 7.1(c). Here, $V_{g3} = 3820\,\text{mV}$. Dotted green curves are guides to the eye, indicating $\varepsilon_-(B)$ and $\varepsilon_+(B)$.

7.2 Device and measurement setup

The device we use consists of a single Ge/Si core/shell nanowire deterministically placed on top of five finger gates, which are equally spaced with a pitch of 50 nm (see Fig. 7.1(a)). The nanowire is an undoped radial heterostructure of a thin Si shell

around a Ge core [Con17]. A hole gas accumulates in the Ge core due to a combination of the type-II staggered band alignment between Ge and Si and interfacial effects [Lau02; Lu05]. The nanowire has an overall radius of 11 nm ± 2 nm, as determined through atomic force microscopy, and a nominal Si shell thickness of 2.5 nm. A 20 nm thick layer of Al_2O_3 in between gates and nanowire serves as electrical insulation. Electrical contact to the nanowire is made through two Ti/Pd contact pads, defined on either side of the nanowire. For more details of the device, see Froning et al. [Fro18]. Previously, we have shown a large degree of control over the formation of quantum dots in such devices, which can be tuned over hundreds of charge transitions down to the few-holes occupation regime [Bra16c; Fro18]. Here, we form a tunnel-coupled double quantum dot by applying positive voltages to the finger gates $g_1 - g_5$ that locally deplete the nanowire hole gas [Lu05]. We use the contact pads to apply a source-drain voltage bias of $V_{SD} = 2\,\text{mV}$ across the nanowire and to measure the current flowing through the double dot. An external magnetic field is applied in the sample plane, perpendicular to the major axis of the nanowire, as indicated in Fig. 7.1(a). All measurements were taken at a temperature of 1.4 K.

7.3 Double quantum dot and Pauli spin blockade

We tune the double dot to an effective occupation of two holes and study the transport cycle $(0,1) \rightarrow (1,1) \rightarrow (0,2) \rightarrow (0,1)$ in a Pauli spin blockade [Ono02; Han07; Hu12] configuration (see Fig. 7.1(b)). Here the first and second numbers refer to the effective hole occupation of the left and right dot, respectively. Even though the absolute occupation number of both dots is roughly 15, we assume the effective picture of a doubly occupied double dot to hold when we observe Pauli spin blockade [Hig14a; Zar17]. Transport in this regime is subject to a spin selection rule imposed by the Pauli exclusion principle: interdot transitions $(1,1) \rightarrow (0,2)$ are blocked for spin triplet states ($|T_{\downarrow\downarrow}\rangle, |T_0\rangle, |T_{\uparrow\uparrow}\rangle$, with spin quantum numbers $s = 1$ and $m_s = \text{-}1, 0, +1$), since

the $|T(0,2)\rangle$ states are energetically inaccessible. In contrast, interdot transitions are energetically allowed for holes in a spin singlet state ($|S\rangle$, $s = m_s = 0$). Therefore, when a triplet $(1,1)$ state gets occupied, current through the double dot is blocked, until mixing with a singlet state takes place.

We exploit such spin-selective transport as a read-out method allowing us to distinguish spin states [Ono02]. Fig. 7.1(c) shows a measurement of the current through the double dot as a function of the voltage on gates g_2 and g_4, taken at zero magnetic field. We identify the area of reduced current, enclosed by the dashed line in Fig. 7.1(c), as a signature of spin blockade. Consistently, for opposite V_{SD}, we obtain a larger current (not shown). Furthermore, as can be seen in the traces of Fig. 7.1(d), the blockade is lifted at a finite magnetic field, resulting in an increased current. Even when in a triplet state, transport can become unblocked [Ono02] through various spin-mixing mechanisms that coherently or incoherently couple triplet and singlet states. Possible spin-mixing mechanisms are based on hyperfine interactions with the nuclear spin bath of the host lattice [Kop05; Dan09; Nad10b], spin-flip cotunneling [Qas09; Coi11; Bie15; Bra16b], g-factor differences in the double quantum dot, and spin-orbit interaction [Dan09; Nad10b; Li15; Bra16b; Zar17]. The dominant spin-mixing mechanism can be investigated through measurements of the increase in current due to lifting of Pauli spin blockade, which we will from here on refer to as leakage current.

7.4 Lifting of Pauli Spin Blockade

We study the lifting of spin blockade in more detail, focussing on the dependence of the resulting leakage current on double-dot detuning ε, magnetic field B, and interdot tunnel coupling strength t_c. Fig. 7.2 shows a measurement of the current through the double dot as a function of magnetic field B and detuning ε. The latter is swept over the entire bias triangle, by changing V_{g2} and V_{g4} following the arrow in Fig. 7.1(c). The white dashed lines in Fig. 7.2 indicate the spin-blockaded regime $0 < \varepsilon < \varepsilon_\Delta$,

with $\varepsilon_\Delta \approx 1\,\mathrm{meV}$ the detuning for which states with one hole in the first orbital excited state becomes energetically available. For detunings exceeding ε_Δ, we observe features with a significantly increased current. We attribute these features to spin-flip transitions involving a higher orbital state, i.e. either $|T_{\uparrow\uparrow,\downarrow\downarrow}(1,1)\rangle \rightarrow |S_\Delta(0,2)\rangle$, or $|S(1,1)\rangle \rightarrow |T_{\uparrow\uparrow,\downarrow\downarrow}(0,2)\rangle$ transitions, where $|S_\Delta\rangle$ refers to a singlet state with one hole in the orbital ground state and one hole in the first orbital excited state. Note that also spin-conserving $|T(1,1)\rangle \rightarrow |T(0,2)\rangle$ transitions can take place for these detunings, but since these transitions are spin-conserving, they do not exhibit a Zeeman splitting and would correspond to a single curve as a function of magnetic field and detuning, in contrast to the multiple curves that we observe in our measurement. Remarkably, we find that in our experiment transitions that do not conserve spin have a higher amplitude than transitions that do conserve spin, as discussed in Section 7.6.

Here we are interested in the spin-blockaded region and in the remaining part we focus on the features between the white lines in Fig. 7.2. In this range of detuning, we see a markedly increased current that correspond to lifting of Pauli spin blockade. These leakage current features form the main topic of this work. We can make two important observations: *1)* for a given sign of B, the leakage current is maximum along two curves as a function of ε and B, marked $\varepsilon_\pm(B)$ in Fig. 7.2; *2)* around zero magnetic field the leakage current is suppressed. These observations form the starting point in identifying the triplet-singlet transitions underlying the leakage current along $\varepsilon_\pm(B)$, as well as the spin-mixing mechanism.

As explained in more detail in Section 7.6, the position of the two curves as a function of detuning and magnetic field allows us to assign them to $|T_{\uparrow\uparrow,\downarrow\downarrow}(1,1)\rangle \rightarrow |S(0,2)\rangle$ transitions. These transitions occur at different detuning depending on the magnetic field, due to an increase in Zeeman splitting, as well as orbital effects of the magnetic field. As shown in the next section, we identify spin-orbit interaction as the dominant

spin-mixing mechanism by evaluating the magnetic field-dependent intensity of these transitions.

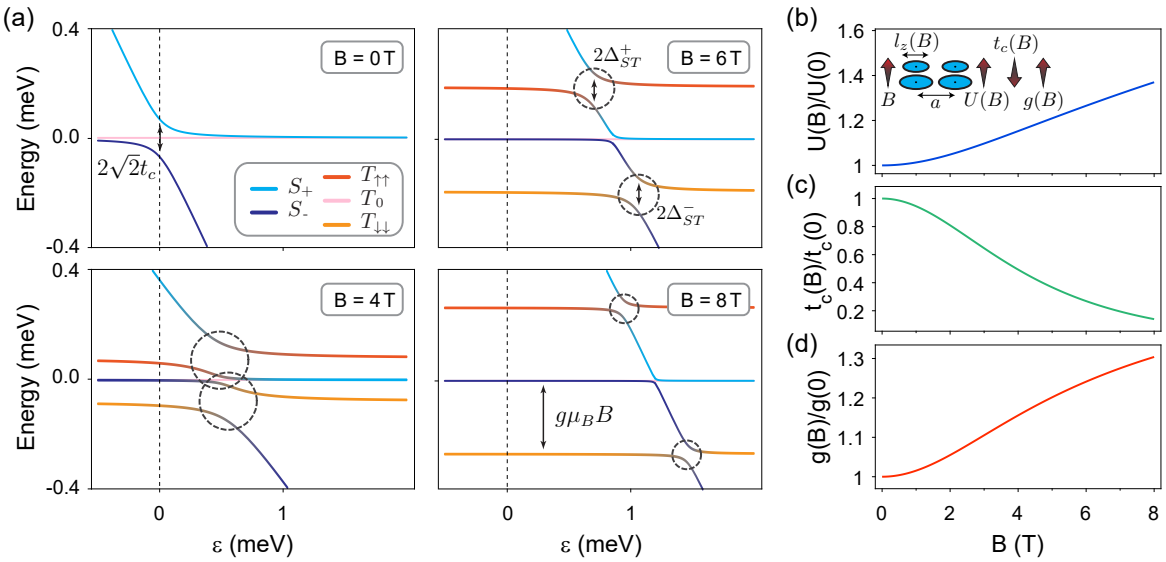

FIGURE 7.3 | Level diagram and magnetic-field dependencies. (a) Double dot energy level diagrams for different values of the magnetic field. For $B = 0\,\mathrm{T}$, the spin-conserving tunnel coupling t_c is maximum and there is no singlet-triplet mixing due to spin-orbit interaction. For large enough magnetic fields ($B > \tilde{B}$), avoided crossings (highlighted by dashed circles) appear when the triplet $(1,1)$ states cross a singlet state with $(0,2)$ component, corresponding to spin-flip tunneling due to spin-orbit interaction. The size of all avoided crossings becomes smaller with increasing magnetic field, as can be understood from (c) and Eq. (7.4). Moreover, due to the magnetic field dependence of the addition energy U (see (b)), as well as the Zeeman energy, all avoided crossings move to higher detuning with magnetic field. Parameters used to plot the diagrams were extracted from the data set shown in Fig. 7.2, using the model described in the text. (b) Calculated magnetic field dependence of the addition energy U (See Eq. (A.30) of Appendix A.4). Inset: Schematic illustration of the effect of increasing magnetic field B on dot size and separation leading to the observed changes in U, t_c and g. Quantities change qualitatively with B as indicated by the arrows. (c) Calculated magnetic field dependence of the spin-conserving tunnel coupling t_c (see Eq. (A.25a) of Appendix A.4). (d) Calculated magnetic field dependence of the g-factor (see Eq. (7.2)). For the plots in (b)-(d), the relevant parameters correspond to those of the measurement of Fig. 7.2.

7.5 Possible Spin-mixing mechanisms

We now discuss the origin of the spin mixing leading to the observed lifting of spin blockade by considering the dependence of possible spin-mixing mechanisms on the magnetic field and detuning. In particular, the zero-field gap can be attributed to spin-orbit interaction, which is not effective at $B = 0\,\mathrm{T}$ due to time-reversal invariance [Gol08b; Dan09], but becomes important at finite B [Sch11a; Bra14]. Furthermore, for $\varepsilon = 0$ and $|B|$ smaller than a characteristic field $\tilde{B}$, the triplet $(1,1)$ states lie within the avoided crossing of $|S(1,1)\rangle$ and $|S(0,2)\rangle$, at which point spin-orbit interaction does not couple them efficiently to the singlet states, leading to a suppressed leakage current [Hu12; Hig14c].

Spin-flip cotunneling can also lead to dips or peaks in the leakage current around $B = 0\,\mathrm{T}$. Such spin-flip cotunneling involves the exchange of a hole spin with one of the lead reservoirs through a process involving a virtual intermediate state, which can lead to decay of the triplet $(1,1)$ to a singlet state. Such cotunneling can result in a leakage current peak at $B = 0\,\mathrm{T}$ that exists for $\varepsilon = 0$, as well as for values of ε up to ε_Δ. A shallow zero-field dip can also result from cotunneling, when the temperature T is small compared to t_c [Coi11; Qas09]. However, the data presented in Fig. 7.2 shows a deep zero-field gap and our operating temperature of $1.4\,\mathrm{K}$ is, as will be shown later, comparable to t_c. We therefore rule out spin-flip cotunneling as the dominant spin-mixing mechanism in our measurements.

Furthermore, fluctuating polarizations of the nuclear spin bath in the double dot can result in triplet-singlet mixing [Kop05; Jou06; Nad10b]. However, as mentioned in the introduction, hyperfine interaction is expected to be very small for hole spins in Ge- and Si-based devices. Moreover, this mechanism is only effective for values of B up to the root mean square value of nuclear field fluctuations, which we estimate to be $< 1\,\mathrm{mT}$ in our system [Kop05]. Most notably, in contrast to what we observe, this spin-mixing

mechanism should result in a leakage current peak [Kop05; Nad10b] around $B = 0\,\mathrm{T}$ for ε up to ε_Δ.

Finally, differences in g-factor between the two dots need to be considered. The effective g-factor for holes in Ge/Si nanowires can depend sensitively on the electric field [Mai13], confinement potential [Tri08; Dmy18], and hole occupation number. At finite field, such a g-factor difference will mix the $|T_0(1,1)\rangle$ and $|S(1,1)\rangle$ states, thus leading to an additional resonance of the leakage current [Mut20]. However, such mixing of $|T_0(1,1)\rangle$ with $|S(1,1)\rangle$ would not result in the two separated curves of increased current that we observe. Note further that such mixing is suppressed as $|T_0(1,1)\rangle$ is split off from the singlet by the exchange energy.

In conclusion, we tentatively identify spin-orbit interaction as the dominant spin-mixing mechanism responsible for the observed leakage current. In a double quantum dot, spin-orbit interaction can flip the spin of a hole tunneling between the quantum dots. This enables triplet-singlet mixing, when these states are aligned in energy, which can effectively lift Pauli spin blockade. As shown in the next section, we can explain the spectroscopy of the observed leakage current using this mechanism.

7.6 Model of the two transitions

Here, we present an analytical model that takes into account non-spin-conserving interdot tunneling and its dependence on magnetic field and detuning. Our model agrees very well with the data and accurately reproduces the field-dependence of the two observed transitions shown in Fig. 7.2, allowing us to identify them as $|T_{\uparrow\uparrow,\downarrow\downarrow}\rangle \rightarrow |S\rangle$ transitions.

As mentioned before, we assume that the spin-blockade and its lifting can be understood in terms of an effectively doubly-occupied double dot. When the spin-conserving interdot tunnel coupling t_c is finite, the singlet states $|S(0,2)\rangle$ and $|S(1,1)\rangle$ are coupled, giving rise to two new eigenstates we refer to as the lower and higher hybridized

singlet states, $|S_-\rangle$ and $|S_+\rangle$, respectively [Ste12a]. These hybridized singlets are defined as $|S_-\rangle = \sin(\theta/2)|S(1,1)\rangle - \cos(\theta/2)|S(0,2)\rangle$ and $|S_+\rangle = \cos(\theta/2)|S(1,1)\rangle + \sin(\theta/2)|S(0,2)\rangle$, with the mixing angle θ being a function of detuning ε and t_c (see Eq. (A.34) for the full expression of θ). The $|S_\pm\rangle$ states exhibit an avoided crossing around $\varepsilon = 0$ with a gap of $2\sqrt{2}t_c$, as shown in Fig. 7.3(a). Importantly, the proportion of $|S(0,2)\rangle$ and $|S(1,1)\rangle$ present in each of the $|S_\pm\rangle$ states depends on the detuning.

In the presence of spin-orbit interaction, spin-flip tunneling couples the $|T_{\uparrow\uparrow,\downarrow\downarrow}(1,1)\rangle$ states with the two hybridized $|S_\pm\rangle$ states, due to the $|S(0,2)\rangle$ content of the latter. The coupling strength of this spin-flip tunneling is given by the strength of the spin-conserving tunnel coupling as well as the strength of the spin-orbit interaction and can be written as $t_{so} = t_c \tan\left(a/\lambda_{so}\right)$ (see Appendix A.4 for derivation), with a the interdot distance and λ_{so} the spin-orbit length (defined by $\pi\lambda_{so}/2$ being the distance a hole has to travel for spin-orbit interaction to induce a π-rotation of its spin state).

This coupling leads to avoided crossings when the energies of the $|T_{\uparrow\uparrow,\downarrow\downarrow}\rangle$ states exactly match the energies of the $|S_\pm\rangle$ states, as illustrated in the energy level diagrams in Fig. 7.3(a). The leakage current is maximum for those values of the detuning where the triplet-singlet avoided crossings occur, which can be written as:

$$\varepsilon_\pm(B) = U(B) - U(0) \pm \left(\frac{2t_c^2(B)}{g(B)\mu_B B} - g(B)\mu_B B \right) . \tag{7.1}$$

Here the indices $+$ and $-$ correspond to the $|T_{\uparrow\uparrow}\rangle \rightarrow |S_+\rangle$ and $|T_{\downarrow\downarrow}\rangle \rightarrow |S_-\rangle$ transitions, respectively. Furthermore, μ_B is the Bohr magneton, g the g-factor in the dot, and U the single-dot addition energy. Eq. (7.1) describes the evolution of spin-blockade leakage current with magnetic field shown in Fig. 7.2 between the white dashed lines, with $\varepsilon_\pm(B)$ giving the detunings of the resonant peaks of the two features as a function of magnetic field.

In order to explain the precise magnetic field dependence of $\varepsilon_{\pm}(B)$, we need to take into account effects that rely on the magnetic field changing the size of the hole orbitals. In the experiment, the magnetic field is oriented perpendicular to the principal nanowire axis and is varied over a wide range of amplitudes ($-8\,\mathrm{T} \leq B \leq 8\,\mathrm{T}$), making such orbital effects significant in this system.

Remarkably, this turns the spin-conserving tunnel coupling t_c, the addition energy U and the g-factor into quantities that all depend on the magnetic field (see inset Fig. 7.3(b)). Such effects are usually dealt with only qualitatively, even though their relative magnitude can be quite large. Here, we take these effects fully into account in our spectroscopic model, enabling us to quantify the g-factor and the spin-orbit length in our device.

To derive the functional dependence of these quantities on B, we start from the Hund-Mulliken theory of atomic orbitals and we assume harmonic confinement in all three directions. By considering an anisotropic 3-dimensional oscillator, we model the effects of a confinement potential that is smoother (sharper) in the direction along (perpendicular to) the nanowire as well as the strain-induced anisotropy of the effective mass [Klo18]. The hole wavefunctions in each dot are confined more by the magnetic field through the cyclotron effect and as a result the spin-conserving tunneling $t_c(B)$ is reduced at large fields while the single-dot addition energy $U(B)$ is enhanced, as shown schematically in the inset of Fig. 7.3(b). The explicit dependencies of $t_c(B)$ and $U(B)$ on magnetic field are given in Eqs. (A.25a) and (A.30) of Appendix A.4, and are plotted in Fig. 7.3(b), (c).

The detunings at which the avoided crossings of $|T_{\uparrow\uparrow,\downarrow\downarrow}\rangle$ with $|S_{\pm}\rangle$ appear also depend on the Zeeman splitting E_{Z} of the $|T_{\uparrow\uparrow,\downarrow\downarrow}\rangle$ states with respect to the singlets. Usually, the Zeeman splitting is a linear function of the magnetic field, which can be written

in terms of the g-factor as $E_Z = g\mu_B|B|$. However, strong spin-orbit interaction can renormalize the g-factor [Tri08; Dmy18] when the size of the quantum dot is changed. In our case, the magnetic field changes the dot size through orbital effects, leading to a dependence of the g-factor on the magnetic field and turning the Zeeman energy into a non-linear function of the magnetic field.

The shrinking of the dot with increasing magnetic field causes the g-factor to be enhanced at large values of the magnetic field and we can write [Tri08; Dmy18]

$$g(B) = g_0 e^{-\frac{l_\parallel^2}{\lambda_{so}^2}\left(1+\frac{B^2}{B_0^2}\right)^{-1/2}}, \tag{7.2}$$

where g_0 is the g-factor without the spin-orbit-induced renormalization. Furthermore, $l_\parallel$ is the field-independent harmonic length of the hole wavefunction ($l_\parallel = l_z(B=0)$, with l_z being the dot confinement length along the wire) and B_0 is a characteristic magnetic field that depends on the average confinement strength in the directions perpendicular to the field. See Appendix A.3 for the precise definition of these quantities. Fig. 7.3(d) shows a plot of Eq. (7.2), with values of $l_\parallel$ and B_0 calculated using ε_Δ as determined from the measurement of Fig. 7.2. We stress that the magnetic-field dependence of the g-factor in Eq. (7.2) is a direct consequence of the strong spin-orbit interaction in the nanowire and it vanishes when the spin-orbit length λ_{so} is much larger than the dot size, which is typically the case for quantum dot systems that have been experimentally realized thus far.

As will be shown in the next section, when taking into account the magnetic field dependence of U, t_c, and g, the resonant positions $\varepsilon_\pm(B)$ of the $|T_{\uparrow\uparrow,\downarrow\downarrow}\rangle \to |S_\pm\rangle$ transitions given by Eq. (7.1) closely reproduce the evolution of the two features of spin blockade leakage current of Fig. 7.2 as a function of magnetic field and detuning.

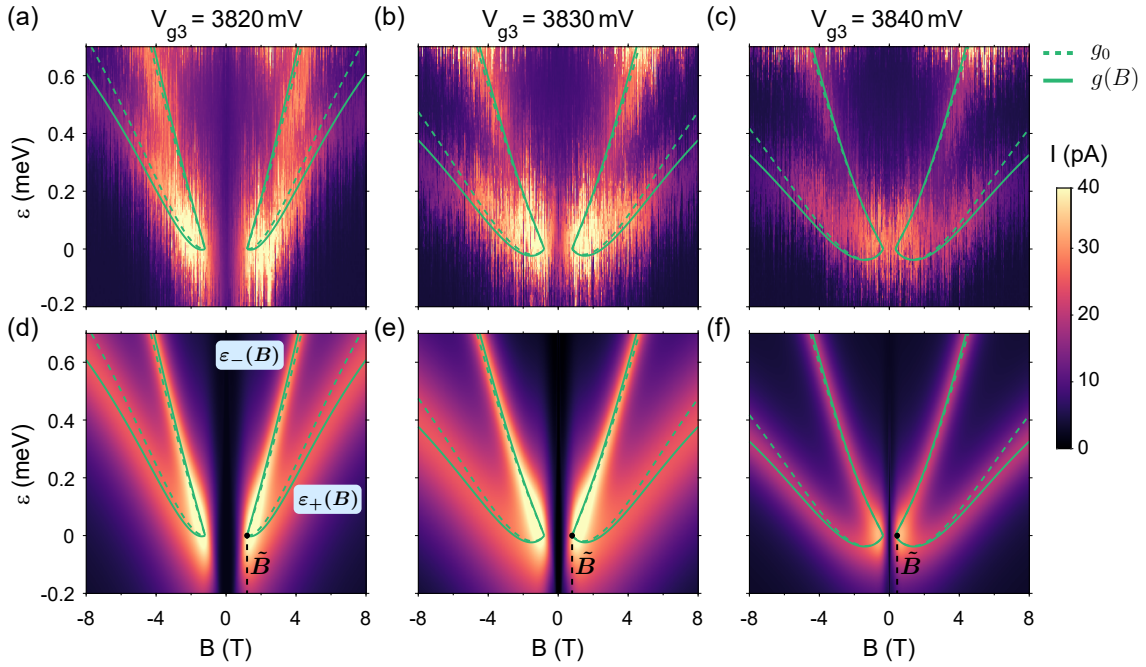

FIGURE 7.4 | Spectroscopy measurements and modelling. (a)-(c) Measured leakage current as a function of magnetic field and detuning $\varepsilon < \varepsilon_\Delta$, for $V_{g3} = 3820$, 3830, and 3840 mV. The green curves are fits of each data set to Eq. (7.1), with (solid) and without (dashed) taking into account g-factor renormalization with magnetic field. (d)-(f), Simulated leakage current as a function of magnetic field and detuning. Here, we used the model discussed in Sections 7.6-7.8 of the main text, with relevant parameters determined from fits of the data shown in (a)-(c). The green curves are identical to the curves in (a)-(c).

7.7 Varying the strength of interdot tunnel coupling

To demonstrate the versatility of our model we now explore the influence of varying the voltage V_{g3} on the middle gate on the leakage current. The main expected effects are a change in the interdot tunnel coupling t_c and a change in the dot confinement. Figs. 7.4(a)-(c) show measurements similar to that of Fig. 7.2, for three values of V_{g3} (see Fig. S1 of the Supplemental Material for extended data sets). Comparing the three data sets, we see that an increase of V_{g3} leads to a closing of the zero-field gap. As discussed before, Pauli spin blockade only becomes lifted through spin-orbit interaction for magnetic fields above a critical value. This critical field $\tilde{B}$ can be written as

$$\tilde{B} = \frac{\sqrt{2}}{\mu_B} \frac{t_c(\tilde{B})}{g(\tilde{B})} , \tag{7.3}$$

where we include the magnetic field dependence of t_c and g. When $|B| = \tilde{B}$, the Zeeman energy matches the size of half of the avoided crossing given by t_c. At this point, $\varepsilon_-(B) = \varepsilon_+(B)$ (see Eq. (7.1)) and both $|T_{\uparrow\uparrow,\downarrow\downarrow}(1,1)\rangle \rightarrow |S_\pm\rangle$ transitions become possible at $\varepsilon \approx 0$ (see Fig. 7.3(a) and Fig. 7.4(a)). For $|B| < \tilde{B}$, each of the singlet-triplet avoided crossings occurs at detunings where the involved $|S_\pm\rangle$ states are mostly composed of $|S(1,1)\rangle$, which does not couple to $|T_{\uparrow\uparrow,\downarrow\downarrow}(1,1)\rangle$ through spin-orbit interaction, leading to a gap in leakage current with characteristic width $\tilde{B}$ around zero magnetic field.

By increasing V_{g3}, we reduce t_c and from Eq. (7.3) it follows that spin blockade can be lifted at smaller magnetic fields. This moves the points of emergence of $\varepsilon_\pm(B)$ for both magnetic field polarities closer together and effectively reduces the width of the zero-field gap of leakage current, in accordance with the observations. In Fig. 7.4(a)-(c), we can clearly see this reduction of the zero-field gap (indicated with $\tilde{B}$) when the middle gate voltage V_{g3} is increased. Using Eq. (7.3), we extract the ratio t_c/g at the critical field $\tilde{B}$ for each data set. When the magnetic field is not much larger than $\tilde{B}$, we neglect as a first approximation the variation of $t_c(B)$ and $g(B)$ from their value at $\tilde{B}$, see Figs. 7.3(a) and (c), and so using Eq. (7.1) we deduce $t_c(\tilde{B})$ and $g(\tilde{B})$ from the relative position of the resonant peaks. Values of $\tilde{B}$, $t_c(\tilde{B})$, and $g(\tilde{B})$ extracted in this way for the three data sets of Fig. 7.4 are listed in Table 7.1.

By taking into account the orbital effects, our model allows us to explain the main features of the resonances at low magnetic fields. By linearly expanding the single-dot addition energy in the vicinity of the critical field, $U(B) \approx U(\tilde{B}) + U'(\tilde{B})\big(B - \tilde{B}\big)$, we can approximate $\varepsilon_-(B) \approx \varepsilon(\tilde{B}) + \Big(U'(\tilde{B}) + g(\tilde{B})\mu_B\Big)\big(B - \tilde{B}\big)$, reproducing the approximately linear dependence of the upper resonance on magnetic field seen in Fig. 7.4. On the other hand, in the expression of the $\varepsilon_+(B)$ resonant peak the term

linear in B is smaller and the $1/B$ term gives a significant contribution, leading to a less pronounced shift in detuning, especially at low magnetic field. Although the $1/B$ term is proportional to the tunnel coupling, its effect is counter-intuitively more pronounced in Fig. 7.4(c), because here Pauli spin blockade is lifted at lower magnetic fields.

To characterize the overall magnetic field dependence of the leakage current, we now find $\varepsilon_{\pm}(B)$ for each data set by fitting to Eq. (7.1). The green curves in Fig. 7.4 are plots of $\varepsilon_{\pm}(B)$ with (solid) and without (dashed) taking into account the renormalization of the g-factor given by Eq. (7.2). The additional features at larger magnetic fields, such as the bending of the $\varepsilon_{+}(B)$ curve, are captured by the model by considering the function $U(B)$ beyond the linear approximation, as well as the renormalization of the g-factor due to spin-orbit interaction. We see that the enhancement of the g-factor captured by Eq. (7.2) is quite important for large magnetic fields, where it causes a sizeable bending of the resonant peaks (see also Fig. S2 of the Supplemental Material). Including the renormalized g-factor gives much better agreement with the measurements over the whole range of magnetic field values.

In order to calculate the renormalized g-factor using Eq. (7.2), we estimate the dot confinement length $l_{\parallel} = \sqrt{\hbar/(m_{\parallel}\omega_{\parallel})}$, which depends on the confinement energy $\omega_{\parallel}$ and on the effective mass $m_{\parallel}$ along the nanowire. We determine $\hbar\omega_{\parallel} \sim 1$ meV from measurements of the double dot charge stability diagram and assume $m_{\parallel} \sim 0.05\, m_0$ (here m_0 is the bare electron mass). This choice of $m_{\parallel}$ is justified by the fact that we still measure a non-zero current even at $|B| = 8\,\mathrm{T}$. If the effective mass along the nanowire growth direction would be smaller, the orbital effects would shrink the wavefunction to the extent that the interdot tunnel coupling would vanish at 8 T. For our experiment, we determine $l_{\parallel} \approx 39 - 45$ nm for the range of V_{g3} used here. All the parameters extracted from our analysis for the three datasets are reported in Table 7.1. These values capture the qualitative trend expected: when the voltage V_{g3} is increased,

the hole wavefunctions become more separated and squeezed, causing a reduction of the tunneling energy t_c and an enhancement of the g-factor because of the strong spin-orbit interaction, as described by Eq. (7.2). As shown in the next section, our model allows us to extract the spin-orbit length for each measurement. The model color plots shown in Fig. 7.4(d)-(f) take into account the extracted values of the spin-orbit length, allowing a full reconstruction of the leakage current in very good agreement with the measurements.

7.8 Spin-orbit length

We now turn to the evaluation of the strength of the spin-orbit interaction from the measurements shown in Fig. 7.4. The model developed in the previous sections facilitates the extraction of this strength from the width of the two leakage current features as a function of detuning in Fig. 7.4(a)-(c). This width is given by the sizes $2\Delta_{\mathrm{ST}}^{\pm}$ of the avoided crossings (see Fig. 7.3(a)) induced by the spin-orbit interaction. Here, the spin-flip tunneling energies $\Delta_{\mathrm{ST}}^{\pm}$ are functions of the spin-orbit length λ_{so} and furthermore depend on the overlap of the wave functions of the $|T_{\uparrow\uparrow,\downarrow\downarrow}(1,1)\rangle$ states with those of the $|S_{\pm}\rangle$ states, as well as on the dot size. The spin-flip tunneling energy can be written as (see Appendix A.5 for the complete derivation)

$$\Delta_{\mathrm{ST}}^{\pm} = t_c \tan\left(\frac{a}{\lambda_{so}}\right)\sqrt{\frac{1 \pm \cos(\theta)}{2}}\ , \tag{7.4}$$

with θ the mixing angle of the $|S_{\pm}\rangle$ states.

The leakage current $I_{\pm}(B)$ corresponding to the resonances around $\varepsilon = \varepsilon_{\pm}(B)$ can be written as [vdWie02a; Naz93; Sto96; Li15]

$$I_{\pm} = I_0 + e\Gamma\frac{\left(\Delta_{\mathrm{ST}}^{\pm}\right)^2}{(\varepsilon-\varepsilon_{\pm})^2 + 3\left(\Delta_{\mathrm{ST}}^{\pm}\right)^2 + h^2\Gamma^2/4}\ . \tag{7.5}$$

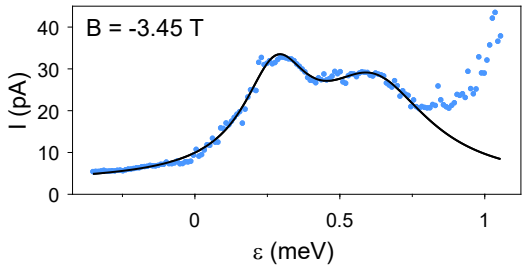

FIGURE 7.5 | Measured leakage current as a function of detuning, for $V_{g3} = 3820\,\text{mV}$ and $B = -3.45\,\text{T}$. The black curve is a fit of Eq. (7.5) to the data.

Here, the lead-to-dot relaxation rate $\Gamma \sim 0.45$ GHz is taken to be symmetric for both of the leads and is estimated by adjusting the formula in Eq. (7.5) for the $|S(0,2)\rangle \rightarrow |S(1,1)\rangle$ transition, and fitting it to the current measured for opposite V_{SD}. The offset current term I_0 contains all incoherent relaxation mechanisms, as well as $|S\rangle/|T_0\rangle$ mixing. Discussing this term in detail is beyond the scope of this paper and we refer the interested reader to Ref. [Dan09]. Additionally, we note that since we operate at relatively high temperature, it might be expected that the transitions are thermally broadened. However, the temperature of 1.4 K is still low compared to the orbital level splitting of 1 meV, making such broadening negligible. The dot-lead tunneling rate Γ is influenced by temperature, but the value of Γ that we determine independently from the measurements already includes this effect.

We therefore conclude that the width of the two leakage current features is given by the spin-flip tunneling energies $\Delta_{\text{ST}}^{\pm}$, which are then deduced by fitting the Lorentzians in Eq. (7.5) to the data sets of Fig. 7.4(a)-(c). An example of this is shown in Fig. 7.5. The color plots of Fig. 7.4(d)-(f) are constructed from the Lorentzians found in this way for different values of the magnetic field. It can be seen that the model plots accurately reproduce the leakage current observed in the corresponding experimental data.

Importantly, the determined $\Delta_{\text{ST}}^{\pm}$ allow to extract the spin-orbit length λ_{so}. Using

Eq. (7.4), we obtain the ratio λ_{so}/a directly from the ratio Δ_{ST}/t_c of the average spin-flip tunneling $\Delta_{\mathrm{ST}} = \left[(\Delta_{\mathrm{ST}}^{+})^2 + (\Delta_{\mathrm{ST}}^{-})^2\right]^{1/2}$ and the spin-conserving tunneling t_c. This yields ratios of λ_{so}/a as shown in Table 7.1 for the different configurations of our double quantum dot. Note that the values of $\tilde{B}$ and t_c obtained for $V_{\mathrm{g3}} = 3840\,\mathrm{mV}$ have a large relative uncertainty due to the absence of a dip in the data around zero magnetic field. In this case, Eq. (7.3) cannot be used and we infer $\tilde{B}$ and t_c solely from fitting Eq. (7.1) to the data, which leads to a higher error margin. However, even in this case, λ_{so}/a and $g(\tilde{B})$ can be determined with good accuracy. The precise value of the interdot distance a cannot be exactly determined from the measurements, but we can roughly estimate $a \sim 90\,\mathrm{nm}$ by considering the distance between the gates g_2 and g_4 (see Fig. 7.1(a)). Using this value, we obtain an average estimated value $\lambda_{so} \sim 65\,\mathrm{nm}$ for the spin-orbit length, with small variation between the measurements of Fig. 7.4(a)-(c). This value of λ_{so} is consistent with our recent complementary study using Rabi oscillations of hole spin qubits defined in a similar device [Fro21b], and it agrees well with earlier results obtained for different regimes, such as with a Ge/Si nanowire without dot confinement [Hao10] and with a quantum dot occupation of hundreds of holes [Hig14b] (in this work, we estimate a dot occupation of roughly 15 holes).

Together with the orbital effects of the magnetic field, this notably small λ_{so} leads to a dependence of the g-factor on the magnetic field, as described by Eq. (7.2). This effect is large, since the spin-orbit length λ_{so} and the confinement length along the wire $l_{\parallel}$ are of the same order of magnitude. In our measurements, this manifests itself in the additional bending of the transitions $\varepsilon_{\pm}(B)$ at high values of the magnetic field.

TABLE 7.1 | Extracted hole spin parameters, obtained for the three datasets shown in Fig. 7.4 by fitting the model to the data as described in the main text.

	V_{g3} (mV)	$\tilde{B}$ (T)	B_0 (T)	$t_c(\tilde{B})$ (μeV)	$g(\tilde{B})$	$ł_{\parallel}$ (nm)	λ_{so}/a
Fig. 7.4(a)	3820	1.2 ± 0.3	3.8 ± 0.2	44 ± 13	0.9 ± 0.15	45 ± 4	0.78 ± 0.06
Fig. 7.4(b)	3830	0.8 ± 0.2	4.8 ± 0.3	33 ± 10	1.0 ± 0.15	41 ± 5	0.72 ± 0.06
Fig. 7.4(c)	3840	0.35 ± 0.35	5.0 ± 0.3	16 ± 16	1.1 ± 0.15	39 ± 6	0.71 ± 0.07

7.9 Conclusions and outlook

Summarizing, we have characterized the strength of spin-orbit interaction for hole spins confined in a double quantum dot in a Ge/Si nanowire, using spectroscopy measurements in Pauli spin blockade. We found the spin-orbit length to be of the same order of magnitude as the dot length and interdot distance. This has the remarkable consequence that the g-factor exhibits a non-linear dependence on magnetic field, which we observe experimentally at high values of the magnetic field.

The observation of this strong spin-orbit interaction in Ge/Si nanowires forms the starting point of various subsequent experiments in this material system. From the value of λ_{so} we can estimate the Rabi frequency for electric dipole induced spin resonance [Gol06; Bul07] mediated through spin-orbit interaction to be in the range of $\sim 0.1 - 1\,\mathrm{GHz}$, for realistic values of microwave amplitudes. When combined with pulsing techniques and microwave control appropriate for high-speed operation, such Rabi frequencies form an excellent basis for the implementation of fast hole spin qubits in this system.

Further characterization studies of the spin-orbit interaction in this platform are of interest, in particular because here a quantitative comparison to relevant theoretical works [Klo11; Mai13; Klo13c; Mai14; Klo18] is challenging, due to the relatively high dot occupation number. For instance, direct Rashba spin-orbit interaction is predicted to lead to a profound dependence of the spin-orbit interaction as well as the g-factor

on electric fields. While we observe a dependence of the g-factor on a gate voltage (see Table 7.1), a more complete investigation of these effects would include measurements of the strength of the spin-orbit interaction as function of electric field amplitude or orientation of magnetic field. Such tunability of g-factor and spin-orbit strength could enable individual addressability of spin qubits in coupling them to microwave fields, as well as provide a way to limit the impact of charge noise on spin coherence.

Acknowledgements

We thank C. Kloeffel for helpful discussions. We acknowledge the support of the Swiss National Science Foundation (Ambizione Grant Nr. PZOOP2161284/1 and Project Grant Nr. 179024), the Swiss Nanoscience Institute (SNI), the EU H2020 Microkelvin Platform EMP (Grant Nr. 824109), the NCCR Quantum Science and Technology (QSIT), the Georg H. Endress Foundation, the EU FET (TOPSQUAD, Grant Nr. 862046), the EU H2020 research and innovation programme (Grant Nr. 862046), and the Netherlands Organization for Scientific Research (NWO).

8 Ultrafast Hole Spin Qubit with Gate-Tunable Spin-Orbit Switch Functionality

F. N. M. Froning, L. C. Camenzind, O. A. H. van der Molen,
D. M. Zumbühl, F. R. Braakman

Department of Physics, University of Basel, 4056 Basel, Switzerland

A. Li, E. P. A. M. Bakkers

Department of Applied Physics, Eindhoven University of Technology, 5600 MB Eindhoven, The Netherlands

QuTech and Kavli Institute of Nanoscience, Delft University of Technology, 2600 GA Delft, The Netherlands

Abstract

Quantum computers promise to execute complex tasks exponentially faster than any possible classical computer, spurring breakthroughs in quantum chemistry, material science, and machine learning. However, quantum computers require fast and selective control of large numbers of individual qubits while maintaining coherence. Qubits based on hole spins in one-dimensional germanium/silicon nanostructures are predicted to experience an exceptionally strong yet electrically tunable spin-orbit interaction, allowing to optimize qubit performance by switching between distinct modes of ultrafast manipulation, long coherence, and individual addressability. Here, we use millivolt gate voltage changes to tune the Rabi frequency of a hole spin qubit in a germanium/silicon nanowire from 31 to 219 MHz, its driven coherence time between 7 and 59 ns, and its Landé g-factor from 0.83 to 1.27. We thus demonstrate spin-orbit switch functionality, with on/off ratios of roughly 7 in this first experimental implementation, which could be further increased through improved gate design. Finally, we use this control to optimize our qubit further and approach the strong driving regime, with spin-flipping times as short as $\sim$1 ns.

This chapter is adapted from [Fro21b].

8.1 Introduction

Spin qubits defined in Si and Ge quantum dots are of particular interest for scaling up quantum circuits due to their small size, speed of operation, and compatibility with semiconductor industry [Zwa13; Klo13a; Van17; Sca20]. Both materials feature a low natural abundance of non-zero nuclear spins, which has led to the demonstration of long qubit coherence times [Zwa13; Tyr12; Yon18], as well as single- [Kaw14; Vel14; Yon18] and two-qubit [Vel15; Zaj18; Wat18a; Hen20a] operations with high fidelity. Most of this research has been performed using electron spin states defining the qubit [Los98]. Hole spin qubits [Bul05; Mau16; Cri19; Sca20] have recently gained attention since they potentially enable faster quantum operations and a higher level of control over qubit parameters [Klo11; Mai13; Klo13b; Klo18]. In addition, hole spins in Ge and Si may have improved relaxation and decoherence times, since they do not exhibit a valley degeneracy and their wave function has reduced overlap with nuclear spins [Yan13; Pre16]. Importantly, spin-orbit interaction (SOI) can be exceptionally strong for hole spins in low-dimensional nanostructures [Dur14; Mar17], particularly in Ge- or Si-based nanowires [Klo11; Klo18]. This enables very fast spin control through electric-dipole spin resonance (EDSR) [Gol06; Now07; Bul07; vdBer13], where a time-varying electric field periodically displaces the hole wave function, thus creating an effective periodic magnetic field through the SOI. In this way, EDSR can be used for all-electrical spin manipulation without requiring micromagnets [Pio08] or co-planar striplines [Kop06], which add to device complexity.

Rabi frequencies of around 100 MHz have been measured for hole spins [Wat18b; Hen20a], but predictions for one-dimensional systems range even up to 5 GHz, made possible by the particularly strong direct Rashba spin-orbit interaction [Klo11; Klo13b]. Conversely, this strong SOI may lead to an undesired enhancement of qubit relaxation and dephasing rates, via coupling to phonons or charge noise. However, the direct Rashba SOI is also predicted to be tunable to a large extent through local electric

fields [Klo11; Mai13; Klo18], enabling electrical control over the SOI strength and Landé g-factor. Such electrical tunability provides a path towards a spin qubit with switchable interaction strength, using what we term a *spin-orbit switch*. The spin-orbit switch can be used to selectively idle a qubit in an isolated configuration of weak SOI and low decoherence (*Idle*-state), while for fast manipulation it is tuned to a regime of strong SOI (*Control*-state) and is selectively coupled to an EDSR driving field or microwave resonator by controlling the qubit Zeeman energy [Klo13b; Bur20]. Here, we experimentally realize the key components of this approach, through the demonstration of an ultrafast and electrically tunable hole spin qubit in a Ge/Si core/shell nanowire. We use SOI-mediated EDSR to perform fast two-axis qubit control and implement Ramsey and Hahn echo pulsing techniques to compare the qubit's coherence times. We then demonstrate a high degree of electrical control over the Rabi frequency, g-factor, and driven qubit decay time by tuning the voltage on one of the dot-defining gates, illustrating the basic ingredients of a spin-orbit switch. The spin-orbit switch functionality that we demonstrate here shows moderate on/off ratios of about 7 for both Rabi frequency and coherence times, which could in future devices likely be increased through improved gate design. We extract a spin-orbit length that is extraordinarily short and electrically tunable over a large range down to 4 nm for holes of heavy-hole mass. This control allows us to optimize our qubit for speed of operation, resulting in Rabi frequencies as large as 435 MHz.

Figure 8.1 **a** shows a scanning electron micrograph of the device comprising five gates beneath a Ge/Si core/shell nanowire [Bra16c; Con17; Fro18]. A depletion-mode few-hole double quantum dot is formed inside the nanowire by positively biasing the five bottom gates. Throughout this work, we perform measurements of electronic transport through the double quantum dot, using the source (S) and drain (D) contacts indicated in Figure 8.1 **a** (for more details about the device and measurement setup, see Methods). We operate the device at a transition exhibiting Pauli spin blockade [Ono02], which

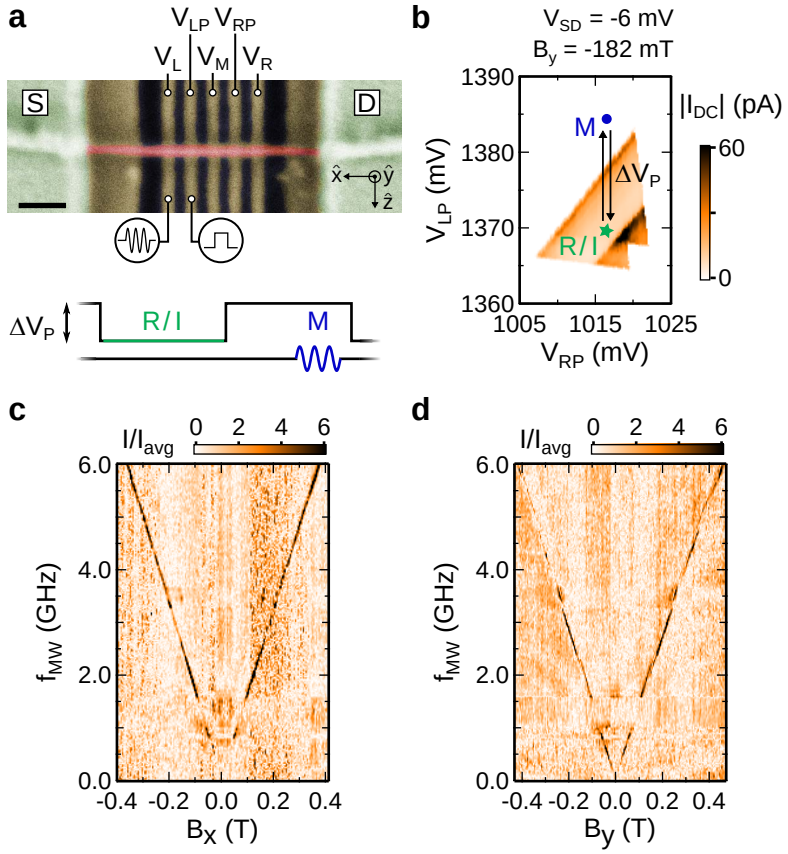

FIGURE 8.1 | **Experimental setup and electric dipole spin resonance. a** Scanning electron micrograph of a cofabricated device, showing source (S) and drain (D) contacts and gates, as labeled. The scalebar corresponds to 100 nm. The inset at the bottom illustrates the pulse scheme. The points R, I and M indicate the locations of the readout, initialization, and manipulation stages, respectively, of the pulsing scheme (see **b**). The depth of the square pulse is ΔV_P. **b** Measurement of a set of bias triangles taken with a source-drain voltage $V_\mathrm{SD} = -6\,\mathrm{mV}$ showing Pauli spin blockade which is partially lifted at a finite magnetic field $B_\mathrm{y} = -182\,\mathrm{mT}$. **c, d** Spin blockade leakage current indicating electric dipole spin resonance as a function of microwave frequency and magnetic field magnitude in $\hat{x}$ (**c**) and $\hat{y}$ (**d**) direction. Horizontal bands of decreased intensity are due to microwave resonances in the high-frequency circuitry. For detailed measurement parameters and description of data analysis, see Methods.

we use for spin readout in transport measurements.

In our setup, gates L and LP are connected via bias-tees to high-frequency lines as indicated in Figure 8.1 **a**, allowing us to apply square voltage pulses and microwave bursts to these gates. The measurements are performed with a two-stage pulse scheme (see inset Fig. 8.1 **a**). First, the system is initialized at point I (see Fig. 8.1 **b**) in a

spin-blockaded triplet state. Then, with a square pulse of depth ΔV_{P}, it is pulsed into Coulomb blockade to point M where a microwave burst of duration t_{burst} is applied. Finally, back at the readout point R, a current signal is measured if the spins were in a singlet configuration after manipulation.

Figures 8.1 **c** and **d** show typical EDSR measurements, where the microwave frequency f_{MW} is swept versus the applied magnetic field $\vec{B}_{\mathrm{ext}}$ along the $\hat{x}$- and $\hat{y}$-axis, respectively. On resonance, the spin is rotated, lifting spin blockade and leading to an increased current. From Figures 8.1 **c** and **d**, we extract $g_{\mathrm{x}} = 1.06$ and $g_{\mathrm{y}} = 1.02$. With $\vec{B}_{\mathrm{ext}}$ aligned along the $\hat{z}$ direction, no EDSR signal could be observed, as will be discussed later.

8.2 Coherent Manipulation and Two-Axis Control

To demonstrate coherent control, we now vary the pulse duration t_{burst} and observe Rabi oscillations, in the form of the typical chevron pattern shown in Figure 8.2 **a**. Figure 8.2 **b** shows the dependence on the microwave power P_{MW}. From line cuts, we extract the Rabi frequency f_{Rabi} (see Methods), which is shown in Figure 8.2 **c** as a function of the microwave amplitude. The data at low amplitudes is in good agreement with a linear fit (black dashed line in Fig. 8.2**c**), as expected theoretically. The saturation behaviour at higher amplitudes likely originates from smaller effective displacement due to anharmonicity [Yon14; Tak16] in dot confinement for the particular gate voltage configuration used here, leading to sub-linear dependence on the amplitude A_{MW} of the microwave driving field. Additionally, the strong and tunable SOI in our system could potentially lead to such non-linearities.

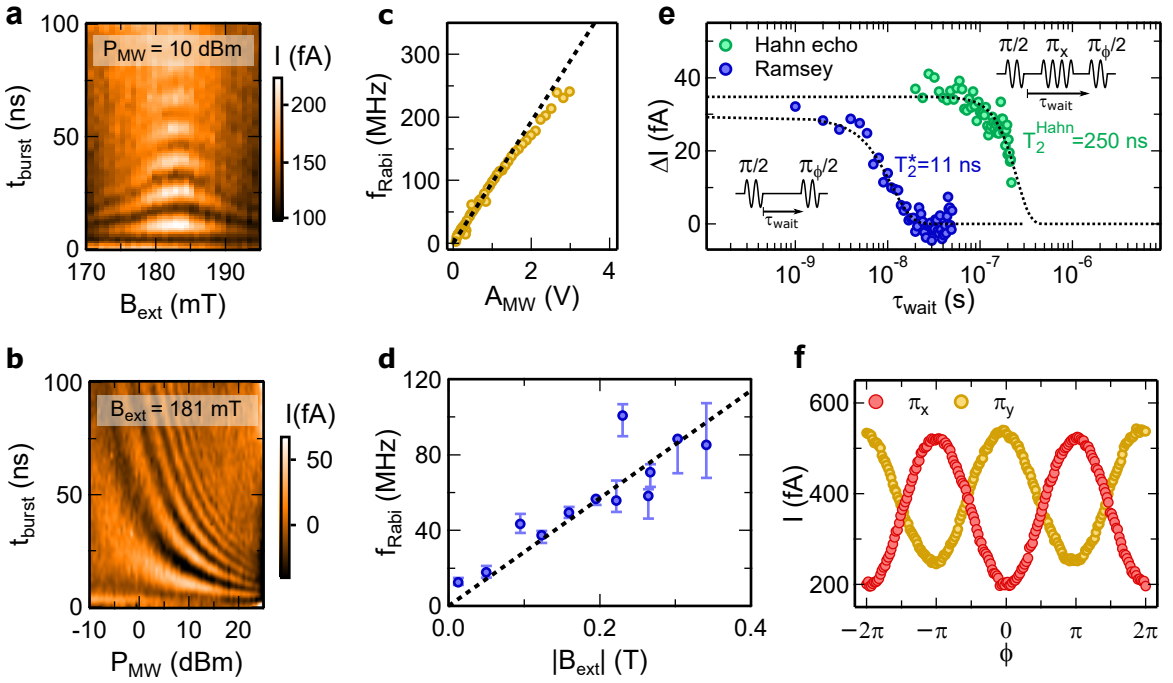

FIGURE 8.2 | **Coherent qubit control.** **a** Measurement of the current as a function of microwave burst duration and magnetic field. We observe a Rabi frequency of 72 MHz. **b** Power dependence of Rabi oscillations in the same configuration as in **a**. **c** Extracted Rabi frequency as a function of the microwave amplitude, from fits of the data in **b** (see Methods for details). The black dashed line is a linear fit to the extracted Rabi frequencies. **d** Rabi frequency as a function of the magnitude of the external magnetic field. The black dashed line is a linear fit to the data over the whole range with zero offset. The error bars correspond to the inaccuracy of the frequency-dependent power calibration (see Section B.1 of the Supplementary Information). **e** Decay of Ramsey fringes (blue points) and Hahn echo (green points) as a function of the waiting time τ_{wait} between the two $\pi/2$-pulses. Insets show pulse sequences used for Ramsey (bottom left) and Hahn echo (top right). Black dotted lines are fits of the data to exponential decay. **f** Demonstration of two-axis qubit control by applying a Hahn echo sequence with two orthogonal π-pulses. The amplitudes of the fringes of the two datasets differ due to an offset in the calibration of the $\pi/2$-pulse duration between the two measurements.

In the presence of SOI, the oscillating electric field on gate V_{LP} due to the microwaves gives rise to an oscillating effective magnetic field $\vec{B}_{\text{eff}}(t)$, with magnitude [Gol06]:

$$|\vec{B}_{\text{eff}}(t)| = 2|\vec{B}_{\text{ext}}| \cdot \frac{l_{\text{dot}}}{l_{\text{so}}} \cdot \frac{e|\vec{E}_{\text{MW}}(t)|l_{\text{dot}}}{\Delta_{\text{orb}}}, \tag{8.1}$$

with e the elementary charge, $\vec{E}_{\text{MW}}(t)$ the ac electric field in the dot generated by

the microwaves, l_{dot} the dot length, $\Delta_{\mathrm{orb}} \propto l_{\mathrm{dot}}^{-2} m_{\mathrm{eff}}^{-1}$ the orbital level splitting, and l_{so} the spin-orbit length, which we define here as setting the distance a hole has to travel along the nanowire to have its spin flipped due to SOI. This effective field $\vec{B}_{\mathrm{eff}}$ drives the Rabi oscillations, with Rabi frequency $f_{\mathrm{Rabi}} = g_{\parallel}\mu_{\mathrm{B}}|\vec{B}_{\mathrm{eff}}(t)|/2h$, with $g_{\parallel}$ the g-factor along the direction of $\vec{B}_{\mathrm{ext}}$. From equation (8.1) we see that $|\vec{B}_{\mathrm{eff}}|$ scales linearly with $|\vec{B}_{\mathrm{ext}}|$. We measure the Rabi frequency for different $|\vec{B}_{\mathrm{ext}}|$ and plot the result in Figure 8.2 **d**. Despite relatively large error bars at higher fields due to the inaccuracy of the frequency-dependent microwave power calibration (see Section B.1 of the Supplementary Information), the measurement agrees well with a linear dependence of the Rabi frequency on $|\vec{B}_{\mathrm{ext}}|$, as expected for SOI-mediated EDSR [Gol06; Now07].

Next, in order to characterize the free induction decay, we apply a Ramsey pulse sequence, as depicted in Figure 8.2 **e**. A fit to a Gaussian decay yields the dephasing time $T_2^* = 11 \pm 1\,\mathrm{ns}$. This value is one order of magnitude smaller than in comparable hole spin qubit systems [Hig14c; Hen20a; Wat18b]. This may be attributed to low-frequency noise, which could for instance be due to gate voltage fluctuations, frequency jitter of the microwave source, charge fluctuators, or residual nuclear spin noise. Nevertheless, we can mitigate this to a large extent using a Hahn echo sequence, prolonging coherence by a factor of ∼25, thus demonstrating efficient decoupling of the qubit from low-frequency noise. In our measurements, we find no clear indication of decay due to spin relaxation. Indeed, previous experimental [Hu12] and theoretical [Mai13] works have found spin relaxation times in Ge/Si nanowires to be in the millisecond to second regime, much longer than can be probed using our pulsing and read-out scheme.

Finally, we use a modified Hahn echo pulse sequence to demonstrate two-axis control. We employ either a π_{x}- or a π_{y}-pulse and vary the phase of the second $\pi_{\phi}/2$-pulse (see schematics in Fig. 8.2 **e**). This results in two sets of Ramsey fringes as shown in Figure 8.2 **f**, which are phase-shifted by π. These measurements demonstrate universal, two-axis control of the hole spin qubit.

8.3 Spin-Orbit Switch Functionality

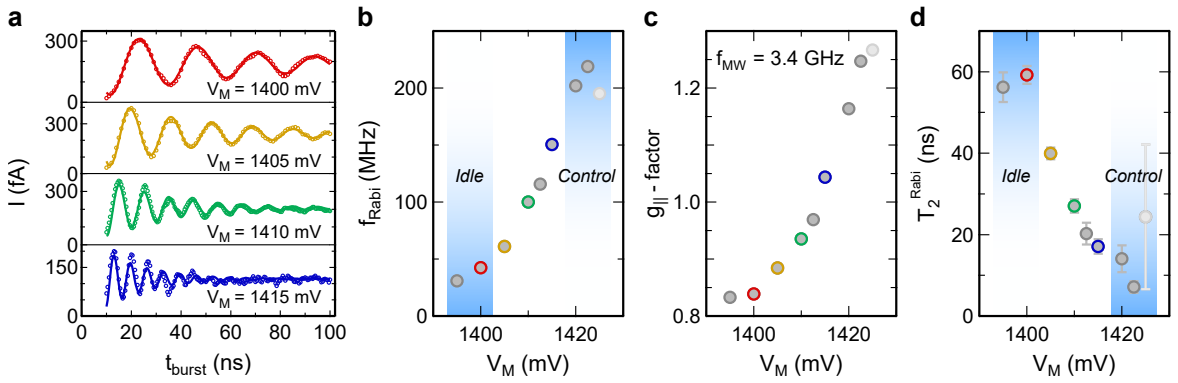

FIGURE 8.3 | **Electrical tunability of qubit parameters.** **a** Rabi oscillations for four different gate voltage values V_M. Here, all parameters were kept constant, except when indicated in the plots. **b, c, d** Rabi frequency, g-factor, and T_2^Rabi as a function of the gate voltage V_M, as extracted from fits to line cuts such as shown in **a**. Error bars correspond to the standard deviations resulting from the fitting. Insets in **b** and **d** indicate possible idling and control points. These points define a spin-orbit switch with on/off ratio of 7.1 and 8.3 for the f_Rabi and T_2^Rabi, respectively. Note that the measurement corresponding to the point at $V_\mathrm{M} = 1425\,\mathrm{mV}$ (light grey) suffers from a low signal-to-noise ratio, due to reduced interdot tunnel coupling, resulting in a large uncertainty in the analysis of the data at this point.

The measurements of Figure 8.2 establish Ge/Si nanowires as a platform for hole spin qubits. The particular direct Rashba SOI [Klo11; Klo18] provides a unique way to electrically control the qubit via the SOI strength and qubit Zeeman energy [Mai13; Klo13b]. This tunability can be exploited for optimizing qubit relaxation and dephasing times, as well as selective coupling of the qubit to EDSR drive fields or microwave resonators [Klo13b; Tri08; Nig17]. Here, we demonstrate this distinct gate-tunability of hole spin qubits in Ge/Si core/shell nanowires, where we investigate electrical control over the g-factor, Rabi frequency, and coherence time.

The gate voltages not only provide the electrostatic confinement but also constitute a static electric field on the order of tens of V/μm inside the quantum dots, which has a significant effect on the strength of SOI [Klo18; Klo11]. Figure 8.3 **a** shows example Rabi oscillations for four different gate voltages V_M. Here, f_MW and P_MW are kept fixed, while $|\vec{B}_\mathrm{ext}|$ is adjusted to compensate for changes in the $g_\parallel$-factor along B_ext,

keeping the qubit on resonance with the microwave drive. As shown in Figure 8.3 **b**, we find that the Rabi frequency depends strongly on V_{M}, with a gate voltage change of 30 mV resulting in a 7-fold increase of the Rabi frequency.

For SOI-mediated spin rotations [Gol06], the Rabi frequency is proportional to the effective magnetic field given by Eq. 8.1 and the g-factor $g_{\parallel}$. For measurements at a fixed microwave resonant frequency f_{MW}, as done here, the apparent g-factor dependence vanishes and the Rabi frequency depends only on the spin-orbit length l_{so}, the quantum dot confinement Δ_{orb}, and the ac electric field $E_{\mathrm{MW}}(t)$ created through the periodic gate voltage modulation (see Supplementary information, Eq. B.1).

We have carefully analyzed each of the contributions to the change of the Rabi frequency (see Section B.2.2 of the Supplementary Information). In particular, we find that the orbital level splitting Δ_{orb} shows only a weak dependence on gate voltage V_{M} and that the electric field amplitude E_{MW} stays roughly constant. These effects are not sufficient to explain the large change in f_{Rabi} and we therefore find that the large change must mostly be attributed to a gate-tunability of the spin-orbit length l_{so}. Using equation (8.1), we extract upper bounds of l_{so} (see Supplementary Information Section B.2.3). We find remarkably short values of l_{so} that are tuned from 23 nm down to 4 nm. Here we assume a heavy-hole effective mass, as suggested by independent transport measurements at high magnetic field [Fro21a]. Such a strong SOI was predicted for the direct Rashba SOI [Klo11; Klo18]. This range of l_{so} overlaps with values found in antilocalization [Hig14b] and spin blockade experiments [Fro21a]. Finally, while the direct Rashba SOI term is predicted to be very strong in this system, additional weaker SOI terms may also be present, but cannot be distinguished here.

Besides the Rabi frequency, also the coherence is strongly affected by V_{M}, as shown in Figure 8.3 **a**. We plot the characteristic driven decay time T_2^{Rabi} in Figure 8.3 **d**, finding that it scales roughly inversely with f_{Rabi} and $g_{\parallel}$: a short decay time coincides with a high Rabi frequency, and vice versa. Together with the tunability of the Rabi

frequency, this control over the qubit coherence time allows us to define (see insets Figs. 8.3 **b** and **d**) a fast qubit manipulation point (*Control*) and a qubit idling point featuring significantly improved coherence (*Idle*). This demonstrates the functionality of a spin-orbit switch, though here with modest on/off ratios for the switching of f_{Rabi} and T_2^{Rabi} between the *Control* and *Idle* points.

Moreover, the variation of $g_{\parallel}$ in Figure 8.3 **c** effectively adds a third mode of operation to the spin-orbit switch, where individual qubits can be selectively tuned, for instance in and out of resonance with a microwave cavity, enabling a switch for qubit-resonator coupling [Tri08; Nig17]. Finally, we find that the pulse depth ΔV_{P} can also be used to tune of f_{Rabi} and $g_{\parallel}$ (see Section B.2.1 of the Supplementary Information), indicating that dynamically pulsing these quantities is feasible.

8.4 Ultrafast Rabi Oscillations

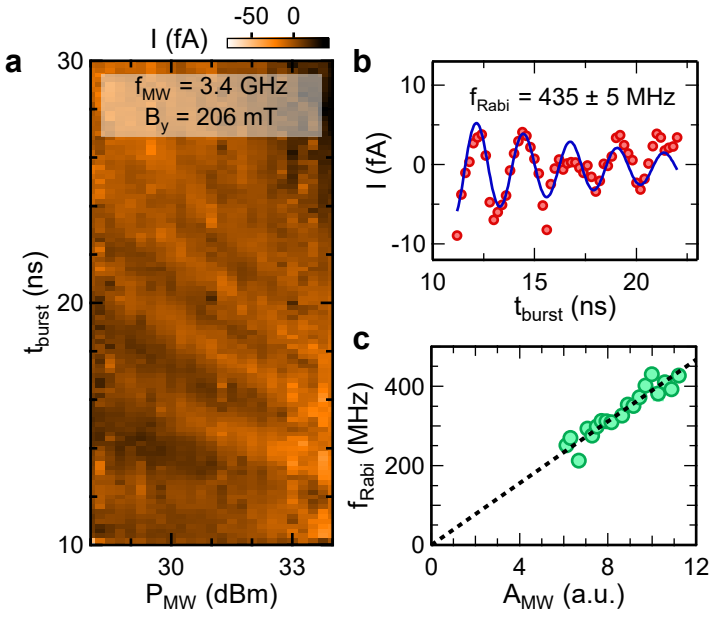

FIGURE 8.4 | **Ultrafast coherent control.** **a** Power-dependence of ultrafast Rabi oscillations. **b** Line cut of data shown in **a** at a microwave power of 34 dBm. The data is fitted (blue solid curve) as in Fig. 8.2, after subtraction of a linear background. **c** Rabi frequency as a function of microwave amplitude, extracted from fits to line cuts in **a**. Dashed black line is a linear fit to the data.

In a next step, we now use the electrical tunability to optimize the gate voltages for a high Rabi frequency and furthermore increase the applied microwave power. In Figure 8.4, we show a measurement of ultrafast Rabi oscillations, with the maximum Rabi frequency reaching a value of $\sim 435\,\mathrm{MHz}$ (see Fig. 8.4 **b**), allowing for spin-flip times of the qubit as short as 1.15 ns. As can be seen in Figure 8.4 **c**, the Rabi frequency scales linearly with applied microwave amplitude in this regime of ultrafast qubit operation and shows no signs of saturation for the gate configuration used here, in contrast to Figure 8.2 **b**. This indicates that even higher Rabi frequencies may be possible through the application of a higher microwave power. Note that pulse imperfections play a larger role for shorter pulse duration and higher amplitudes, which likely partially explains the decrease in T_2^{Rabi} with increased microwave amplitude.

Notably, the observed Rabi frequencies of over 400 MHz are roughly 1/8 of the Larmor precession frequency of 3.4 GHz. The system is thus approaching the strong driving regime where the rotating wave approximation is not applicable anymore, opening the possibility for ultrafast, non-sinusoidal spin-flipping [Kat03; Lau16] that has not been realized before with conventional spin qubits. We note that in our experiment, effects of strong driving [Lau16] could contribute to the reduced visibility of Rabi oscillations at the high Rabi frequencies shown in the measurements of Figure 8.4.

8.5 Conclusions

We have demonstrated ultrafast two-axis control via EDSR of a hole spin qubit in a Ge/Si core/shell nanowire. Our measurements firmly demonstrate the feasibility of single-spin qubit operations on nanosecond timescales. Ideally, such fast operations would be combined with long qubit coherence times. We observe a relatively short inhomogeneous dephasing time, which is likely related to technical pulsing challenges at such short timescales. This may be resolved with improved instrument control. Also, we measure a much larger spin echo decay time, which indicates the presence of

low-frequency noise affecting our qubit. Finally, the use of a charge sensor will allow to decouple the quantum dots from the neighboring Fermi reservoirs, likely leading to a significant further enhancement of the coherence time.

We have demonstrated a 7-fold increase of the Rabi frequency for a relatively small change in gate voltage. Similarly, we find that the driven decay time of our qubit can be tuned by the same gate voltage, demonstrating the working principle of a spin-orbit switch. Thus far, the spin-orbit switch is limited to moderate on/off ratios of f_{Rabi} and T_2^{Rabi}. However, improved devices with gates designed for precise engineering of the electric field profile could in future experiments lead to a higher level of control over the SOI, resulting in higher on/off ratios as suggested by theoretical work [Klo13b]. Our measurements indicate the presence of an exceptionally strong spin-orbit interaction in Ge/Si core/shell nanowires, in qualitative agreement with predictions of direct Rashba SOI [Klo11; Klo18]. A more quantitative comparison to theory, as well as improved gate switching, requires precise engineering of the electric field and single-hole dot occupation, both of which can be achieved through optimization of the gate design.

The high tunability of the qubit demonstrates the suitability of the platform for the implementation of a qubit with switchable interaction strengths. The effect of the gate voltages and the pulse depth on the qubit resonance frequency and the Rabi frequency have the potential to dynamically pulse the characteristic qubit parameters and interaction strengths from a qubit manipulation to an idling point. Furthermore, the spin-orbit switch could allow tuning to 'sweet spots' of operation, where the SOI strength is to first order insensitive to charge noise, leading to enhancement of qubit coherence [Klo18]. Finally, the strong spin-orbit interaction holds potential for realizing fast entangling operations between distant spin qubits, mediated by a microwave resonator [Tri08; Nig17; Klo13b; Bor20; Bur20].

8.6 Methods

8.6.1 Device Fabrication

The device features a set of five gates with a width of 20 nm and a pitch of 50 nm defined by electron beam lithography on a p^{++}-doped Si chip covered with 290 nm of thermal oxide. The gates are covered by a 20 nm thick layer of Al_2O_3 grown by atomic layer deposition in order to electrically insulate them from the nanowire. A single Ge/Si core/shell nanowire with a core radius of about 10 nm and a shell thickness of 2.5 nm [Con17] is placed deterministically across the set of gates using a micromanipulator. The nanowire is roughly aligned with the coordinate system in Figure 8.1 **b** but the exact angle in the $\hat{x}\hat{z}$ plane is unknown. Finally, ohmic contacts are fabricated by electron beam lithography and metallized with Ti/Pd following a short dip in hydrofluic acid to remove the native oxide. The scanning electron micrograph shown in Fig. 8.1 **a** is from a similarly fabricated device as used here.

8.6.2 Experimental Setup

The sample is wire-bonded to a printed-circuit board providing dc wiring and RF lines, coupled via bias tees. The circuit board is mounted in a Bluefors dilution refrigerator with a base temperature around $T_{\text{base}} = 10\,\text{mK}$, at which tempreature all measurements are taken. Each high-frequency line includes attenuators with combined values of ∼30 dB. A Basel Precision Instruments LNHR DAC is used to supply the dc voltages, and a Basel Precision Instruments LNHS I/V converter is used for readout of the qubit in transport.

A Tektronix 7122C or AWG5208 arbitrary waveform generator is used to generate the square voltage pulses applied to gate V_{LP}. To drive the qubit, either an analog Keysight E8257D signal generator or a E8267D vector signal generator supplies the microwave tone. For measurements at high microwave power a RF-Lambda model

RFQ132070 amplifier was used. Two different configurations of the setup are used for microwave burst generation. For the measurements in Figures 8.1 **c-d**, 8.2 **d**, 8.3, and 8.4, the amplitude of the microwaves is modulated by means of an RF-switch (ZASWA-2-50DRA+ from MiniCircuits), triggered by the arbitrary waveform generator. The RF-switch has a minimum pulse width of 10 ns. For the measurements in Figures 8.1 **b**, 8.2 **a-c, e, f**, the microwave bursts are generated by IQ modulation of the vector signal generator's microwave tone. Here, the minimum pulse width is 6 ns. In either configuration, a lock-in amplifier is used to chop the bursted microwaves at a frequency of 89.75 Hz and the I/V converter output is demodulated at his frequency. This allows us to separate the current signal due to the applied microwaves from the background.

8.6.3 Data Analysis

Rabi frequencies are extracted from fits to $I\left(t_{\mathrm{burst}}\right) = I_0 + C \cdot \sin\left(2\pi f_{\mathrm{Rabi}} t_{\mathrm{burst}} + \phi\right) \cdot \exp\left(-t_{\mathrm{burst}}/T_2^{\mathrm{Rabi}}\right)$. Here, I_0 is an offset, C the amplitude, ϕ a phase shift, and T_2^{Rabi} the characteristic decay time. Furthermore, we post-processed raw data sets in the following ways. The data in Fig. 8.1 **c** (8.1 **d**) was offset by 10 mT (20 mT) to compensate for trapped magnetic flux. Furthermore, the average value has been subtracted from each column and row of the raw data. Then each row has been divided by the average row value. Similarly, for the plots of Fig.8.2 **b** and 8.4 **a**, the average value has been subtracted from each column and row of the raw data. In Fig. 8.4 **a**, data for microwave burst times below the minimum pulse width achievable by our electronics is omitted.

8.6.4 Measurement Details

In the following we list the relevant parameters that were used for the various measurements. For the measurements of Figs. 8.1 **c-d**, a fixed pulse amplitude $\Delta V_{\mathrm{P}} = 0.55\,\mathrm{V}$ and a burst duration $t_{\mathrm{burst}} = 15\,\mathrm{ns}$ was used. In Figs. 8.2 **a-c**, $\vec{B}_{\mathrm{ext}}$ was oriented along

the $-\hat{y}$-axis. For Fig. 8.2 **d**, $f_{\mathrm{MW}} = 3.4\,\mathrm{GHz}$ was used and $\vec{B}_{\mathrm{ext}}$ was oriented in the $\hat{x}\hat{y}$-plane, making an angle of 40° with the $\hat{y}$-axis. In Fig. 8.2 **e**, the duration of the π-pulse $t_\pi = 13\,\mathrm{ns}$, $P_{\mathrm{MW}} = 3\,\mathrm{dBm}$, $f_{\mathrm{MW}} = 2.6\,\mathrm{GHz}$, and $|\vec{B}_{\mathrm{ext}}| = 181\,\mathrm{mT}$ along the $-\hat{x}$-axis. For Fig. 8.2 **f**, we used $P_{\mathrm{MW}} = 14\,\mathrm{dBm}$, $f_{\mathrm{MW}} = 3.4\,\mathrm{GHz}$ and $|\vec{B}_{\mathrm{ext}}| = 292\,\mathrm{mT}$, along the same direction as used for Fig. 8.2 **d**. Finally, for the measurements of Fig. 8.3, we used $P_{\mathrm{MW}} = 25\,\mathrm{dBm}$ and the orientation of $|\vec{B}_{\mathrm{ext}}|$ was the same as in Fig. 8.2 **d**.

For completeness, we also mention the other gate voltages used for the measurements of Fig. 8.3: $V_{\mathrm{L}} = 3710\,\mathrm{mV}$ and $V_{\mathrm{R}} = 1495\,\mathrm{mV}$, V_{LP} and V_{RP} depend on V_{M}, but are similar to the values used for Fig. 8.1 **b**.

Data availability

The data supporting the plots of this paper are available at the Zenodo repository with the following DOI: 10.5281/zenodo.4290131

Acknowledgements

We thank Stefano Bosco, Bence Hetényi, Christoph Kloeffel, Daniel Loss, Arne Laucht, and Alex Hamilton for useful discussions. Furthermore, we acknowledge Sascha Martin and Michael Steinacher for technical support. This work was partially supported by the Swiss Nanoscience Institute (SNI), the NCCR QSIT, the NCCR SPIN, the Georg H. Endress Foundation, Swiss NSF (grant nr. 179024), the EU H2020 European Microkelvin Platform EMP (grant nr. 824109), and FET TOPSQUAD (grant nr. 862046).

8.7 Author correction

In the version of this Article originally published, the dependence of the Rabi frequency on the g-factor was stated incorrectly in the main text below Eq. 8.1 and in Eq. B.1 of the Supplementary information. Following Golovach, Borhani and Loss, *Phys. Rev. B* **74**, 165319 (2006) (Ref. [Gol06] in the manuscript), the corrected versions are (main text):

$$f_{\mathrm{Rabi}} = g_{\parallel}\mu_{\mathrm{B}}|\vec{B}_{\mathrm{eff}}(t)|/(2h) \ , \tag{8.2}$$

and (Supplementary information):

$$f_{\mathrm{Rabi}} = f_{\mathrm{MW}} \cdot \frac{l_{\mathrm{dot}}}{l_{\mathrm{so}}} \cdot \frac{e|\vec{E}_{\mathrm{MW}}(t)|l_{\mathrm{dot}}}{\Delta_{\mathrm{orb}}}. \tag{8.3}$$

These changes leave the results of the Article unaffected, except for changing the values of the gate-voltage dependent spin-orbit lengths slightly. The corrected range extends from 4 nm to 23 nm (before correction 3 nm to 28 nm). These values are revised in the corrected manuscript (section 8) and Supplementary information (appendix B).

In the uncorrected version, part of the tuning gate-range of spin-orbit lengths could potentially be attributed to the g-factor. Furthermore, when measuring at a constant value of the external magnetic field B_{ext}, also in the correct formulation f_{Rabi} and l_{so} still depend on the g-factor. However, when measuring at a fixed resonant microwave frequency $f_{\mathrm{MW}} = g_{\parallel}\mu_{\mathrm{B}}B_{\mathrm{ext}}/h$, any change of the g-factor is compensated by an inversely proportional change of B_{ext}, and the apparent g-factor dependence vanishes from the equation of the Rabi frequency, thus making the observation of a gate-voltage dependent spin-orbit coupling strength more robust. This is now also reflected in the changed manuscript.

9 Summary

On the path to a fault-tolerant quantum computer, spin qubits in semiconductors are candidates for fast and reliable qubit operation. The compatibility with modern semiconductor technology combined with their small footprint inspire the vision of a large-scale quantum computer chip with densely packed spin qubits. But the size implies more than just economical packaging of a large number of spin qubits. As discussed in section 2, the reduction of structure size to the nanometer scale and dimensionality to one- and zero-dimension enables control over material properties, that are not available otherwise. In particular, hole spin states in one-dimensional Ge experience a strong and tunable spin-orbit interaction and promise long coherence times. Taken together, these properties allow for the implementation of a new kind of spin qubit. Quantum dots in Ge systems can therefore host hole spin qubits that meet the requirements of qubit operation, as outlined in section 3, in a way that allows them to become the cornerstone of a fast and scalable quantum computing platform.

Accordingly, in this thesis we explore Ge/Si core/shell nanowires as a material system that provides features useful for the operation of hole spin qubits. The hole spin are confined in quantum dots, which thus need to enable a high level of control over the charge and spin state of the confined holes. In section 6 the basic nanowire quantum dot device is introduced and the formation of quantum dots is described. Quantum dots are electrostatically defined with a set of metallic gates which locally deplete the hole gas that is formed in the core of Ge/Si core/shell nanowires. These gates enables a high level of control over size and position of single quantum dots, as summarized in table 6.1, in which also the typical estimated number of holes occupying the quantum dot is listed. In particularly small quantum dots, defined by two neighbouring gates as shown in Figure 6.2, signatures of a singly occupied quantum dot are observed. The gate-controlled nanowire device also enables the formation of double and even triple quantum dots (Figure 6.4). The interdot tunnel coupling strength can be adjusted,

which allows to tune the device continuously from a single to a double quantum dot configuration. The nanowire geometry enables precise control over the quantum dot confinement with only a small number of closely spaced metal gates. The large contribution of the natural confinement of a nanowire to one dimension also allows for the observation of a vast number of quantum dot charge transitions. Amongst these, transitions equivalent to an effective (1,1)-(0,2) configuration, but at higher filled orbitals, can be observed. Because these transitions resemble the case of a quantum dot with only two holes, the current is rectified due to Pauli spin blockade. The observation of Pauli spin blockade is an important ingredient for spin readout in future experiments. In conclusion, the findings of section 6 make quantum dots in Ge/Si core/shell nanowires suitable candidates for spin qubit experiments.

In section 7, we use such a Ge/Si core/shell nanowire quantum dot device to study the leakage current in Pauli spin blockade. The strong spin-orbit interaction mixes the $T_{\Uparrow,\Downarrow}(1,1)$ states to the $S(0,2)$ state, thereby lifting the spin blockade, giving rise to a finite leakage current. The measurement of these transitions as a function of magnetic field reveal a minimum of leakage current around zero magnetic field, strong orbital effects and a magnetic field dependent g-factor. The strong orbital effects result in a magnetic field dependence of the quantum dot addition energy and interdot tunnel coupling. In combination with the strong SOI, the orbital effects give rise to an enhancement of the Landé g-factor with magnetic field. All of these features are accounted for in a spectroscopic model which well reproduces the observed experimental data. This model enabled us to extract a value of the spin-orbit length of $\sim$65 nm, demonstrating the presence of very strong spin-orbit interaction in Ge/Si core/shell nanowires.

In the last part of this thesis, we exploited the properties of Ge/Si core/shell nanowires for the implementation of an ultra-fast and gate-tunable hole spin qubit. The spin-orbit interaction allows for electric dipole spin resonance (EDSR), leading to the controlled

lifting of Pauli spin blockade when the frequency of a microwave tone applied on of the gates is on resonance with the qubit transition (see Figure 8.1). Coherent Rabi oscillations are observed as a function of microwave burst time, with the Rabi frequency depending linearly on the magnitude of the external magnetic field, in agreement with EDSR mediated by spin-orbit interaction. Ramsey interference measurements determine a coherence time $T_2^* = 11\,\mathrm{ns}$, which can be enlarged by a factor 25 by using spin echo techniques, identifying low-frequency noise as the limitation. Furthermore, two-axis control of the hole spin qubit is demonstrated. Finally, we find a remarkable gate-tunability of the Rabi frequency. By relatively small variations of the gate voltages, the Rabi frequency can be tuned in a wide range from roughly 30 MHz to above 200 MHz. The variation of the Rabi frequency can be ascribed to either an increase of the spin-orbit interaction strength or a change of direction of the effective magnetic field $\vec{B}_{\mathrm{eff}}$. For the spin-orbit interaction length we extract an upper limit of 20 nm. Eventually, in an optimal configuration we demonstrate ultrafast coherent Rabi oscillations above 400 MHz.

In conclusion, the aforementioned results constitute important milestones for the implementation of an all-electrical and configurable hole spin qubit in Ge/Si core/shell nanowires. The proof-of-principle studies of fabrication and operation of a fast qubit in these nanowires allow for advanced experiments and research regarding improvements in a variety of aspects. These future prospects form the topic of section 10.

10 Outlook

The results discussed in this thesis demonstrate that Ge/Si core/shell nanowires can host fast and electrically tunable hole spin qubits. Naturally, this serves only as a starting point for more advanced characterization and optimization. This section outlines possible future routes on the way to viable hole spin qubits in Ge/Si core/shell nanowires. The fabrication of qubit devices with improved and advanced characteristics will remain an integral part and is discussed in section 10.1. Closely related to this topic is the engineering of the electric field profile, which will, for instance, enable more precise control over magnitude and direction of the spin-orbit interaction in these electrically controllable hole spin qubits. The impact of electric field strength and direction on the qubit is pronounced, and, as discussed in section 10.2, has the potential to optimize qubit gates, coherence, and couplings. Finally, as a long-term goal, considerations regarding the implementation of a large scale qubit network are discussed in section 10.3.

10.1 Prospects of Device Fabrication

First generation Ge/Si nanowire devices, that are fabricated as described in section 4, already enable a multitude of experiments as discussed in the other sections of this thesis and summarized in section 9. Starting from the formation of highly tunable (arrays of) quantum dots, studies of spin physics and finally one- and two-axis hole spin qubit control are possible. However, certain performance limitations of first generation devices, such as the short coherence time, but also demands for more advanced and complex experiments stimulate the development of more sophisticated fabrication processes. Therefore, this section describes some routes for future devices, sorted in four categories.

10.1.1 Future Routes for Nanowire Growth

First, the Ge/Si core/shell nanowire itself has not been a parameter within the framework of this thesis. Due to the sophisticated growth as outlined in section 4.1, only a limited number of nanowires with varying characteristics are available. This limits the exploration of implications of different nanowire parameters regarding the qubit performance. Future studies could investigate the impact of morphological properties such as the Ge core radius, the Si shell thickness and the strain resulting from it, but also the effect of isotopic purification.

Because strain is both determining the properties of holes occupying the lowest energy subbands in Ge/Si core/shell nanowires [Klo11] but also inducing crystal defects [Day13; Gol08a; Gol09], precise knowledge of the formation and relaxation of strain during the nanowire growth is key. The large impact of strain on electronic transport and quantum dots [Con17] also motivates the investigation of consequences on the qubit performance.

Besides an engineered strain profile, also other innovations at the level of nanowire growth, such as growing very thin nanowires, might help to achieve the regime of single hole quantum dot occupation. So far, quantum dots in Ge/Si core/shell nanowires have been mostly operated in the multi-hole occupation regime, which, from a scientific point of view, challenges comparisons to theory, and, from a practical point of view, affects properties of hole spins, as they can differ tremendously depending on the occupied subband.

Finally, the effect of isotopic purification [Ito14] of the starting materials Ge and Si on the qubit performance is unexplored, yet such purification has yielded large enhancements of the electron spin qubit coherence time in two-dimensional Si structures [Vel14].

In the long term, as the growth concepts of nanowires are developed further [ORe14; Wen19; Gün19], also control over the site, for instance by templated growth, or control

over the crystal direction of nanowires is conceivable. These new methods have the potential to eliminate the manual transfer of nanowires, which is a major obstacle for upscaling [Gao20].

10.1.2 Improving Electronic Properties

The second category of fabrication routes aims at improving the electronic properties of quantum dot devices. Here, especially the mitigation of charge noise, and ensuing qubit decoherence, is a main concern. Naturally, already during the nanowire growth the electronic properties can be influenced, for instance by reducing incorporation of gold impurities or engineering the strain. But also the post-growth assembly of the qubit device leaves room for optimization. For instance, section 4.4 discusses various material choices for the gate dielectric separating the gates from the nanowire, which can be a major source of charge noise. In a future experiment, different materials need to be compared regarding their suitability for low noise qubit devices. Another change that will be implemented in the next generation of qubit devices is the transition from p^{++} doped to intrinsic silicon substrates. This would render the thick thermal SiO_2 unnecessary, thus eliminating an additional layer of potentially impure oxide. First trials with intrinsic silicon substrates, however, showed large gate-to-gate leakage [Mül19], hence requiring additional measures such as a thin insulating layer on top of the substrate. For such stacked heterostructures, generally the complex interface physics [Spr18] at boundaries of oxides, metals and semiconductors must be considered as well.

10.1.3 Quantum Dot Samples Providing New Features

The third category concerns enhancements of the lithography of existing devices and additional micro- and nanostructures, that could be added to regular devices and provide extra functionalities. One example are side gates, which are already implemented

as shown in Figure 4.1, but have not been used extensively in experiments so far. The idea of side gates is to apply an additional electric field to the quantum dot, without changing the confinement potential, which is inevitably the case if the electric field arising from the bottom gates is changed. A possible application of such extra gates is discussed in section 10.2.

Another route is to work towards devices which can reliably host quantum dots in the single hole occupation regime. In the devices used for the work of this thesis, upon further depletion of quantum dots by raising the plunger gate voltage, the quantum dot splits up into a double quantum dot. This, together with indications of the single hole occupation regime as observed in section 6, suggests that a more narrowly spaced gate structure might enable the full depletion of quantum dots. However, the further reduction of the gate pitch makes high demands at or beyond the limit of feasibility of the current lift-off technique. As the separation between parallel lines is further reduced, the PMMA mask becomes unstable and single lines can not be resolved after metallization. Figure 10.1 **a** shows an example of unsuccessful reduction of the gate pitch to 40 nm, where the collapse of the PMMA mask lead to interruptions of the lines. Furthermore, the increased dose density leads to overexposure, which results in merged lines.

Therefore, other techniques can be considered [Ste12b], such as a focused helium ion beam, which can be used for both milling [Vol07] and lithography [Win09]. Both techniques profits from the reduced interaction volume of helium ions compared to electrons and a smaller resolvable feature size. However, in ion milling processes swelling and other damages due to, for instance, ion implantation are common [Liv09; Ste12b].

Besides fabricating bottom gates in a single layer, and thus reducing the line separation ever more, two layers of interleaved gates can be fabricated. Figures 10.1 **b** and **c** show the results of a trial to interleave two sets of five lines with a pitch of 50 nm each. On the upside, this approach allows to keep the line spacing in a technically feasible regime

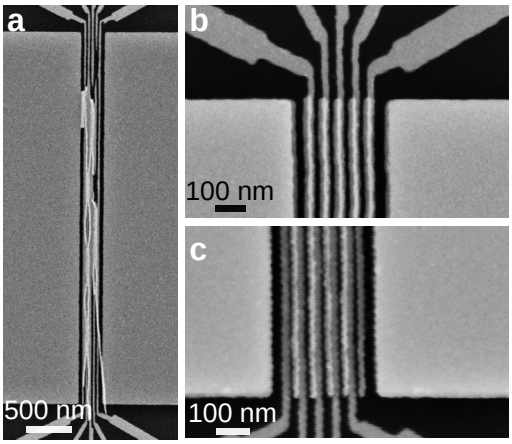

FIGURE 10.1 | **Miniaturization of bottom gate structure. a** | Fabrication of parallel lines with a pitch of less than 50 nm often results in pattern collapse, as seen in the top part, or overexposure, as seen in the center part. **b,c** | Two interleaving sets of gates with a pitch of 50 nm each would reduce the effective gate-to-gate distance at the cost of requiring very high alignment precision and an additional insulating layer between the two gate layers. Here, random offsets of subsequent layers are observed.

yet it halves the effective pitch. On the downside, an extra insulating layer might be required in order to insulate the two gate layers from each other and, additionally, this approach requires very high alignment capabilities. As can be seen in Figures 10.1 **b** and **c**, the alignment procedure used here yields uncontrollable pattern shifts with the two gate layers overlapping partially.

One example of a quantum dot device with additional functionality comprises an integrated charge sensor for quantum dot readout (see also section 3.4 for qubit readout techniques). In Ge/Si nanowires, a capacitively quantum dot in a nearby nanowire has been demonstrated to be capable of serving as a charge sensor [Hu07; Hu12]. In this case, top-gated nanowires were used and the main quantum dot was coupled via a floating gate to the sensor quantum dot in a nearby nanowire. For bottom gated nanowires, as used in this thesis, a proposed layout is shown in Figure 10.2 **a**. The layout is based on the bottom gate design as described in section 4.3, and the capacitive coupling would be mediated by a floating gate. The nanowires hosting the main quantum dot and the sensor quantum dot are aligned at an angle, which allows independent gating of

the two quantum dots. In Figure 10.2 **b** a proof-of-principle study has been conducted to investigate if the precision of the nanowire transfer with a micromanipulator would be sufficient. Apart from multiple nanowires being transferred due to bundling, the nanowires can be aligned in a rectangular configuration. No electrical measurements were conducted so far on these devices.

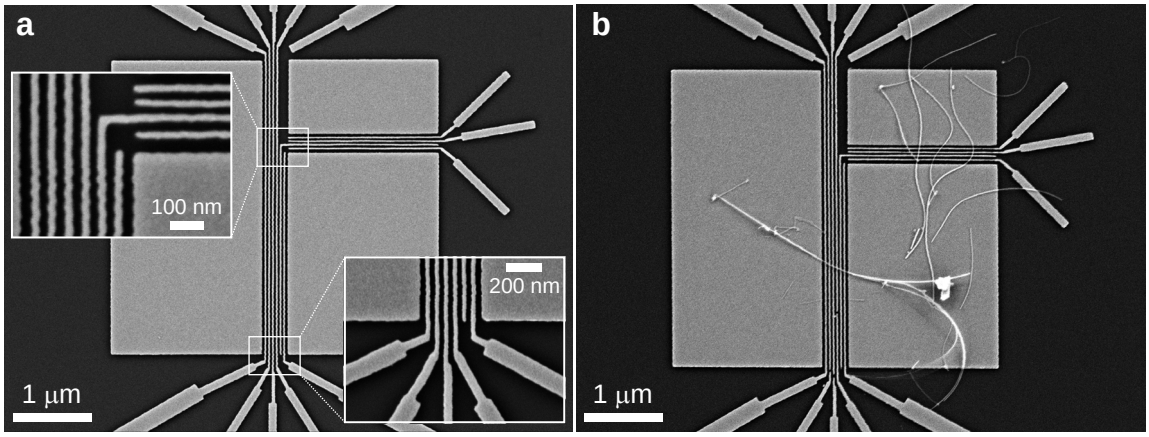

FIGURE 10.2 | **Charge sensor fabrication proposal. a** | Proposal for a bottom gate layout for a quantum dot device with charge sensor in an adjacent nanowire. The gates defining the main and the charge sensor quantum dot are aligned in a rectangular configuration. The capacitive coupling is mediated by a floating gate. Insets show zoom ins of the interesting regions as indicated. **b** | Proof of principle study investigating if two nanowires can be transferred with a micromanipulator in a rectangular configuration. Unfortunately, in this example multiple nanowires were bundling together.

However, complex readout techniques involving charge sensors or quantum point contacts are not suitable for readout of large qubit arrays. As discussed in section 3.4, gate reflectometry is a powerful and compact readout technique. Here, a lumped element resonator is attached to a gate which is capacitively coupled to the qubit. A dispersive shift of the resonator frequency depending on the qubit state can be detected by measuring the reflected signal of the resonator. With this method, single-shot qubit readout has been demonstrated [Wes19; Pak18; Urd19]. This readout technique adds complexity to the setup, yet the actual qubit device does not require additional micro- or nanostructures. Alternatively, also on-chip superconducting resonators, as discussed

next, can serve for qubit readout [Zhe19]. Fast single-shot readout with such a resonator then allows for qubit readout in dense qubit arrays.

10.1.4 Hybrid Semiconductor-Superconductor Devices

The fourth group of future devices comprises the large category hybrid devices, where a semiconductor qubit is combined with a superconducting microwave resonator. The fabrication of such devices is split into the superconducting resonator part and the spin qubit part. While the resonators are fabricated by collaborating groups (see also section 4.5), the spin qubit part is similar to the general fabrication of quantum dot devices as discussed in section 4.2. First results towards a superconducting microwave resonator with integrated Ge/Si core/shell nanowire are shown in Figure 4.6. Due to the importance of such hybrid systems for long-distance qubit-qubit coupling and ultimately qubit networks, these will be treated separately in section 10.3.

10.2 All Electrically Tunable Hole Spin Qubit

Ge/Si core/shell nanowires feature strong direct Rashba spin-orbit interaction, as discussed in section 2.2.4 and experimentally investigated in section 7. Not only the strength, allowing for ultra-fast coherent control of hole spins (see section 8), but also the large tunability with external fields hold promise for a highly tunable hole spin qubit. As discussed in section 3.1, the prospects are a qubit which can be electrically switched from a control mode, with large coupling strengths, to an idle mode, where the qubit is better isolated from the environment. Such a qubit would thus benefit from both a fast operation speed and long coherence. It is therefore of high priority to understand and control the effects of electric fields on the qubit.

Electric fields and electrical noise affect qubits to a large extent. For instance, the impact of charge noise and phonons on qubit relaxation and coherence, especially in presence of spin-orbit interaction, are important to understand. Experimentally, there

is little known about the decoherence mechanisms of hole spins in Ge/Si core/shell nanowires, although electrical noise might be detrimental due to the strong and electric field tunable spin-orbit interaction. A full characterization of the noise leading to the relatively short coherence time observed in section 8 will yield information about the sources of decoherence [Cha18]. To do so, a dynamical decoupling pulse scheme, essentially a series of Hahn echo pulses, can be employed, which allows to characterize the frequency spectrum of the noise. For hole spin qubits, sweet spots with reduced dephasing rates are expected, which allow to optimize the operation point in certain electric field or gate configurations [Klo13b; Wan19b]. Not only the magnitude, but also the direction of the electric field has important implications, for instance with regard to relaxation of hole spins. Optimal configurations for the directions of electric and magnetic fields with respect to the nanowire axis are proposed for maximum relaxation times [Mai13]. In these configurations, relaxation times up to tens of milliseconds are predicted.

Another consequence of the electric field profile is the anisotropy of spin-orbit interaction, resulting in a distinct direction of the effective magnetic field $\vec{B}_{\mathrm{SO}}$. The anisotropic spin-orbit interaction has a profound impact on Pauli spin blockade in double quantum dot devices [Bra16b; Wan16; Wan18b]. Typically, the direction of $\vec{B}_{\mathrm{SO}}$ is not known, and has to be mapped out [Nad12; Wan18b]. However, despite the complexity in realistic devices, knowledge of the electric field profile in and around the nanowire is vital for the future operation of qubits, for instance in order to avoid unwanted qubit relaxation processes and to drive the qubit most effectively. To obtain more control, precise engineering of the electric field profile in combination with simulations may be helpful.

Closely related to the anisotropic spin-orbit interaction is the anisotropic g-factor. In Ge/Si core/shell nanowires, a strong electric field tunability is expected [Mai13] as well as experimentally observed in reference [Bra16a] and in section 8. Via the electrically

tunable g-factor, the Zeeman splitting can be dynamically changed with an additional voltage pulse on the gates. This changes the qubit resonance frequency for the time of the pulse duration and corresponds to a rotation around the z axis of the Bloch sphere, or a Z-gate. In case of Ge/Si core/shell nanowires, the shift of the resonance frequency due to the pulse depth on the plunger gate (see Figure B.2) will enable the implementation of such a Z-gate. Together with the single qubit rotations around the x and the y axis of the Bloch sphere, by controlling the frequency, phase and duration of the microwave burst that drives electric dipole spin resonance, qubit rotations around any axis can be electrically controlled.

Additionally, the electrical control over the qubit resonance also allows to drive qubit rotations with an always-on microwave drive. Here, the qubit is switched into resonance for the duration of the qubit gate, and otherwise detuned from the microwave drive. Because the microwave drive is always on, in this way detrimental pulse imperfections can be avoided to affect the qubit, which is particularly important for very fast qubits with short gate times. Furthermore, in this manner the qubit coupling to the electric field of a resonator, hence the qubit-qubit interactions mediated by the photon field of the resonator (see also section 10.3), can be electrically toggled.

It becomes clear, that control over electric field strength and direction are inevitable for all electrical control of spin qubits and in particular hole spin qubits. Next, we discuss the conclusions regarding an all electrically tunable hole spin qubit in a Ge/Si core/shell nanowire. The electrical tunability of the Rabi frequency shown in section 8 is a first indication of the possible electrical control of the spin-orbit interaction length in Ge/Si core/shell nanowires. In contrast to other material systems [Kan11], already very small changes of gate voltage lead to a significant variations of the spin-orbit interaction strength, demonstrating the increased sensitivity of this hole system to electric fields. Small changes of the voltages on the gates providing the quantum dot confinement allow electrical control over the qubit because, in a realistic device, also the

electric field generated by the confinement gates induces a strong electric field inside the nanowire. This is due to the close proximity of these gates, which are only separated by the 20 nm thin dielectric layer. Estimates from a simple plate capacitor model yield sizeable electric field strengths on the order of 50 V/µm inside the nanowire for typical gate voltages on the order of 1 V. In a more advanced experiment, ideally an electric field independent from the quantum dot confinement should be used to investigate the electrical tunability detached from the concurrent modification of quantum dot characteristics such as tunneling rates.

Side gates on either side of the nanowire are capable of inducing a transverse electric field inside the nanowire with considerable electric field strength on the order of 1 V/µm, which can be used for instance to control the electron orbitals [Rod11] and also hold promise to electrically control the direction of $\vec{B}_{\mathrm{SO}}$ [Dor19]. For bottom gated nanowires the alignment of side gates nearby the nanowire is difficult as the nanowire is placed only at the end of the fabrication process and its exact position is not fully controllable. Figure 4.1 shows a Ge/Si core/shell nanowire quantum dot device with adjacent side gates in parallel to the principle axis of the nanowire. In this particular case, the electric field strength inside the nanowire induced by biasing these side gates with voltages of up to 5 V with opposite polarity is unknown. However, assuming comparable structures and finite element simulations of the electric field therein [Rod11], roughly 10 % of the electric field strength expected from a simple plate capacitor model can be expected to be induced inside the nanowire. The actually induced electric field is much smaller due to the mismatch of the relative permittivity of the nanowire and the vacuum. For the geometry of Figure 4.1 this would imply an electric field of about 1 V/µm inside the Ge/Si core/shell nanowire. An electric field of this magnitude is at the lower end of the necessary electric field strength in order to give rise to direct Rashba spin-orbit interaction [Klo18], yet in theory sufficient for substantial modifications of the g-factor [Mai13].

In conclusion, the implications of electric field strength and direction on the performance of hole spin qubits in Ge/Si core/shell nanowires are experimentally largely unexplored. Yet precise engineering and knowledge of the electric field profile of the entire gate structure will be important for future experiments. More control over the electric field of the confinement gates can be achieved, for instance, with wrap-around gates [Sto12; Bur15; She15; Glu19], and additional side gates enable electrical control over the spin-orbit interaction [Dor19]. With well-defined directions of $\vec{B}_{\mathrm{SO}}$ and the electric field, the dependence of qubit characteristics such as the Rabi frequency and the coherence time, on magnitude, direction and relative orientation of electric and magnetic field can be investigated. Ultimately, this will allow for the implementation of an all electrically tunable hole spin qubit, with characteristics as envisioned in section 3.1, where the qubit can be toggled between a control and an idle mode with a designated gate.

10.3 Large Scale Qubit Network

In the long term, large scale quantum computers will comprise a vast amount of qubits in order to provide the necessary computing capacity. At this point, errors in state preparation, qubit gates and readout on the single qubit level become significant for the reliability of the entire computing unit. Besides high fidelity qubits, also the implementation of error correction schemes will be required in order to achieve a reliable quantum computer [Ter15]. The most promising quantum error correction scheme is the surface code [Fow12], which requires a number of physical qubits to build one logical qubit, thus underlining the need for a large number of physical qubits in upscaled systems.

In any case, even in large networks, each qubit has to be addressable individually. This poses a challenge for the architecture due to the amount of gates and wiring that is necessary. Furthermore, a scalable interface between the qubits and classical electronics

needs to be developed [Van17; Vel17; Li18a]. Here, qubits in the semiconductors Si and Ge hold promise to facilitate such an architecture (see also section 2.2.1) due to the compatibility with current CMOS technology.

Finally, for large scale qubit networks, interactions between a large number of qubits need to be provided. Nearest-neighbour interactions can be expanded over the whole qubit array by shuttling or swapping qubits [Mil19; Fuj17]. In order to achieve direct long-distance coupling between unmovable qubits, floating gates and microwave resonators have been proposed. Floating gates connect distant qubits capacitively and the interactions can be switched on and off by controlling the position of the qubit with respect to the floating gate [Tri12]. Microwave resonators can mediate interactions between qubits via the photon field and lead to the emergence of circuit quantum electrodynamics (cQED) [Bur20].

The term circuit QED stems from the similarity to cavity QED, which describes the light matter interaction between a photon and an atom in an optical cavity. The field of cQED is well established in condensed matter systems, for instance with superconducting qubits [Bla04; Wal04], and provides a way to coherently couple distant qubits via photons of a cavity. The cavity is often realized as a superconducting coplanar waveguide resonator, fabricated on-chip, for microwave frequencies that match the discrete energy level splitting of the qubit.

A single charge confined in a semiconductor double quantum dot can also couple to photons of microwave resonators via the electric dipole interaction. The charge occupies either the left or the right quantum dot and in presence of an interdot coupling, the charge delocalizes over the length of the interdot separation due to the hybridization of the charge ground states, which gives rise to an electric dipole. Direct coupling of the spin to the cavity mode, however, is hard to achieve since the spin does not couple to electric fields and the magnetic dipole coupling between the spin and the cavity mode is weak. Therefore, mechanisms are required which provide coupling of the spin to

an electric dipole, thus essentially entangle orbital and spin states. At the heart, this is the same challenge as for single spin manipulation techniques, which are discussed in section 3.2, and therefore also spin-resonator coupling methods resemble the spin-to-charge conversion schemes, for instance exploiting the Pauli exclusion principle, or mediating electric dipole spin resonance with micromagnets [Klo13a; Chi04; Bur06; Rus15]. Similarly, spin-orbit interaction enables spin-cavity coupling [Tri08]. Here, the orbital motion of a an electron is perturbed by the electrical cavity mode, which in presence of spin-orbit coupling, provides a coupling between the photon of the cavity and the spin of the electron. Such an architecture is also proposed for Ge/Si core/shell nanowires, where, due to the direct Rashba spin-orbit interaction excellent operation speed and electrical control is expected [Klo13b].

Experimentally, important milestones have been achieved towards a hybrid spin qubit-superconducting cavity system for long-distance qubit-qubit interactions. Since the first demonstration of cQED with an InAs nanowire [Pet12], strong photon-cavity coupling [Mi17a; Sto17; Lan18], strong spin-cavity coupling [Mi18a; Sam18], and spin-spin interactions mediated by the cavity field [Bor20] have been demonstrated Also hybrid systems employing a Ge/Si core/shell nanowire have been reported [Wan19a], however, not yet in the strong coupling regime. In section 4.5, first steps towards the fabrication of a device that couples a hole spin qubit in a Ge/Si core/shell nanowire to a high impedance superconducting resonator are shown. High impedance resonators are preferred since the charge-photon coupling scales with the impedance $\sqrt{L/C}$, where L is the inductance and C the capacitance of the resonator. The capacitance can not be reduced arbitrarily much due to the parasitic capacitances, thus the goal is to increase the inductance. Example resonators with a large inductance are transmission lines made of NbTiN [Sam16] and SQUID arrays [Mas12; Cas07]. Both types of resonators have different characteristics such as sensitivity to magnetic fields and tunability of the resonance frequency, and therefore form an excellent basis for the exploration of cQED

physics with Ge/Si core/shell nanowires [Klo13a; Klo13b]. Finally, not only the strong spin-photon coupling with its implications for quantum computation are of interest, but also the strong or even ultrastrong charge-photon coupling enable the exploration of new physics [Koc19; For19].

A Supplementary Information: Strong spin-orbit interaction and g-factor renormalization of hole spins in Ge/Si nanowire quantum dots

A.1 Extended data sets

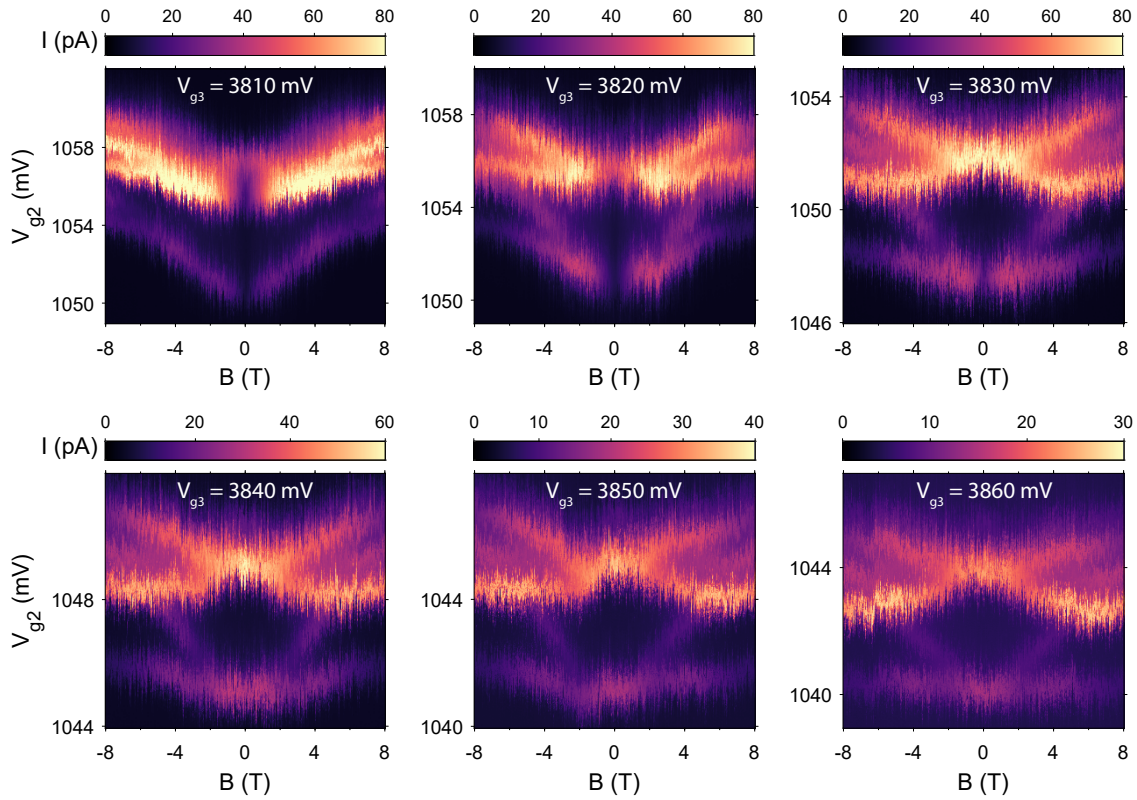

FIGURE A.1 | Extended data sets over full range of detuning, for values of V_{g3} as indicated in each plot. Here, V_{g4} is swept simultaneously with V_{g2}, along the detuning arrow shown in Fig. 7.1 (c) of the main text.

A.2 Zoom-in of Fig.7.4 (a)

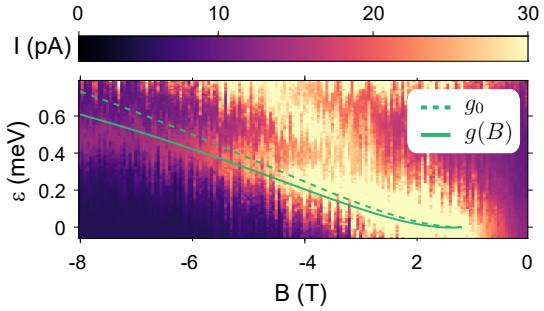

FIGURE A.2 | Zoom-in of Fig. 7.4 (a) of the main text, highlighting the role of g-factor renormalization at high magnetic field. Green curves are identical to those in main curves, corresponding to $\varepsilon_{\pm}(B)$ with (solid) and without (dashed) taking into account the g-factor renormalization with magnetic field given by Eq. 7.2.

A.3 Model Hamiltonian

Here, we provide a more detailed analysis of the theoretical model used in the main text. The relevant physics of a single hole confined in a quantum dot can be captured by the effective 2-dimensional Hamiltonian

$$H = H_o + H_{so} + H_Z \ , \tag{A.1}$$

with

$$\begin{aligned} H_o &= \frac{\pi_x^2}{2m_\perp} + \frac{\pi_y^2}{2m_\perp} + \frac{\pi_z^2}{2m_\parallel} + \frac{m_\parallel \omega_\parallel^2}{2} z^2 \\ &\quad + \frac{m_\perp \omega_\perp^2}{2}(x^2 + y^2) \ , \end{aligned} \tag{A.2a}$$

$$H_{so} = \alpha \pi_z \sigma_y \ , \tag{A.2b}$$

$$H_Z = \frac{g_0 \mu_B}{2} \mathbf{B} \cdot \boldsymbol{\sigma} \ . \tag{A.2c}$$

Here, we define the dynamical momentum $\boldsymbol{\pi} = -i\hbar\nabla - e\mathbf{A}$, where $\mathbf{A}$ is the vector potential accounting for an externally applied magnetic field $\mathbf{B}$. These operators satisfy

the commutation relations $[\pi_i, \pi_j] = i\epsilon_{ijk}\hbar e B_k$, $[\pi_i, x_j] = -i\hbar\delta_{ij}$. We model the confinement potential by an anisotropic harmonic oscillator, with confinement frequencies $\omega_\perp$ and $\omega_\parallel$, and effective masses $m_\perp$ and $m_\parallel$ in the direction perpendicular and parallel to the nanowire growth direction, respectively. In the following, we assume $\omega_\perp > \omega_\parallel$. Because of the magnetic field, the spin states are split in energy by the Zeeman energy; here g_0 is the g-factor of the system and the field $\mathbf{B}$ is assumed to be homogeneous. The interaction between different spin states is captured by a Rashba-like spin-orbit interaction H_{so} [Klo18; Klo11].

Our final goal is to extract from the measurements the spin-orbit interaction parameter α. It is convenient to introduce the spin-orbit length

$$\lambda_{so} = \frac{\hbar}{m_\parallel \alpha} \ , \tag{A.3}$$

and to perform the unitary spin-dependent displacement of states [Lev03]

$$S = e^{i\sigma_y z/\lambda_{so}} \ , \tag{A.4}$$

that diagonalizes the spin-orbit interaction in spin-space

$$S\Big(H_o + H_{so}\Big)S^\dagger = H_o - \frac{\hbar^2}{2m_\parallel \lambda_{so}^2} \ , \tag{A.5}$$

converting the Zeeman term to a position-dependent quantity. We now focus on the case where the magnetic field points in the x-direction, i.e. $\mathbf{B} = B\mathbf{e}_x$, and we obtain

$$SH_Z S^\dagger = \frac{g_0\mu_B}{2} B \left[\sigma_x \cos\Big(\frac{2z}{\lambda_{so}}\Big) + \sigma_z \sin\Big(\frac{2z}{\lambda_{so}}\Big)\right] \ . \tag{A.6}$$

In the harmonic confinement approximation, the orbital Hamiltonian H_o can always

be diagonalized exactly. Assuming $B > 0$, we can introduce the vector of gauge-independent canonical positions $\mathbf{Q}$ and momenta $\mathbf{P}$

$$\mathbf{Q} = \begin{pmatrix} \frac{z}{l_B} - \frac{l_B}{\hbar}\pi_y \\ \frac{l_B}{\hbar}\pi_y \\ x \end{pmatrix} \quad \text{and} \quad \mathbf{P} = \begin{pmatrix} \frac{y}{l_B} + \frac{l_B}{\hbar}\pi_z \\ \frac{l_B}{\hbar}\pi_z \\ -i\partial_x \end{pmatrix} , \tag{A.7}$$

satisfying $[Q_i, P_j] = i\delta_{ij}$; here $l_B = \sqrt{\hbar/(e|B|)}$ is the magnetic length. When $B < 0$, the first two positions and momenta are swapped. The coupled harmonic oscillators can be decoupled by the symplectic Bogoliubov transformation

$$\begin{pmatrix} \mathbf{Q} \\ \mathbf{P} \end{pmatrix} = \begin{pmatrix} \mathcal{A}(r) & 0 \\ 0 & \mathcal{A}(-r)^T \end{pmatrix} \begin{pmatrix} \mathbf{q} \\ \mathbf{p} \end{pmatrix} , \tag{A.8}$$

where 3-dimensional matrix $\mathcal{A}(r)$ is defined by

$$\mathcal{A}(r) = \begin{pmatrix} \cosh(r) & -\frac{\omega_\perp}{\omega_\parallel}\sinh(r) & 0 \\ -\frac{\omega_\parallel}{\omega_\perp}\sinh(r) & \cosh(r) & 0 \\ 0 & 0 & 1 \end{pmatrix} , \tag{A.9}$$

with squeezing parameter

$$r = \frac{1}{2}\mathrm{arccoth}\left(\frac{\frac{e^2B^2}{m_\perp m_\parallel} + \omega_\perp^2 + \omega_\parallel^2}{2\omega_\perp\omega_\parallel} \right) . \tag{A.10}$$

In the new coordinate system with positions $\mathbf{q}$ and momenta $\mathbf{p}$, we obtain three independent harmonic oscillators with frequencies $\omega_\perp$ and $\omega_1 < \omega_2$, where the Fock-Darwin

frequencies are

$$\begin{aligned}\omega_1 &= \omega_2 \tanh(r) \\ &= \frac{\sqrt{m_\parallel m_\perp}}{eB}\omega_\parallel\omega_\perp\sqrt{\left(1-\frac{\omega_\parallel}{\omega_\perp}\tanh(r)\right)\left(1-\frac{\omega_\perp}{\omega_\parallel}\tanh(r)\right)}\,. \end{aligned} \tag{A.11}$$

We point out that when $B \to 0$, Eq. (A.11) is still valid and it leads to the expected result $\omega_1 = \omega_\parallel$ and $\omega_2 = \omega_\perp$.

The groundstate $|0\rangle$ is the state simultaneously annihilated by the annihilation operators in this coordinate system

$$a_j = \frac{1}{\sqrt{2}}\left(\beta_j q_j + \frac{i}{\beta_j}p_j\right)\,, \tag{A.12}$$

where

$$\beta_j = \left[\left(\frac{\omega_\parallel m_\parallel}{\omega_\perp m_\perp}\gamma\right)^{1/4},\ \left(\frac{\omega_\parallel m_\parallel}{\omega_\perp m_\perp}\frac{1}{\gamma}\right)^{1/4},\ \sqrt{m_\perp\omega_\perp/\hbar}\right]_j\,, \tag{A.13}$$

and $\gamma = \frac{\omega_\parallel}{\omega_\perp}\frac{\omega_\parallel/\omega_\perp - \coth(r)}{\omega_\perp/\omega_\parallel - \coth(r)}$. To determine the groundstate wavefunction in real-space, we need to specify a gauge. In the symmetric gauge $\mathbf{A} = \mathbf{B}\times\mathbf{r}/2$, and combining Eqs. (A.7), (A.8) and (A.12), we obtain

$$\psi_0(\mathbf{r}) = \frac{1}{\pi^{3/4}\sqrt{l_x l_y l_z}}e^{-\frac{1}{2}\left(\frac{x^2}{l_x^2}+\frac{y^2}{l_y^2}+\frac{z^2}{l_z^2}\right)+i\frac{yz}{2l_B^2}\left(\frac{\omega_\parallel-\omega_\perp}{\omega_\parallel+\omega_\perp}\right)}\,, \tag{A.14}$$

where we defined the magnetic field-dependent lengths

$$l_y = l_\perp\left(1+\frac{B^2}{B_0^2}\right)^{-1/4} \quad\text{and}\quad l_z = l_\parallel\left(1+\frac{B^2}{B_0^2}\right)^{-1/4}\,, \tag{A.15}$$

and the usual harmonic lengths

$$l_x = l_\perp = \sqrt{\frac{\hbar}{m_\perp\omega_\perp}} \quad\text{and}\quad l_\parallel = \sqrt{\frac{\hbar}{m_\parallel\omega_\parallel}}\,. \tag{A.16}$$

The characteristic magnetic field B_0 in Eq. (A.15) determines the relevant field at which the orbital effects start to become significant and it is defined by

$$B_0 = \frac{\sqrt{m_\parallel m_\perp}}{e}(\omega_\parallel + \omega_\perp) \ . \tag{A.17}$$

Projecting the Hamiltonian in Eq. (A.1) onto the groundstate subspace and subtracting a constant energy term, we obtain the effective low energy Hamiltonian

$$H_{GS} = \frac{g\mu_B B}{2}\sigma_x \ , \tag{A.18}$$

where we introduce the effective g-factor

$$g = g_0 e^{-l_z^2/\lambda_{so}^2} \ . \tag{A.19}$$

We emphasize that the g-factor is renormalized by the spin-orbit interaction, and it acquires a magnetic field dependence via l_z, see Eq. (A.15).

We remark that because of the transformation in Eq. (A.4), we are now treating spin-orbit interaction exactly, and the perturbation coupling different orbital states comes from the space-dependent magnetic field in the Zeeman energy, see Eq. (A.6). This approach is the most convenient to describe the results of this experiment, where a strong spin-orbit interaction is measured. Because of this term, the orbital ground state is coupled to the first excited orbital state $|1\rangle$ with energy $\hbar\omega_1$. In particular, the interaction is

$$\langle 0|H|1\rangle = \frac{l_B}{\sqrt{2}\lambda_{so}\beta_1}\left(\cosh(r) - \frac{\omega_\parallel}{\omega_\perp}\sinh(r)\right) g\mu_B B\sigma_z \ . \tag{A.20}$$

Using the values extracted in the main text, see Table 7.1, we find that the amplitude of this interaction term is $\sim 20\%$ of the energy gap $\sim \hbar\omega_1$ at the maximal field measured $B = 8$ T. Consequently, in the following we focus on the ground state subspace only.

A.4 Double-dot Hamiltonian

We now construct the double-dot effective Hamiltonian by using the Hund-Mulliken method. To do so, we create an orthonormal basis of harmonic eigenfunctions whose center of mass is at the positions $z = \pm a/2$. Here, a is the interdot distance. Following the conventional procedure, we find the overlap matrix between the orbital ground states of the two dots: $\mathcal{P}_{ij} = \langle \Psi_i | \Psi_j \rangle$, where

$$\begin{aligned} |\Psi\rangle = \Big(& T_z\big(-a/2\big) S^\dagger |\psi_0 \uparrow\rangle,\ T_z\big(-a/2\big) S^\dagger |\psi_0 \downarrow\rangle, \\ & T_z\big(+a/2\big) S^\dagger |\psi_0 \uparrow\rangle,\ T_z\big(+a/2\big) S^\dagger |\psi_0 \downarrow\rangle \Big) \end{aligned} \tag{A.21}$$

The magnetic translation operators are defined as $T_z(X) = e^{iX(\pi_z/\hbar + y/l_B^2)}$ and ψ_0 is the ground state wavefunction in Eq. (A.14). Importantly, because the unitary $S^\dagger$ in Eq. (A.4) is spin-dependent, here $\mathcal{P}$ is a 4×4 matrix. Explicitly, we find

$$\mathcal{P} = \tau_0\sigma_0 + s\cos\left(\frac{a}{\lambda_{so}}\right)\tau_x\sigma_0 + s\sin\left(\frac{a}{\lambda_{so}}\right)\tau_y\sigma_y \ , \tag{A.22}$$

where τ_i are Pauli matrices acting on the different dots, σ_i are acting on spins and we define the small parameter

$$s = e^{-\frac{a^2}{4l_z^2}\left(1+\frac{(\omega_\perp-\omega_\parallel)^2}{4\omega_\perp\omega_\parallel}\frac{B^2}{B^2+B_0^2}\right)} \ . \tag{A.23}$$

Orthogonal and symmetric states $|O\rangle$ are constructed from the non-orthogonal states $|NO\rangle$ by the linear map $|O\rangle = |NO\rangle\mathcal{P}^{-1/2}$ and single-particle operators H transform as $H_O = \mathcal{P}^{-1/2} H_{NO} \mathcal{P}^{-1/2}$. The generalization to two-body operators is straightforward.

For rather general double-dot confinement potentials, we find that the orbital Hamiltonian in the orthonormal basis has the form

$$H_o = t_c\tau_x\sigma_0 + t_{so}\tau_y\sigma_y + \frac{\varepsilon}{2}\tau_z\sigma_0 \ . \tag{A.24}$$

Here, ε is the detuning between the two dots typically caused by an electric field along the wire, t_c is the spin-conserving tunneling energy and t_{so} is the spin-flip tunneling energy caused by the spin-orbit interaction. In particular, we find that

$$t_c = \frac{s}{1-s^2} t_0 \cos\left(\frac{a}{\lambda_{so}}\right) \quad \text{and} \tag{A.25a}$$

$$t_{so} = \frac{s}{1-s^2} t_0 \sin\left(\frac{a}{\lambda_{so}}\right) = t_c \tan\left(\frac{a}{\lambda_{so}}\right) \ . \tag{A.25b}$$

where t_0 is a characteristic energy dependent on the details of the confinement potential and the leading magnetic field dependence of the tunneling energy is caused by the exponential dependence of the overlap s on B, see Eq. (A.23).

Also, the Zeeman energy in the orthogonal basis is

$$H_Z = \frac{g\mu_B B}{2}\Big(g_1\tau_0\sigma_x + g_2\tau_x\sigma_x + g_3\tau_z\sigma_z\Big) \ , \tag{A.26}$$

where we introduce the dimensionless prefactors

$$\begin{aligned} g_1 &= \frac{1+\sqrt{1-s^2}-2s^2\cos\left(\frac{a}{\lambda_{so}}\right)}{2-2s^2} \\ &\quad + \frac{\left(1-\sqrt{1-s^2}\right)\cos\left(\frac{2a}{\lambda_{so}}\right)}{2-2s^2} \\ &= 1+\mathcal{O}(s^2) \ , \end{aligned} \tag{A.27}$$

$$g_2 = \frac{1-\cos\left(\frac{a}{\lambda_{so}}\right)}{1-s^2} s \ , \tag{A.28}$$

$$g_3 = \frac{s^2-\left(1-\sqrt{1-s^2}\right)\cos\left(\frac{a}{\lambda_{so}}\right)}{1-s^2} \sin\left(\frac{a}{\lambda_{so}}\right) = \mathcal{O}(s^2) \ . \tag{A.29}$$

Neglecting corrections of order s^2, we can discard the term proportional to g_3, that couple the triplet states $T_{\uparrow\downarrow}(1,1)$ to the singlet state $S(1,1)$. The term proportional to g_2 arise when the spin-orbit interaction is large and cause interactions between the triplet $T_0(1,1)$ and the doubly-occupied singlet states $S(2,0)$ and $S(0,2)$. This term causes an extra resonant peak of the leakage current, however, in the present

experiment the energy of this interaction is of a few microelectronvolts, much smaller than the contribution due to the spin-flip tunneling. Consequently, in the following, we will ignore it and consider only $H_Z \approx g\mu_B B\tau_0\sigma_x/2$.

Coulomb interactions are also required to understand the physics of the system. In particular, the most relevant electrostatic interaction element for the current experiment is the addition energy,

$$\begin{aligned} U &= \langle \Psi_i \Psi_i | \frac{e^2}{4\pi\epsilon_s r} | \Psi_i \Psi_i \rangle \\ &= \frac{e^2}{4\pi\epsilon_s} \sqrt{\frac{2}{\pi}} \frac{F\left(\cos^{-1}\left(\frac{l_z}{l_x}\right) | \frac{l_x^2 - l_y^2}{l_x^2 - l_z^2}\right)}{\sqrt{l_x^2 - l_z^2}} , \end{aligned} \tag{A.30}$$

where $F(a|b)$ is the elliptic F function and $\epsilon_s = 16\epsilon_0$ is the dielectric constant of germanium times the vacuum permittivity ϵ_0. Eq. (A.30) holds for general values of lengths l_i provided that the appropriate limit is taken carefully. The next largest Coulomb interaction elements are the Hartree and Fock terms $U_H = \langle \Psi_i \Psi_{j\neq i} | \frac{e^2}{4\pi\epsilon_s r} | \Psi_{j\neq i} \Psi_i \rangle$ and $U_F = \langle \Psi_i \Psi_{j\neq i} | \frac{e^2}{4\pi\epsilon_s r} | \Psi_i \Psi_{j\neq i} \rangle$, respectively. In the present experiment, the overlap s between wave functions of different dots is expected to be small, and so we discard the corrections of order $\mathcal{O}(s^2)$ and we ignore the exchange interaction $U_F \approx 0$.

A.5 Singlet-Triplet basis

We can now rewrite the Hamiltonian in the singlet-triplet basis. Neglecting higher orbital states, the relevant triplet states are

$$\begin{aligned} |T_{\uparrow\uparrow,\downarrow\downarrow}(1,1)\rangle &= c^\dagger_{-,\uparrow(\downarrow)} c^\dagger_{+,\uparrow(\downarrow)} |0\rangle \quad \text{and} \\ |T_0(1,1)\rangle &= \frac{c^\dagger_{-,\uparrow} c^\dagger_{+,\downarrow} + c^\dagger_{-,\downarrow} c^\dagger_{+,\uparrow}}{\sqrt{2}} |0\rangle , \end{aligned} \tag{A.31}$$

and the singlets are

$$|S(0,2)\rangle = c^\dagger_{+,\uparrow}c^\dagger_{+,\downarrow}|0\rangle \quad \text{and}$$
$$|S_0(1,1)\rangle = \frac{c^\dagger_{-,\uparrow}c^\dagger_{+,\downarrow} - c^\dagger_{-,\downarrow}c^\dagger_{+,\uparrow}}{\sqrt{2}}|0\rangle \ , \tag{A.32}$$

where we introduce the fermionic ladder operators $c^\dagger_{i,\sigma}$ creating an electron at the ith dot with spin σ. We do not consider here the singlet state $S(2,0)$ because it is far detuned in energy, and so the interactions of these states with it are suppressed by the large energy difference.

By aligning the spin quantization axis to the direction of the magnetic field, we find in the singlet-triplet basis $\Big(S(0,2), S(1,1), T_{\uparrow\uparrow}(1,1), T_{\downarrow\downarrow}(1,1), T_0(1,1)\Big)^T$

$$H = \begin{pmatrix} U-\varepsilon & \sqrt{2}t_c & t_{so} & -t_{so} & 0 \\ \sqrt{2}t_c & U_H & 0 & 0 & 0 \\ t_{so} & 0 & U_H + g\mu_B B & 0 & 0 \\ -t_{so} & 0 & 0 & U_H - g\mu_B B & 0 \\ 0 & 0 & 0 & 0 & U_H \end{pmatrix} , \tag{A.33}$$

where t_c, t_{so} and g and U are defined in Eqs. (A.25a), (A.19) and (A.30), respectively. The singlet sector is hybridized by the spin-conserving tunneling energy. By introducing the hybridized singlet states $S_\pm$ obtained by rotating the singlet sector by $\theta/2$, where θ is

$$\theta = \arctan\left(\frac{2\sqrt{2}t_c}{U - U_H - \varepsilon}\right) \ , \tag{A.34}$$

we can rewrite the Hamiltonian in the convenient form

$$H = \begin{pmatrix} E_+ & 0 & \Delta_{\mathrm{ST}}^+ & -\Delta_{\mathrm{ST}}^+ & 0 \\ 0 & E_- & -\Delta_{\mathrm{ST}}^- & \Delta_{\mathrm{ST}}^- & 0 \\ \Delta_{\mathrm{ST}}^+ & -\Delta_{\mathrm{ST}}^- & U_H + g\mu_B B & 0 & 0 \\ -\Delta_{\mathrm{ST}}^+ & \Delta_{\mathrm{ST}}^- & 0 & U_H - g\mu_B B & 0 \\ 0 & 0 & 0 & 0 & U_H \end{pmatrix} , \tag{A.35}$$

where we defined the hybridized singlet energies $E_\pm$ and the spin-orbit interaction $\Delta_{\mathrm{ST}}^\pm$ via

$$E_\pm = \frac{1}{2}\left(U + U_H - \varepsilon\right) \pm \sqrt{2t_c^2 + \frac{1}{4}\left(U - U_H - \varepsilon\right)^2} , \tag{A.36a}$$

$$\Delta_{\mathrm{ST}}^\pm = t_{so}\sqrt{\frac{1 \pm \cos(\theta)}{2}} . \tag{A.36b}$$

Note that in the limit of weak spin orbit coupling, i.e., $a/\lambda_{so} \ll 1$, we recover the result obtained previously for the ST splitting [Ste12a].

The leakage current is related to the matrix elements $\Delta_{\mathrm{ST}}^\pm$ between singlet and triplet states via [Naz93; Li15; Sto96; vdWie02a]

$$I_\pm = e\Gamma_L \frac{\left(\Delta_{\mathrm{ST}}^\pm\right)^2}{(\varepsilon - \varepsilon_\pm)^2 + \left(\Delta_{\mathrm{ST}}^\pm\right)^2\left(\frac{\Gamma_L}{\Gamma_R} + 2\right) + h^2{\Gamma_L}^2/4} . \tag{A.37}$$

where $\Gamma_{R(L)}$ is the coupling between the right, occupied (left, unoccupied) dot to the metallic lead and $\varepsilon_\pm$ is the position of the triplet $T_{\uparrow\uparrow,\downarrow\downarrow}(1,1)$ and the singlet $S_\pm$ anti-crossing. In particular, by using Eq. (A.36a), we find

$$\varepsilon_\pm = U - U_H \pm \left(\frac{2t_c^2}{g\mu_B B} - g\mu_B B\right) . \tag{A.38}$$

Neglecting the corrections due to the Hartree energy U_H, small compared to the addition energy U, and assuming symmetric dot-lead coupling $\Gamma_L \approx \Gamma_R = \Gamma$, we obtain

Eqs. (7.1) and (7.5) of the main text. Note that in the main text the detuning is measured from the singlet-singlet anti-crossing, therefore Eq. (7.1) contains a constant energy shift.

B Supplementary Information: Ultrafast Hole Spin Qubit with Gate-Tunable Spin-Orbit Switch Functionality

B.1 Microwave Power Calibration

The transmission of the high-frequency part of the setup is frequency-dependent in the GHz regime. In addition to a continuously increasing attenuation at higher frequencies, there are also a number of pronounced, sharp, resonances where transmission is strongly attenuated due to impedance mismatch e.g. on the printed circuit board on which the sample is mounted. Changing the microwave frequency can therefore lead to a highly nonlinear change of microwave power, thus affecting the Rabi frequency for these technical reasons (see Fig. 8.2 **b** of the main text). Therefore, in order to acquire the data shown in Fig. 8.2 **d** of the main text, we calibrate the microwave power arriving at the sample for each data point. To do so, we measure the linewidth of the zero-detuning line which is broadened due to inelastic tunneling assisted by the microwave drive on the gate [vdWie02b; Now07]. In case of a dot-reservoir tunnel coupling Γ that is large in comparison to the drive frequency f_{MW}, applying a microwave tone predominantly leads to broadening and a power-dependent splitting with continuous shift of peak positions with applied microwave power. As shown in Figure B.3, this results in a V-shaped dependence when detuning is plotted as a function of power. Here, $f_{\mathrm{MW}} = 3.75\,\mathrm{GHz}$, which corresponds to the datapoint at $|B_{\mathrm{ext}}| = 264\,\mathrm{mT}$ in Fig. 8.2 **d** of the main text. We compare line cuts along the detuning axis to a reference measurement at $f_{\mathrm{MW}} = 6\,\mathrm{GHz}$ and $P_{\mathrm{MW}} = 25\,\mathrm{dBm}$ applied at the signal generator (blue dashed curve in Figure B.3 **b**), and match the linewidth by adjusting P_{MW} for each f_{MW}. For the case of $f_{\mathrm{MW}} = 3.75\,\mathrm{GHz}$, shown in Figure B.3, the reference linewidth is best matched for a power of 19 dBm (green curve). The highest (lowest) power which still gives a good

overlap with the reference measurement (red curves in Figure B.3 **b**) then determines the vertical error bars in Figure 8.2 **d** in positive (negative) direction, where we assume a linear dependence of f_{Rabi} on A_{MW}.

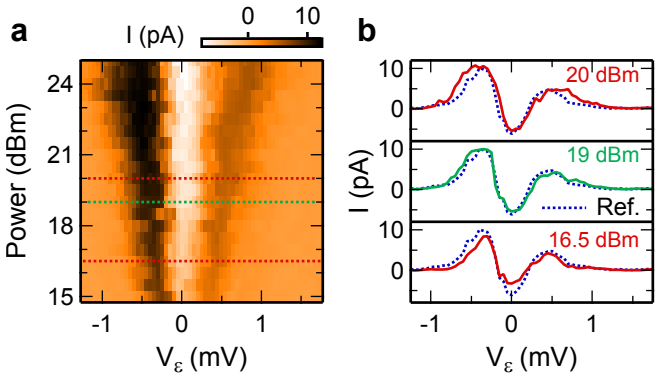

FIGURE B.1 | **Microwave power calibration.** **a** Linewidth measurement of the zero-detuning line with varying microwave power for calibrating the microwave power arriving at the sample. The drive frequency in this case is $f_{\mathrm{MW}} = 3.75\,\mathrm{GHz}$. **b** Line cuts along the detuning axis at different powers, as indicated in **a**. The reference measurement (blue dashed curve) corresponds to $f_{\mathrm{MW}} = 6\,\mathrm{GHz}$ and $P_{\mathrm{MW}} = 25\,\mathrm{dBm}$. Comparing the linewidth, the best match for $f_{\mathrm{MW}} = 3.75\,\mathrm{GHz}$ is found for $P_{\mathrm{MW}} = 19\,\mathrm{dBm}$ (green curve) and the upper (lower) limits are $P_{\mathrm{MW}} = 20\,\mathrm{dBm}$ (16.5 dBm), resulting in the error bars in Figure 8.2 **d** of the main text.

B.2 Electrical Qubit Tunability

B.2.1 Tuning of Qubit Resonance with ΔV_P

For coherent manipulation with EDSR, the qubit is pulsed deeply into Coulomb blockade in order to protect it from unintended effects of the applied microwave burst. We measure EDSR for different pulse depths ΔV_P of the square voltage pulse which pulses the system into Coulomb blockade (see pulsing scheme depicted in Fig. 8.1 of the main text). Figure B.1 shows the result as a function of the magnetic field $|B_\mathrm{ext}|$ and the pulse depth ΔV_P, while t_burst and f_MW are kept constant. The two vertical features in Figure B.1 **a** at $\Delta V_\mathrm{P} = -0.1\,\mathrm{V}$ and $\Delta V_\mathrm{P} = 0.2\,\mathrm{V}$, between which the region of Pauli spin blockade is located (blue shaded area in Figure B.1 **b** and **c**), correspond to the $T(1,1)$-$T(2,0)$ transition and the zero-detuning line of the bias triangle, respectively. The two curved features at $|B_\mathrm{ext}| = 320\,\mathrm{mT}$ and $360\,\mathrm{mT}$ correspond to the microwave induced $T_+(1,1) - S(1,1)$ and $T_-(1,1) - S(1,1)$ EDSR transitions, respectively.

For $-0.1\,\mathrm{V} \lesssim \Delta V_\mathrm{P} \lesssim 0.2\,\mathrm{V}$, spin manipulation takes place inside the bias triangle, leading to comparably bright features because charge transitions are not inhibited by Coulomb blockade, resulting in large interdot and dot-reservoir tunneling rates. The readout point, indicated by the green line in Figure B.1 **b** and **c**, is positioned inside this area at $\Delta V_\mathrm{P} = 0\,\mathrm{V}$. For pulse amplitudes above $\Delta V_\mathrm{P} \gtrsim 0.2\,\mathrm{V}$, spin manipulation takes place inside Coulomb blockade, which prevents dot-reservoir tunneling during the microwave burst. This leads to the faint EDSR resonance indicated by the red dashed line in Figure B.1 **a**. Note that due to the exchange interaction the resonance splits up for $\Delta V_\mathrm{P} \lesssim 0.35\,\mathrm{V}$.

Moreover, we observe a pronounced shift of the qubit resonance frequency as a function of the pulse depth ΔV_P, corresponding to a decrease of the g-factor. Figure B.1 **b** shows a relative change of the g-factor by up to $20\,\%$ in a different gate configuration than the data shown in Figure B.1 **a**. We emphasize here that when pulsing into Coulomb

blockade, one must compensate for the induced change in g-factor at the manipulation point M. For a hole spin qubit tuned to be on resonance in the PSB region, the Coulomb pulse will easily drive it far off-resonance, thus obliviating Rabi oscillations. Next, we measure the Rabi frequency for different values of ΔV_P along the red dotted line in Figure B.1 **a** and find the results shown in Figure B.1 **c**. The Rabi frequency is highest at manipulation points with small ΔV_P and decreases from 180 MHz to 130 MHz when increasing ΔV_P.

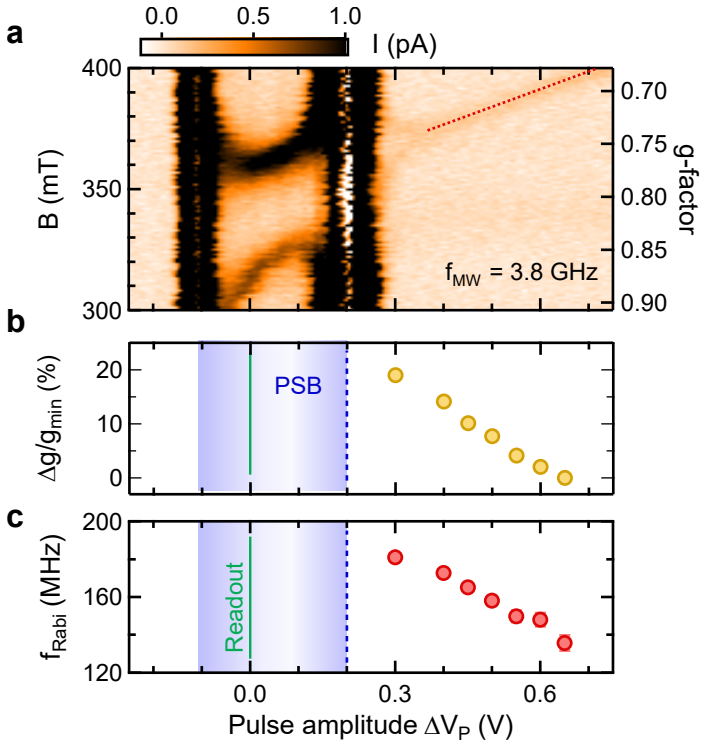

FIGURE B.2 | **Rabi frequency as a function of the Coulomb pulse amplitude. a** Measurement of the EDSR resonances as a function of magnetic field B_ext and Coulomb pulse amplitude ΔV_P. The microwave burst $t_\mathrm{burst} = 100\,\mathrm{ns}$, the frequency $f_\mathrm{MW} = 3.8\,\mathrm{GHz}$, and the power $P_\mathrm{MW} = 23\,\mathrm{dBm}$ are constant. When the spin manipulation is performed inside the Coulomb-blockaded region, the resonance signal is weak in intensity (red dashed line). **b, c** Relative change of g-factor and Rabi frequency as a function of the Coulomb pulse depth ΔV_P for a different dataset than shown in **a**. The region of Pauli spin blockade (shaded blue) and the readout point at $\Delta V_\mathrm{P} = 0\,\mathrm{V}$ (green line) are indicated.

B.2.2 Electrical Tunability with V_M

The main text discusses the variation of the Rabi frequency due to changes of the voltage V_M. In addition to the spin-orbit length, also the electric field amplitude $|\vec{E}_{MW}(t)|$, the g-factor and the orbital level splitting Δ_{orb} determine the Rabi frequency, which can be written as (see also equation 8.1 of the main text):

$$f_{Rabi} = f_{MW} \cdot \frac{l_{dot}}{l_{so}} \cdot \frac{e|\vec{E}_{MW}(t)|l_{dot}}{\Delta_{orb}}. \tag{B.1}$$

Here, we used $f_{Rabi} = g_{\parallel}\mu_B|\vec{B}_{eff}(t)|/(2h)$ with $|\vec{B}_{eff}(t)|$ as defined in Eq. 8.1 of the main text, and $|\vec{B}_{ext}(t)|$ is converted to f_{MW} via the resonance condition $g_{\parallel}\mu_B|\vec{B}_{ext}(t)| = hf_{MW}$, since f_{MW} is held fixed. In order to stay on resonance, we compensate the variation of $g_{\parallel}$ (shown in Figure 8.3 **c** of the main text) with a proportional change of $|\vec{B}_{ext}(t)|$ in the opposite direction, effectively making f_{Rabi} independent of $g_{\parallel}$. We note that $l_{dot} = \hbar/\sqrt{\Delta_{orb} m_{eff}}$ with the effective hole mass m_{eff}.

Because several quantities in equation (B.1) could depend on the gate voltages, we discuss the relative contributions of these individual terms to the 7-fold change of the Rabi frequency as observed in Figure 8.3 **b** of the main text. We treat the contribution of the change in spin-orbit length l_{so} separately in section B.2.3.

First, we investigate the contribution of the electric field amplitude, which can change as a function of V_M even at constant applied microwave power, due to changes of the quantum dot shape, size, or position, which may alter the electric dipole coupling. To roughly estimate the microwave electric field amplitude at the quantum dot for different configurations of V_M, we convert the voltage drop over gate V_L into an electric field across the quantum dot. The voltage drop, in turn, we determine from linewidth measurements of the modified zero-detuning line[Now07], as discussed in section B.1. We assume that the microwave voltage drops over 50 nm, corresponding to the distance

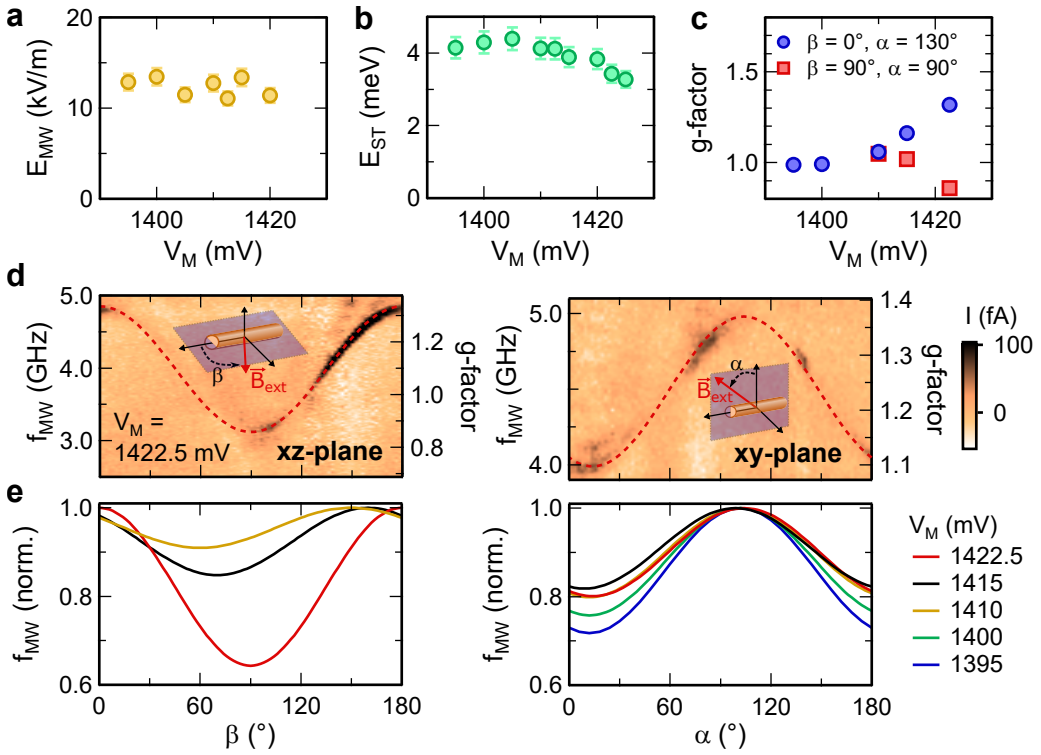

FIGURE B.3 | **Additional data supporting the qubit tunability with electric fields.** **a** Electric field strength of the microwave drive for different values of V_M in the same range as in Figure 8.3 of the main text. The values are extracted from the shift of the zero detuning line (see section B.1) at the used microwave power $P = 11\,\mathrm{dBm}$. **b** Singlet-triplet splitting E_ST as a function of V_M extracted from line cuts in the bias triangle along the detuning line. **c** g-factor in perpendicular directions compared to the magnetic field orientation in Figure 8.3 of the main text. **d** Anisotropy measurements of the g-factor in the $\hat{x}\hat{z}$- (left) and $\hat{x}\hat{y}$- (right) plane for $V_\mathrm{M} = 1422.5\,\mathrm{mV}$ and $B_\mathrm{ext} = 260\,\mathrm{mT}$. The anisotropy is highlighted by the red dashed line. **e** From measurements as shown in **d**, the g-factor anisotropy in the $\hat{x}\hat{z}$- (left) and $\hat{x}\hat{y}$- (right) plane is extracted for several values of V_M. In order to compare differences of the g-factor anisotropy due to a change in V_M, each curve is normalized to its maximum.

between two neighboring gates. Figure B.2 **a** shows the microwave electric field amplitude in the dot as a function of gate voltage V_M in the same range as used in the main text. Overall, the microwave electric field amplitude does not change significantly, which rules out an unintentional variation of the microwave power while changing the value of V_M.

Second, the Rabi frequency scales with the orbital level splitting Δ_orb roughly as $\sim 1/\Delta_\mathrm{orb}^2$ (see equation (B.1)). In order to estimate this contribution, we extract the

single-dot singlet-triplet splitting E_{ST} for all values of V_{M} used in the main text and plot it in Figure B.2 **b**. Note that $E_{\mathrm{ST}} = \Delta_{\mathrm{orb}} - E_{\mathrm{exchange}}$ includes contributions from both Δ_{orb} and the single-dot exchange energy E_{exchange}, which is not easily determined independently. In a realistic case, a more positive V_{M} increases both Δ_{orb} and E_{exchange} as the holes become more confined. Here, however, we disregard any changes in E_{exchange} as a function of V_{M} and assign the observed decrease of E_{ST} in Figure B.2 **b** solely to a change of Δ_{orb}. Note that this approach leads to an overestimation of the role of a change in Δ_{orb} with V_{M}. If the exchange energy indeed varies with V_{M}, the decrease of Δ_{orb} would be even smaller and therefore contribute less to the change in f_{Rabi}. If Δ_{orb} increases with V_{M}, it would even lead to a downward trend of f_{Rabi} with V_{M}.

We conclude that the reduction of the orbital level splitting Δ_{orb} from 4.1 meV to 3.3 meV can therefore maximally account for only a factor 1.5 out of the 7-fold increase of the Rabi frequency observed in the main text.

In conclusion, we estimate the contributions from changes in electric field amplitude (no change) and orbital level splitting to account for a total of not more than a 1.5-fold change of the Rabi frequency. The very large change of the Rabi frequency by a factor of 7 can therefore be attributed mainly to an electrically tunable spin-orbit interaction, as expected from a direct Rashba type of spin-orbit interaction.

We also study the evolution of the g-factor in other directions as a function of V_{M}. Figure B.2 **c** shows g-factors in two directions that are perpendicular to the orientation of $\vec{B}_{\mathrm{ext}}$ as function of V_{M}, extracted from measurements of the Larmor frequency. We find that the g-factor in the $\hat{x}\hat{z}$-plane (red dots in Figure B.2 **c**) does not change significantly as a function of V_{M}. In the $\hat{x}\hat{y}$-plane (blue dots in Figure B.2 **c**), we find that the g-factor increases as a function of V_{M} by a factor of 1.3.

This increase is somewhat less but comparable to the change of $g_{\parallel}$ in Figure 8.3 **c** of the main text, which increases by a factor of 1.5 in the same range of V_{M}, indicating that the changes in g-factor are indeed rather isotropic.

Although indicative of an isotropic change of g-factors, a full proof would entail determination of the complete g-matrix. Our measurements do not allow for such a full characterization, but we can give more indications for the g-matrix variation by providing measurements of the g-factor anisotropy in various planes, and as a function of V_{M}.

We measure the complete g-factor anisotropy in the $\hat{x}\hat{y}$ and in the $\hat{x}\hat{z}$ planes for a relevant range of V_{M}. Figure B.2 **d** shows examples of such anisotropy measurements, for V_{M} =1422.5 mV. We extract the anisotropic g-factor, indicated by the red dashed curves, for different values of V_{M} as shown in Figure B.2 **e**.

Each curve in Figure B.2 **e** has been normalized to the maximum in order to better compare the change of the anisotropy. Overall, the g-factor anisotropy in the $\hat{x}\hat{y}$-plane decreases by about 10 % with increasing voltage V_{M}. Conversely, in the $\hat{x}\hat{z}$-plane the anisotropy increases by about 30 % with increasing voltage V_{M} and furthermore the position of the minimum g-factor shifts.

After estimating the impact of $|\vec{E}(t)|$, g-factor and Δ_{orb}, we now estimate the value of l_{so}.

B.2.3 Estimation of spin-orbit length

We estimate the spin-orbit length l_{so} using equation (B.1) directly from the measured Rabi frequency f_{Rabi}. Here, we use an effective value of l_{so} defined by $\pi l_{\mathrm{so}}/2$ being the length along the nanowire which a hole has to travel in order to have its spin flipped. This definition of l_{so} includes the possibility that the direction of the spin-orbit field $\vec{B}_{\mathrm{so}}$ with respect to the external magnetic field $\vec{B}_{\mathrm{ext}}$ can be non-optimal for EDSR, i.e. $\angle(\vec{B}_{\mathrm{so}}, \vec{B}_{\mathrm{ext}}) \neq 90°$. In this case, $|\vec{B}_{\mathrm{eff}}|$ assumes a smaller value, leading to lower Rabi frequencies than achievable with $\vec{B}_{\mathrm{so}} \perp \vec{B}_{\mathrm{ext}}$.

In our experiment, we do not determine the direction of $\vec{B}_{\mathrm{so}}$. However, values extracted for l_{so} from Eq. (1) of the main text using this effective definition correspond to upper

bounds of the spin-orbit length defined in terms of the Rashba coefficient α as $\hbar/(m_{\text{eff}}\alpha)$ as obtained by taking the optimal orientation $\vec{B}_{\text{so}} \perp \vec{B}_{\text{ext}}$. We estimate such upper bounds for l_{so} for four different values of V_{M}. The corresponding values of $|\vec{B}_{\text{ext}}|$ are given by matching the Larmor frequency to f_{MW} and we determine the values of the remaining parameters $|E(t)|$, Δ_{orb}, and l_{dot} from other measurements. Note that these four values of V_{M} form a subset of those used in the main text.

The electric field amplitude $|E(t)|$ is estimated as described in section B.2.2 and shown in Figure B.2 **a**. Given the assumption that the entire voltage of the applied microwaves drops over the distance of 50 nm between neighbouring gates the value of $|E(t)| \approx 13\,\text{kV}\,\text{m}^{-1}$ (see Figure B.2 **a**) will result in conservative values for l_{so}, as taking a larger distance over which the voltage drops would result in a weaker electric field and hence larger l_{so}. For Δ_{orb} we take the values shown in Figure B.2 **b**, which were obtained from anisotropy measurements and bias triangles, respectively. Note again that for determining Δ_{orb}, we neglect the exchange energy and a possible variation of it with V_{M}. Therefore, Δ_{orb} could be larger than we estimate here, which would make the extracted values of l_{so} even smaller than those we find.

Lastly, to estimate the longitudinal dot length l_{dot}, we use $l_{\text{dot}} = \hbar/\sqrt{\Delta_{\text{orb}} m_{\text{eff}}}$, given an effective hole mass m_{eff}. For holes in Ge/Si nanowires, the effective mass depends strongly on the number of holes in the quantum dot[Klo11; Klo18]. Since we did not independently measure m_{eff}, we estimate l_{dot} and l_{so} both for m_{eff} being equal to the heavy-hole (HH) mass ($0.28\,m_0$, with m_0 the electron mass) and for m_{eff} being equal to the light-hole (LH) mass ($0.044\,m_0$). Table B.1 and Fig. B.4 present the calculated upper bounds for l_{dot} and l_{so} for the four different values of V_{M}. For the measurement with $V_{\text{M}} = 1422.5\,\text{mV}$, corresponding to the highest Rabi frequency, we find extremely short spin-orbit lengths of maximally 4 nm (26 nm) assuming a HH (LH) effective mass. Note that the fact that the current running through the double dot does not get significantly quenched even for high values of a magnetic field transverse

to the nanowire (up to 6 T, not shown) points towards m_{eff} being rather closer to the HH mass than to the LH mass [Fro21a]. Further, note that for the relatively low microwave powers used here, equation (B.1) of the main text is valid even in the case that $l_{\text{so}} < l_{\text{dot}}$ [5].

TABLE B.1 | Extracted values of l_{dot} and upper bounds of l_{so} for different values of V_{M}. Here LH (HH) corresponds to the case of a light-hole (heavy-hole) effective mass. The errors on all extracted values of l_{dot} and l_{so} are smaller than 15 %.

V_{M} (mV)	l_{dot} HH (nm)	l_{dot} LH (nm)	**l_{so} HH (nm)**	l_{so} LH (nm)
1395	8	21	**23**	146
1400	8	20	**15**	98
1410	8	21	**7**	44
1422.5	9	23	**4**	26

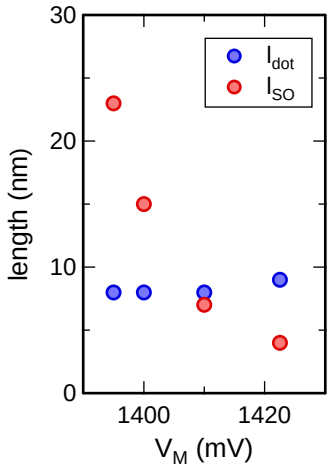

FIGURE B.4 | **Estimation of spin-orbit length and dot length.** Plot of l_{so} and l_{dot} as a function of V_{M}, estimated using measured values of Δ_{orb} and $|E_{\text{MW}}$ for each value of V_{M} as described in text. Here m_{eff} corresponds to the heavy-hole mass. Note that assuming another mass will change the absolute values of l_{so} and l_{dot}, but will leave the tunability with V_{M} unaffected.

[5] Private communication with S. Bosco and D. Loss

C Fabrication Recipes

For the fabrication as described in section 4, electron beam lithography (EBL) with subsequent metallization by electron beam evaporation have been used. General information about EBL [Ste12b, Ch. 2] and resists [All20d] can be found elsewhere, and are not subject of this section. Here, only commonly used process parameters are listed. Note that all parameters are subject to alteration and need to be adjusted regularly with a dose test.

C.1 Miscellaneous Metallized Structures

TABLE C.1 | **Process parameters for miscellaneous structures**

Step	Parameters	Comment
Wafer cleaning	acetone, isopropanol	Si wafer
Resist	4.5 % PMMA 950K	*Allresist GmbH*, AR-P 671 or AR-P 672 series [All20c]
	4000-6000/4/40 (speed [rpm]/ramp [s]/time [s])	
	bake 7 min at 180 °C	hotplate
EBL	20 kV, 10 µm or 120 µm aperture	working distance and writefield as necessary
	area dose 400 µC/cm^2	
Development	IPA:MIBK 3:1 developer with 1.3 % MEK	developer AR 600-56 [All20b], mix with MEK
	60 s at $T_{\mathrm{dev}} = 4$ °C	
	stop 30 s in isopropanol	
	blow dry with N_2	
Metallization	O_2 reactive ion etch for 1 min	parameters: 30 W, 16 % O_2, base pressure 5×10^{-5} mbar, working pressure 250 mTorr
	Ti/Pd, thickness variable	electron beam evaporation
Lift-off	acetone bath at $T = 50$ °C	

C.2 Finger Gates

The fabrication of the narrowly spaced finger gates seen in Figure 4.2 is described in section 4.3. Here, only detailed process parameters are listed which were commonly used.

TABLE C.2 | **Process parameters for fabrication of finger gates** The main steps and process parameters are listed here, while a detailed discussion of each step can be found in section 4.3. Note that some parameters need regular adjustments.

Step	Parameters	Comment
Wafer cleaning	acetone, isopropanol	Si wafer
Resist	1.8 % PMMA 950K	*Allresist GmbH*, AR-P 671 or AR-P 672 series [All20c]
		dilute if necessary (e.g. with AR 600-02) [All20f]
	6000/4/40 (speed [rpm]/ramp [s]/time [s])	depends on concentration of resist
	bake 7 min at 180 °C	hotplate
		final thickness around 45 nm to 50 nm
EBL	30 kV, 7.5 µm aperture, 9.1 mm working distance, 50 µm writefield	
	line dose 2700 pC/cm	determined by dose test
	area dose 1000 µC/cm^2	determined by dose test
Development	IPA:MIBK 3:1 developer with 1.3 % MEK	developer AR 600-56 [All20b], mix with MEK
	30 s at $T_{\mathrm{dev}} = -15$ °C	IPA bath, cool with dry ice
	blow dry with N_2	prevent water condensation
Metallization	O_2 reactive ion etch for 10 s	parameters: 30 W, 16 % O_2, base pressure 5×10^{-5} mbar, working pressure 250 mTorr
	1 nm Ti, 12 nm Pd	electron beam evaporation
Lift-off	acetone bath at $T = 50$ °C	

C.3 Ohmic Contacts to Nanowire

Ohmic contacts are fabricated after removing the thin native oxide prior to metallization. During this wet etch with hydrofluoric acid, an adhesion promoter is employed.

TABLE C.3 | **Process parameters for fabrication of ohmic contacts**

Step	Parameters	Comment
Transfer nanowires		micromanipulator
Pre-Treatment	dip 2 min in acetone, then in isopropanol	optional
Adhesion promoter	4000/4/40 (speed [rpm]/ramp [s]/time [s])	AR 300-80 [All20a]
	bake 2 min at 185 °C	hotplate
	immerse 7 min in acetone, 1 min in isopropanol, blow dry	
Resist	two step spinning process: *(i)* 250/0/15 *(ii)* 4000/4/40 (speed [rpm]/ramp [s]/time [s])	copolymer resist [Kay20] MMA(8.5)MAA EL6
	bake 90 s at $T = 185$ °C	hotplate
	repeat	in total, two layers of resist
EBL	30 kV, 10 µm aperture	
	9.1 mm working distance	
	100 µm writefield	
	area dose 140 µC/cm^2	
Development	IPA:MIBK 3:1 developer	developer AR 600-56 [All20b], no MEK added
	60 s at room temperature	
	stop with 10 s rinse in isopropanol	
Metallization	O_2 reactive ion etch for 1 min	parameters: 30 W, 16 % O_2, base pressure 5×10^{-5} mbar, working pressure 250 mTorr
	10 s etch with buffered HF	rinse in DI water
	0.3 nm Ti, 50 nm Pd	electron beam evaporation
Lift-off	acetone bath at $T = 50$ °C	

Bibliography

[Akt06] M. Aktary, M. Stepanova, and S. K. Dew, "Simulation of the spatial distribution and molecular weight of polymethylmethacrylate fragments in electron beam lithography exposures", J. Vac. Sci. Technol. B **24**, 768 (2006) (cited on pages 73–75).

[Ali10] J. Alicea, "Majorana fermions in a tunable semiconductor device", en, Phys. Rev. B **81**, 125318 (2010) (cited on page 100).

[All20a] AllResist GmbH, *Adhesion Promoter AR 300-80 new*, en-GB, (2020) https://www.allresist.com/portfolio-item/adhesion-promoter-ar-300-80-new/ (visited on 05/26/2020) (cited on page 178).

[All20b] AllResist GmbH, *Developer AR 600-56*, en-GB, (2020) https://www.allresist.com/portfolio-item/developer-ar-600-56/ (visited on 05/26/2020) (cited on pages 176–178).

[All20c] AllResist GmbH, *E-Beam Resist AR-P 672-Serie*, en-GB, (2020) https://www.allresist.com/portfolio-item/e-beam-resist-ar-p-672-serie/ (visited on 05/26/2020) (cited on pages 176, 177).

[All20d] AllResist GmbH, *Resist Wiki*, en-GB, (2020) https://www.allresist.com/resist-wiki/ (visited on 05/26/2020) (cited on page 176).

[All20e] AllResist GmbH, *Resist-Wiki: Haftfestigkeit des AR 300-80*, en-GB, (2020) https://www.allresist.com/resist-wiki-adhesive-strength-of-ar-300-80/ (visited on 05/26/2020) (cited on page 70).

[All20f] AllResist GmbH, *Thinner AR 600-02*, en-GB, (2020) https://www.allresist.com/portfolio-item/thinner-ar-600-02/ (visited on 05/26/2020) (cited on page 177).

[Ama11] M. Amato, S. Ossicini, and R. Rurali, "Band-Offset Driven Efficiency of the Doping of SiGe Core-Shell Nanowires", en, Nano Lett. **11**, 594 (2011) (cited on page 21).

[Ama14] M. Amato, M. Palummo, R. Rurali, and S. Ossicini, "Silicon–Germanium Nanowires: Chemistry and Physics in Play, from Basic Principles to Advanced Applications", en, Chem. Rev. **114**, 1371 (2014) (cited on page 18).

[Ami18] S. V. Amitonov, P. C. Spruijtenburg, M. W. S. Vervoort, W. G. van der Wiel, and F. A. Zwanenburg, "Depletion-mode quantum dots in intrinsic silicon", Applied Physics Letters **112**, 023102 (2018) (cited on page 77).

[And60] R. L. Anderson, "Germanium-Gallium Arsenide Heterojunctions [Letter to the Editor]", IBM J. Res. & Dev. **4**, 283 (1960) (cited on page 19).

[Ara20] H. Arab, S. MohammadNejad, A. KhodadadKashi, and S. Ahadzadeh, "Recent advances in nanowire quantum dot (NWQD) single-photon emitters", Quantum Information Processing **19**, 44 (2020) (cited on pages 11, 13).

[Aru19] F. Arute et al., "Quantum supremacy using a programmable superconducting processor", en, Nature **574**, 505 (2019) (cited on page 1).

[Ban03] S. Bandyopadhyay, "Single-spin measurement in the solid state: A reader for a spin qubit", en, Phys. Rev. B **67**, 193304 (2003) (cited on page 58).

[Ban20] R. Banino, *20 new technology trends we will see in the 2020s*, en, (Mar. 2020) `https://www.sciencefocus.com/future-technology/new-technology-trends-2020s/` (visited on 05/03/2020) (cited on page 1).

[Bas20a] Basel Cryogenics, *Microwave Filters*, (2020) `https://baselcryogenics.unibas.ch/` (visited on 05/11/2020) (cited on page 82).

[Bas20b] Basel Precision Instruments, *Low-Noise Ultra-Stable Electronics for Cutting-Edge R&D*, en, (2020) `https://www.baspi.ch` (visited on 05/11/2020) (cited on page 84).

[Ber92] G. H. Bernstein, D. A. Hill, and W.-p. Liu, "New high-contrast developers for poly(methyl methacrylate) resist", Journal of Applied Physics **71**, 4066 (1992) (cited on page 75).

[Bet14] A. C. Betz, M. F. Gonzalez-Zalba, G. Podd, and A. J. Ferguson, "Ambipolar quantum dots in intrinsic silicon", en, Appl. Phys. Lett. **105**, 153113 (2014) (cited on page 29).

[Bie15] D. E. F. Biesinger, C. P. Scheller, B. Braunecker, J. Zimmerman, A. C. Gossard, and D. M. Zumbühl, "Intrinsic Metastabilities in the Charge Configuration of a Double Quantum Dot", Physical Review Letters **115**, 106804 (2015) (cited on pages 41, 95, 105).

[Bjö05] M. T. Björk, A. Fuhrer, A. E. Hansen, M. W. Larsson, L. E. Fröberg, and L. Samuelson, "Tunable effective g factor in InAs nanowire quantum dots", en, Phys. Rev. B **72**, 201307 (2005) (cited on page 46).

[Bjö04] M. T. Björk, C. Thelander, A. E. Hansen, L. E. Jensen, M. W. Larsson, L. R. Wallenberg, and L. Samuelson, "Few-Electron Quantum Dots in Nanowires", Nano Lett. **4**, 1621 (2004) (cited on pages 14, 93).

[Bla04] A. Blais, R.-S. Huang, A. Wallraff, S. M. Girvin, and R. J. Schoelkopf, "Cavity quantum electrodynamics for superconducting electrical circuits: An architecture for quantum computation", en, Phys. Rev. A **69**, 062320 (2004) (cited on page 151).

[Blu20] Bluefors Oy, *Dilution refrigerators for quantum and nano technology research*, en-US, (2020) https://bluefors.com/ (visited on 05/11/2020) (cited on page 81).

[Blu10] H. Bluhm, S. Foletti, D. Mahalu, V. Umansky, and A. Yacoby, "Enhancing the Coherence of a Spin Qubit by Operating it as a Feedback Loop That Controls its Nuclear Spin Bath", en, Phys. Rev. Lett. **105**, 216803 (2010) (cited on page 4).

[Blu11] H. Bluhm, S. Foletti, I. Neder, M. Rudner, D. Mahalu, V. Umansky, and A. Yacoby, "Dephasing time of GaAs electron-spin qubits coupled to a nuclear bath exceeding 200 μs", en, Nature Phys. **7**, 109 (2011) (cited on page 65).

[Bor20] F. Borjans, X. G. Croot, X. Mi, M. J. Gullans, and J. R. Petta, "Resonant microwave-mediated interactions between distant electron spins", en, Nature **577**, 195 (2020) (cited on pages 6, 132, 152).

[Bra14] F. R. Braakman, J. Danon, L. R. Schreiber, W. Wegscheider, and L. M. K. Vandersypen, "Dynamics of spin-flip photon-assisted tunneling", en, Phys. Rev. B **89**, 075417 (2014) (cited on page 108).

[Bra19] F. R. Braakman and M. Poggio, "Force sensing with nanowire cantilevers", en, Nanotechnology **30**, 332001 (2019) (cited on page 13).

[Bra16a] M. Brauns, J. Ridderbos, A. Li, E. P. A. M. Bakkers, and F. A. Zwanenburg, "Electric-field dependent g-factor anisotropy in Ge-Si core-shell nanowire quantum dots", Physical Review B **93**, 121408 (2016) (cited on pages 9, 47, 88, 102, 147).

[Bra16b] M. Brauns, J. Ridderbos, A. Li, E. P. A. M. Bakkers, W. G. van der Wiel, and F. A. Zwanenburg, "Anisotropic Pauli spin blockade in hole quantum dots", Physical Review B **94**, 041411 (2016) (cited on pages 43, 95, 97, 102, 105, 147).

[Bra16c] M. Brauns, J. Ridderbos, A. Li, W. G. van der Wiel, E. P. A. M. Bakkers, and F. A. Zwanenburg, "Highly tuneable hole quantum dots in Ge-Si core-shell nanowires", Applied Physics Letters **109**, 143113 (2016) (cited on pages 8, 9, 14, 88, 102, 104, 123).

[Bri93] J. C. Brighten, I. D. Hawkins, A. R. Peaker, R. A. Kubiak, E. H. C. Parker, and T. E. Whall, "The determination of valence band discontinuities and interface charge densities in Si/Si $_{1-y}$ Ge $_{y}$ /Si heterojunctions", Semicond. Sci. Technol. **8**, 1487 (1993) (cited on page 19).

[Bru19] C. D. Bruzewicz, J. Chiaverini, R. McConnell, and J. M. Sage, "Trapped-Ion Quantum Computing: Progress and Challenges", en, Applied Physics Reviews **6**, 021314 (2019) (cited on page 2).

[Buc05] J. Buckley, B. De Salvo, D. Deleruyelle, M. Gely, G. Nicotra, S. Lombardo, J. F. Damlencourt, P. Hollinger, F. Martin, and S. Deleonibus, "Reduction of fixed charges in atomic layer deposited Al2O3 dielectrics", en, Microelectronic Engineering **80**, 210 (2005) (cited on page 78).

[Bul07] D. V. Bulaev and D. Loss, "Electric Dipole Spin Resonance for Heavy Holes in Quantum Dots", en, Phys. Rev. Lett. **98**, 097202 (2007) (cited on pages 100, 119, 122).

[Bul05] D. V. Bulaev and D. Loss, "Spin Relaxation and Decoherence of Holes in Quantum Dots", en, Phys. Rev. Lett. **95**, 076805 (2005) (cited on pages 100, 122).

[Bur20] G. Burkard, M. J. Gullans, X. Mi, and J. R. Petta, "Superconductor-semiconductor hybrid-circuit quantum electrodynamics", en, Nat Rev Phys **2**, 129 (2020) (cited on pages 6, 100, 123, 132, 151).

[Bur06] G. Burkard and A. Imamoglu, "Ultra-long-distance interaction between spin qubits", en, Phys. Rev. B **74**, 041307 (2006) (cited on page 152).

[Bur15] A. M. Burke, D. J. Carrad, J. G. Gluschke, K. Storm, S. Fahlvik Svensson, H. Linke, L. Samuelson, and A. P. Micolich, "InAs Nanowire Transistors with Multiple, Independent Wrap-Gate Segments", Nano Lett. **15**, 2836 (2015) (cited on page 150).

[Cai19] Z. Cai, M. A. Fogarty, S. Schaal, S. Patomaki, S. C. Benjamin, and J. J. L. Morton, "A Silicon Surface Code Architecture Resilient Against Leakage Errors", en, Quantum **3**, 212 (2019) (cited on page 4).

[Cam19] L. Camenzind, "Spins and orbits in semiconductor quantum dots", eng, Doctoral Thesis (University of Basel, Basel, Switzerland, 2019) (cited on pages 82, 83).

[Cam18] L. C. Camenzind, L. Yu, P. Stano, J. D. Zimmerman, A. C. Gossard, D. Loss, and D. M. Zumbühl, "Hyperfine-phonon spin relaxation in a single-electron GaAs quantum dot", en, Nat Commun **9**, 1 (2018) (cited on page 88).

[Car54] H. Y. Carr and E. M. Purcell, "Effects of Diffusion on Free Precession in Nuclear Magnetic Resonance Experiments", en, Phys. Rev. **94**, 630 (1954) (cited on page 65).

[Cas07] M. A. Castellanos-Beltran and K. W. Lehnert, "Widely tunable parametric amplifier based on a superconducting quantum interference device array resonator", Applied Physics Letters **91**, 083509 (2007) (cited on pages 79, 152).

[Cas18] D. Castelvecchi, "Silicon gains ground in quantum-computing race", en, Nature **553**, 136 (2018) (cited on page 5).

[Cha18] K. W. Chan, W. Huang, C. H. Yang, J. C. C. Hwang, B. Hensen, T. Tanttu, F. E. Hudson, K. M. Itoh, A. Laucht, A. Morello, and A. S. Dzurak, "Assessment of a Silicon Quantum Dot Spin Qubit Environment via Noise Spectroscopy", en, Phys. Rev. Applied **10**, 044017 (2018) (cited on page 147).

[Chi04] L. Childress, A. S. Sørensen, and M. D. Lukin, "Mesoscopic cavity quantum electrodynamics with quantum dots", en, Phys. Rev. A **69**, 042302 (2004) (cited on page 152).

[Coi11] W. A. Coish and F. Qassemi, "Leakage-current line shapes from inelastic cotunneling in the Pauli spin blockade regime", Physical Review B **84**, 245407 (2011) (cited on pages 41, 105, 108).

[Col13] J. I. Colless, A. C. Mahoney, J. M. Hornibrook, A. C. Doherty, H. Lu, A. C. Gossard, and D. J. Reilly, "Dispersive readout of a few-electron double quantum dot with fast rf gate sensors", en, Phys. Rev. Lett. **110**, 046805 (2013) (cited on pages 59, 60).

[Con17] S. Conesa-Boj, A. Li, S. Koelling, M. Brauns, J. Ridderbos, T. T. Nguyen, M. A. Verheijen, P. M. Koenraad, F. A. Zwanenburg, and E. P. A. M. Bakkers, "Boosting hole mobility in coherently strained [110]-Oriented ge-si core-shell nanowires", Nano Letters **17**, 2259 (2017) (cited on pages 21, 67–69, 89, 104, 123, 133, 141).

[Cor07] B. Cord, J. Lutkenhaus, and K. K. Berggren, "Optimal temperature for development of poly(methylmethacrylate)", J. Vac. Sci. Technol. B **25**, 2013 (2007) (cited on pages 74, 75).

[Cri19] A. Crippa, R. Ezzouch, A. Aprá, A. Amisse, R. Laviéville, L. Hutin, B. Bertrand, M. Vinet, M. Urdampilleta, T. Meunier, M. Sanquer, X. Jehl, R. Maurand, and S. De Franceschi, "Gate-reflectometry dispersive readout and coherent control of a spin qubit in silicon", en, Nat Commun **10**, 2776 (2019) (cited on pages 6, 59, 122).

[Cri18] A. Crippa, R. Maurand, L. Bourdet, D. Kotekar-Patil, A. Amisse, X. Jehl, M. Sanquer, R. Laviéville, H. Bohuslavskyi, L. Hutin, S. Barraud, M. Vinet, Y.-M. Niquet, and S. De Franceschi, "Electrical spin driving by g-Matrix modulation in spin-orbit qubits", Physical Review Letters **120**, 137702 (2018) (cited on page 55).

[Cro76] J. R. Crooks and M. J. Hampshire, "A study of the interface between germanium and silicon", en, J. Phys. D: Appl. Phys. **9**, 643 (1976) (cited on page 19).

[Cro19] A. W. Cross, L. S. Bishop, S. Sheldon, P. D. Nation, and J. M. Gambetta, "Validating quantum computers using randomized model circuits", en, Phys. Rev. A **100**, 032328 (2019) (cited on page 1).

[Cso09] D. Csontos, P. Brusheim, U. Zülicke, and H. Q. Xu, "Spin-3/2 physics of semiconductor hole nanowires: Valence-band mixing and tunable interplay between bulk-material and orbital bound-state spin splittings", Physical Review B **79**, 155323 (2009) (cited on page 22).

[Cui03] Y. Cui, Z. Zhong, D. Wang, W. U. Wang, and C. M. Lieber, "High Performance Silicon Nanowire Field Effect Transistors", Nano Lett. **3**, 149 (2003) (cited on page 17).

[Dan09] J. Danon and Y. V. Nazarov, "Pauli spin blockade in the presence of strong spin-orbit coupling", Physical Review B **80**, 1 (2009) (cited on pages 42, 105, 108, 117).

[Day11] S. A. Dayeh, N. H. Mack, J. Y. Huang, and S. T. Picraux, "Advanced core/multishell germanium/silicon nanowire heterostructures: The Au-diffusion bottleneck", Applied Physics Letters **99**, 023102 (2011) (cited on page 68).

[Day13] S. A. Dayeh, W. Tang, F. Boioli, K. L. Kavanagh, H. Zheng, J. Wang, N. H. Mack, G. Swadener, J. Y. Huang, L. Miglio, K.-N. Tu, and S. T. Picraux, "Direct Measurement of Coherency Limits for Strain Relaxation in Heteroepitaxial Core/Shell Nanowires", Nano Lett. **13**, 1869 (2013) (cited on pages 22, 141).

[Dea10] C. R. Dean, A. F. Young, I. Meric, C. Lee, L. Wang, S. Sorgenfrei, K. Watanabe, T. Taniguchi, P. Kim, K. L. Shepard, and J. Hone, "Boron nitride substrates for high-quality graphene electronics", Nature Nanotechnology **5**, 722 (2010) (cited on page 78).

[dFra10] S. de Franceschi, L. Kouwenhoven, C. Schönenberger, and W. Wernsdorfer, "Hybrid superconductor–quantum dot devices", en, Nature Nanotech **5**, 703 (2010) (cited on page 13).

[dFra03] S. de Franceschi, J. A. van Dam, E. P. A. M. Bakkers, L. F. Feiner, L. Gurevich, and L. P. Kouwenhoven, "Single-electron tunneling in InP nanowires", Appl. Phys. Lett. **83**, 344 (2003) (cited on pages 11, 14).

[Deh13] J. P. Dehollain, J. J. Pla, E. Siew, K. Y. Tan, A. S. Dzurak, and A. Morello, "Nanoscale broadband transmission lines for spin qubit control", Nanotechnology **24**, 015202 (2013) (cited on page 54).

[dJon19] D. de Jong, J. van Veen, L. Binci, A. Singh, P. Krogstrup, L. P. Kouwenhoven, W. Pfaff, and J. D. Watson, "Rapid Detection of Coherent Tunneling in an InAs Nanowire Quantum Dot through Dispersive Gate Sensing", en, Phys. Rev. Applied **11**, 044061 (2019) (cited on page 60).

[Dev13] M. H. Devoret and R. J. Schoelkopf, "Superconducting Circuits for Quantum Information: An Outlook", en, Science **339**, 1169 (2013) (cited on pages 2, 44).

[Dev92] M. H. Devoret, D. Esteve, and C. Urbina, "Single-electron transfer in metallic nanostructures", en, Nature **360**, 547 (1992) (cited on page 11).

[dVri18] F. K. de Vries, J. Shen, R. J. Skolasinski, M. P. Nowak, D. Varjas, L. Wang, M. Wimmer, J. Ridderbos, F. A. Zwanenburg, A. Li, S. Koelling, M. A. Verheijen, E. P. A. M. Bakkers, and L. P. Kouwenhoven, "Spin–Orbit Interaction and Induced Superconductivity in a One-Dimensional Hole Gas", Nano Lett. **18**, 6483 (2018) (cited on pages 9, 49).

[Din10] G. Dingemans, W. Beyer, M. C. M. van de Sanden, and W. M. M. Kessels, "Hydrogen induced passivation of Si interfaces by Al2O3 films and SiO2/Al2O3 stacks", Applied Physics Letters **97**, 152106 (2010) (cited on page 77).

[DiV00a] D. P. DiVincenzo, D. Bacon, J. Kempe, G. Burkard, and K. B. Whaley, "Universal quantum computation with the exchange interaction", Nature **408**, 339 (2000) (cited on page 89).

[DiV00b] D. P. DiVincenzo, "The Physical Implementation of Quantum Computation", en, Fortschritte der Physik **48**, 771 (2000) (cited on pages 3, 4, 44).

[Dmy18] O. Dmytruk, D. Chevallier, D. Loss, and J. Klinovaja, "Renormalization of the quantum dot g-factor in superconducting Rashba nanowires", en, Phys. Rev. B **98**, 165403 (2018) (cited on pages 103, 109, 112).

[Dor19] S. Dorsch, B. Dalelkhan, S. Fahlvik, and A. M. Burke, "Side-gated, enhancement mode, InAs nanowire double quantum dot devices—toward controlling transverse electric fields in spin-transport measurements", en, Nanotechnology **30**, 144002 (2019) (cited on pages 149, 150).

[Dua08] X. Duan, "Nanowire Thin-Film Transistors: A New Avenue to High-Performance Macroelectronics", IEEE Transactions on Electron Devices **55**, 3056 (2008) (cited on page 17).

[Dur14] M. V. Durnev, M. M. Glazov, and E. L. Ivchenko, "Spin-orbit splitting of valence subbands in semiconductor nanostructures", en, Phys. Rev. B **89**, 075430 (2014) (cited on page 122).

[Dur19] M. Durrani, *Physics in the 2020s: what will happen over the decade ahead*, en-GB, (Dec. 2019) `https://physicsworld.com/a/physics-in-the-2020s-what-will-happen-over-the-decade-ahead/` (visited on 05/03/2020) (cited on page 1).

[Eat16] S. W. Eaton, A. Fu, A. B. Wong, C.-Z. Ning, and P. Yang, "Semiconductor nanowire lasers", Nature Reviews Materials **1**, 16028 (2016) (cited on pages 11, 13).

[Eck13] J. N. Eckstein and J. Levy, "Materials issues for quantum computation", MRS Bull. **38**, 783 (2013) (cited on page 44).

[Elz03] J. M. Elzerman, R. Hanson, J. S. Greidanus, L. H. Willems van Beveren, S. De Franceschi, L. M. K. Vandersypen, S. Tarucha, and L. P. Kouwenhoven, "Few-electron quantum dot circuit with integrated charge read out", en, Phys. Rev. B **67**, 161308 (2003) (cited on page 4).

[Elz04] J. M. Elzerman, R. Hanson, L. H. Willems van Beveren, B. Witkamp, L. M. K. Vandersypen, and L. P. Kouwenhoven, "Single-shot read-out of an individual electron spin in a quantum dot", Nature **430**, 431 (2004) (cited on pages 4, 58).

[Eri13] M. Eriksson, S. Coppersmith, and M. Lagally, "Semiconductor quantum dot qubits", MRS Bull. **38**, 794 (2013) (cited on pages 44, 58).

[Esc10] C. C. Escott, F. A. Zwanenburg, and A. Morello, "Resonant tunnelling features in quantum dots", Nanotechnology **21**, 274018 (2010) (cited on pages 91, 93).

[Fas07] C. Fasth, A. Fuhrer, L. Samuelson, V. N. Golovach, and D. Loss, "Direct Measurement of the Spin-Orbit Interaction in a Two-Electron InAs Nanowire Quantum Dot", Physical Review Letters **98**, 266801 (2007) (cited on pages 14, 46).

[Fas05] C. Fasth, A. Fuhrer, M. T. Björk, and L. Samuelson, "Tunable Double Quantum Dots in InAs Nanowires Defined by Local Gate Electrodes", Nano Lett. **5**, 1487 (2005) (cited on pages 11, 14).

[Fer20] E. Ferraro and E. Prati, "Is all-electrical silicon quantum computing feasible in the long term?", en, Physics Letters A **384**, 126352 (2020) (cited on page 5).

[Fie18] B. Field and T. Simula, "Introduction to topological quantum computation with non-Abelian anyons", en, Quantum Sci. Technol. **3**, 045004 (2018) (cited on pages 4, 48).

[Fie93] M. Field, C. G. Smith, M. Pepper, D. A. Ritchie, J. E. F. Frost, G. A. C. Jones, and D. G. Hasko, "Measurements of Coulomb blockade with a noninvasive voltage probe", en, Phys. Rev. Lett. **70**, 1311 (1993) (cited on page 58).

[Fis08] J. Fischer, W. A. Coish, D. V. Bulaev, and D. Loss, "Spin decoherence of a heavy hole coupled to nuclear spins in a quantum dot", en, Phys. Rev. B **78**, 155329 (2008) (cited on page 102).

[Flö11] K. Flöhr, M. Liebmann, K. Sladek, H. Y. Günel, R. Frielinghaus, F. Haas, C. Meyer, H. Hardtdegen, T. Schäpers, D. Grützmacher, and M. Morgenstern, "Manipulating InAs nanowires with submicrometer precision", en, Rev. Sci. Instrum. **82**, 113705 (2011) (cited on page 70).

[Fol09] S. Foletti, H. Bluhm, D. Mahalu, V. Umansky, and A. Yacoby, "Universal quantum control of two-electron spin quantum bits using dynamic nuclear polarization", en, Nature Phys **5**, 903 (2009) (cited on page 4).

[For19] P. Forn-Díaz, L. Lamata, E. Rico, J. Kono, and E. Solano, "Ultrastrong coupling regimes of light-matter interaction", en, Rev. Mod. Phys. **91**, 025005 (2019) (cited on page 153).

[Fow12] A. G. Fowler, M. Mariantoni, J. M. Martinis, and A. N. Cleland, "Surface codes: Towards practical large-scale quantum computation", en, Phys. Rev. A **86**, 032324 (2012) (cited on pages 1, 4, 5, 150).

[Fre12] T. Frey, P. J. Leek, M. Beck, A. Blais, T. Ihn, K. Ensslin, and A. Wallraff, "Dipole Coupling of a Double Quantum Dot to a Microwave Resonator", en, Phys. Rev. Lett. **108**, 046807 (2012) (cited on page 5).

[Fro13] S. M. Frolov, S. R. Plissard, S. Nadj-Perge, L. P. Kouwenhoven, and E. P. A. M. Bakkers, "Quantum computing based on semiconductor nanowires", MRS Bulletin **38**, 809 (2013) (cited on pages 13, 14, 45).

[Fro21a] F. N. M. Froning, M. J. Rančić, B. Hetényi, S. Bosco, M. K. Rehmann, A. Li, E. P. A. M. Bakkers, F. A. Zwanenburg, D. Loss, D. M. Zumbühl, and F. R. Braakman, "Strong spin-orbit interaction and g -factor renormalization of hole spins in Ge/Si nanowire quantum dots", Phys. Rev. Research **3**, 013081 (2021) (cited on pages 99, 129, 175, 216).

[Fro18] F. N. M. Froning, M. K. Rehmann, J. Ridderbos, M. Brauns, F. A. Zwanenburg, A. Li, E. P. A. M. Bakkers, D. M. Zumbühl, and F. R. Braakman, "Single, double, and triple quantum dots in Ge/Si nanowires", Applied Physics Letters **113**, 073102 (2018) (cited on pages 87, 102, 104, 123, 216).

[Fro21b] F. N. M. Froning, L. C. Camenzind, O. A. H. van der Molen, A. Li, E. P. A. M. Bakkers, D. M. Zumbühl, and F. R. Braakman, "Ultrafast hole spin qubit with gate-tunable spin–orbit switch functionality", Nat. Nanotechnol. **16**, 308 (2021) (cited on pages 118, 121, 216).

[Fuj17] T. Fujita, T. A. Baart, C. Reichl, W. Wegscheider, and L. M. K. Vandersypen, "Coherent shuttle of electron-spin states", en, npj Quantum Inf **3**, 22 (2017) (cited on pages 6, 151).

[Fuk15] N. Fukata, M. Yu, W. Jevasuwan, T. Takei, Y. Bando, W. Wu, and Z. L. Wang, "Clear Experimental Demonstration of Hole Gas Accumulation in Ge/Si Core - Shell Nanowires", ACS Nano **9**, 12182 (2015) (cited on page 20).

[Gao20] F. Gao, J.-H. Wang, H. Watzinger, H. Hu, M. J. Rančić, J.-Y. Zhang, T. Wang, Y. Yao, G.-L. Wang, J. Kukučka, L. Vukušić, C. Kloeffel, D. Loss, F. Liu, G. Katsaros, and J.-J. Zhang, "Site-Controlled Uniform Ge/Si Hut Wires with Electrically Tunable Spin–Orbit Coupling", en, Advanced Materials **32**, 1906523 (2020) (cited on pages 15, 142).

[Gib19] E. Gibney, "Quantum gold rush: the private funding pouring into quantum start-ups", en, Nature **574**, 22 (2019) (cited on page 1).

[Glu19] J. G. Gluschke, J. Seidl, A. M. Burke, R. W. Lyttleton, D. J. Carrad, A. R. Ullah, S. Fahlvik, S. Lehmann, H. Linke, and A. P. Micolich, "Achieving short high-quality gate-all-around structures for horizontal nanowire field-effect transistors", en, Nanotechnology **30**, 064001 (2019) (cited on page 150).

[Gol09] I. A. Goldthorpe, A. F. Marshall, and P. C. McIntyre, "Inhibiting Strain-Induced Surface Roughening: Dislocation-Free Ge/Si and Ge/SiGe Core-Shell Nanowires", Nano Letters **9**, 3715 (2009) (cited on pages 22, 68, 69, 141).

[Gol08a] I. A. Goldthorpe, A. F. Marshall, and P. C. McIntyre, "Synthesis and Strain Relaxation of Ge-Core/Si-Shell Nanowire Arrays", Nano Letters **8**, 4081 (2008) (cited on pages 22, 68, 141).

[Gol14] P. Goley and M. Hudait, "Germanium Based Field-Effect Transistors: Challenges and Opportunities", en, Materials **7**, 2301 (2014) (cited on page 6).

[Gol06] V. N. Golovach, M. Borhani, and D. Loss, "Electric-dipole-induced spin resonance in quantum dots", Physical Review B **74**, 165319 (2006) (cited on pages 55, 100, 119, 122, 126, 127, 129, 136).

[Gol08b] V. N. Golovach, A. Khaetskii, and D. Loss, "Spin relaxation at the singlet-triplet crossing in a quantum dot", en, Phys. Rev. B **77**, 045328 (2008) (cited on page 108).

[Gor13] L. Gordon, J. R. Weber, J. B. Varley, A. Janotti, D. D. Awschalom, and C. G. Van de Walle, "Quantum computing with defects", en, MRS Bull. **38**, 802 (2013) (cited on page 2).

[Gra10] G. Granger, L. Gaudreau, A. Kam, M. Pioro-Ladrière, S. A. Studenikin, Z. R. Wasilewski, P. Zawadzki, and A. S. Sachrajda, "Three-dimensional transport diagram of a triple quantum dot", Physical Review B **82**, 075304 (2010) (cited on page 97).

[Gün19] L. Güniat, P. Caroff, and A. Fontcuberta i Morral, "Vapor Phase Growth of Semiconductor Nanowires: Key Developments and Open Questions", Chemical Reviews **119**, 8958 (2019) (cited on page 141).

[Hah50] E. L. Hahn, "Spin echoes", Physical Review **80**, 580 (1950) (cited on page 63).

[Han07] R. Hanson, L. P. Kouwenhoven, J. R. Petta, S. Tarucha, and L. M. K. Vandersypen, "Spins in few-electron quantum dots", Reviews of Modern Physics **79**, 1217 (2007) (cited on pages 29, 34, 44, 53, 59, 88, 89, 95, 100, 104).

[Han05] R. Hanson, L. H. W. van Beveren, I. T. Vink, J. M. Elzerman, W. J. M. Naber, F. H. L. Koppens, L. P. Kouwenhoven, and L. M. K. Vandersypen, "Single-Shot Readout of Electron Spin States in a Quantum Dot Using Spin-Dependent Tunnel Rates", en, Phys. Rev. Lett. **94**, 196802 (2005) (cited on pages 58, 59).

[Han08] R. Hanson and D. D. Awschalom, "Coherent manipulation of single spins in semiconductors", Nature **453**, 1043 (2008) (cited on page 53).

[Hao10] X.-J. Hao, T. Tu, G. Cao, C. Zhou, H.-O. Li, G.-C. Guo, W. Y. Fung, Z. Ji, G.-P. Guo, and W. Lu, "Strong and Tunable Spin-Orbit Coupling of One-Dimensional Holes in Ge/Si Core/Shell Nanowires", Nano Letters **10**, 2956 (2010) (cited on pages 9, 28, 118).

[Har17] A. W. Harrow and A. Montanaro, "Quantum computational supremacy", en, Nature **549**, 203 (2017) (cited on page 1).

[Hei07] D. Heiss, S. Schaeck, H. Huebl, M. Bichler, G. Abstreiter, J. J. Finley, D. V. Bulaev, and D. Loss, "Observation of extremely slow hole spin relaxation in self-assembled quantum dots", Phys. Rev. B **76**, 241306 (2007) (cited on page 46).

[Hen18] N. W. Hendrickx, D. P. Franke, A. Sammak, M. Kouwenhoven, D. Sabbagh, L. Yeoh, R. Li, M. L. V. Tagliaferri, M. Virgilio, G. Capellini, G. Scappucci, and M. Veldhorst, "Gate-controlled quantum dots and superconductivity in planar germanium", en, Nat Commun **9**, 1 (2018) (cited on page 8).

[Hen20a] N. W. Hendrickx, D. P. Franke, A. Sammak, G. Scappucci, and M. Veldhorst, "Fast two-qubit logic with holes in germanium", en, Nature **577**, 487 (2020) (cited on pages 8, 57, 65, 101, 122, 127).

[Hen20b] N. W. Hendrickx, W. I. L. Lawrie, L. Petit, A. Sammak, G. Scappucci, and M. Veldhorst, "A single-hole spin qubit", en, Nat Commun **11**, 3478 (2020) (cited on pages 8, 46, 101).

[Her19] E. D. Herbschleb, H. Kato, Y. Maruyama, T. Danjo, T. Makino, S. Yamasaki, I. Ohki, K. Hayashi, H. Morishita, M. Fujiwara, and N. Mizuochi, "Ultra-long coherence times amongst room-temperature solid-state spins", en, Nat Commun **10**, 3766 (2019) (cited on page 2).

[Hig14a] A. P. Higginbotham, F. Kuemmeth, M. P. Hanson, A. C. Gossard, and C. M. Marcus, "Coherent Operations and Screening in Multielectron Spin Qubits", en, Phys. Rev. Lett. **112**, 026801 (2014) (cited on page 104).

[Hig14b] A. P. Higginbotham, F. Kuemmeth, T. W. Larsen, M. Fitzpatrick, J. Yao, H. Yan, C. M. Lieber, and C. M. Marcus, "Antilocalization of Coulomb Blockade in a Ge/Si Nanowire", Physical Review Letters **112**, 216806 (2014) (cited on pages 9, 28, 118, 129).

[Hig14c] A. P. Higginbotham, T. W. Larsen, J. Yao, H. Yan, C. M. Lieber, C. M. Marcus, and F. Kuemmeth, "Hole Spin Coherence in a Ge/Si Heterostructure Nanowire", en, Nano Lett. **14**, 3582 (2014) (cited on pages 46, 60, 108, 127).

[Hit13] D. Hite, Y. Colombe, A. Wilson, D. Allcock, D. Leibfried, D. Wineland, and D. Pappas, "Surface science for improved ion traps", en, MRS Bull. **38**, 826 (2013) (cited on page 2).

[Hu04] W. Hu, K. Sarveswaran, M. Lieberman, and G. H. Bernstein, "Sub-10 nm electron beam lithography using cold development of poly(methylmethacrylate)", J. Vac. Sci. Technol. B **22**, 1711 (2004) (cited on page 75).

[Hu07] Y. Hu, H. O. H. Churchill, D. J. Reilly, J. Xiang, C. M. Lieber, and C. M. Marcus, "A Ge/Si heterostructure nanowire-based double quantum dot with integrated charge sensor", Nature Nanotechnology **2**, 622 (2007) (cited on pages 8, 9, 60, 93, 144).

[Hu12] Y. Hu, F. Kuemmeth, C. M. Lieber, and C. M. Marcus, "Hole spin relaxation in Ge-Si core-shell nanowire qubits", Nature Nanotechnology **7**, 47 (2012) (cited on pages 61, 104, 108, 127, 144).

[Hua19] W. Huang, C. H. Yang, K. W. Chan, T. Tanttu, B. Hensen, R. C. C. Leon, M. A. Fogarty, J. C. C. Hwang, F. E. Hudson, K. M. Itoh, A. Morello, A. Laucht, and A. S. Dzurak, "Fidelity benchmarks for two-qubit gates in silicon", en, Nature **569**, 532 (2019) (cited on page 5).

[Hun20] M. Hunter, *IBM BrandVoice: The Quantum Computing Era Is Here. Why It Matters-And How It May Change Our World.* en, (Jan. 2020) https://www.forbes.com/sites/ibm/2020/01/16/the-quantum-computing-era-is-here-why-it-mattersand-how-it-may-change-our-world/ (visited on 05/03/2020) (cited on page 1).

[IBM20] IBM Q Experience, *IBM Quantum Experience*, en, (2020) https://quantum-computing.ibm.com/ (visited on 05/06/2020) (cited on page 1).

[Ito14] K. M. Itoh and H. Watanabe, "Isotope engineering of silicon and diamond for quantum computing and sensing applications", en, MRS commun. **4**, 143 (2014) (cited on pages 5, 141).

[Jia19] C. Jia, Z. Lin, Y. Huang, and X. Duan, "Nanowire Electronics: From Nanoscale to Macroscale", Chemical Reviews **119**, 9074 (2019) (cited on pages 11, 12, 17).

[Jia01] H. W. Jiang and E. Yablonovitch, "Gate-controlled electron spin resonance in GaAs/AlxGa1-xAs heterostructures", en, Phys. Rev. B **64**, 041307 (2001) (cited on page 55).

[Jou06] O. N. Jouravlev and Y. V. Nazarov, "Electron Transport in a Double Quantum Dot Governed by a Nuclear Magnetic Field", en, Phys. Rev. Lett. **96**, 176804 (2006) (cited on page 108).

[Jun12] M. Jung, M. D. Schroer, K. D. Petersson, and J. R. Petta, "Radio frequency charge sensing in InAs nanowire double quantum dots", en, Appl. Phys. Lett. **100**, 253508 (2012) (cited on page 60).

[Kan11] Y. Kanai, R. S. Deacon, S. Takahashi, A. Oiwa, K. Yoshida, K. Shibata, K. Hirakawa, Y. Tokura, and S. Tarucha, "Electrically tuned spin–orbit interaction in an InAs self-assembled quantum dot", en, Nature Nanotech **6**, 511 (2011) (cited on page 148).

[Kan98] B. E. Kane, "A silicon-based nuclear spin quantum computer", en, Nature **393**, 133 (1998) (cited on page 3).

[Kar14] V. G. Karpov, "Electrostatic Theory of Metal Whiskers", Physical Review Applied **1**, 044001 (2014) (cited on page 12).

[Kat03] Y. Kato, R. C. Myers, D. C. Driscoll, A. C. Gossard, J. Levy, and D. D. Awschalom, "Gigahertz Electron Spin Manipulation Using Voltage-Controlled g-Tensor Modulation", en, Science **299**, 1201 (2003) (cited on pages 55, 131).

[Kaw14] E. Kawakami, P. Scarlino, D. R. Ward, F. R. Braakman, D. E. Savage, M. G. Lagally, M. Friesen, S. N. Coppersmith, M. A. Eriksson, and L. M. K. Vandersypen, "Electrical control of a long-lived spin qubit in a Si/SiGe quantum dot", en, Nat. Nanotechnol. **9**, 666 (2014) (cited on page 122).

[Kay20] Kayaku Advanced Material, *NANO™ PMMA and Copolymer*, (2020) https://kayakuam.com/wp-content/uploads/2019/09/PMMA_Data_Sheet.pdf (visited on 08/06/2020) (cited on page 178).

[Kel18] J. Kelly, *A Preview of Bristlecone, Google's New Quantum Processor*, en, (Mar. 2018) http://ai.googleblog.com/2018/03/a-preview-of-bristlecone-googles-new.html (visited on 05/06/2020) (cited on page 1).

[Kin56] R. H. Kingston, "Review of Germanium Surface Phenomena", en, Journal of Applied Physics **27**, 101 (1956) (cited on page 19).

[Kit03] A. Y. Kitaev, "Fault-tolerant quantum computation by anyons", en, Annals of Physics **303**, 2 (2003) (cited on page 3).

[Kja20] M. Kjaergaard, M. E. Schwartz, J. Braumüller, P. Krantz, J. I.-J. Wang, S. Gustavsson, and W. D. Oliver, "Superconducting Qubits: Current State of Play", en, Annu. Rev. Condens. Matter Phys. **11**, 369 (2020) (cited on page 2).

[Kli12] J. Klinovaja and D. Loss, "Composite Majorana fermion wave functions in nanowires", en, Phys. Rev. B **86**, 085408 (2012) (cited on page 100).

[Klo13a] C. Kloeffel and D. Loss, "Prospects for Spin-Based Quantum Computing in Quantum Dots", Annu. Rev. Condens. Matter Phys. **4**, 51 (2013) (cited on pages 14, 23, 26, 40, 41, 45, 60, 79, 122, 152, 153).

[Klo18] C. Kloeffel, M. J. Rančić, and D. Loss, "Direct Rashba spin-orbit interaction in Si and Ge nanowires with different growth directions", Physical Review B **97**, 235422 (2018) (cited on pages 7, 27, 47, 88, 100, 111, 119, 122, 123, 128, 129, 132, 149, 156, 174).

[Klo14] C. Kloeffel, M. Trif, and D. Loss, "Acoustic phonons and strain in core/shell nanowires", en, Phys. Rev. B **90**, 115419 (2014) (cited on page 22).

[Klo11] C. Kloeffel, M. Trif, and D. Loss, "Strong spin-orbit interaction and helical hole states in Ge/Si nanowires", Phys. Rev. B **84**, 195314 (2011) (cited on pages 7, 22, 26, 27, 88, 95, 100, 119, 122, 123, 128, 129, 132, 141, 156, 174).

[Klo13b] C. Kloeffel, M. Trif, P. Stano, and D. Loss, "Circuit QED with hole-spin qubits in Ge/Si nanowire quantum dots", Phys. Rev. B **88**, 241405 (2013) (cited on pages 46–48, 88, 122, 123, 128, 132, 147, 152, 153).

[Klo13c] C. Kloeffel, M. Trif, P. Stano, and D. Loss, "Circuit QED with hole-spin qubits in Ge/Si nanowire quantum dots", Physical Review B **88**, 241405 (2013) (cited on pages 100, 101, 119).

[Koc19] A. F. Kockum, A. Miranowicz, S. D. Liberato, S. Savasta, and F. Nori, "Ultrastrong coupling between light and matter", en, Nat Rev Phys **1**, 19 (2019) (cited on page 153).

[Kop05] F. H. L. Koppens, "Control and Detection of Singlet-Triplet Mixing in a Random Nuclear Field", en, Science **309**, 1346 (2005) (cited on pages 102, 105, 108, 109).

[Kop08] F. H. L. Koppens, K. C. Nowack, and L. M. K. Vandersypen, "Spin Echo of a Single Electron Spin in a Quantum Dot", en, Phys. Rev. Lett. **100**, 236802 (2008) (cited on pages 46, 63).

[Kop06] F. H. L. Koppens, C. Buizert, K. J. Tielrooij, I. T. Vink, K. C. Nowack, T. Meunier, L. P. Kouwenhoven, and L. M. K. Vandersypen, "Driven coherent oscillations of a single electron spin in a quantum dot", Nature **442**, 766 (2006) (cited on pages 4, 54, 122).

[Kou01] L. P. Kouwenhoven, D. G. Austing, and S. Tarucha, "Few-electron quantum dots", Reports on Progress in Physics **64**, 701 (2001) (cited on pages 29, 30, 91).

[Kou98] L. Kouwenhoven and C. Marcus, "Quantum dots", Phys. World **11**, 35 (1998) (cited on pages 11, 28).

[Kou97] L. P. Kouwenhoven, C. M. Marcus, P. L. McEuen, S. Tarucha, R. M. Westervelt, and N. S. Wingreen, "Electron Transport in Quantum Dots", en, in *Mesoscopic Electron Transport*, edited by L. L. Sohn, L. P. Kouwenhoven, and G. Schön, NATO ASI Series (Springer Netherlands, Dordrecht, 1997), pages 105–214 (cited on page 11).

[Kro19] J. Kroll, F. Borsoi, K. van der Enden, W. Uilhoorn, D. de Jong, M. Quintero-Pérez, D. van Woerkom, A. Bruno, S. Plissard, D. Car, E. Bakkers, M. Cassidy, and L. Kouwenhoven, "Magnetic-Field-Resilient Superconducting Coplanar-Waveguide Resonators for Hybrid Circuit Quantum Electrodynamics Experiments", Physical Review Applied **11**, 064053 (2019) (cited on page 79).

[Kuh18] A. V. Kuhlmann, V. Deshpande, L. C. Camenzind, D. M. Zumbühl, and A. Fuhrer, "Ambipolar quantum dots in undoped silicon fin field-effect transistors", Applied Physics Letters **113**, 122107 (2018) (cited on page 29).

[Kys75] D. F. Kyser and N. S. Viswanathan, "Monte Carlo Simulation of Spatially Distributed Beams in Electron-Beam Lithography.", J. Vac. Sci. Technol. **12**, 1305 (1975) (cited on page 73).

[Lad10] T. D. Ladd, F. Jelezko, R. Laflamme, Y. Nakamura, C. Monroe, and J. L. O'Brien, "Quantum computers", en, Nature **464**, 45 (2010) (cited on page 44).

[Lah17] V. Lahtinen and J. Pachos, "A Short Introduction to Topological Quantum Computation", en, SciPost Phys. **3**, 021 (2017) (cited on pages 4, 48).

[Lai07] E. A. Laird, C. Barthel, E. I. Rashba, C. M. Marcus, M. P. Hanson, and A. C. Gossard, "Hyperfine-mediated gate-driven electron spin resonance", Physical Review Letters **99**, 1 (2007) (cited on page 55).

[Lan18] A. J. Landig, J. V. Koski, P. Scarlino, U. C. Mendes, A. Blais, C. Reichl, W. Wegscheider, A. Wallraff, K. Ensslin, and T. Ihn, "Coherent spin-photon coupling using a resonant exchange qubit", Nature **560**, 179 (2018) (cited on pages 5, 89, 152).

[Lau16] A. Laucht, S. Simmons, R. Kalra, G. Tosi, J. P. Dehollain, J. T. Muhonen, S. Freer, F. E. Hudson, K. M. Itoh, D. N. Jamieson, J. C. McCallum, A. S. Dzurak, and A. Morello, "Breaking the rotating wave approximation for a strongly driven dressed single-electron spin", Phys. Rev. B **94**, 1 (2016) (cited on page 131).

[Lau02] L. J. Lauhon, M. S. Gudiksen, D. Wang, and C. M. Lieber, "Epitaxial core-shell and core-multishell nanowire heterostructures", Nature **420**, 57 (2002) (cited on pages 20, 22, 104).

[Lei06] H. Leidecker and J. Brusse, *Tin Whiskers: A History of Documented Electrical System Failures*, (Apr. 2006) `https://nepp.nasa.gov/whisker/reference/tech_papers/2006-Leidecker-Tin-Whisker-Failures.pdf` (visited on 05/12/2020) (cited on page 12).

[Les02] M. Leskelä and M. Ritala, "Atomic layer deposition (ALD): from precursors to thin film structures", Thin Solid Films **409**, 138 (2002) (cited on page 77).

[Lev03] L. S. Levitov and E. I. Rashba, "Dynamical spin-electric coupling in a quantum dot", en, Phys. Rev. B **67**, 115324 (2003) (cited on page 156).

[Li11] L. Li, D. J. Smith, E. Dailey, P. Madras, J. Drucker, and M. R. McCartney, "Observation of hole accumulation in Ge/Si core/shell nanowires using off-axis electron holography", Nano Letters **11**, 493 (2011) (cited on page 20).

[Li15] R. Li, F. E. Hudson, A. S. Dzurak, and A. R. Hamilton, "Pauli Spin Blockade of Heavy Holes in a Silicon Double Quantum Dot", Nano Letters **15**, 7314 (2015) (cited on pages 95, 97, 105, 116, 164).

[Li18a] R. Li, L. Petit, D. P. Franke, J. P. Dehollain, J. Helsen, M. Steudtner, N. K. Thomas, Z. R. Yoscovits, K. J. Singh, S. Wehner, L. M. K. Vandersypen, J. S. Clarke, and M. Veldhorst, "A crossbar network for silicon quantum dot qubits", en, Sci. Adv. **4**, eaar3960 (2018) (cited on pages 6, 151).

[Li18b] Y. Li, S.-X. Li, F. Gao, H.-O. Li, G. Xu, K. Wang, D. Liu, G. Cao, M. Xiao, T. Wang, J.-J. Zhang, G.-C. Guo, and G.-P. Guo, "Coupling a Germanium Hut Wire Hole Quantum Dot to a Superconducting Microwave Resonator", en, Nano Lett. **18**, 2091 (2018) (cited on page 8).

[Lia07] G. Liang, J. Xiang, N. Kharche, G. Klimeck, C. M. Lieber, and M. Lundstrom, "Performance analysis of a Ge/Si core/shell nanowire field-effect transistor", Nano Letters **7**, 642 (2007) (cited on page 21).

[Lil18] S. D. Liles, R. Li, C. H. Yang, F. E. Hudson, M. Veldhorst, A. S. Dzurak, and A. R. Hamilton, "Spin filling and orbital structure of the first six holes in a silicon metal-oxide-semiconductor quantum dot", Nat Commun **9**, 3255 (2018) (cited on page 25).

[Liu18] G.-Q. Liu and X.-Y. Pan, "Quantum information processing with nitrogen–vacancy centers in diamond", en, Chinese Phys. B **27**, 020304 (2018) (cited on page 2).

[Liu10] N. Liu, Y.-R. Li, N. Lu, Y.-X. Yao, X.-W. Fang, C.-Z. Wang, and K.-M. Ho, "Charge localization in [1 1 2] Si/Ge and Ge/Si core–shell nanowires", en, J. Phys. D: Appl. Phys. **43**, 275404 (2010) (cited on page 21).

[Liv09] R. Livengood, S. Tan, Y. Greenzweig, J. Notte, and S. McVey, "Subsurface damage from helium ions as a function of dose, beam energy, and dose rate", Journal of Vacuum Science and Technology B **27**, 3244 (2009) (cited on page 143).

[Los98] D. Loss and D. P. DiVincenzo, "Quantum computation with quantum dots", Physical Review A **57**, 120 (1998) (cited on pages 3, 4, 14, 36, 88, 100, 122).

[Lu03] W. Lu, Z. Ji, L. Pfeiffer, K. W. West, and A. J. Rimberg, "Real-time detection of electron tunnelling in a quantum dot", en, Nature **423**, 422 (2003) (cited on pages 4, 60).

[Lu05] W. Lu, J. Xiang, B. P. Timko, Y. Wu, and C. M. Lieber, "One-dimensional hole gas in germanium/silicon nanowire heterostructures", Proceedings of the National Academy of Sciences **102**, 10046 (2005) (cited on pages 20, 21, 90, 104).

[Luo20] M. Luong, E. Robin, N. Pauc, P. Gentile, M. Sistani, A. Lugstein, M. Spies, B. Fernandez, and M. I. Den Hertog, "In-Situ Transmission Electron Microscopy Imaging of Aluminum Diffusion in Germanium Nanowires for the Fabrication of Sub-10 nm Ge Quantum Disks", en, ACS Appl. Nano Mater. **3**, 1891 (2020) (cited on page 49).

[Lut10] R. M. Lutchyn, J. D. Sau, and S. Das Sarma, "Majorana Fermions and a Topological Phase Transition in Semiconductor-Superconductor Heterostructures", en, Phys. Rev. Lett. **105**, 077001 (2010) (cited on page 100).

[Mai14] F. Maier, J. Klinovaja, and D. Loss, "Majorana fermions in Ge/Si hole nanowires", Physical Review B **90**, 195421 (2014) (cited on pages 23, 28, 49, 100, 102, 119).

[Mai13] F. Maier, C. Kloeffel, and D. Loss, "Tunable g-factor and phonon-mediated hole spin relaxation in Ge/Si nanowire quantum dots", Physical Review B **87**, 161305 (2013) (cited on pages 46, 47, 88, 102, 109, 119, 122, 123, 127, 128, 147, 149).

[Man15] A. Manchon, H. C. Koo, J. Nitta, S. M. Frolov, and R. A. Duine, "New perspectives for Rashba spin–orbit coupling", en, Nature Mater **14**, 871 (2015) (cited on page 24).

[Män19] H. Mäntynen, N. Anttu, Z. Sun, and H. Lipsanen, "Single-photon sources with quantum dots in III-V nanowires", Nanophotonics **8**, 747 (2019) (cited on pages 11, 13).

[Mar17] E. Marcellina, A. R. Hamilton, R. Winkler, and D. Culcer, "Spin-orbit interactions in inversion-asymmetric two-dimensional hole systems: A variational analysis", en, Phys. Rev. B **95**, 075305 (2017) (cited on page 122).

[Mar20] B. Marr, *These 25 Technology Trends Will Define The Next Decade*, en, (Apr. 2020) https://www.forbes.com/sites/bernardmarr/2020/04/20/these-25-technology-trends-will-define-the-next-decade/ (visited on 05/03/2020) (cited on page 1).

[Mas12] N. A. Masluk, I. M. Pop, A. Kamal, Z. K. Minev, and M. H. Devoret, "Microwave Characterization of Josephson Junction Arrays: Implementing a Low Loss Superinductance", Physical Review Letters **109**, 137002 (2012) (cited on pages 79, 152).

[Mau12] B. M. Maune, M. G. Borselli, B. Huang, T. D. Ladd, P. W. Deelman, K. S. Holabird, A. A. Kiselev, I. Alvarado-Rodriguez, R. S. Ross, A. E. Schmitz, M. Sokolich, C. A. Watson, M. F. Gyure, and A. T. Hunter, "Coherent singlet-triplet oscillations in a silicon-based double quantum dot", en, Nature **481**, 344 (2012) (cited on page 5).

[Mau16] R. Maurand, X. Jehl, D. Kotekar-Patil, A. Corna, H. Bohuslavskyi, R. Laviéville, L. Hutin, S. Barraud, M. Vinet, M. Sanquer, and S. De Franceschi, "A CMOS silicon spin qubit", en, Nat Commun **7**, 13575 (2016) (cited on pages 5, 46, 57, 63, 65, 122).

[McC19] D. McClure and J. Gambetta, *Quantum computation center opens*, en-US, (Sept. 2019) https://www.ibm.com/blogs/research/2019/09/quantum-computation-center/ (visited on 05/03/2020) (cited on page 1).

[McI20] P. McIntyre and A. Fontcuberta i Morral, "Semiconductor nanowires: to grow or not to grow?", en, Materials Today Nano **9**, 100058 (2020) (cited on page 15).

[Med13] J. Medford, J. Beil, J. M. Taylor, S. D. Bartlett, A. C. Doherty, E. I. Rashba, D. P. Divincenzo, H. Lu, A. C. Gossard, and C. M. Marcus, "Self-consistent measurement and state tomography of an exchange-only spin qubit", Nature Nanotechnology **8**, 654 (2013) (cited on page 89).

[Mei58] S. Meiboom and D. Gill, "Modified Spin-Echo Method for Measuring Nuclear Relaxation Times", en, Rev. Sci. Instrum. **29**, 688 (1958) (cited on page 65).

[Mey94] B. S. Meyerson, "High-Speed Silicon-Germanium Electronics", Scientific American **270**, 62 (1994) (cited on page 16).

[Mi18a] X. Mi, M. Benito, S. Putz, D. M. Zajac, J. M. Taylor, G. Burkard, and J. R. Petta, "A coherent spin-photon interface in silicon", Nature **555**, 599 (2018) (cited on pages 6, 89, 152).

[Mi17a] X. Mi, J. V. Cady, D. M. Zajac, P. W. Deelman, and J. R. Petta, "Strong coupling of a single electron in silicon to a microwave photon", en, Science **355**, 156 (2017) (cited on pages 6, 152).

[Mi18b] X. Mi, S. Kohler, and J. R. Petta, "Landau-Zener interferometry of valley-orbit states in Si/SiGe double quantum dots", en, Phys. Rev. B **98**, 161404 (2018) (cited on page 17).

[Mi17b] X. Mi, C. G. Péterfalvi, G. Burkard, and J. R. Petta, "High-Resolution Valley Spectroscopy of Si Quantum Dots", en, Phys. Rev. Lett. **119**, 176803 (2017) (cited on page 17).

[Mil19] A. R. Mills, D. M. Zajac, M. J. Gullans, F. J. Schupp, T. M. Hazard, and J. R. Petta, "Shuttling a single charge across a one-dimensional array of silicon quantum dots", en, Nat Commun **10**, 1063 (2019) (cited on pages 6, 151).

[Moh10] M. A. Mohammad, T. Fito, J. Chen, M. Aktary, M. Stepanova, and S. K. Dew, "Interdependence of optimum exposure dose regimes and the kinetics of resist dissolution for electron beam nanolithography of polymethylmethacrylate", J. Vac. Sci. Technol. B **28**, L1 (2010) (cited on page 75).

[Mor18] P.-A. Mortemousque, E. Chanrion, B. Jadot, H. Flentje, A. Ludwig, A. D. Wieck, M. Urdampilleta, C. Bauerle, and T. Meunier, "Coherent control of individual electron spins in a two dimensional array of quantum dots", en, arXiv:1808.06180 (2018) (cited on page 6).

[Möt10] M. Möttönen, K. Y. Tan, K. W. Chan, F. A. Zwanenburg, W. H. Lim, C. C. Escott, J.-M. Pirkkalainen, A. Morello, C. Yang, J. A. van Donkelaar, A. D. C. Alves, D. N. Jamieson, L. C. L. Hollenberg, and A. S. Dzurak, "Probe and control of the reservoir density of states in single-electron devices", Physical Review B **81**, 161304 (2010) (cited on page 93).

[Muk18] U. Mukhopadhyay, J. P. Dehollain, C. Reichl, W. Wegscheider, and L. M. K. Vandersypen, "A 2 x 2 quantum dot array with controllable inter-dot tunnel couplings", Applied Physics Letters **112**, 183505 (2018) (cited on page 36).

[Mül19] F. Müller, "Gate Dielectrics for Quantum Dots in Ge/Si Core/Shell Nanowires", en, Master Thesis (University of Basel, Basel, Switzerland, 2019) (cited on pages 76–78, 142).

[Mut20] P. M. Mutter and G. Burkard, "G -tensor resonance in double quantum dots with site-dependent g -tensors", Mater. Quantum Technol. **1**, 015003 (2020) (cited on page 109).

[Nad10a] S. Nadj-Perge, S. M. Frolov, E. Bakkers, and L. P. Kouwenhoven, "Spin-orbit qubit in a semiconductor nanowire", Nature **468**, 1084 (2010) (cited on pages 46, 57, 63, 65, 100).

[Nad10b] S. Nadj-Perge, S. M. Frolov, J. W. W. van Tilburg, J. Danon, Y. V. Nazarov, R. Algra, E. P. A. M. Bakkers, and L. P. Kouwenhoven, "Disentangling the effects of spin-orbit and hyperfine interactions on spin blockade", Physical Review B **81**, 201305 (2010) (cited on pages 43, 46, 102, 105, 108, 109).

[Nad12] S. Nadj-Perge, V. S. Pribiag, J. W. G. van den Berg, K. Zuo, S. R. Plissard, E. P. A. M. Bakkers, S. M. Frolov, and L. P. Kouwenhoven, "Spectroscopy of Spin-Orbit Quantum Bits in Indium Antimonide Nanowires", en, Phys. Rev. Lett. **108**, 166801 (2012) (cited on pages 14, 46, 57, 147).

[Nah12] J. Nah, D. C. Dillen, K. M. Varahramyan, S. K. Banerjee, and E. Tutuc, "Role of Confinement on Carrier Transport in Ge–Si $_x$ Ge $_{1-x}$ Core–Shell Nanowires", en, Nano Lett. **12**, 108 (2012) (cited on page 21).

[Nak20] T. Nakajima, A. Noiri, K. Kawasaki, J. Yoneda, P. Stano, S. Amaha, T. Otsuka, K. Takeda, M. R. Delbecq, G. Allison, A. Ludwig, A. D. Wieck, D. Loss, and S. Tarucha, "Coherence of a Driven Electron Spin Qubit Actively Decoupled from Quasistatic Noise", en, Phys. Rev. X **10**, 011060 (2020) (cited on page 4).

[Naz93] Y. V. Nazarov, "Quantum interference, tunnel junctions and resonant tunneling interferometer", en, Physica B: Condensed Matter **189**, 57 (1993) (cited on pages 116, 164).

[Ndu08] A. Nduwimana, R. N. Musin, A. M. Smith, and X.-Q. Wang, "Spatial Carrier Confinement in Core-Shell and Multishell Nanowire Heterostructures", en, Nano Lett. **8**, 3341 (2008) (cited on page 21).

[Ngu14] B. M. Nguyen, Y. Taur, S. T. Picraux, and S. A. Dayeh, "Diameter-independent hole mobility in Ge/Si Core/shell nanowire field effect transistors", Nano Letters **14**, 585 (2014) (cited on page 21).

[Nig17] S. E. Nigg, A. Fuhrer, and D. Loss, "Superconducting Grid-Bus Surface Code Architecture for Hole-Spin Qubits", Phys. Rev. Lett. **118**, 147701 (2017) (cited on pages 128, 130, 132).

[Nil09] H. A. Nilsson, P. Caroff, C. Thelander, M. Larsson, J. B. Wagner, L.-E. Wernersson, L. Samuelson, and H. Q. Xu, "Giant, Level-Dependent g Factors in InSb Nanowire Quantum Dots", en, Nano Lett. **9**, 3151 (2009) (cited on page 46).

[Nov04] K. S. Novoselov, "Electric Field Effect in Atomically Thin Carbon Films", Science **306**, 666 (2004) (cited on page 78).

[Now07] K. C. Nowack, F. H. L. Koppens, Y. V. Nazarov, and L. M. K. Vandersypen, "Coherent control of a single electron spin with electric fields", Science **318**, 1430 (2007) (cited on pages 4, 56, 57, 100, 122, 127, 166, 170).

[ORe14] C. O'Regan, S. Biswas, N. Petkov, and J. D. Holmes, "Recent advances in the growth of germanium nanowires: synthesis, growth dynamics and morphology control", J. Mater. Chem. C **2**, 14 (2014) (cited on page 141).

[Oli13] W. D. Oliver and P. B. Welander, "Materials in superconducting quantum bits", en, MRS Bull. **38**, 816 (2013) (cited on page 2).

[Ono02] K. Ono, D. G. Austing, Y. Tokura, and S. Tarucha, "Current rectification by pauli exclusion in a weakly coupled double quantum dot system", Science **297**, 1313 (2002) (cited on pages 4, 89, 95, 102, 104, 105, 123).

[Ono17] K. Ono, G. Giavaras, T. Tanamoto, T. Ohguro, X. Hu, and F. Nori, "Hole Spin Resonance and Spin-Orbit Coupling in a Silicon Metal-Oxide-Semiconductor Field-Effect Transistor", en, Phys. Rev. Lett. **119**, 156802 (2017) (cited on page 26).

[Ono19] K. Ono, T. Mori, and S. Moriyama, "High-temperature operation of a silicon qubit", Scientific Reports **9**, 469 (2019) (cited on page 59).

[Ore10] Y. Oreg, G. Refael, and F. von Oppen, "Helical Liquids and Majorana Bound States in Quantum Wires", en, Phys. Rev. Lett. **105**, 177002 (2010) (cited on page 100).

[Pak18] P. Pakkiam, A. V. Timofeev, M. G. House, M. R. Hogg, T. Kobayashi, M. Koch, S. Rogge, and M. Y. Simmons, "Single-shot single-gate rf spin readout in silicon", en, Phys. Rev. X **8**, 041032 (2018) (cited on pages 60, 145).

[Pal17] M. Palma, D. Maradan, L. Casparis, T.-M. Liu, F. N. M. Froning, and D. M. Zumbühl, "Magnetic cooling for microkelvin nanoelectronics on a cryofree platform", en, Rev. Sci. Instrum. **88**, 043902 (2017) (cited on page 216).

[Paw19] R. Pawlak, S. Hoffman, J. Klinovaja, D. Loss, and E. Meyer, "Majorana fermions in magnetic chains", en, Progress in Particle and Nuclear Physics **107**, 1 (2019) (cited on page 49).

[Ped19] E. Pednault, J. Gunnels, D. Maslov, and J. Gambetta, *On "Quantum Supremacy"*, en-US, (Oct. 2019) https://www.ibm.com/blogs/research/2019/10/on-quantum-supremacy/ (visited on 05/03/2020) (cited on page 1).

[Pei11] L. Z. Pei and Z. Y. Cai, "A Review on Germanium Nanowires", en, Recent Patents on Nanotechnology **6**, 44 (2011) (cited on page 17).

[Pei12] R. Peibst, E. P. Rugeramigabo, and K. R. Hofmann, "Electrical characterization and modelling of n–n Ge-Si heterojunctions with relatively low interface state densities", en, Journal of Applied Physics **112**, 124502 (2012) (cited on pages 19, 20).

[Pet12] K. D. Petersson, L. W. McFaul, M. D. Schroer, M. Jung, J. M. Taylor, A. A. Houck, and J. R. Petta, "Circuit quantum electrodynamics with a spin qubit", Nature **490**, 380 (2012) (cited on pages 15, 46, 152).

[Pet10] K. D. Petersson, J. R. Petta, H. Lu, and A. C. Gossard, "Quantum Coherence in a One-Electron Semiconductor Charge Qubit", en, Phys. Rev. Lett. **105**, 246804 (2010) (cited on page 50).

[Pet20] L. Petit, H. G. J. Eenink, M. Russ, W. I. L. Lawrie, N. W. Hendrickx, S. G. J. Philips, J. S. Clarke, L. M. K. Vandersypen, and M. Veldhorst, "Universal quantum logic in hot silicon qubits", en, Nature **580**, 355 (2020) (cited on pages 6, 59).

[Pet05] J. R. Petta, A. C. Johnson, J. M. Taylor, E. A. Laird, A. Yacoby, M. D. Lukin, C. M. Marcus, R. Hanson, and A. C. Gossard, "Coherent Manipulation of Coupled Electron Spins in Semiconductor Quantum Dots", Science **309**, 2180 (2005) (cited on pages 4, 36, 58, 59, 65).

[Pfu07] A. Pfund, I. Shorubalko, K. Ensslin, and R. Leturcq, "Suppression of Spin Relaxation in an InAs Nanowire Double Quantum Dot", Phys. Rev. Lett. **99**, 036801 (2007) (cited on pages 14, 43).

[Pil11] R. Pillarisetty, "Academic and industry research progress in germanium nanodevices", en, Nature **479**, 324 (2011) (cited on pages 6, 16, 17).

[Pio08] M. Pioro-Ladrière, T. Obata, Y. Tokura, Y.-S. Shin, T. Kubo, K. Yoshida, T. Taniyama, and S. Tarucha, "Electrically driven single-electron spin resonance in a slanting Zeeman field", Nature Phys. **4**, 776 (2008) (cited on pages 54, 122).

[Pla12] J. J. Pla, K. Y. Tan, J. P. Dehollain, W. H. Lim, J. J. L. Morton, D. N. Jamieson, A. S. Dzurak, and A. Morello, "A single-atom electron spin qubit in silicon", Nature **489**, 541 (2012) (cited on page 54).

[Pot11] A. Potié, T. Baron, L. Latu-Romain, G. Rosaz, B. Salem, L. Montès, P. Gentile, J. Kreisel, and H. Roussel, "Controlled growth of SiGe nanowires by addition of HCl in the gas phase", J. Appl. Phys. **110**, 024311 (2011) (cited on page 68).

[Pre16] J. H. Prechtel, A. V. Kuhlmann, J. Houel, A. Ludwig, S. R. Valentin, A. D. Wieck, and R. J. Warburton, "Decoupling a hole spin qubit from the nuclear spins", Nat. Mater. **15**, 981 (2016) (cited on pages 40, 46, 122).

[Pre12] J. Preskill, "Quantum computing and the entanglement frontier", en, arXiv:1203.5813 (2012) (cited on page 1).

[Pre18] J. Preskill, "Quantum Computing in the NISQ era and beyond", en, Quantum **2**, 79 (2018) (cited on pages 1, 4, 10).

[Pri13] V. S. Pribiag, S. Nadj-Perge, S. M. Frolov, J. W. G. van den Berg, I. van Weperen, S. R. Plissard, E. P. A. M. Bakkers, and L. P. Kouwenhoven, "Electrical control of single hole spins in nanowire quantum dots", Nature Nanotechnology **8**, 170 (2013) (cited on pages 14, 46, 57).

[Qas09] F. Qassemi, W. A. Coish, and F. K. Wilhelm, "Stationary and Transient Leakage Current in the Pauli Spin Blockade", en, Phys. Rev. Lett. **102**, 176806 (2009) (cited on pages 105, 108).

[Rib05] G. Ribes, J. Mitard, M. Denais, S. Bruyere, F. Monsieur, C. Parthasarathy, E. Vincent, and G. Ghibaudo, "Review on high-k dielectrics reliability issues", IEEE Transactions on Device and Materials Reliability **5**, 5 (2005) (cited on page 77).

[Rid20] J. Ridderbos, M. Brauns, F. K. de Vries, J. Shen, A. Li, S. Kölling, M. A. Verheijen, A. Brinkman, W. G. van der Wiel, E. P. A. M. Bakkers, and F. A. Zwanenburg, "Hard Superconducting Gap and Diffusion-Induced Superconductors in Ge–Si Nanowires", en, Nano Lett. **20**, 122 (2020) (cited on page 49).

[Rio04] M. Riordan, "The lost history of the transistor", IEEE Spectrum **41**, 44 (2004) (cited on page 16).

[Rod08] S. Roddaro, A. Fuhrer, P. Brusheim, C. Fasth, H. Q. Xu, L. Samuelson, J. Xiang, and C. M. Lieber, "Spin States of Holes in Ge/Si Nanowire Quantum Dots", Physical Review Letters **101**, 186802 (2008) (cited on pages 8, 9).

[Rod11] S. Roddaro, A. Pescaglini, D. Ercolani, L. Sorba, and F. Beltram, "Manipulation of Electron Orbitals in Hard-Wall InAs/InP Nanowire Quantum Dots", en, Nano Lett. **11**, 1695 (2011) (cited on page 149).

[Rus15] M. Russ and G. Burkard, "Long distance coupling of resonant exchange qubits", en, Phys. Rev. B **92**, 205412 (2015) (cited on page 152).

[Rus17] M. Russ and G. Burkard, "Three-electron spin qubits", Journal of Physics: Condensed Matter **29**, 393001 (2017) (cited on pages 36, 44, 65).

[Rus18] M. Russ, J. R. Petta, and G. Burkard, "A quadrupolar exchange-only spin qubit", en, Phys. Rev. Lett. **121**, 177701 (2018) (cited on page 44).

[Sab19] D. Sabonis, E. C. T. O'Farrell, D. Razmadze, D. M. T. van Zanten, J. Suter, P. Krogstrup, and C. M. Marcus, "Dispersive sensing in hybrid InAs/Al nanowires", en, Appl. Phys. Lett. **115**, 102601 (2019) (cited on page 60).

[Sal14] J. Salfi, J. A. Mol, R. Rahman, G. Klimeck, M. Y. Simmons, L. C. L. Hollenberg, and S. Rogge, "Spatially resolving valley quantum interference of a donor in silicon", en, Nature Mater **13**, 605 (2014) (cited on page 17).

[Sal10] J. Salfi, S. Roddaro, D. Ercolani, L. Sorba, I. Savelyev, M. Blumin, H. E. Ruda, and F. Beltram, "Electronic properties of quantum dot systems realized in semiconductor nanowires", Semiconductor Science and Technology **25**, 024007 (2010) (cited on pages 12, 13).

[Sal01] G. Salis, Y. Kato, K. Ensslin, D. C. Driscoll, A. C. Gossard, and D. D. Awschalom, "Electrical control of spin coherence in semiconductor nanostructures", Nature **414**, 619 (2001) (cited on page 55).

[Sam16] N. Samkharadze, A. Bruno, P. Scarlino, G. Zheng, D. P. DiVincenzo, L. DiCarlo, and L. M. K. Vandersypen, "High-Kinetic-Inductance Superconducting Nanowire Resonators for Circuit QED in a Magnetic Field", en, Phys. Rev. Applied **5**, 044004 (2016) (cited on page 152).

[Sam18] N. Samkharadze, G. Zheng, N. Kalhor, D. Brousse, A. Sammak, U. C. Mendes, A. Blais, G. Scappucci, and L. M. K. Vandersypen, "Strong spin-photon coupling in silicon", Science **359**, 1123 (2018) (cited on pages 6, 89, 152).

[Sam19] A. Sammak, D. Sabbagh, N. W. Hendrickx, M. Lodari, B. Paquelet Wuetz, A. Tosato, L. Yeoh, M. Bollani, M. Virgilio, M. A. Schubert, P. Zaumseil, G. Capellini, M. Veldhorst, and G. Scappucci, "Shallow and Undoped Germanium Quantum Wells: A Playground for Spin and Hybrid Quantum Technology", en, Adv. Funct. Mater. **29**, 1807613 (2019) (cited on pages 18, 19, 22).

[Sca20] G. Scappucci, C. Kloeffel, F. A. Zwanenburg, D. Loss, M. Myronov, J.-J. Zhang, S. De Franceschi, G. Katsaros, and M. Veldhorst, "The germanium quantum information route", en, Nat Rev Mater, 10.1038/s41578-020-00262-z (2020) (cited on pages 6–8, 19, 23, 25, 100, 122).

[Sch97] F. Schäffler, "High-mobility Si and Ge structures", Semiconductor Science and Technology **12**, 1515 (1997) (cited on pages 16, 18).

[Sch14] C. P. Scheller, S. Heizmann, K. Bedner, D. Giss, M. Meschke, D. M. Zumbühl, J. D. Zimmerman, and A. C. Gossard, "Silver-epoxy microwave filters and thermalizers for millikelvin experiments", en, Appl. Phys. Lett. **104**, 211106 (2014) (cited on page 82).

[Sch05] V. Schmidt, S. Senz, and U. Gösele, "Diameter-Dependent Growth Direction of Epitaxial Silicon Nanowires", Nano Letters **5**, 931 (2005) (cited on page 69).

[Sch98] R. J. Schoelkopf, "The Radio-Frequency Single-Electron Transistor (RF-SET): A Fast and Ultrasensitive Electrometer", Science **280**, 1238 (1998) (cited on page 60).

[Sch11a] L. Schreiber, F. Braakman, T. Meunier, V. Calado, J. Danon, J. Taylor, W. Wegscheider, and L. Vandersypen, "Coupling artificial molecular spin states by photon-assisted tunnelling", en, Nat Commun **2**, 556 (2011) (cited on page 108).

[Sch18] L. R. Schreiber and H. Bluhm, "Toward a silicon-based quantum computer", en, Science **359**, 393 (2018) (cited on page 5).

[Sch11b] M. D. Schroer, K. D. Petersson, M. Jung, and J. R. Petta, "Field Tuning the g Factor in InAs Nanowire Double Quantum Dots", en, Phys. Rev. Lett. **107**, 176811 (2011) (cited on pages 46, 57).

[Sch07] D. Schröer, A. D. Greentree, L. Gaudreau, K. Eberl, L. C. L. Hollenberg, J. P. Kotthaus, and S. Ludwig, "Electrostatically defined serial triple quantum dot charged with few electrons", Physical Review B **76**, 075306 (2007) (cited on page 97).

[She15] L.-F. Shen, S. Yip, Z.-x. Yang, M. Fang, T. Hung, E. Y. B. Pun, and J. C. Ho, "High-Performance Wrap-Gated InGaAs Nanowire Field-Effect Transistors with Sputtered Dielectrics", en, Sci Rep **5**, 1 (2015) (cited on page 150).

[She19] G. Shen and Y.-L. Chueh, editors, *Nanowire Electronics*, Nanostructure Science and Technology (Springer, Singapore, 2019) (cited on page 11).

[Sho06] I. Shorubalko, A. Pfund, R. Leturcq, M. T. Borgström, F. Gramm, E. Müller, E. Gini, and K. Ensslin, "Tunable few-electron quantum dots in InAs nanowires", en, Nanotechnology **18**, 044014 (2006) (cited on page 14).

[Sig19] A. Sigillito, J. Loy, D. Zajac, M. Gullans, L. Edge, and J. Petta, "Site-Selective Quantum Control in an Isotopically Enriched Si 28 / Si 0.7 Ge 0.3 Quadruple Quantum Dot", en, Phys. Rev. Applied **11**, 061006 (2019) (cited on page 5).

[Sim15] D. K. Simon, P. M. Jordan, T. Mikolajick, and I. Dirnstorfer, "On the Control of the Fixed Charge Densities in Al2O3-Based Silicon Surface Passivation Schemes", ACS Appl. Mater. Interfaces **7**, 28215 (2015) (cited on page 78).

[Sis19] M. Sistani, J. Delaforce, R. B. G. Kramer, N. Roch, M. A. Luong, M. I. den Hertog, E. Robin, J. Smoliner, J. Yao, C. M. Lieber, C. Naud, A. Lugstein, and O. Buisson, "Highly Transparent Contacts to the 1D Hole Gas in Ultrascaled Ge/Si Core/Shell Nanowires", en, ACS Nano **13**, 14145 (2019) (cited on page 49).

[Spr18] P. C. Spruijtenburg, S. V. Amitonov, W. G. van der Wiel, and F. A. Zwanenburg, "A fabrication guide for planar silicon quantum dot heterostructures", Nanotechnology **29**, 143001 (2018) (cited on pages 77, 142).

[Sta13] T. D. Stanescu and S. Tewari, "Majorana fermions in semiconductor nanowires: fundamentals, modeling, and experiment", en, J. Phys.: Condens. Matter **25**, 233201 (2013) (cited on pages 13, 49).

[Sta56] H. Statz, G. A. deMars, L. Davis, and A. Adams, "Surface States on Silicon and Germanium Surfaces", en, Phys. Rev. **101**, 1272 (1956) (cited on page 19).

[Ste12a] D. Stepanenko, M. Rudner, B. I. Halperin, and D. Loss, "Singlet-triplet splitting in double quantum dots due to spin-orbit and hyperfine interactions", en, Phys. Rev. B **85**, 075416 (2012) (cited on pages 110, 164).

[Ste10] M. Stepanova, T. Fito, Z. Szabó, K. Alti, A. P. Adeyenuwo, K. Koshelev, M. Aktary, and S. K. Dew, "Simulation of electron beam lithography of nanostructures", J. Vac. Sci. Technol. B **28**, C6C48 (2010) (cited on pages 73, 74).

[Ste12b] M. Stepanova and S. Dew, editors, *Nanofabrication* (Springer, Vienna, 2012) (cited on pages 66, 69, 77, 143, 176).

[Sto17] A. Stockklauser, P. Scarlino, J. V. Koski, S. Gasparinetti, C. K. Andersen, C. Reichl, W. Wegscheider, T. Ihn, K. Ensslin, and A. Wallraff, "Strong Coupling Cavity QED with Gate-Defined Double Quantum Dots Enabled by a High Impedance Resonator", Physical Review X **7**, 011030 (2017) (cited on pages 5, 79, 152).

[Sto96] T. H. Stoof and Y. V. Nazarov, "Time-dependent resonant tunneling via two discrete states", en, Phys. Rev. B **53**, 1050 (1996) (cited on pages 116, 164).

[Sto12] K. Storm, G. Nylund, L. Samuelson, and A. P. Micolich, "Realizing Lateral Wrap-Gated Nanowire FETs: Controlling Gate Length with Chemistry Rather than Lithography", Nano Lett. **12**, 1 (2012) (cited on page 150).

[Sun18] J. Sun, R. S. Deacon, R. Wang, J. Yao, C. M. Lieber, and K. Ishibashi, "Helical Hole State in Multiple Conduction Modes in Ge/Si Core/Shell Nanowire", en, Nano Lett. **18**, 6144 (2018) (cited on page 9).

[Tak20] K. Takeda, A. Noiri, J. Yoneda, T. Nakajima, and S. Tarucha, "Resonantly Driven Singlet-Triplet Spin Qubit in Silicon", en, Phys. Rev. Lett. **124**, 117701 (2020) (cited on page 5).

[Tak16] K. Takeda, J. Kamioka, T. Otsuka, J. Yoneda, T. Nakajima, M. R. Delbecq, S. Amaha, G. Allison, T. Kodera, S. Oda, and S. Tarucha, "A fault-tolerant addressable spin qubit in a natural silicon quantum dot", Science Advances **2**, e1600694 (2016) (cited on pages 5, 125).

[Tay05] J. M. Taylor, H.-A. Engel, W. Dür, A. Yacoby, C. M. Marcus, P. Zoller, and M. D. Lukin, "Fault-tolerant architecture for quantum computation using electrically controlled semiconductor spins", Nature Phys. **1**, 177 (2005) (cited on page 89).

[Tay13] J. M. Taylor, V. Srinivasa, and J. Medford, "Electrically protected resonant exchange qubits in triple quantum dots", Physical Review Letters **111**, 1 (2013) (cited on page 89).

[Ter15] B. M. Terhal, "Quantum error correction for quantum memories", en, Rev. Mod. Phys. **87**, 307 (2015) (cited on pages 1, 150).

[Ter20] L. A. Terrazos, E. Marcellina, S. N. Coppersmith, M. Friesen, A. R. Hamilton, X. Hu, B. Koiller, A. L. Saraiva, D. Culcer, and R. B. Capaz, "Theory of Hole-Spin Qubits in Strained Germanium Quantum Dots", arXiv:1803.10320 (2020) (cited on pages 7, 22).

[The03] C. Thelander, T. Mårtensson, M. T. Björk, B. J. Ohlsson, M. W. Larsson, L. R. Wallenberg, and L. Samuelson, "Single-electron transistors in heterostructure nanowires", Appl. Phys. Lett. **83**, 2052 (2003) (cited on pages 11, 13).

[Tok06] Y. Tokura, W. G. van der Wiel, T. Obata, and S. Tarucha, "Coherent Single Electron Spin Control in a Slanting Zeeman Field", en, Phys. Rev. Lett. **96**, 047202 (2006) (cited on page 54).

[Tri08] M. Trif, V. N. Golovach, and D. Loss, "Spin dynamics in InAs nanowire quantum dots coupled to a transmission line", en, Phys. Rev. B **77**, 045434 (2008) (cited on pages 103, 109, 112, 128, 130, 132, 152).

[Tri12] L. Trifunovic, O. Dial, M. Trif, J. R. Wootton, R. Abebe, A. Yacoby, and D. Loss, "Long-distance spin-spin coupling via floating gates", Physical Review X **2**, 011006 (2012) (cited on pages 6, 100, 151).

[Tyr12] A. M. Tyryshkin, S. Tojo, J. J. L. Morton, H. Riemann, N. V. Abrosimov, P. Becker, H.-J. Pohl, T. Schenkel, M. L. W. Thewalt, K. M. Itoh, and S. A. Lyon, "Electron spin coherence exceeding seconds in high-purity silicon", Nature Mater **11**, 143 (2012) (cited on page 122).

[Urd19] M. Urdampilleta, D. J. Niegemann, E. Chanrion, B. Jadot, C. Spence, P.-A. Mortemousque, C. Bäuerle, L. Hutin, B. Bertrand, S. Barraud, R. Maurand, M. Sanquer, X. Jehl, S. De Franceschi, M. Vinet, and T. Meunier, "Gate-based high fidelity spin readout in a CMOS device", en, Nat. Nanotechnol. **14**, 737 (2019) (cited on pages 6, 60, 145).

[vdBer13] J. W. G. van den Berg, S. Nadj-Perge, V. S. Pribiag, S. R. Plissard, E. P. A. M. Bakkers, S. M. Frolov, and L. P. Kouwenhoven, "Fast Spin-Orbit Qubit in an Indium Antimonide Nanowire", Physical Review Letters **110**, 066806 (2013) (cited on pages 14, 46, 57, 100, 101, 122).

[vdWie02a] W. G. van der Wiel, S. De Franceschi, J. M. Elzerman, T. Fujisawa, S. Tarucha, and L. P. Kouwenhoven, "Electron transport through double quantum dots", Reviews of Modern Physics **75**, 1 (2002) (cited on pages 29, 94, 116, 164).

[vdWie02b] W. G. van der Wiel, T. H. Oosterkamp, S. de Franceschi, C. J. P. M. Harmans, and L. P. Kouwenhoven, "Photon assisted tunneling in quantum dots", in *Strongly correlated fermions and bosons in low-dimensional disordered systems* (Springer Netherlands, Dordrecht, 2002), pages 43–68 (cited on page 166).

[vdWal86] C. G. van de Walle and R. M. Martin, "Theoretical calculations of heterojunction discontinuities in the Si/Ge system", Physical Review B **34**, 5621 (1986) (cited on page 18).

[Van17] L. M. K. Vandersypen, H. Bluhm, J. S. Clarke, A. S. Dzurak, R. Ishihara, A. Morello, D. J. Reilly, L. R. Schreiber, and M. Veldhorst, "Interfacing spin qubits in quantum dots and donors—hot, dense, and coherent", npj Quantum Information **3**, 34 (2017) (cited on pages 6, 122, 151).

[Van19] L. M. K. Vandersypen and M. A. Eriksson, "Quantum computing with semiconductor spins", en, Physics Today **72**, 38 (2019) (cited on page 3).

[vOpd69] C. J. M. van Opdorp, "Si-Ge isotype heterojunctions", Doctoral Thesis (Eindhoven University of Technology, Eindhoven, 1969) (cited on page 19).

[Vel17] M. Veldhorst, H. G. J. Eenink, C. H. Yang, and A. S. Dzurak, "Silicon CMOS architecture for a spin-based quantum computer", en, Nat Commun **8**, 1766 (2017) (cited on pages 5, 44, 151).

[Vel14] M. Veldhorst, J. C. Hwang, C. H. Yang, A. W. Leenstra, B. De Ronde, J. P. Dehollain, J. T. Muhonen, F. E. Hudson, K. M. Itoh, A. Morello, and A. S. Dzurak, "An addressable quantum dot qubit with fault-tolerant control-fidelity", Nat. Nanotechnol. **9**, 981 (2014) (cited on pages 5, 54, 122, 141).

[Vel15] M. Veldhorst, C. H. Yang, J. C. C. Hwang, W. Huang, J. P. Dehollain, J. T. Muhonen, S. Simmons, A. Laucht, F. E. Hudson, K. M. Itoh, A. Morello, and A. S. Dzurak, "A two-qubit logic gate in silicon", en, Nature **526**, 410 (2015) (cited on pages 5, 122).

[Vil20] B. Villalonga, D. Lyakh, S. Boixo, H. Neven, T. S. Humble, R. Biswas, E. G. Rieffel, A. Ho, and S. Mandrà, "Establishing the quantum supremacy frontier with a 281 Pflop/s simulation", en, Quantum Sci. Technol. **5**, 034003 (2020) (cited on page 1).

[Vol07] C. A. Volkert and A. M. Minor, "Focused Ion Beam Microscopy and Micromachining", MRS Bulletin **32**, 389 (2007) (cited on page 143).

[Vuk17] L. Vukušić, J. Kukučka, H. Watzinger, and G. Katsaros, "Fast Hole Tunneling Times in Germanium Hut Wires Probed by Single-Shot Reflectometry", en, Nano Lett. **17**, 5706 (2017) (cited on page 60).

[Vuk18] L. Vukušić, J. Kukučka, H. Watzinger, J. M. Milem, F. Schäffler, and G. Katsaros, "Single-Shot Readout of Hole Spins in Ge", en, Nano Lett. **18**, 7141 (2018) (cited on pages 8, 46).

[Wag64] R. S. Wagner and W. C. Ellis, "Vapor-Liquid-Solid mechanism of single crystal growth", Applied Physics Letters **4**, 89 (1964) (cited on page 12).

[Wal04] A. Wallraff, D. I. Schuster, A. Blais, L. Frunzio, R. S. Huang, J. Majer, S. Kumar, S. M. Girvin, and R. J. Schoelkopf, "Strong coupling of a single photon to a superconducting qubit using circuit quantum electrodynamics", en, Nature **431**, 162 (2004) (cited on page 151).

[Wan16] D. Q. Wang, O. Klochan, J. T. Hung, D. Culcer, I. Farrer, D. A. Ritchie, and A. R. Hamilton, "Anisotropic Pauli Spin Blockade of Holes in a GaAs Double Quantum Dot", Nano Letters **16**, 7685 (2016) (cited on pages 42, 43, 147).

[Wan03] D. Wang, Q. Wang, A. Javey, R. Tu, H. Dai, H. Kim, P. C. McIntyre, T. Krishnamohan, and K. C. Saraswat, "Germanium nanowire field-effect transistors with SiO2 and high-κ HfO2 gate dielectrics", Appl. Phys. Lett. **83**, 2432 (2003) (cited on page 17).

[Wan18a] K. Wang, H.-O. Li, M. Xiao, G. Cao, and G.-P. Guo, "Spin manipulation in semiconductor quantum dots qubit", Chinese Physics B **27**, 090308 (2018) (cited on pages 43, 53).

[Wan17] R. Wang, R. S. Deacon, J. Yao, C. M. Lieber, and K. Ishibashi, "Electrical modulation of weak-antilocalization and spin-orbit interaction in dual gated Ge/Si core/shell nanowires", Semiconductor Science and Technology **32**, 094002 (2017) (cited on pages 9, 28).

[Wan19a] R. Wang, R. S. Deacon, J. Sun, J. Yao, C. M. Lieber, and K. Ishibashi, "Gate Tunable Hole Charge Qubit Formed in a Ge/Si Nanowire Double Quantum Dot Coupled to Microwave Photons", Nano Letters **19**, 1052 (2019) (cited on pages 8, 78, 152).

[Wan18b] J.-Y. Wang, G.-Y. Huang, S. Huang, J. Xue, D. Pan, J. Zhao, and H. Xu, "Anisotropic Pauli Spin-Blockade Effect and Spin-Orbit Interaction Field in an InAs Nanowire Double Quantum Dot", Nano Letters **18**, 4741 (2018) (cited on page 147).

[Wan19b] Z. Wang, E. Marcellina, A. R. Hamilton, S. Rogge, J. Salfi, and D. Culcer, "Suppressing charge-noise sensitivity in high-speed Ge hole spin-orbit qubits", en, arXiv:1911.11143, 1 (2019) (cited on pages 46, 65, 147).

[Wat18a] T. F. Watson, S. G. J. Philips, E. Kawakami, D. R. Ward, P. Scarlino, M. Veldhorst, D. E. Savage, M. G. Lagally, M. Friesen, S. N. Coppersmith, M. A. Eriksson, and L. M. K. Vandersypen, "A programmable two-qubit quantum processor in silicon", en, Nature **555**, 633 (2018) (cited on pages 5, 122).

[Wat16] H. Watzinger, C. Kloeffel, L. Vukušić, M. D. Rossell, V. Sessi, J. Kukučka, R. Kirchschlager, E. Lausecker, A. Truhlar, M. Glaser, A. Rastelli, A. Fuhrer, D. Loss, and G. Katsaros, "Heavy-Hole States in Germanium Hut Wires", en, Nano Lett. **16**, 6879 (2016) (cited on pages 7, 22).

[Wat18b] H. Watzinger, J. Kukučka, L. Vukušić, F. Gao, T. Wang, F. Schäffler, J.-J. Zhang, and G. Katsaros, "A germanium hole spin qubit", Nature Communications **9**, 3902 (2018) (cited on pages 8, 46, 57, 101, 122, 127).

[Web17] W. M. Weber and T. Mikolajick, "Silicon and germanium nanowire electronics: physics of conventional and unconventional transistors", en, Rep. Prog. Phys. **80**, 066502 (2017) (cited on page 21).

[Wen19] X. Weng, J. Yang, D. Li, R. Wang, F. Qiu, C. Wang, and Y. Yang, "Review of the Preparation and Structures of Si Nanowires, Ge Quantum Dots and Their Composites", Nano **14**, 1930004 (2019) (cited on pages 18, 141).

[Wer16] F. Werschler, C. Hinz, F. Froning, P. Gumbsheimer, J. Haase, C. Negele, T. de Roo, S. Mecking, A. Leitenstorfer, and D. V. Seletskiy, "Coupling of Excitons and Discrete Acoustic Phonons in Vibrationally Isolated Quantum Emitters", en, Nano Lett. **16**, 5861 (2016) (cited on page 216).

[Wes19] A. West, B. Hensen, A. Jouan, T. Tanttu, C.-H. Yang, A. Rossi, M. F. Gonzalez-Zalba, F. Hudson, A. Morello, D. J. Reilly, and A. S. Dzurak, "Gate-based single-shot readout of spins in silicon", Nat. Nanotechnol. **14**, 437 (2019) (cited on pages 6, 59, 60, 145).

[Wil01] G. D. Wilk, R. M. Wallace, and J. M. Anthony, "High-κ gate dielectrics: Current status and materials properties considerations", Journal of Applied Physics **89**, 5243 (2001) (cited on page 77).

[Win03] R. Winkler, *Spin-Orbit Coupling Effects in Two-Dimensional Electron and Hole Systems*, edited by G. Höhler, J. H. Kühn, T. Müller, J. Trümper, A. Ruckenstein, P. Wölfle, and F. Steiner, Vol. 191, Springer Tracts in Modern Physics (Springer, Berlin, Heidelberg, 2003) (cited on pages 26, 55, 100).

[Win09] D. Winston, B. M. Cord, B. Ming, D. C. Bell, W. F. DiNatale, L. A. Stern, A. E. Vladar, M. T. Postek, M. K. Mondol, J. K. W. Yang, and K. K. Berggren, "Scanning-helium-ion-beam lithography with hydrogen silsesquioxane resist", Journal of Vacuum Science & Technology B **27**, 2702 (2009) (cited on page 143).

[Wu14] X. Wu, D. R. Ward, J. R. Prance, D. Kim, J. K. Gamble, R. T. Mohr, Z. Shi, D. E. Savage, M. G. Lagally, M. Friesen, S. N. Coppersmith, and M. A. Eriksson, "Two-axis control of a singlet-triplet qubit with an integrated micromagnet", en, Proceedings of the National Academy of Sciences **111**, 11938 (2014) (cited on page 5).

[Wu01] Y. Wu and P. Yang, "Direct observation of vapor-liquid-solid nanowire growth", Journal of the American Chemical Society **123**, 3165 (2001) (cited on page 67).

[Xia06] J. Xiang, W. Lu, Y. Hu, Y. Wu, H. Yan, and C. M. Lieber, "Ge/Si nanowire heterostructures as high-performance field-effect transistors", en, Nature **441**, 489 (2006) (cited on page 20).

[Xu20a] G. Xu, F. Gao, K. Wang, T. Zhang, H. Liu, G. Cao, T. Wang, J.-J. Zhang, H.-W. Jiang, H.-O. Li, and G.-P. Guo, "Hole spin in tunable Ge hut wire double quantum dot", en, Appl. Phys. Express **13**, 065002 (2020) (cited on page 8).

[Xu20b] G. Xu, Y. Li, F. Gao, H.-O. Li, H. Liu, K. Wang, G. Cao, T. Wang, J.-J. Zhang, G.-C. Guo, and G.-P. Guo, "Dipole coupling of a hole double quantum dot in germanium hut wire to a microwave resonator", New J. Phys. **22**, 083068 (2020) (cited on page 8).

[Yan20] C. H. Yang, R. C. C. Leon, J. C. C. Hwang, A. Saraiva, T. Tanttu, W. Huang, J. C. Lemyre, K. W. Chan, K. Y. Tan, F. E. Hudson, K. M. Itoh, A. Morello, M. Pioro-Ladrière, A. Laucht, and A. S. Dzurak, "Operation of a silicon quantum processor unit cell above one kelvin", en, Nature **580**, 350 (2020) (cited on pages 6, 59).

[Yan13] C. H. Yang, A. Rossi, R. Ruskov, N. S. Lai, F. A. Mohiyaddin, S. Lee, C. Tahan, G. Klimeck, A. Morello, and A. S. Dzurak, "Spin-valley lifetimes in a silicon quantum dot with tunable valley splitting", en, Nat. Commun. **4**, 2069 (2013) (cited on pages 102, 122).

[Yan08] L. Yang, R. N. Musin, X.-Q. Wang, and M. Y. Chou, "Quantum confinement effect in Si/Ge core-shell nanowires: First-principles calculations", en, Phys. Rev. B **77**, 195325 (2008) (cited on pages 20–22).

[Yon14] J. Yoneda, T. Otsuka, T. Nakajima, T. Takakura, T. Obata, M. Pioro-Ladrière, H. Lu, C. J. Palmstrøm, A. C. Gossard, and S. Tarucha, "Fast Electrical Control of Single Electron Spins in Quantum Dots with Vanishing Influence from Nuclear Spins", en, Phys. Rev. Lett. **113**, 267601 (2014) (cited on pages 101, 125).

[Yon20] J. Yoneda, K. Takeda, A. Noiri, T. Nakajima, S. Li, J. Kamioka, T. Kodera, and S. Tarucha, "Quantum non-demolition readout of an electron spin in silicon", Nature Communications **11**, 1 (2020) (cited on page 6).

[Yon18] J. Yoneda, K. Takeda, T. Otsuka, T. Nakajima, M. R. Delbecq, G. Allison, T. Honda, T. Kodera, S. Oda, Y. Hoshi, N. Usami, K. M. Itoh, and S. Tarucha, "A quantum-dot spin qubit with coherence limited by charge noise and fidelity higher than 99.9%", en, Nature Nanotech **13**, 102 (2018) (cited on pages 5, 65, 101, 122).

[Zaj16] D. M. Zajac, T. M. Hazard, X. Mi, E. Nielsen, and J. R. Petta, "Scalable Gate Architecture for a One-Dimensional Array of Semiconductor Spin Qubits", Physical Review Applied **6**, 054013 (2016) (cited on page 36).

[Zaj18] D. M. Zajac, A. J. Sigillito, M. Russ, F. Borjans, J. M. Taylor, G. Burkard, and J. R. Petta, "Resonantly driven CNOT gate for electron spins", Science **359**, 439 (2018) (cited on pages 5, 122).

[Zar17] A. Zarassi, Z. Su, J. Danon, J. Schwenderling, M. Hocevar, B. M. Nguyen, J. Yoo, S. A. Dayeh, and S. M. Frolov, "Magnetic field evolution of spin blockade in Ge/Si nanowire double quantum dots", Physical Review B **95**, 155416 (2017) (cited on pages 43, 95, 97, 102, 104, 105).

[Zha16] A. Zhang, G. Zheng, and C. M. Lieber, *Nanowires - Building Blocks for Nanoscience and Nanotechnology*, NanoScience and Technology (Springer International Publishing, Cham, 2016) (cited on pages 12, 13, 17, 66).

[Zha10] S. Zhang, F. J. Lopez, J. K. Hyun, and L. J. Lauhon, "Direct Detection of Hole Gas in Ge-Si Core-Shell Nanowires by Enhanced Raman Scattering", Nano Letters **10**, 4483 (2010) (cited on pages 20, 22).

[Zha18] X. Zhang, W. Jevasuwan, K. C. Pradel, T. Subramani, T. Takei, and N. Fukata, "Hole gas accumulation in Si/Ge core-shell and Si/Ge/Si core-double shell nanowires", Nanoscale **10**, 21062 (2018) (cited on page 20).

[Zhe19] G. Zheng, N. Samkharadze, M. L. Noordam, N. Kalhor, D. Brousse, A. Sammak, G. Scappucci, and L. M. K. Vandersypen, "Rapid gate-based spin read-out in silicon using an on-chip resonator", en, Nat. Nanotechnol. **14**, 742 (2019) (cited on pages 6, 146).

[Zwa13] F. A. Zwanenburg, A. S. Dzurak, A. Morello, M. Y. Simmons, L. C. L. Hollenberg, G. Klimeck, S. Rogge, S. N. Coppersmith, and M. A. Eriksson, "Silicon quantum electronics", Reviews of Modern Physics **85**, 961 (2013) (cited on pages 5, 17, 25, 122).

[Zwa09] F. A. Zwanenburg, C. E. W. M. van Rijmenam, Y. Fang, C. M. Lieber, and L. P. Kouwenhoven, "Spin States of the First Four Holes in a Silicon Nanowire Quantum Dot", Nano Lett. **9**, 1071 (2009) (cited on page 14).

Acknowledegment

I would like to thank Prof. Dominik Zumbühl for giving me the opportunity to work on this very exciting project and for supervising my PhD. Thank you for all the support, and everything I could learn about physics, lab work, and many other things. I enjoyed all the fantastic dinners, BBQs and excursions.

A very special thanks goes to Dr. Floris Braakman. I am very grateful for all the scientific as well as personal input and guidance, all your efforts regarding this project and I am sorry for the hard times that I gave you sometimes.

At this point I would also like to thank Prof. Menno Veldhorst and Prof. Georgios Katsaros for their time and engagement in my PhD committee.

Next, I would like to thank the whole Ge/Si team, which has grown tremendously in the past years. Considering the small team from where we started off, I am very happy that the project attracted so many smart people who eased the workload and contributed knowledge and ideas.

Dr. Leon Camenzind, thank you for joining the team and boosting the progress that we had in the past two years. Although our fast work pace sometimes posed a challenge to me, I enjoyed our common time in the lab as well as the time off, with beers, burgers and interesting discussions. Thank you for all your efforts, the numerous scientific discussions, for proof-reading my thesis and the general support in all kinds of questions.

Dr. Mirko Rehmann, you are probably the calmest and relaxed person that I know. Thanks for joining the team, your scientific contributions and the support. You truly reminded me more than once that there is more to life than our bubble of scientific problems. I enjoyed discussing with you and listening to your points of view.

Miguel J. Carballido, so many times that we thought the same nonsense. Thanks for your contributions to the project as well as all the enliving and funny moments.

Last but not least I would like to thank Fabian Müller, for your hard work during your Master thesis, and our newest team members, Pierre Chevallier-Kwon and Simon Svab.

Many things we see in the lab need a proper interpretation with regard to the theory. Therefore, thank you a lot Dr. Christoph Kloeffel and Prof. Daniel Loss, for the nice explanations, your general support of the Ge/Si project and, Daniel, for the participation as chairman of my committee.

To the nice everyday work environment many more people contributed and should be mentioned here. Thank you Dr. Pirmin Weigele and Dr. Mario Palma. I enjoyed the

time together a lot and thank you, Pirmin, for the insights into the life hurdles of a Swabian in Switzerland. And Mario, I think every group needs a vivid Italian member like you. Thanks to Dr. Bilal Kalyoncu, for interesting discussions and leaving the nice office desk including the plants. Furthermore and in no particular order, Dr. Christian Scheller, Dr. Taras Patlatiuk, Henok Weldeyesus, Dr. Mohammad Samani, Simon Geyer, Dr. Andreas Kuhlmann, Dr. Liuqi Yu and Orson van der Molen. Thank you all for all the funny moments as well as serious scientific discussions. Lastly, thanks to all other current and former group members.

Much work in the lab requires input and hands-on work from the workshop staff. In particular, I would like to thank Dominik Sifrig, for always being helpful with short-term and unforeseen Helium issues. Thanks also to Patrick Stöcklin, Sascha Martin, Davide Mastrapasqua, Michael Steinacher and Sascha Linder.

I am very grateful for the administrative support of Barbara Kammerman, Astrid Kalt, Stephan Weitnauer and Mile Mirkovic, who were and are always eager to help out where necessary. Thanks for the support and sorry for all the wrong travel expense forms.

I would also like to thank the countless other members of the Department of Physics which I met and had funny and informative conversations as well as a good time with.

The base for this thesis was laid already much earlier, thus I would like to thank everyone who accompanied me during my time in Konstanz. Thanks so much for all the great experiences and see you soon!

Finally, I would like to thank my family, especially my parents Gisela and Reinhold, for their long-time support. Thank you!

Curriculum Vitae

Florian Norbert Matthias Froning

Born	30.04.1991 in Ludwigsburg, Germany
Citizenship	German

2016 - 2020	**PhD** in Experimental Physics
	University of Basel, Switzerland
	Title: *Hole Spin Qubits in Ge/Si Core/Shell Nanowires*
	Advisor: Prof. Dominik Zumbühl and Dr. Floris Braakman
Sep. 2015	**Master thesis**
	Title: *Elementare Wechselwirkungen in einzelnen kolloidalen Halbleiter-Quantenpunkten und plamonischen Nanoantennen*
	Advisor: Prof. Alfred Leitenstorfer
2013 - 2015	**Master of Science** in Physics
	University of Konstanz, Germany
Aug. 2013	**Bachelor thesis** at Trumpf Inc., Farmington, CT, USA
	Title: *Multi-Kilowatt Coaxial RF-Excited Carbon Monoxide Laser for Metal Cutting Application*
	Advisors: Prof. Alfred Leitenstorfer (U Konstanz) and
	Dr. Francisco Villareal (Trumpf Inc.)
2010 - 2013	**Bachelor of Science** in Physics
	University of Konstanz, Germany
2001 - 2010	**Abitur**
	Mörike-Gymnasium Ludwigsburg, Germany
1997 - 2001	**Elementary School**
	Oststadtschule Ludwigsburg, Germany
	Deutsche Schule Madrid, Spain

List of Publications

1. F. N. M. Froning, L. C. Camenzind, O. A. H. van der Molen, A. Li, E. P. A. M. Bakkers, D. M. Zumbühl, and F. R. Braakman, "Ultrafast hole spin qubit with gate-tunable spin–orbit switch functionality", Nat. Nanotechnol. **16**, 308 (2021)

2. F. N. M. Froning, M. J. Rančić, B. Hetényi, S. Bosco, M. K. Rehmann, A. Li, E. P. A. M. Bakkers, F. A. Zwanenburg, D. Loss, D. M. Zumbühl, and F. R. Braakman, "Strong spin-orbit interaction and g -factor renormalization of hole spins in Ge/Si nanowire quantum dots", Phys. Rev. Research **3**, 013081 (2021)

3. F. N. M. Froning, M. K. Rehmann, J. Ridderbos, M. Brauns, F. A. Zwanenburg, A. Li, E. P. A. M. Bakkers, D. M. Zumbühl, and F. R. Braakman, "Single, double, and triple quantum dots in Ge/Si nanowires", Applied Physics Letters **113**, 073102 (2018)

4. M. Palma, D. Maradan, L. Casparis, T.-M. Liu, F. N. M. Froning, and D. M. Zumbühl, "Magnetic cooling for microkelvin nanoelectronics on a cryofree platform", en, Rev. Sci. Instrum. **88**, 043902 (2017)

5. F. Werschler, C. Hinz, F. Froning, P. Gumbsheimer, J. Haase, C. Negele, T. de Roo, S. Mecking, A. Leitenstorfer, and D. V. Seletskiy, "Coupling of Excitons and Discrete Acoustic Phonons in Vibrationally Isolated Quantum Emitters", en, Nano Lett. **16**, 5861 (2016)